Ferry-observed variability of currents and bedforms in the Marsdiep inlet

Ferry-observed variability of currents and bedforms in the Marsdiep inlet

Variabiliteit van stromingen en bodemvormen
gemeten vanaf een veerboot in het Marsdiep

(met een samenvatting in het Nederlands)

PROEFSCHRIFT

ter verkrijging van de graad van doctor aan de Universiteit Utrecht
op gezag van de rector magnificus, prof. dr. W.H. Gispen,
ingevolge het besluit van het college voor promoties
in het openbaar te verdedigen op
woensdag 10 oktober 2007 des middags om 2.30 uur

door

Maarten Cornelis Buijsman

geboren op 28 november 1973 te Den Helder

Promotores: Prof. dr. J.T.F. Zimmerman
Prof. dr. ir. H. Ridderinkhof

Contents

Chapter 1

Introduction

This thesis presents analyses of unique long-term observations of currents and bedforms obtained with ferry and vessel-mounted ADCPs in the Marsdiep tidal inlet, the Netherlands (Fig. 1.1). The general objectives are to determine the influence of tides, density differences, and wind on water transport and currents and explain their relation to sediment transport and bedform migration. In this introductory chapter, the general importance of tidal inlets is discussed first. In the Tidal inlets worldwide section, the studies performed in the Marsdiep inlet are placed in a larger context. In the following section, the study area is presented and the physics and the geomorphodynamics of the Marsdiep inlet are described. Finally, the research questions and approach of this thesis are discussed.

1.1 The general importance of tidal inlets

A tidal inlet is a strait that connects the ocean with a shallow basin, such as an estuary or a lagoon. The tidal currents in the strait keep the inlet open. Tidal inlets have important economic and natural values. They facilitate harbours and population centres. Inlets are used for navigation, sand mining, fishing, and recreation. Inlets also have important ecological values: they harbour a rich biodiversity (Day, 1989). Maintaining this biodiversity has an important economic feedback. Moreover, tidal inlets play a critical role in the sediment budgets of adjacent sandy coasts (e.g. Oertel, 1988; Louters and Gerritsen, 1994; Komar, 1996; Elias et al., 2003). For example, tidal basins can act as sinks in the case of relative sea-level rise. As a consequence, the sediment transport pathways along the coast are affected and the increased demand from the tidal basin may lead to coastal erosion.

To better comprehend the influence of man and nature on tidal inlets, it is important to determine and understand the physical processes, e.g. currents and sediment transport, in tidal inlets. In the Marsdiep tidal inlet this is done with the ferry 'Schulpengat' (Fig. 1.2) that has continuously measured, since 1998, oceanographic parameters such as currents, temperature, and salinity (Ridderinkhof et al., 2002). Using a ferry has several advantages: the regular collection of data allows for the observation of the spatial and temporal variability in these parameters, and the costs are significantly reduced compared to a dedicated survey vessel that sails at the same frequency. Aboard the ferry Schulpengat, passengers can watch screens that display real-time measurements of current velocity,
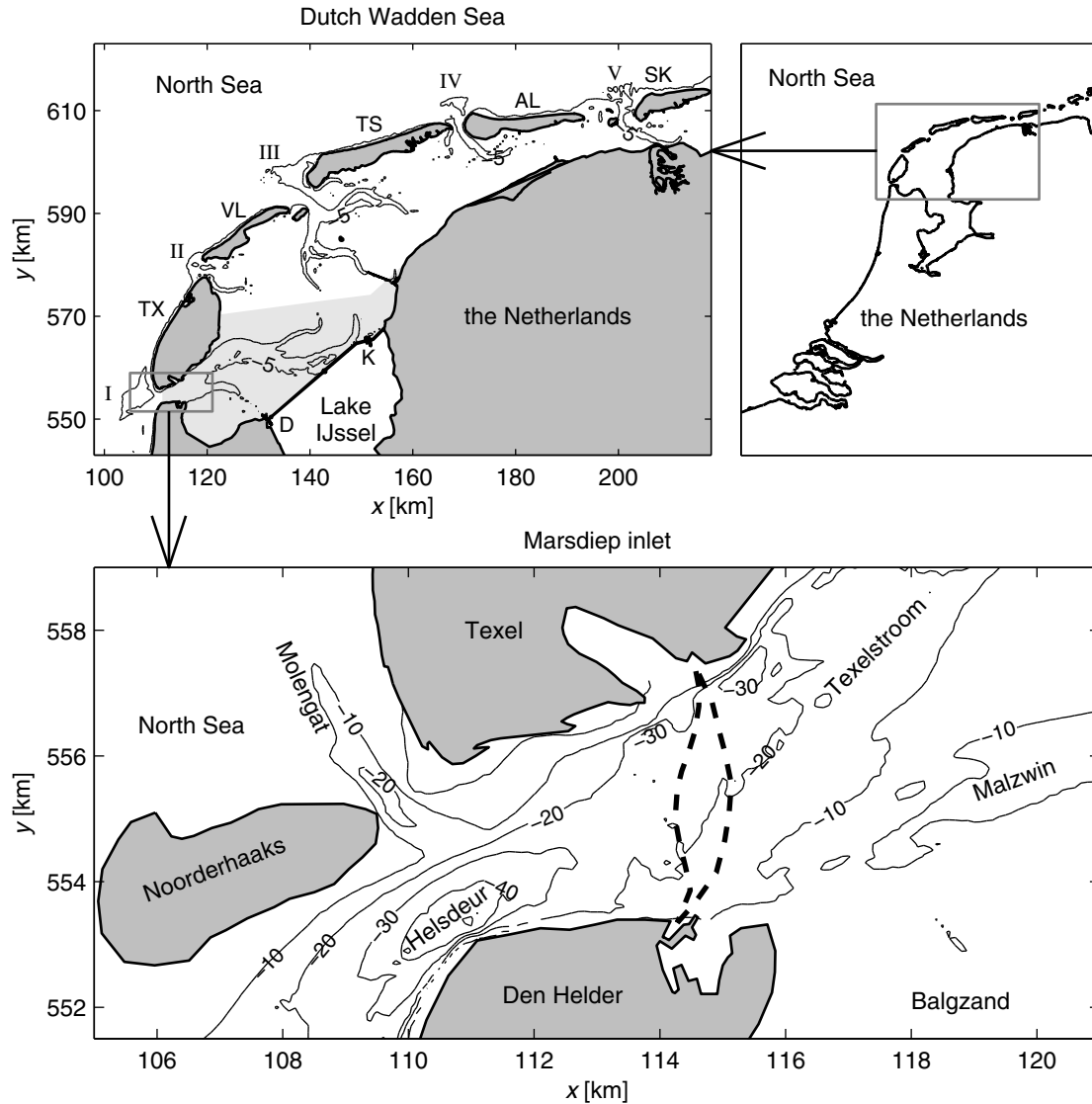
Figure 1.1. The Marsdiep inlet (bottom panel) in the western Dutch Wadden Sea (top left panel). In the top left panel, the Marsdiep basin is indicated by the light-grey shaded plane. The islands of Texel, Vlieland, Terschelling, Ameland, and Schiermonnikoog are abbreviated with TX, VL, TS, AL, and SK, respectively. The Marsdiep, Eierland, Vlie, Ameland, and Frisian inlets are marked by numerals I-V, respectively. The Lake IJssel sluices at Den Oever and Kornwerderzand are abbreviated with D and K. In the bottom panel the envelope of ferry crossings is marked by the dashed line. The bathymetry is contoured in [m] relative to mean sea level.

temperature, and salinity. This is another advantage of the ferry observations: it brings science closer to the general public. Other studies in which ferries have been used to monitor physical processes in marine water bodies include Hanawa et al. (1996), Takikawa et al. (2003), Petersen et al. (2004), Takikawa et al. (2005), and Codiga and Aurin (2007).

Figure 1.2. The ferry Schulpengat in the Marsdiep inlet. Photo by Oscar Bos.

1.2   Tidal inlets worldwide

Tidal inlets can be found on coastal plains, i.e. barrier tidal inlets, and along high relief coasts, i.e. drowned river valley inlets or river tidal inlets (Dronkers, 2005). Examples of these inlet types are shown in Fig. 1.3. Barrier tidal inlets form after barrier breaching due to storms and transgression of the coastal plain due to sea-level rise. Generally, there is little river inflow into barrier tidal inlets. As a consequence, the dominant processes are the tides and waves. Due to the relative unimportance of river inflow, most of the sediment in the basin originates from the ocean. Examples of barrier tidal inlets include the inlets of the Wadden Sea and the Eastern Scheldt in the Netherlands and the inlets along the US Atlantic coast. In contrast to barrier tidal inlets, freshwater inflow from rivers strongly affects the dynamics in river tidal inlets. The river brings muddy sediments to the basin, while sand can be imported from the ocean. Examples of river tidal inlets are the Columbia River, the Hudson, Delaware Bay, and Chesapeake Bay in the US, the Thames and Humber in Great Britain, and the Seine and Gironde in France.

Physical processes in these inlets, such as water flow and the dispersal of sediments and dissolved matter, have been investigated in numerous studies. Some of these studies have similarities to studies in the Marsdiep inlet and they are listed below. Examples of studies in barrier tidal inlets are: Li (2002) measured tidal currents in Sand Shoal inlet along the US Atlantic coast; Hench and Luettich Jr. (2003) analysed transient momentum balances with a numerical model in Beaufort inlet along the US Atlantic coast; Bartholdy et al. (2002) documented bedform characteristics in the Gradyb inlet in the Danish Wadden Sea; Bruun (1978) discussed the stability of barrier tidal inlets and presented engineering solutions. Examples of studies in river tidal inlets are: Pape III and Garvine (1982) studied the subtidal circulation in Delaware Bay; Carter and Pritchard (1988) provided a description of the oceanography of Chesapeake Bay; Valle-Levinson et al. (1998) observed tidal and subtidal flows in the entrance of Chesapeake Bay; Jay and Smith (1990) analysed the variability in tidal and subtidal flows and the salt balance in the Columbia River estuary; Sherwood et al. (1990) studied bathymetric change, sediment transport, and bedforms in the Columbia River estuary; Preddy (1954) applied a simple analytical model
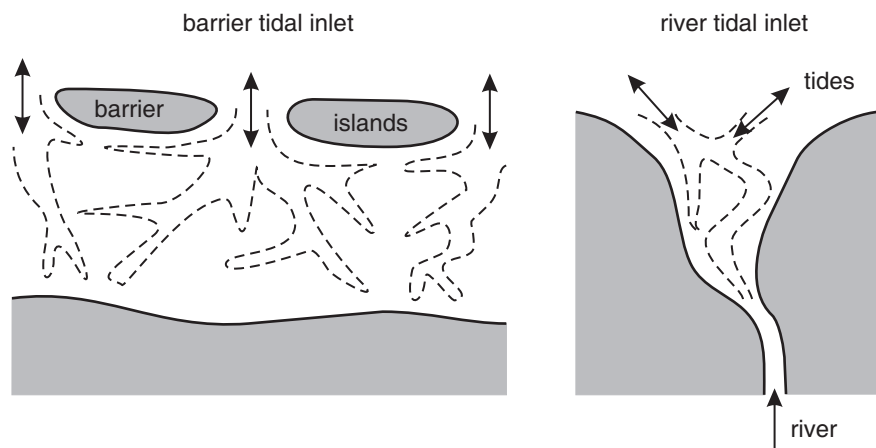
Figure 1.3. Barrier and river tidal inlets (Dronkers, 2005). Dark shades indicate land and dashed lines indicate tidal channels.

of the dispersal of dissolved matter to the Thames estuary; Le Hir et al. (2001) observed and modelled transport of fine sediment in the Seine estuary.

The Marsdiep inlet can be typified as a barrier tidal inlet, but it also has characteristics of a river tidal inlet due to the discharge of freshwater into the basin. However, the mud content in this freshwater is very low. The Marsdiep inlet has been subject to similar studies by Postma (1954) who presented observations of the hydrography, sediment transport, and chemistry, by Zimmerman (1976a) who studied mixing with an analytical model, by Zimmerman (1976b) who developed a theory for residual eddies, by Ridderinkhof (1990) who applied a hydrodynamic numerical model to study mixing and dispersion, by Sha (1990) who considered the geology of the inlet and ebb-tidal delta, and by Elias (2006) who applied a morphodynamic numerical model. The physical processes and the geomorphodynamics of the Marsdiep inlet are further discussed in the next section.

1.3   The Marsdiep tidal inlet

1.3.1   Overview of the study area

The Marsdiep tidal inlet is located in the western Dutch Wadden Sea (Fig. 1.1). The Wadden Sea consists of a string of barrier islands that runs from the Netherlands to Denmark and shallow tidal basins that drain through the inlets between the islands (Postma, 1982). These basins feature deep tidal channels flanked by shallow mud flats. The Marsdiep inlet, also called Texel inlet, is located between the mainland city of Den Helder and the barrier island Texel and drains the Marsdiep tidal basin. The Marsdiep basin has a horizontal area of about 600 km^2 and a mean depth of about 4.5 m (Ridderinkhof, 1988b). The inlet features a minimum width of about 2.5 km and a maximum depth of 53 m. At the ferry transect the inlet is about 4 km wide and maximally 27 m deep. The inlet channel bifurcates in the Texelstroom and Malzwin channels. Branches of the Texelstroom channel are connected with channels of the adjacent Vlie basin, located to the north.
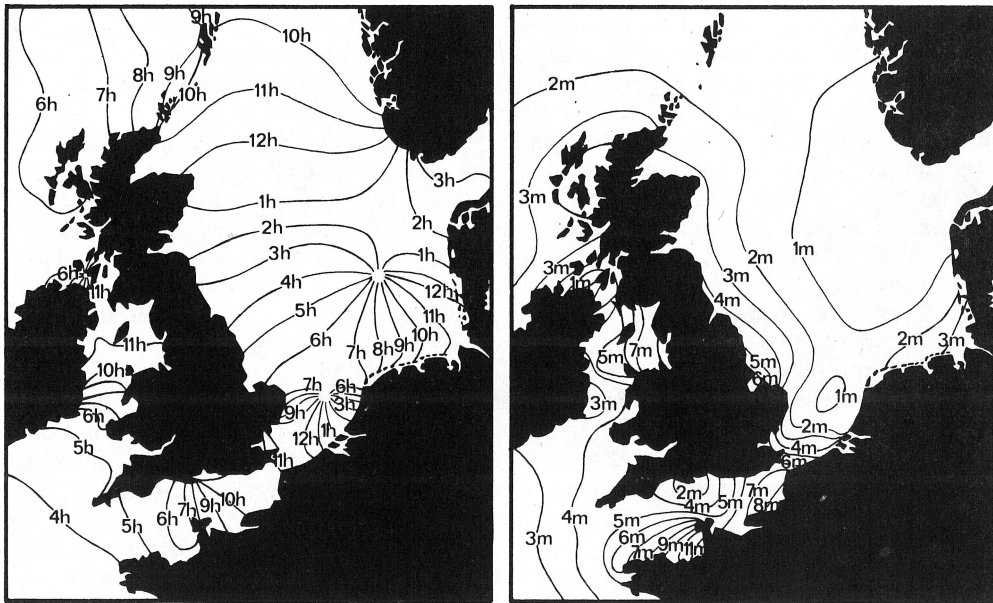
Figure 1.4. Left panel shows contours of equal times of high water and right panel shows the tidal range during spring tide in the North Sea (Postma, 1982). The tidal wave that enters the North Sea from the Atlantic Ocean rotates counterclockwise around two amphidromic points in the North Sea.

1.3.2 Physical processes

Tides

Tides are one of the most important physical processes in the western Wadden Sea (e.g. Postma, 1954; Zimmerman, 1976a,b; Ridderinkhof, 1990). Astronomic tidal waves, of which the semi-diurnal frequencies M_2 and S_2 are the most important, enter the northern North Sea from the Atlantic Ocean and propagate as Kelvin waves southward along the east coast of England (Hansen, 1952). The semi-diurnal tidal wave rotates counterclockwise around two amphidromic points, one located in the southern North Sea between the Netherlands and England and one to the west of Denmark (Fig. 1.4), and proceeds northward along the Belgian, Dutch, German, and Danish coasts. As a consequence, the tidal wave first arrives at the Marsdiep inlet and about 3 h later at the island of Schiermonnikoog (Fig. 1.1). The mean tidal range is about 1.4 m at Den Helder and 2.3 m at Schiermonnikoog. The tidal waves enter the inlets, propagate through the channels, and meet behind the barriers at the watersheds. Since the tidal wave enters each subsequent inlet about 45 min later, the watersheds are located closer to the downstream inlet. The watershed between the Marsdiep and Vlie basins is not closed and allows for exchange of water between the basins (Zimmerman, 1976a; Ridderinkhof, 1990). The tidal wave is reflected at the end of the basin. Bottom friction decreases the amplitude of the reflected wave and this causes the tidal wave in the inlet channel to be between progressive and standing (i.e. the tidal currents reverse about 1-2 h after high water; Postma, 1982).

The tidal currents that result from longitudinal water-level gradients are strong in the tidal inlets (up to $2 \, \text{m s}^{-1}$) and decrease in landward direction. In the western Wadden Sea,

the rise of the water levels is faster than the descent. As a consequence, the flood currents are stronger than the ebb currents, but the ebb duration is longer (Postma, 1982). Tides also generate mean currents, i.e. residual eddies and throughflow. The residual eddies feature mean velocities of $\mathcal{O}(0.1 \text{ m s}^{-1})$ and have horizontal dimensions of $\mathcal{O}(1 \text{ km})$ and result from the interaction of the tidal currents with the channel bathymetry (Zimmerman, 1976b; Ridderinkhof, 1989). These residual eddies are important for the longitudinal diffusion of dissolved matter (e.g. salinity and nutrients). With a numerical model, Ridderinkhof (1988a) computed a mean throughflow from the Vlie to the Marsdiep basin. Ridderinkhof (1988b) used a simple analytical model to illustrate that the throughflow is due to tidal stresses. The tidal stresses are governed by a larger tidal water-level amplitude at the Vlie compared to the Marsdiep inlet.

Freshwater discharge

The salinity in the Marsdiep and Vlie tidal basins is primarily governed by freshwater discharge from the Lake IJssel sluices at Den Oever and Kornwerderzand that are located at the landward ends of the Malzwin and Texelstroom channels, respectively (Fig. 1.1), and to a smaller degree by freshwater discharge from the Rhine river that flows northward along the Dutch North Sea coast (Zimmerman, 1976a). The total mean discharge from the sluices is about 450 m^3 s^{-1} (Ridderinkhof, 1990). Due to the discharge of fresh water into the Marsdiep basin, it can be regarded an estuary. Based on observations, Postma (1954) argued that the strong tidal currents in the Marsdiep basin mix the freshwater through the water column, reducing stratification and estuarine circulation (i.e. surface outflow and bottom inflow due to longitudinal baroclinic pressure gradients; Hansen and Rattray, 1965).

The ratio between tidal mixing and buoyancy input can be expressed in the estuarine Richardson number Ri_e (Fischer et al., 1979):

$$Ri_e = \frac{\Delta \rho g Q_f}{\rho B U^3}, \tag{1.1}$$

where $\rho = 1000$ kg m^{-3} is the density, $\Delta \rho = 25$ kg m^{-3} the difference in density between freshwater and ocean water, $g = 9.81$ m s^{-2} the gravitational acceleration, $Q_f = 450$ m^3 s^{-1} the freshwater discharge, $B = 4000$ m the width of the inlet at the ferry transect, and $U = 0.8$ m s^{-1} the root-mean-square tidal velocity. Substituting these values in Eq. (1.1) yields $Ri_e = 0.05$, which indicates that the Marsdiep tidal basin is indeed a well-mixed estuary. The transition from a well-mixed to a stratified estuary occurs for $0.08 < Ri_e < 0.8$.

Although Eq. (1.1) suggests that the Marsdiep inlet is well-mixed, this does not have to be the case during the entire tidal cycle. The interaction of the tidal currents with the discharge of freshwater causes transient density gradients and stratification. Horizontal density gradients drive estuarine circulation and secondary (cross-channel) currents (e.g. Nunes and Simpson, 1985; Dronkers, 1996; Lacy and Monismith, 2001) and stratification dampens turbulent mixing (e.g. Munk and Anderson, 1948; Miles, 1961). The influence of transient density gradients and stratification on currents in the Marsdiep inlet has never been determined.

Wind

Local winds cause water transport through the inlets and may push water over the watersheds of the Wadden Sea into the adjacent tidal basins. Zimmerman (1976a) observed, by means of salinity distributions, that southwesterly winds push water from the Marsdiep to the Vlie basin and northerly winds govern a transport in the opposite direction. Remote winds on the ocean set up water levels along the coast and this may also cause a water transport through the inlets (coastal pumping; Garvine, 1985). The influence of wind on the hydrodynamics in the Marsdiep inlet has not yet been quantified.

1.3.3   Geomorphodynamics

Sediment transport

On average, sediments in the western Wadden Sea consist of about 83% sand (> 63 μm) and 17% mud (< 63 μm; Van Ledden, 2003). The median grain sizes increase with increasing current strength and wave action. As a consequence, sediments are coarsest and sandiest in the inlet channels (> 400 μm) and become gradually finer and muddier in landward direction (Postma, 1954; Postma, 1957; Winkelmolen and Veenstra, 1974; Sha, 1990). Most of the sediments in the western Wadden Sea are imported through the tidal inlets, whereas the direct supply from rivers into the basins is negligible. The transport mechanisms and directions of the transport have been the subject of debate. Fine grains are transported as suspended load, while coarse grains are transported as bedload. Postma (1961) argued that there is a net influx of fine sediment into the Wadden Sea due to differences in settling and scour lag, inward decrease of tidal-current velocities and depth, and the asymmetric shape of the current-velocity curve in the small tidal channels. These mechanisms have been studied with simple analytical models by Groen (1967) and Ridderinkhof (1997). Bedload transport is governed by local instantaneous currents. Time-mean bedload transport is due to tidal asymmetries (e.g. Pingree and Griffiths, 1979; Van de Kreeke and Robaczewska, 1993; Hoitink et al., 2003) and due to residual currents caused by tides and storms.

Bedforms

The interaction of the tidal currents with the sandy sea bed allows small perturbations to grow to ripples and dunes or sand waves (Fig. 1.5; Engelund and Fredsoe, 1982; Hulscher et al., 1993; Hulscher, 1996; Besio et al., 2006). As the currents increase, suspension transport becomes more dominant and eventually the sand waves are washed out (upper stage plane bed; Dyer, 1986). A further increase of the current velocities (super critical flow, Froude numbers > 1) leads to the formation of anti-dunes, which migrate upstream. Sand waves with lengths of $\mathcal{O}(100$ m) and heights of $\mathcal{O}(1$ m) and superposed megaripples are common bedform features in the North Sea (e.g. Van Veen, 1935; McCave, 1971) and the Marsdiep tidal inlet (Sha, 1986; Elias et al., 2006). While the sand waves in the North Sea have received considerable attention, the spatial and temporal variability in sand-wave shape and migration in the Marsdiep inlet is poorly documented. The asymmetry of sand waves and their migration direction may provide insight in the sediment transport

ripples   dunes   antidunes
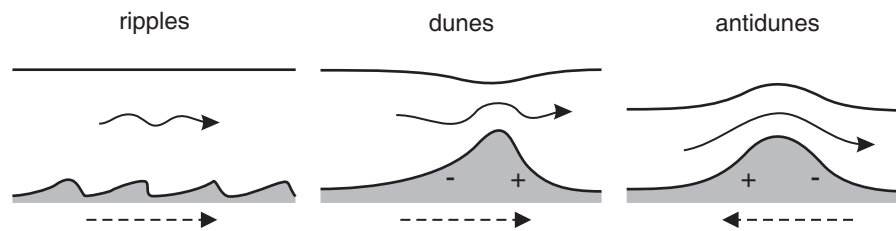
Figure 1.5. Diagrammatic representation of the flow over ripples, dunes, and anti-dunes (Dyer, 1986). Solid curly (dashed straight) arrows indicate direction of water motion (bedform migration). + (-) refer to deposition (erosion).

pathways in the Marsdiep inlet.

Geomorphology

According to Hayes (1979), the western Wadden Sea can be classified as mesotidal, i.e. tides are more important than waves in shaping the morphology of the tidal-inlet system. Characteristic morphologic features in such a system are the ebb and flood-tidal deltas (Hayes, 1980). The ebb-tidal delta is a shallow sand bar located at the seaward end of the deep inlet channel (e.g. Noorderhaaks in front of the Marsdiep inlet in Fig. 1.1). The ebb-tidal delta has been formed by the ebb current that carries sediment seaward. As its sediment-transport capacity decreases, the sediment settles and shapes into the shallow sand bar. Ebb-tidal deltas affect the bypassing of littoral transport (Bruun and Gerritsen, 1959). Sha (1989b) argued that the updrift orientation of the Marsdiep ebb-tidal delta is due to the interaction of the onshore-offshore tidal currents through the inlet with the shore-parallel tidal currents. His hypothesis was in part successfully tested with idealised analytical and numerical models (e.g. Van der Vegt et al., 2006; Van Leeuwen et al., 2003). The flood-tidal delta in the tidal basin comprises a network of shallow channels flanked by subtidal shoals and salt marshes. The tidal channels on the flood-tidal delta are organised in deep ebb channels and shallow flood channels (Van Veen, 1950), resembling a fractal pattern (Cleveringa and Oost, 1999). The effects on tidal-inlet system morphology of large-scale impacts such as relative sea-level rise, sand mining, and channel closure have been studied with semi-empirical long-term models (e.g. Van Dongeren and De Vriend, 1994; Stive et al., 1998) and quasi-realistic morphodynamic models (Wang et al., 1995).

Overviews of the geology and the historical development of the Marsdiep ebb and flood deltas are presented by Sha (1990), Oost (1995), and Elias and Van der Spek (2006). According to Oost (1995), the Marsdiep inlet was formed in the 10th century. The tidal basin consisted of peat land intersected by tidal channels. Tides and storms eroded the peat land, which was replaced by sandy tidal flats. In 1932, the 'Zuider Zee' (the present day 'IJsselmeer' or Lake IJssel; Fig. 1.1) was closed off with a 32 km long dam. Although the horizontal area of the basin decreased, the tidal range and tidal prism increased due to the reflection of the tidal wave against the dam (Lorentz, 1926). Since 1932, the Marsdiep basin has responded to the damming by infilling and ebb-tidal delta erosion (Elias et al., 2003).

Figure 1.6. The protective frame around the ADCP under the hull of the ferry Schulpengat (left photo) and a close-up of the ADCP (right photo). Photos by Bert Aggenbach.

1.4 Research questions

Although the Marsdiep is a well-studied tidal inlet, there are still many unknowns about water and sediment transport in the inlet (some of which have been mentioned in the previous section). In particular, there is a need for long-term observations to determine the temporal and spatial variability of these processes. The research questions addressed in this thesis are:

What is the spatial and/or temporal variability in and what are the mechanisms that govern:

$Q1$ instantaneous streamwise and secondary currents and water transport?

$Q2$ time-mean streamwise and secondary currents and water transport?

$Q3$ bedforms?

1.5 Research approach

To address these questions the ferry Schulpengat was equipped in 1998 with an acoustic Doppler current profiler (ADCP) and other apparatus to measure salinity, temperature, and fluorescence. Only the ADCP data are discussed in this thesis. The ADCP was mounted under the hull of the ferry at 4.3 m below the water level (Fig. 1.6). It measures water depth and horizontal and vertical water velocities and acoustic backscatter (ABS) in bins of 0.5/1 m under the ferry. In addition to providing insight in processes, the data and the results of the data analysis presented in this thesis are also relevant to numerical modellers for model calibration and validation. For instance, in Elias et al. (2006) the ferry-ADCP data were applied to calibrate a numerical model of the western Wadden Sea.

The research questions are addressed in Chapters 2-6, after which overall conclusions and recommendations are presented in Chapter 7. A short description of Chapters 2-6 is given below. **Chapter 2** addresses $Q1$ and $Q2$. The ferry-ADCP measurement

techniques are presented and the methodology to process the current data, obtained in the period 1998-2002, is discussed. A least-squares harmonic analysis is applied to study the contribution of the tides to the water transport, depth-averaged currents, currents as a function of water depth, and water level. The harmonic analysis provides insight in amplitudes and phases of important tidal constituents and tidal-mean circulation.

Chapter 3 answers $Q1$. The variability in the instantaneous secondary currents during well-mixed and stratified conditions for the period 1999-2002 is identified with the ferry-ADCP measurements. Vertical profiles of salinity and temperature and ADCP-current data, collected during additional 13-h surveys, are applied in the curvilinear transverse momentum balance to determine the governing mechanisms. The gradient Richardson number and a simple parametrisation of the eddy viscosity are used to asses the importance of stratification for turbulent mixing and secondary velocities.

Chapter 4 deals with $Q2$. The mechanisms that govern the variability in the measured subtidal water transport in the Marsdiep inlet are scrutinised by applying an analytical model of the Marsdiep and Vlie basins. The model by Ridderinkhof (1988b), which represents the tidal-mean water transport through a tidal channel due to tidal stresses, is extended to include the effects on the subtidal water transport of wind stress, subtidal water-level gradients, and density gradients. The time-mean values and the variability of the measured and predicted subtidal water transport are compared.

Chapter 5 addresses $Q3$ and discusses the spatial and temporal variability in size, shape, orientation, and migration of sand waves in the Marsdiep inlet for the period 1998-2005. Two relatively novel techniques are presented: a technique to ensemble bathymetric maps using water depths recorded with the ferry-mounted ADCP and a spatial cross-correlation technique to track the migration of sand waves that are visible on the bathymetric maps.

Chapter 6 also addresses $Q3$. The ADCP-current measurements are applied to explain the sand-wave observations presented in Chapter 5. Bedload transport is predicted using depth-averaged currents for period 1999-2002 and compared with the measured bedload transport (i.e. based on sand-wave shape and migration speed). The mechanisms that govern the time-mean predicted bedload transport (i.e. tidal asymmetries, tidal-mean currents, storms, and estuarine circulation) are investigated. The height and migration speed of the sand waves as a function of time are correlated with wind stress, a proxy for estuarine circulation, bedload transport, and fall velocity to determine the mechanisms that govern the seasonal variability in sand-wave height and migration speed.

Chapter 2

Long-term ferry-ADCP observations of tidal currents in the Marsdiep inlet

Abstract

A unique, five year long data set of ferry-mounted ADCP measurements in the Marsdiep inlet, the Netherlands, obtained between the beginning of 1998 and the end of 2002, is presented. A least-squares harmonic analysis was applied to the water transport, (depth-averaged) currents, and water level to study the contribution of the tides. With 144 tidal constituents, maximally 98% of the variance in the water transport and streamwise currents is explained by the tides, whereas for the transverse currents this is maximally 50%. The most important constituent is the semi-diurnal M_2 constituent, which is modulated by the second-largest S_2 constituent (about 27% of M_2). Compound and overtides, such as $2MS_2$, $2MN_2$, M_4, and M_6, are important in the inlet. Due to interaction of M_2 with its quarter-diurnal overtide M_4, the tidal asymmetry in the southern two-thirds of the inlet is flood dominant. The amplitudes of all non-astronomic constituents are largest during spring tides, strongly distorting the water level and velocity curves. The M_2 water transport is 40° ahead in phase compared to the M_2 water level, reflecting the progressive character of the tidal wave in the inlet. The currents are strongly rectilinear and they are sheared vertically and horizontally, with the highest currents at the surface above the deepest part of the inlet. During spring tides, near-surface currents can be as large as 1.8 m s^{-1}. Due to the relative importance of inertia compared to friction, the M_2 currents near the centre (surface) lag maximal 20° (3°) in phase with the currents near the sides (bottom). The tidal-mean currents are directed into the basin in the shallower channel to the south and out of the basin in the deeper channel to the north.[1]

---

[1] This chapter is based on Buijsman and Ridderinkhof (2007a).

2.1 Introduction

Vessel-mounted acoustic Doppler current profilers (ADCPs) have been widely used to measure current velocities in estuaries and coastal seas (e.g. Geyer and Signell, 1990; Simpson et al., 1990; Lwiza et al., 1991; Valle-Levinson et al., 1995; Li et al., 2000; Lacy and Monismith, 2001; Cáceres et al., 2003). Usually they are mounted under small vessels that sail up and down transects for one or two semi-diurnal tidal cycles (13 or 25 h). Although the spatial resolution is high, practical considerations limit the duration of such observations to about 25 h. The application of an upward looking ADCP mounted on a tripod has the great advantage that the temporal coverage may be several months (e.g. Trowbridge et al., 1999; Chant, 2002) but the disadvantage is that the measurements are restricted to a single point. To overcome both these disadvantages, an ADCP was mounted in 1998 under the ferry 'Schulpengat' that traverses the 4 km wide Marsdiep tidal inlet between Den Helder and the island of Texel, the Netherlands. The goals of this multi-year project are to continuously collect data on current velocities, acoustic backscatter (ABS), and water depths and to ultimately gain insight in the variability of the currents, sediment transport, and the long-term stability of the inlet.

There is a long tradition of oceanographic studies on the Marsdiep tidal basin, located in the western Dutch Wadden Sea. One of the first was Postma (1954) with an overview of the chemistry of the western Wadden Sea. In Postma (1961) the transport of suspended matter in the Dutch Wadden Sea is discussed. Zimmerman (1976a,b) studied mechanisms for flushing and mixing in the Wadden Sea. Zimmerman (1976b) also reported on current measurements across the Marsdiep inlet that reveal counterclockwise horizontal residual circulation. He attributed this and other observed circulation cells to the interaction of the tide with the complicated bathymetry. In Sha (1990) an overview is presented of the geology, sand-transport processes, and bedforms in the Marsdiep tidal inlet. Sha (1990) argued that the updrift orientation of the Marsdiep ebb-tidal delta is due to the interaction of the onshore-offshore tidal currents through the inlet with the shore-parallel tidal currents. In his thesis, Ridderinkhof (1990) presented numerical model results on currents and mixing in the Wadden Sea. His model results confirm the residual circulation cells observed by Zimmerman (1976b) and show that there is a throughflow from the Vlie basin to the adjacent Marsdiep basin. Recently, Bonekamp et al. (2002) and Elias et al. (2006) modelled the sediment transport pathways in the Marsdiep inlet and ebb-tidal delta.

The objective of this chapter is to use these long-term observations to study the contribution of the tides to the water transport, the depth-mean currents, and the horizontal and vertical current structure in the inlet. For this purpose, a least-squares harmonic analysis was applied to the ADCP measurements obtained in the period from 1998 to the end of 2002. These measurements were conducted with a 1.5-Mhz ADCP that was corrected for ferry speed using a differential global positioning system (DGPS). So far, this data set has only been cursorily presented in Ridderinkhof et al. (2002) and it has been used for model calibration by Bonekamp et al. (2002) and Elias et al. (2006). Therefore, the collection techniques and the accuracy of the ADCP data are also discussed here.

This chapter starts with an overview of the study area. In the Data section, the collection techniques, the accuracy of the data, the harmonic analysis, and the gridding are

discussed. In the Results section, the contribution of the tides to the water transport and (depth-averaged) currents is studied. This chapter ends with a discussion and conclusions.

2.2   Study area

The ferry crosses the Marsdiep inlet between the ferry harbours of Den Helder and Texel. Located at 52.985° N and 4.785° W, it is the southwesternmost inlet of the Wadden Sea in the Netherlands (Fig. 2.1). The Marsdiep basin has a length of about 50 km, a horizontal area of about 680 km^2, and it drains into the North Sea. The basin borders the Eierland basin to the northwest and the Vlie basin to the northeast. To the north the inlet mouth is bordered by the sand plains of the barrier island of Texel and to the south by the sea dike of the mainland town of Den Helder. To the west the ebb-tidal delta, with its subtidal sand shoal Noorderhaaks, shelters the inlet from surface waves from (north)western directions. The inlet is about 4 km wide and maximally 28 m deep where the ferry crosses. At the basin side of the study area, the inlet channel bifurcates in the northern main channel Texelstroom and the southern secondary Malzwin channel. The Marsdiep seafloor consists of medium size sands and features large bedforms with wave lengths of 100-200 m and heights of several metres (Sha, 1990). In the estuary, tidal flats consisting of mud and sand border the tidal channels.

The currents in the Marsdiep inlet are primarily governed by the semi-diurnal tides. These tides co-oscillate with the tides in the adjacent North Sea basin, which in turn co-oscillate with the tides in the Atlantic Ocean. The tides enter the North Sea from the Atlantic as a Kelvin wave that propagates southward along the east coast of the United Kingdom (Dronkers, 1964; Pingree and Griffiths, 1979). At the English Channel, between the United Kingdom and France, the Kelvin wave is reflected and turns counterclockwise to propagate northward along the coast of the Netherlands. The tidal wave enters the Marsdiep channel from the south near Den Helder and propagates northward towards Texel and eastward into the inlet. At the mouth near Den Helder, the mean tidal range is 1.4 m. Due to the amplification of the tide (Lorentz, 1926; Dronkers, 1964) the tidal range at the head near Harlingen is over 2 m.

Zimmerman (1976a) extensively described the horizontal salinity distribution in the western Wadden Sea. He found that the salinity in the Marsdiep tidal basin is primarily governed by saline water from the North Sea and by freshwater discharged from the Lake IJssel sluices near Den Oever and Kornwerderzand. The salinity at the seaward side of the mouth varies around 30 psu and is mainly governed by freshwater from the river Rhine that is advected northward along the Dutch coast. Furthermore, Zimmerman (1976a) showed that the water column in the tidal channels is well-mixed and that density stratification is only of importance near the sluices during periods with high freshwater discharge.
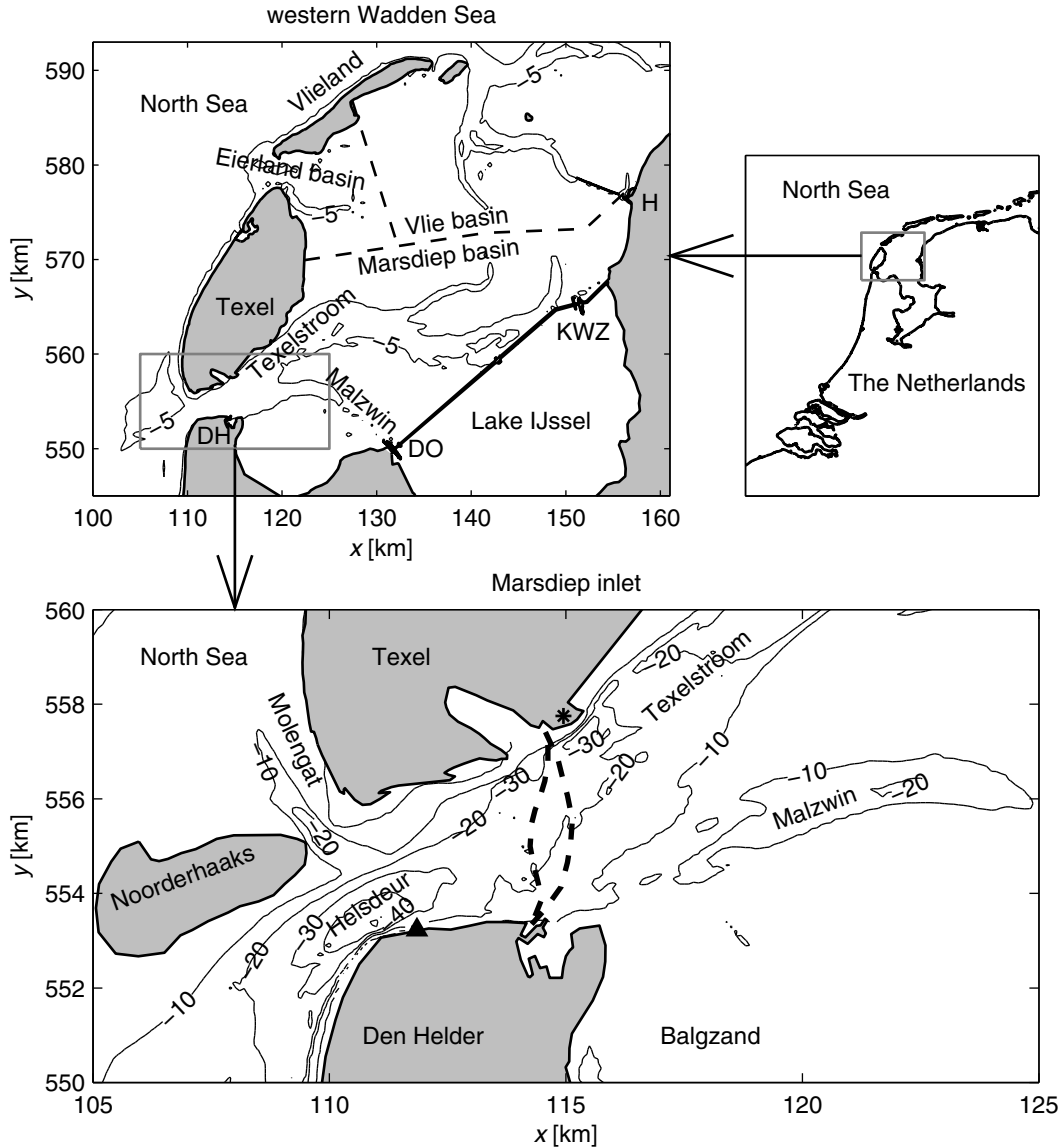
Figure 2.1. The western Wadden Sea and the Marsdiep tidal inlet in the Netherlands. In the top left panel, the towns of Den Helder and Harlingen and the Lake IJssel sluices at Den Oever and Kornwerderzand are indicated by DH, H, DO, and KWZ, respectively. The thin dashed lines indicate the approximate locations of the watersheds. The tidal channels are marked by the isobath of -5 m (relative to mean sea level). The thick dashed lines in the bottom panel indicate the envelope of ferry crossings. The bathymetry is contoured in intervals of 10 m. The location of the tidal station at Den Helder is indicated by the black triangle and NIOZ to the east of the Texel ferry harbour is indicated by the asterisk.

2.3   Data

2.3.1   Data collection

In cooperation with the ferry company 'Texels Eigen Stoomboot Onderneming' (TESO), the Royal Netherlands Institute for Sea Research (NIOZ) has conducted ferry-mounted
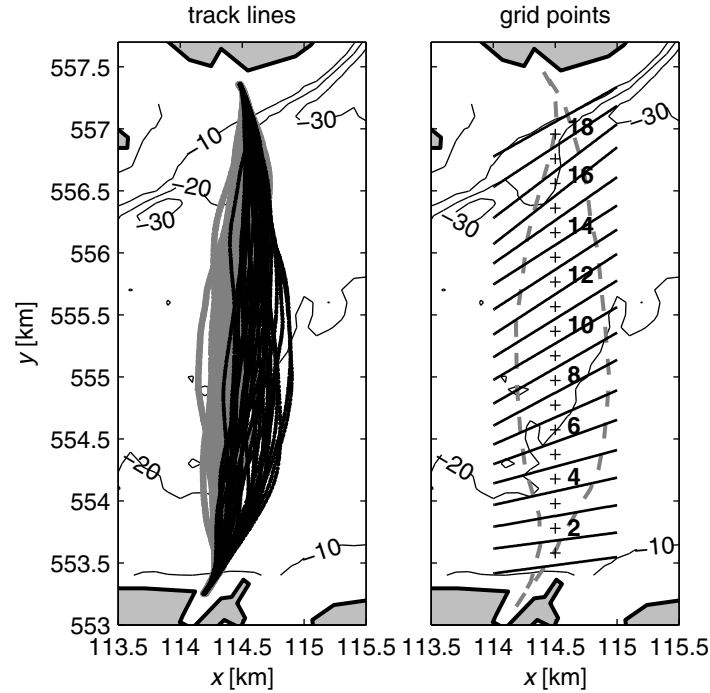
Figure 2.2. Track lines of the ferry for two days in 2001 (left) and the location of the 18 grid points or stations in the Marsdiep inlet (right). In the left panel, the up (down) crossings towards the north (south) are indicated by grey (black) dots. In the right panel, the grid points are indicated by the crosses and the boundaries of the grid cells by the tilted black lines. The envelope of ferry crossings is approximated by the grey dashed line.

ADCP measurements in the Marsdiep tidal inlet since 1998. The ADCP measures current speeds and acoustic backscatter (ABS). The ferry crosses the Marsdiep inlet twice per hour at a speed of about 17 km h^{-1}, up to 32 times per day, 7 d per week, about 300 d per year. Every year, in January and/or February the ferry docks for maintenance and no data are collected. The ferry sails up and down without reversing, i.e. starboard becomes port side when sailing back. Due to protocol, the up crossings of the ferry towards Texel are situated more westward than the down crossings towards Den Helder (Fig. 2.2). While the ferry sails across the inlet, the ADCP data are stored and each time the ferry docks in the harbour of Texel the data are automatically transferred by telemetry to a computer at NIOZ, located about 300 m to the east of the Texel ferry harbour.

The downward-looking ADCP is mounted under the hull at 4.3 m below the water surface near the horizontal centre of the ferry. Till the end of 2002, data were collected with a Nortek 1.5-Mhz vessel-mounted ADCP, which measured at a rate varying between 0.26 Hz and 0.35 Hz. This ADCP has three beams that make an angle of 25° with the vertical and a vertical bin size and a blanking distance of 0.5 m. The single ping standard deviation is 28 cm s^{-1}. With about 35 samples per sampling interval of 4 s this standard deviation is reduced to 5 cm s^{-1}. Water depths were estimated by locating the peaks near the bottom in each of the three ABS signals. The accuracy of the bottom estimation is half a bin size.

Differential global positioning system (DGPS) and gyrocompass aboard the ferry were

used to correct for vessel speed and heading. The ferry uses two Leica MX412 DGPS stations and a Sperry SR220 gyrocompass in combination with a Lemkuhl LR40AC digital repeater. One GPS station is located on the Texel (north) side and one on the Den Helder (south) side of the ferry. When the ADCP was installed in 1998, the GPS located on the south side of the ferry was initially used for the measurements. However, due to GPS malfunctioning on May 14, 1998, the GPS on the north side was used. On April 23, 2002, this GPS started malfunctioning and the GPS station on the Den Helder side was used again. The fact that the GPS was not located above the ADCP introduced some errors in the data, in particular during turns before entering and after leaving the ferry harbours. All horizontal GPS positions were corrected for horizontal offsets and mapped to the actual ADCP position using the heading data. Heading offsets of the ADCP were reduced during dedicated calibration cruises.

In early 2003, the 1.5-Mhz ADCP was replaced by a 1-Mhz Nortek ADCP that uses bottom-track and gyrocompass to correct for vessel speed and heading. In this chapter only the data from the 1.5-Mhz ADCP with DGPS correction are discussed.

In addition to the ferry data, 10 min water-level data from the Den Helder tide gauge (Fig. 2.1) were obtained from the Dutch Ministry of Transport, Public Works and Water Management. These data have a vertical accuracy of about 1 cm.

2.3.2   Uncertainties

Positioning and heading

The uncertainties in the horizontal positioning and gyrocompass are fairly small. Standard deviations were determined by tracking the DGPS and heading while the ferry was docked for (un)loading. The ferry always docks in exactly the same location, and the movement of the ferry is minimal during the docking. The accuracy of the ferry-operated DGPS is about 0.74-1 m in the eastward x direction and 1.07-1.78 m in the northward y direction. However, from January 6, 1999 to April 1, 1999 the standard deviations in the x and y directions are larger, measuring 2.36 m and 6.03 m, respectively. It is not yet known what caused the standard deviation to be larger. The standard deviations of the gyrocompass are small at 0.15-0.17°.

Heading offset and tilt

The ADCP data may be affected by heading offsets and errors due to the tilt of the ADCP beams (Joyce, 1989). Other sources of error may be turn-related 'Schuler' oscillations of the gyrocompass and a gyrocompass speed error (Trump and Marmorino, 1997). More-over, the heading offset can also be a function of the vessel's heading (Munchow et al., 1995; Trump and Marmorino, 1997). This error can be identified with an ADCP with bottom-track correction. It is assumed that the contributions of Schuler oscillations and speed errors are minor. Consequently, only the heading offset and tilt are discussed.

The heading offset (α) can be corrected for with a simple coordinate transformation and the tilt in the ADCP beams can be overcome by correcting the ADCP data with a scaling factor $1 + \beta$. Joyce (1989) showed that corrected water velocities in the true

Table 2.1. Mean values of α and $1 + \beta$ and their standard deviations σ_α and $\sigma_{1+\beta}$. Mean values of α and $1 + \beta$ were determined for periods of about 50 d using the least-squares solution by Joyce (1989).

Year	α [°]	$1 + \beta$	σ_α [°]	$\sigma_{1+\beta}$
1998	0.74	0.9869	0.64	0.0098
1999	0.44	0.9896	0.66	0.0089
2000	-1.52	1.0041	0.66	0.0095
2001	-1.28	1.0007	0.70	0.0095
2002	-1.38	1.0038	0.60	0.0100

coordinate frame can be obtained with:

$$
\begin{aligned}
u_{\mathrm{w}} &= u_{\mathrm{s}} + (1 + \beta)(u'_{\mathrm{d}} \cos \alpha - v'_{\mathrm{d}} \sin \alpha) \\
v_{\mathrm{w}} &= v_{\mathrm{s}} + (1 + \beta)(u'_{\mathrm{d}} \sin \alpha + v'_{\mathrm{d}} \cos \alpha),
\end{aligned}
\tag{2.1}
$$

where u and v are the eastward and northward velocities in the true coordinate frame, $'$ indicates the rotated coordinate frame due to the heading offset, u_{w} is the water velocity, u_{s} the ship velocity obtained with DGPS, and u_{d} the velocity measured by the ADCP.

Although the DGPS-corrected ADCP was calibrated, the data was still checked for heading offsets. A simple least-squares technique by Joyce (1989) was used to calculate α and $1 + \beta$. In this technique, the absolute difference $\epsilon^2 = \epsilon_u^2 + \epsilon_v^2$ between the u_{w} and v_{w} velocities of the up and down crossings is minimised. The underlying assumption is that the water velocities do not change. For each year, velocity measurements were selected for a period of about 50 d. Depth-averaged current velocities were used and only transects were selected within an area of 2-km length, centrally located in the inlet. In this area the ferry tracks have minimal curvature. In this method, $(u'_{\mathrm{d}}, v'_{\mathrm{d}})$ were obtained by subtracting $(u_{\mathrm{s}}, v_{\mathrm{s}})$ from $(u_{\mathrm{w}}, v_{\mathrm{w}})$. Values for α and $1 + \beta$ were calculated for each set of up and down crossings around maximum flood and ebb current velocities, when the rate of change in currents is lowest. Mean values of α and $1 + \beta$ and their standard deviations are listed in Table 2.1. Although α and $1 + \beta$ are small, they are not constant. In the periods 1998-1999 and 2000-2002 α and $1 + \beta$ are about the same. The difference between the two periods can be related to maintenance and recalibration of the ADCP in early 2000.

The depth-averaged velocities were corrected with Eq. (2.1) using mean values of α and $1 + \beta$ and are shown for a spring tide on July 8, 2000 in Fig. 2.3. The uncorrected velocities and 'smoothed' velocities are also included in the figure. The latter velocities were calculated by averaging over each pair of up and down or down and up crossings. The uncorrected velocities portray a clear 'zigzag' pattern that is stronger for the u_{w} velocities. The corrected velocities are smoother but the zigzag is not entirely removed. This is to be expected because the variance in α is relatively large and small changes in α already affect the smoothness of the graph. Averaging over subsequent crossings can be regarded as a form of low-pass filtering and completely removes the zigzag pattern. Apart from the zigzag, the differences between velocities obtained with averaging and correcting for offset and tilt are small. Tidal-mean values of the smoothed and corrected velocities are nearly identical and the main axis of the corrected and smoothed velocities are within 2°. Therefore, *only* the velocities of subsequent crossings of the entire data set from 1998 to
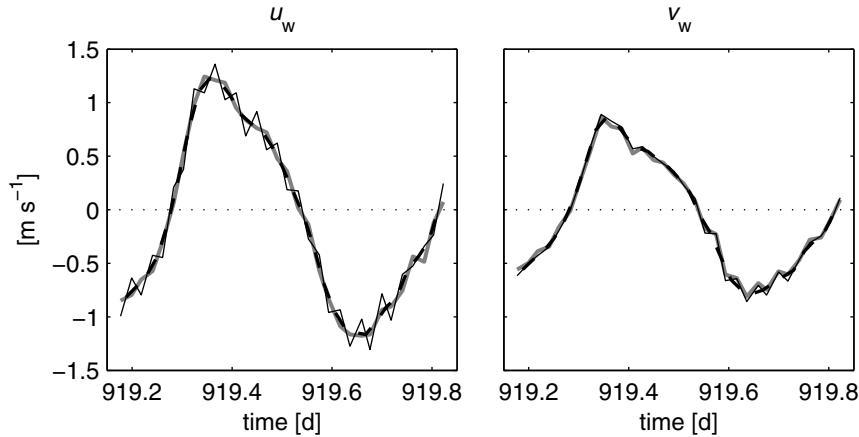
Figure 2.3. Uncorrected (thin black line), corrected (thick grey line) and smoothed velocities (thick dashed black line) for July 8, 2000. Days are relative to midnight of January 1, 1998.

the end of 2002 were averaged. This operation was performed after the horizontal and vertical gridding operation discussed in the next section.

2.3.3   Data reduction

Gridding

Before the velocity data were gridded, each velocity measurement was subjected to quality control. First, all bins above the bottom were selected. The bottom was determined as the minimum water depth of the three beams. To limit the influence of side lobe interference, the data in the first complete cell above the bottom were excluded. The ferry disturbs the water flow and as a result the first 3 m under the hull contains poor velocity data. These data were also rejected. To remove outliers, all velocity data with absolute depth-mean velocities larger than 2 m s^{-1} and all data with absolute depth-mean northward velocities larger than 1.5 m were excluded. For every measurement, the standard deviations over the difference between the u, v, and w profiles and their linear fits were calculated. Bad data were characterised by large standard deviations, and therefore velocity profiles with standard deviations larger than cutoff values of 0.5 m s^{-1}, 0.5 m s^{-1}, and 0.30 m s^{-1} for the u, v, and w profiles, respectively, were omitted. In addition, if the vertical difference between one depth estimate and the other two exceeded 5 m, the data were also excluded. In general, less than 10% of the original data were rejected.

To better handle the huge amount of velocity and depth data, the filtered data were mapped to 18 fixed grid points or 'stations' between the ferry harbours (Fig. 2.2) with a horizontal spacing of about 198 m. The ferry rarely sails in a straight line, but in an arc. To correctly map the ADCP positions to the stations, the boundaries of the grid cells were aligned with the flow directions and it was assumed that the currents within the grid cells are uniform. For each crossing, all velocity data within the grid cells were mapped to the related grid points. Then the velocity data were regridded on 40 bottom-following vertical coordinates (σ-coordinates) between the bottom and the water surface and all values within each σ-coordinate were averaged. In a final step the velocity data were

averaged over subsequent crossings. These data were then used for further analysis.

Least-squares harmonic analysis

A least-squares harmonic analysis (e.g. Dronkers, 1964; Godin, 1972; Li, 2002) was applied to differentiate between tidal and non-tidal influence. This method is very elegant because it allows time-series that are not equidistant. In this analysis, the measured velocity u_i ($i = 0, 1, 2, .., N$, N is the number of data points) is approximated by the best harmonic fit $\hat{u}_i$:

$$\hat{u}_i = A_0 + \sum_{j=1}^{M}[a_j \cos(\omega_j t_i) + b_j \sin(\omega_j t_i)], \tag{2.2}$$

where $j = 1, 2, .., M$, M is the number of tidal frequencies, A_0 is the tidal mean, a_j and b_j are tidal constituents, ω_j is the tidal frequency, and t_i is time. Eq. (2.2) is equivalent to:

$$\hat{u}_i = A_0 + \sum_{j=1}^{M}[U_j \cos(\omega_j t_i - \phi_j)], \tag{2.3}$$

where $\phi_j = \arctan(b_j/a_j)$ is the phase and $U_j = \sqrt{a_j^2 + b_j^2}$ the amplitude. Generally, the quality of the fit is represented by the standard deviation σ and the coefficient of determination r^2 (Emery and Thomson, 2001; Li, 2002). The coefficient of determination is the ratio of the explained variance to the total variance. The standard deviation of the residual is:

$$\sigma = \sqrt{\frac{SSE}{N - (2M + 1)}}, \tag{2.4}$$

where

$$SSE = SST - SSR, \ SST = \sum_{i=1}^{N}(u_i - \langle u \rangle)^2, \text{ and } SSR = \sum_{i=1}^{N}(\hat{u}_i - \langle u \rangle)^2,$$

in which $\langle \rangle$ represents the mean velocity. The coefficient of determination is:

$$r^2 = \frac{SSR}{SST}. \tag{2.5}$$

The number of tidal frequencies that can be resolved is limited by the resolution and the length of the time series. There are three criteria (Emery and Thomson, 2001). First, the period T of the lowest (fundamental) frequency that can be resolved is smaller than or equal to the duration of the time series ($T \leq N\Delta t$, where Δt is the sampling interval). Second, the period of the highest (Nyquist) frequency that can be resolved is larger than or equal to twice the duration of the sampling interval ($T \geq 2\Delta t$). And third, the Rayleigh criterion demands that two adjacent frequencies can only be resolved if the reciprocal of the frequency difference is smaller than or equal to the duration of the time series ($1/\Delta f \leq N\Delta t$, where Δf is the frequency difference). For the five-year data series this implies that the lowest frequency to be resolved is Sa ($T = 365.243$ d) and the highest frequency $4M_2S_{12}$ ($T = 2.05$ h). The Rayleigh criterion demands that the data series have a minimal duration of 1616 d to allow for the resolution of frequencies $3MKS_2$ ($T = 0.5582$ d) and $2NS_2$ ($T = 0.5580$ d).

2.4   Results

2.4.1   Water level and water transport

In this section, the contribution of the tides to the water transport and water levels by means of a least-squares harmonic analysis is studied. The water transport Q was calculated by integrating the eastward velocity $u(z)$ over the water depth and the 18 stations. Near the surface and bottom no velocity data were available. The near-surface velocities were assumed to be equal to the mean of the velocities in the first 5 σ-coordinates with available data. The near-bottom velocities were determined as the mean of zero and the first velocity value above the bottom. During some crossings, poor-quality ADCP data were collected. The omittance of these data resulted in empty time slots at some stations during some crossings. If this was the case then all time slots at all stations in the same crossing were omitted. In this way about 4% of the data were excluded. The time series of the water transport from February 18, 1998 (48 d) to December 25, 2002 (1819 d) are presented in Fig. 2.4. The amplitude of the measured water transport fluctuates between 50.000 m^3 s^{-1} and 90.000 m^3 s^{-1}. From June 21, 1998 (171 d) to April 2, 1999 (456 d) the water transport data are of poor quality and feature a larger amplitude. The cause is unclear and these data were excluded from the analysis. The water level η at the Den Helder tide gauge ranges between -1 m and $+2$ m and is also plotted in Fig. 2.4.

Harmonic analyses were performed for the water transport and water level. A total of 144 astronomic and shallow-water tidal frequencies were used. The lowest frequency is Sa with a period of 365.2425 d and the highest frequency is $4M_2S_{12}$ with a period of 2.0462 h. The origin of the time axis is midnight of January 1, 1998. The results of the harmonic analyses are presented in Table 2.2, which lists the 25 largest constituents of the water transport, as well as the annual, semi-annual, monthly, and fortnightly constituents. The water-level constituents in Table 2.2 are equal to the water-transport constituents and consequently they are not in order. Fig. 2.5 presents the water transport and water-level data as well as their harmonic fits for half a spring-neap cycle from September 3 to September 11, 2002. Fig. 2.5 shows that for about 8 h during each night no ADCP data were collected. From Table 2.2 and Figs. 2.4 and 2.5 some interesting facts arise. They are listed below:

- With 144 constituents, about 97.7% of the variance in the water transport is explained due to the tides. Using the 25 largest constituents, the variance explained in the water transport is 96.8%, and using the 15 largest constituents it is still 96%. In contrast to the water transport, only 80.6% of the variance in the water level is explained due to the tides. The higher value of r^2 for the water transport compared to the water level indicates both the high quality of the current measurements and the high level of residual energy in the water-level data. The high residual energy may be attributed to wind set-up in the adjacent North Sea, which can be more than 1 m according to Fig. 2.4. Fig. 2.5 shows that the residual water levels feature larger periods than the semi-diurnal period. It can be illustrated with the simplified continuity equation for relatively short basins $Q \sim \partial\eta/\partial t$ that on these time scales the residual water transport is much smaller than the tidal water transport. Hence, the residual energy in the water transport is also smaller.
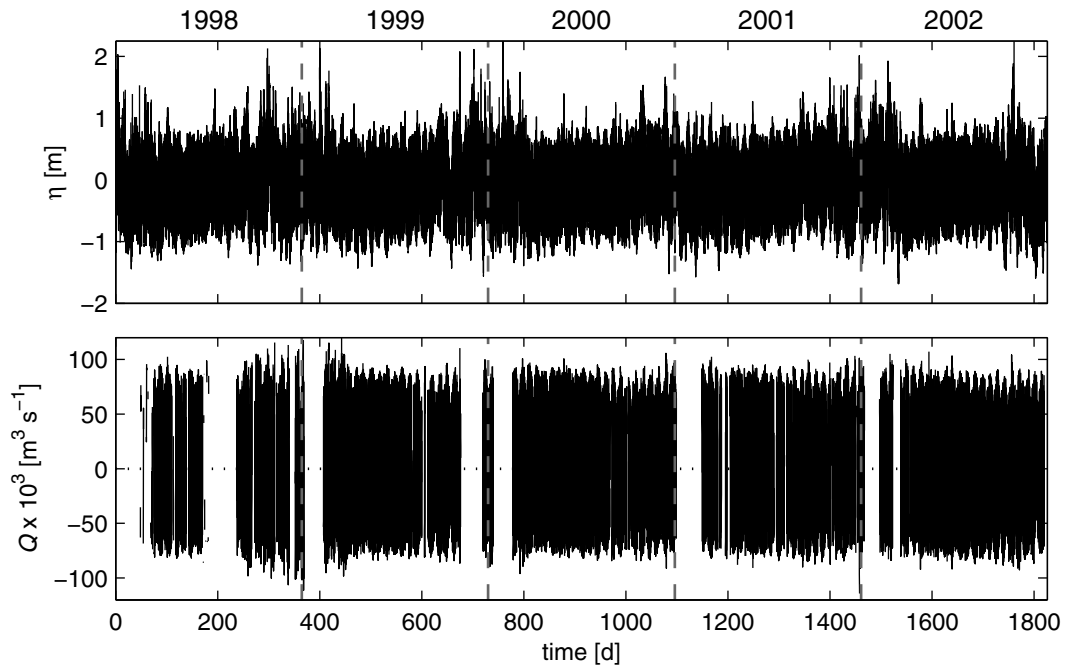
Figure 2.4. Time series of water level η at Den Helder and water transport Q at the ferry transect in the Marsdiep inlet. The vertical dashed lines indicate midnight of each new year. The years are plotted above the top panel.
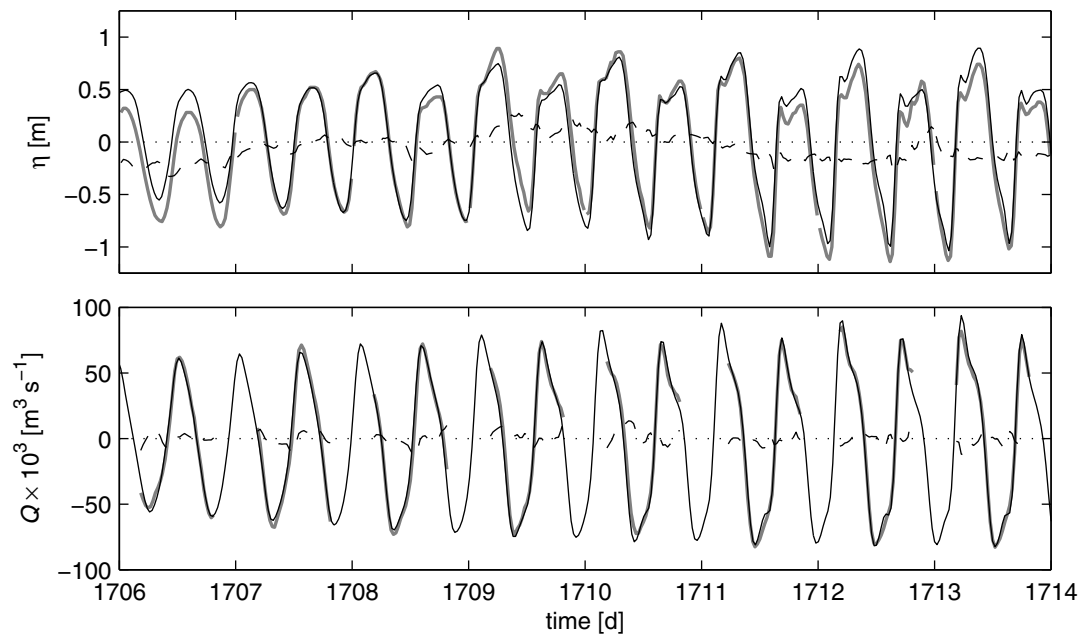
Figure 2.5. Data (thick grey line), harmonic fit (thin black line), and residual (thin black dashed line) of the water level and water transport from September 3 (neap) to September 11, 2002 (spring).

Table 2.2. Amplitudes (A) and phases (ϕ) of water transport (Q) and water level (η) tidal constituents for period 1. The 25 largest constituents for water transport are listed, as well as the annual, semi-annual, monthly, and fortnightly constituents. Compound tides with the same frequencies as the astronomic constituents are in parentheses.

		water transport (Q) 7.92×10^3 m^3 s^{-1} 98%			water level (η) 0.26 m 81%		
σ r^2	T [d]	$A \times 10^3$ [m^3 s^{-1}]	%M$_2$	ϕ [°]	A [m]	%M$_2$	ϕ [°]
A_0		-2.91	4.4		0.03	4.1	
M$_2$	0.518	65.75	100.0	187.3	0.66	100.0	227.2
S$_2$	0.500	17.95	27.3	190.7	0.18	27.3	227.1
N$_2$	0.527	9.76	14.8	120.6	0.10	15.5	159.8
μ_2(2MS$_2$)	0.536	9.03	13.7	344.2	0.08	12.2	21.1
L$_2$(2MN$_2$)	0.508	7.17	10.9	64.2	0.07	9.9	100.8
M$_4$	0.259	6.75	10.3	301.8	0.11	17.0	293.5
M$_6$	0.173	6.59	10.0	108.7	0.06	9.0	97.8
2MS$_6$	0.171	6.08	9.3	95.0	0.06	8.4	83.7
K$_2$	0.499	4.75	7.2	2.8	0.05	7.7	40.1
O$_1$	1.076	4.42	6.7	192.2	0.10	14.6	254.2
ν_2	0.526	4.34	6.6	255.6	0.04	6.1	298.4
K$_1$	0.997	4.06	6.2	289.1	0.07	10.8	347.9
2MN$_6$	0.174	3.55	5.4	32.6	0.03	5.0	21.0
MS$_4$	0.254	3.26	5.0	290.6	0.06	9.8	287.4
λ_2	0.509	2.85	4.3	260.7	0.03	4.2	292.6
MN$_4$	0.261	2.50	3.8	227.1	0.04	6.2	220.0
3MS$_2$	0.557	2.28	3.5	166.6	0.02	2.9	205.4
NLK$_2$(2MK$_2$)	0.538	2.22	3.4	176.0	0.02	3.1	216.9
2SM$_2$	0.484	2.12	3.2	321.9	0.02	3.2	359.8
ϵ_2(MNS$_2$)	0.547	1.89	2.9	277.5	0.02	2.7	315.0
MSL$_6$	0.169	1.80	2.7	338.5	0.01	2.1	328.9
3MS$_8$	0.128	1.71	2.6	214.4	0.03	4.9	184.0
2MK$_3$	0.349	1.70	2.6	50.9	0.01	1.2	64.3
MPS$_2$	0.518	1.67	2.5	65.8	0.02	3.1	116.0
ζ(MSN$_2$)	0.491	1.64	2.5	66.3	0.02	2.5	93.3
Sa	365.243	1.18	1.8	340.6	0.10	14.6	321.2
Ssa	182.621	0.84	1.3	284.7	0.02	3.2	63.4
Msm	31.812	0.49	0.7	246.2	0.01	2.0	36.4
Mm	27.555	0.52	0.8	258.1	0.01	1.6	276.7
Msf	14.765	0.50	0.8	208.9	0.01	1.8	65.2
Mf	13.661	0.36	0.5	342.1	0.01	1.3	82.2

- The most important tidal constituent in the inlet is the semi-diurnal M_2 component with a vertical amplitude of 0.66 m and a horizontal amplitude of 65.75×10^3 m^3 s^{-1}. The second and third largest constituents are the astronomic semi-diurnal S_2 ($\sim$27% of M_2) and N_2 ($\sim$15% of M_2).

- The ratio $(K_1+O_1)/(M_2+S_2)$ of water level amplitudes is often used to identify if a tide is semi-diurnal ($<$ 0.25), mixed ($>$ 0.25 & $<$ 1.25), or diurnal ($>$ 1.25) (Dronkers, 1964). In the Marsdiep inlet this ratio is equal to 0.20 and therefore the tide is classified as semi-diurnal. The small amplitudes of the diurnal frequencies result in a small daily inequality of the water level and water transport amplitudes as shown in Fig. 2.5.

- The interaction between the M_2 and S_2 constituents results in the spring-neap cycle. This cycle with a period of 14.76 d is one of the most prominent modulations of the semi-diurnal tidal cycle. The spring-neap cycle in turn fluctuates with a period of about seven months due to the contributions of the N_2 and L_2 constituents (Godin, 1972). This is best visible in the measured water transport in Fig. 2.4, where in the spring and fall of each year ($\sim$600 d, 800 d, 1000 d, 1200 d, ..., etc.) the differences between the amplitudes of spring and neap tides are largest.

- The relative amplitudes of the O_1, K_1, and P_1 constituents (P_1 is not shown in Table 2.2) of the water level are nearly twice as large as the relative amplitudes of the water transport. This difference can be explained using the simplified continuity equation for relatively short basins and the fact that the diurnal periods are about twice as long as the M_2 period. Similarly, the annual component Sa and semi-annual Ssa play a more dominant role in the water level (14.6% and 3.2% of M_2) than in the water transport (1.8% and 1.3% of M_2).

- The phase difference between the water level and the water transport indicates whether a tidal wave is progressive (phase difference is 0°) or standing (phase difference is 90°) (Dronkers, 1964). If the energy of the reflected tidal wave is dissipated, then the tidal wave becomes progressive at the mouth. In the Marsdiep tidal inlet, the semi-diurnal frequencies M_2, S_2, N_2, etc., all feature phase differences of about 40°, indicating that the semi-diurnal tidal waves are both partially progressive and standing. In contrast, the diurnal frequencies O_1 and K_1 have phase differences of about 60°, being more of a standing tidal wave. Finally, the quarter and sixth-diurnal frequencies M_4, M_6, etc., generally are more progressive with phase differences of $0 \pm 10°$.

- Fig. 2.5 clearly shows a double high water, or 'agger', in the measured and predicted water levels. The agger is more pronounced during spring tides.

- In a shallow estuary like the Marsdiep tidal inlet, nonlinear effects such as nonlinear continuity, quadratic friction, and longitudinal advection modify the astronomic tides into overtides and compound tides. See Parker (1991) for an extensive overview of the effects of these nonlinearities. The most important overtides and compound tides in the Marsdiep inlet are M_4, M_6, $2MS_2$, $2MN_2$, $2MS_6$, $2MN_6$, and MS_4. The

Table 2.3. The variability in amplitudes and phases of the M_2, S_2, N_2, and K_2 water-transport constituents for period 1998-2002 and individual years from 1999 to 2002. The units of r^2, σ and A, and ϕ are [%], $\times 10^3$ [m^3 s^{-1}], and [°], respectively.

				M_2		S_2		N_2		K_2	
	r^2	σ	A_0	A	ϕ	A	ϕ	A	ϕ	A	ϕ
1998-2002	97.7	7.92	-2.91	65.75	187.3	17.95	190.7	9.76	120.6	4.75	2.8
1999	98.4	6.78	-1.94	65.67	188.0	16.81	198.4	10.13	121.0	4.68	5.0
2000	97.8	7.77	-0.56	65.69	187.1	15.99	193.4	9.20	123.7	4.17	17.6
2001	98.1	7.42	-2.08	66.56	187.9	16.14	188.9	9.99	119.3	4.69	8.5
2002	98.2	7.18	-3.12	65.06	187.8	16.40	191.0	9.78	122.8	5.66	6.5

compound tides $2MS_2$, $2MN_2$, MNS_2, and MSN_2 have the same frequencies as the astronomic constituents μ_2, L_2, ϵ_2, and ζ, respectively. The principal constituents M_2, S_2, and N_2 of these compound tides are dominant in the Marsdiep inlet, and therefore their compound tides may mask the astronomic constituents with the same frequencies.

- If it is assumed that the tidal energy of each constituent is proportional to the square of the amplitude, then the overtides and compound tides of the top 25 largest constituents make up about 6% of the total energy. The astronomic M_2, S_2, and N_2 constituents make up about 92% of the energy.

- The mean volume of water, integrated from the least-squares water transport, entering and leaving the inlet during one tidal cycle (tidal prism) amounts to 964 million m^3 and is close to reported values of Louters and Gerritsen (1994). The minimum and maximum flood volumes are 579 and 1170 million m^3 and the minimum and maximum ebb volumes are 709 and 1300 million m^3.

To illustrate the robustness of the harmonic analysis for the five-year period, harmonic analyses were performed with 130 constituents for 274-d periods in each year from 1999 to 2002. Every year, each period starts at the same phase of the Sa cycle. A duration of 274 d was selected because this is the remainder of usable data in 1999. The results for A_0, M_2, S_2, N_2 and K_2 are listed in Table 2.3. For comparison, the results for 1998-2002 were also included. In contrast to the small variation in the phase and amplitude of the M_2 constituent, the variation of the other semi-diurnal constituents is a little larger. Most of the energy is contained in the M_2 constituent and consequently the amplitudes and phases of this constituent are easiest to determine with the harmonic analysis, while this is more difficult for constituents with significantly smaller and more equal amplitudes. The variability in the tidal-mean transport is small with $\pm 1 \times 10^3$ m^3 s^{-1} and it remains negative for all years.

2.4.2 Depth-mean velocities

At each station the velocities were depth averaged and rotated to the streamwise (s) and transverse (n) coordinate axes. The streamwise axis, also called the major or main axis, is

Table 2.4. Amplitudes (A) and phases (ϕ) of the 15 largest tidal constituents for depth-averaged streamwise currents (u_s) for the period 1998-2002 at stations 2, 6, 10, 14, and 18. The orientation ψ of the streamwise axis is relative to the x-axis. $\Delta\phi$ is the relative phase difference between M_2 and M_4. The amplitudes of A_0 and the M_2 constituent in *italics* are in [m s^{-1}], and the amplitudes of the remaining constituents are in [%] relative to the M_2 amplitude. Period T is in [d] and ϕ in [°].

station		2		6		10		14		18	
depth [m]		-14.34		-19.17		-24.20		-23.78		-17.46	
ψ [°]		7.23		21.09		31.59		32.41		27.05	
r^2 [%]		95.0		96.8		97.3		97.4		95.8	
σ [m s^{-1}]		0.14		0.13		0.14		0.15		0.15	
$\Delta\phi$ [°]		45		59		80		88		102	
	T	A	ϕ	A	ϕ	A	ϕ	A	ϕ	A	ϕ
A_0		*0.05*		*-0.00*		*-0.08*		*-0.10*		*-0.15*	
M_2	0.518	*0.77*	174	*0.93*	186	*1.10*	193	*1.15*	190	*0.89*	187
S_2	0.500	28.3	180	27.8	189	27.3	195	25.8	193	27.9	190
N_2	0.527	15.0	109	14.7	120	15.1	126	14.9	123	15.5	120
$\mu_2(2MS_2)$	0.536	14.0	325	14.0	340	13.3	349	14.0	350	13.9	335
$L_2(2MN_2)$	0.508	11.1	52	11.1	63	10.8	69	10.7	67	10.9	61
M_6	0.173	10.1	93	10.2	107	10.1	114	9.6	114	8.6	88
$2MS_6$	0.171	9.7	76	9.5	95	9.5	100	8.7	101	8.1	74
M_4	0.259	10.9	303	8.1	313	9.7	305	11.4	292	14.4	271
K_2	0.499	7.9	355	7.2	2	7.5	9	7.1	7	8.1	3
O_1	1.076	6.7	187	6.0	191	6.6	193	6.2	192	6.8	180
ν_2	0.526	6.7	239	7.0	254	6.4	259	6.5	261	6.9	250
K_1	0.997	5.2	296	5.7	292	6.2	289	5.5	286	5.4	274
$2MN_6$	0.174	5.5	18	5.5	29	5.2	35	5.2	38	4.5	11
MS_4	0.254	5.0	288	3.5	298	5.2	296	5.7	281	7.5	264
λ_2	0.509	4.2	248	4.3	260	4.3	267	4.3	264	4.7	256

defined as the axis along which the depth-averaged velocities feature the largest variance. This yields the streamwise and transverse velocities u_s and u_n. The counterclockwise orientation of the streamwise axis with the x-axis is the inclination ψ. At each station, a harmonic analysis was performed with 144 constituents for the depth-averaged streamwise and transverse currents for the five-year period. Table 2.4 lists the amplitudes and phases of the 15 largest tidal constituents of the streamwise currents. Similar to the water transport, the explained variance along the s-axis is about 97%. In contrast, the explained variance along the n-axis is maximally 32%. The largest tidal constituents of the water transport in Table 2.2 are also the largest of the depth-averaged velocities. The variation of the amplitudes and phases of the constituents along the transect is similar to M_2, with the largest phases and amplitudes in the deepest part of the inlet near station 14. There is little variation of the amplitudes relative to M_2. An exception is M_4, which increases relative to M_2 in northward direction.

The depth-averaged M_2 ellipses, the harmonic fit of the maximum flood and ebb ve-
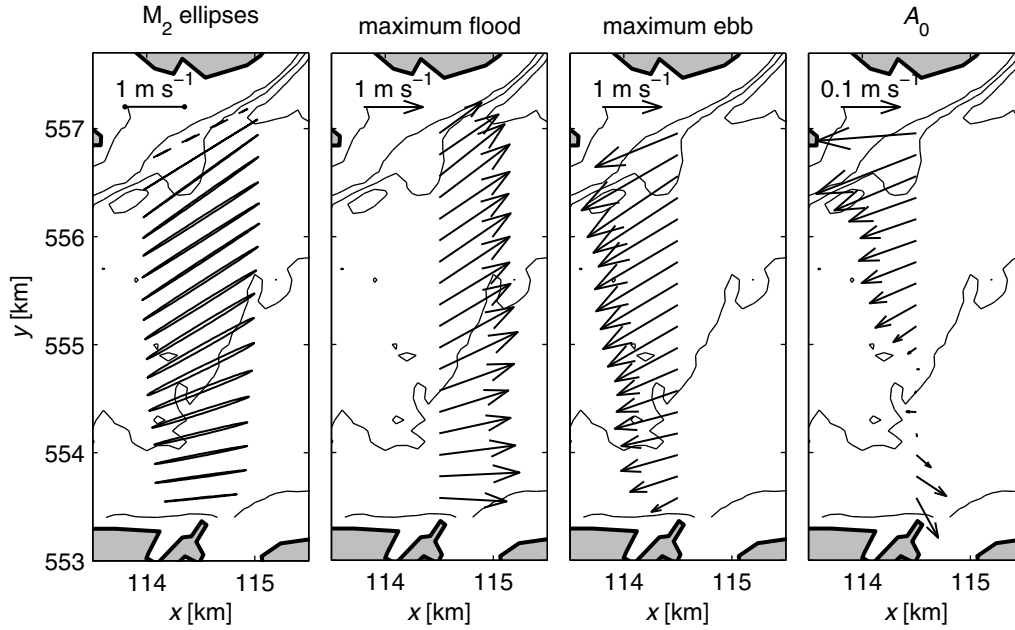
Figure 2.6. Depth-averaged M_2 tidal ellipses (left panel), maximum flood velocities (second panel) and ebb velocities (third panel) during a spring tide on September 10, 2002 (1713 d), and tidal-mean currents for 1998-2002 (right panel). Solid (dashed) ellipses in left panel indicate counterclockwise (clockwise) rotation.

locities during a spring tide on September 10, 2002 (1713 d), and the tidal-mean currents (A_0) for 1998-2002 are portrayed in Fig. 2.6. The M_2 currents are fairly rectilinear and rotate counterclockwise in the horizontal plane. The ellipses with the largest eccentricity occur on the south slope of the channel near $y = 555$ km ($\sim$station 8). The tidal ellipses of other constituents have similar eccentricity and orientation to the M_2 ellipses and are not shown here. The current vectors show that during maximum flood, inflow is more equally distributed across the inlet, while during maximum ebb the bulk of the outflow occurs in the deeper main channel to the north. Moreover, the current vectors are about parallel in the main channel during flood and ebb, whereas they are divergent during flood and convergent during ebb in the shallower part of the channel to the south. The convergence and divergence may be attributed to differential rotation of the tidal ellipses and spatial variations of the major axes of the ellipses, which are governed by cross-channel differences in bottom friction (Li, 2002, and references herein). Similar to the water transport, the tidal-mean depth-averaged currents reflect a net outflow. Due to the spatial differences in inflow and outflow, the tidal-mean flow shows a pattern of flood dominance in the southern half and ebb dominance in the northern half of the inlet.

The depth-averaged currents as a function of time at stations 2, 10, and 18 and the water level at Den Helder are shown in Fig. 2.7. Although their amplitudes and phases differ, the shapes of the currents at the three stations are similar. If the tidal-mean currents are excluded, station 2 features stronger currents than station 18 during flood, while the reverse is true during ebb. The ratio between the flood and ebb duration increases from 0.91 at station 2, to 0.98 at station 10, to 1.04 at station 18. Pingree and Griffiths (1979)
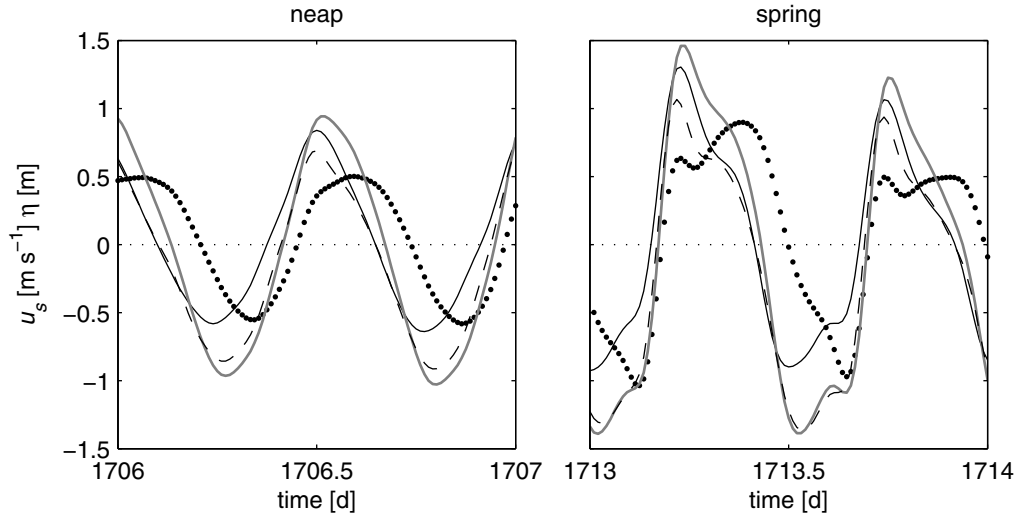
Figure 2.7. Least-squares fit of depth-averaged streamwise velocities at stations 2 (thin black line), 10 (thick grey line), and 18 (thin black dashed line) and water levels (black dotted line) on a neap tide (September 3, 2002) and a spring tide (September 11, 2002).

showed that the asymmetry in maximum velocities and the duration of the flood and ebb phase is primarily governed by the relative phase difference between M_2 and its quarter-diurnal overtide M_4. The phase difference is defined as $\Delta\phi = 2\phi_2 - \phi_4$, where ϕ_2 and ϕ_4 are the phases of M_2 and M_4, respectively. If $-90° < \Delta\phi < 90°$, the flood duration is shorter than the ebb duration and the maximum flood velocity is larger than the maximum ebb velocity. Values of $\Delta\phi$ in Table 2.2 correspond with the observed differences in maximum velocities and duration. To the south of station 12 the tidal asymmetry is flood dominant ($\Delta\phi < 90$), at stations 12 to 15 it is neutral ($\Delta\phi \sim 90$), and at stations 16 to 18 it is ebb dominant ($\Delta\phi > 90$). The M_2-M_4 tidal asymmetry is important for bed load transport because bed load transport is assumed to be proportional to U^n, where U is the absolute depth-mean velocity and $3 \le n \le 5$ (Soulsby, 1997, and references herein).

Fig. 2.7 also reveals significant differences between neap and spring tides. During neap tides the current and water-level graphs are more sinusoidal and symmetrical than during spring tides. During spring tides the rise of the water level from low water to high water is fastest and precedes the time of maximum flood water velocities. Furthermore, the duration of the flood period during spring tides is generally shorter than during neap tides. Both the faster rise and shorter duration during spring tides enhance the flood-dominated tidal asymmetry.

2.4.3   Vertical current structure

A harmonic analysis was also performed for a two-year period from 2001 to the end of 2002 with 140 harmonic constituents for all vertical grid cells of all 18 stations. The analysis was performed for currents that were rotated to the depth-averaged streamwise and transverse axes at each station, yielding streamwise velocities u_s and transverse or secondary velocities u_n.
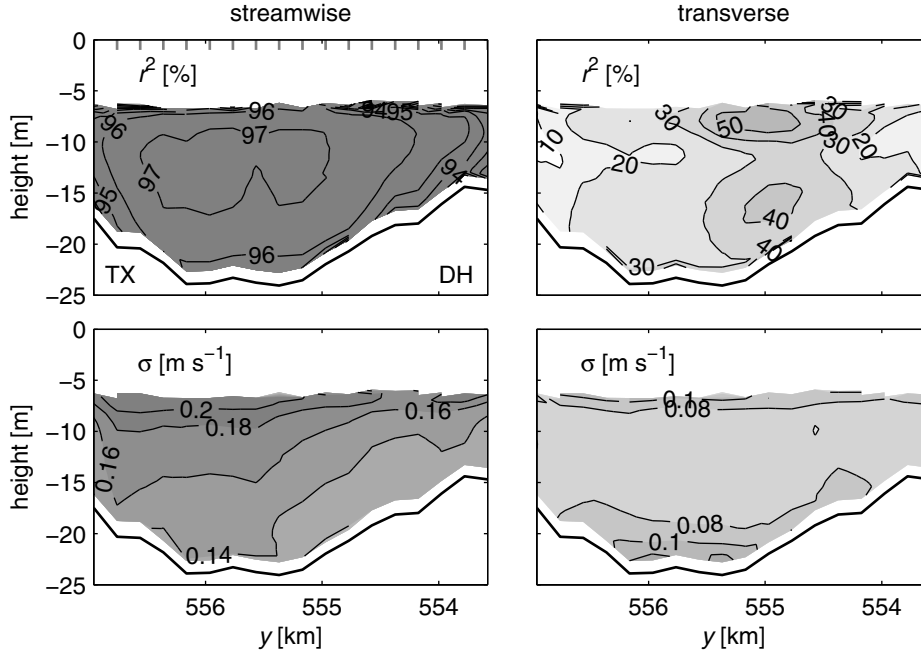
Figure 2.8. Streamwise and transverse r^2 and σ. Values are derived from a harmonic analysis using 140 constituents for a two-year period from 2001 to 2002. High (low) values are indicated by dark (light) shades of grey. The view is eastward in the flood direction. Den Helder (DH) is located to the right (south) and Texel (TX) to the left (north). The locations of the stations are indicated by the vertical grey lines in the top left graph.

Fig. 2.8 shows that the explained variance for the streamwise directions is much higher (93-97%) than for the transverse directions (10-50%). This implies that the tides dominate in the streamwise direction while they do not in the transverse direction. For the transverse direction, the influence of the tides is strongest on the southern slope near $y = 555$ km ($r^2 = 40$-50%). The standard deviation of the currents in the streamwise direction increases from seabed to surface, similar to the amplitude of the streamwise currents. The standard deviation of the secondary velocities is lower but shows an increase from middepth towards the surface and the bottom. This increase also corresponds with an increase in secondary currents as shown in Fig. 2.9.

The harmonic fit of the streamwise and secondary tidal currents during a neap tide on September 3, 2002 (1706 d) and a spring tide on September 10, 2002 (1713 d) are presented in Fig. 2.9. In general, the strongest streamwise flood currents occur in the centre of the inlet, whereas the strongest ebb currents occur to the north. During spring tides the streamwise currents are nearly twice as strong ($\sim$1.8 m s^{-1} under the ferry) as during neap tides ($\sim$1 m s^{-1}). Both the magnitude of the secondary currents (maximal 0.20 m s^{-1}) and the variation between neap and spring tides are much smaller than the streamwise currents. Their magnitude is of the same order as the standard deviation. During flood, the secondary circulation is clockwise with surface currents to the south and bottom currents to the north. During ebb there are two circulation cells: a small clockwise cell to the north and a large counterclockwise cell to the south.

Fig. 2.10 shows the streamwise vertical velocity profiles at maximum ebb and flood
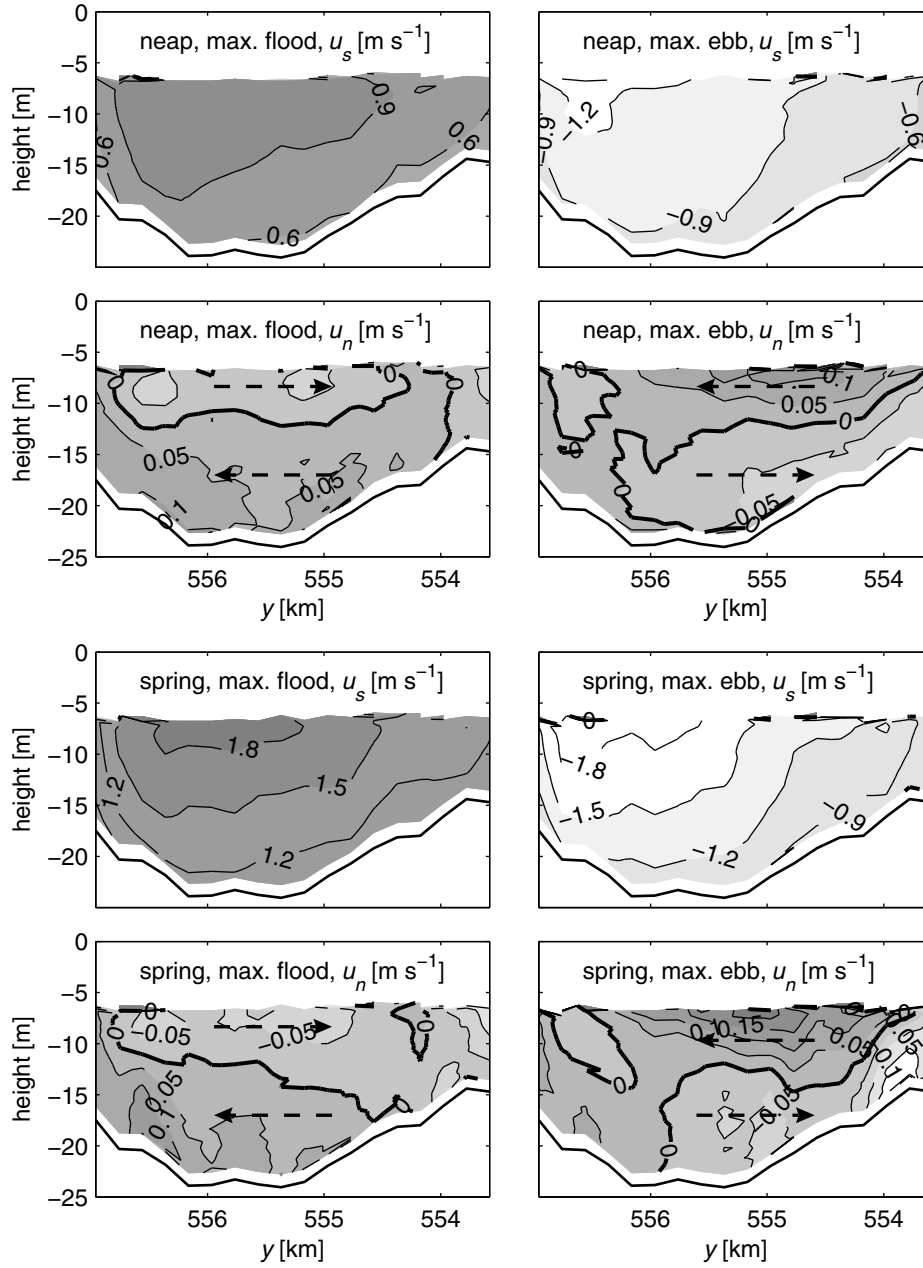
Figure 2.9. The harmonic fit of the streamwise and secondary tidal currents during a neap tide on September 3, 2002 (1706 d) and a spring tide on September 10, 2002 (1713 d). Dark (light) shades of grey indicate floodward (ebbward) streamwise currents and northward (southward) secondary currents. Dashed arrows refer to the direction of the secondary currents.

during a neap tide (1706 d) and a spring tide (1713 d) at station 10. These profiles were least-squares fitted to the well-known logarithmic profile:

$$u_s = \frac{u_*}{\kappa} \ln\left(\frac{z}{z_0}\right) \tag{2.6}$$
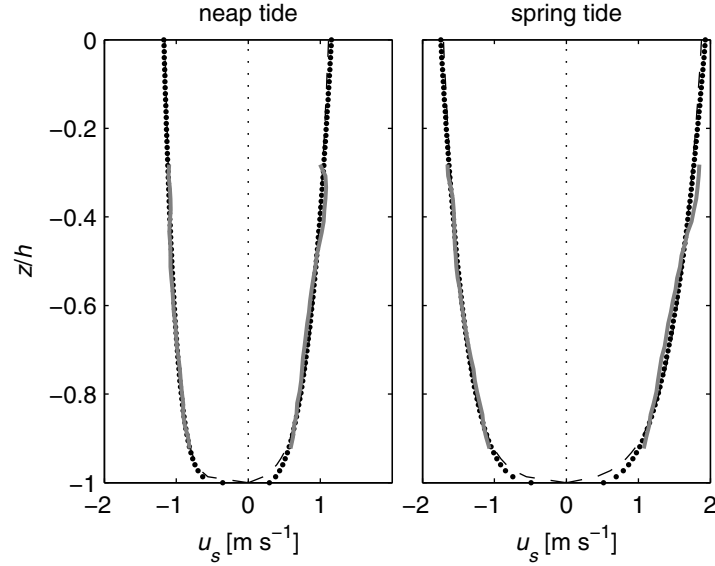
Figure 2.10. Neap (1706 d) and spring (1713 d) velocity profiles (solid line), logarithmic fits (dashed line), and power-law fits (dots) at station 10 at maximum ebb and flood. On the vertical axis the height is scaled with the mean water depth $h = 24.1$ m.

and the power-law profile (Van Veen, 1938):

$$u_s = az^{1/q}, \tag{2.7}$$

where u_s is the streamwise velocity as a function of height z above the bed, u_* the friction velocity, κ the von Karman's constant (~ 0.4), z_0 the roughness length, and a and q are constants. Furthermore, the drag coefficient for logarithmic profiles (Soulsby, 1990) was calculated according to:

$$C_\mathrm{D} = \left[\frac{\kappa}{1 + \ln\left(\frac{z_0}{h}\right)} \right]^2, \tag{2.8}$$

where h is the water depth. This equation was derived using $C_\mathrm{D} = (u_*/U)^2$, where U is the depth-mean velocity based on Eq. 2.6. Lueck and Lu (1997) fitted log profiles in a 30 m deep tidal channel and found that the log-layer extended up to 15-20 m above the bed during maximum depth-mean velocities of about 0.8 m s^{-1}. The velocities at station 10 are at least of that magnitude and therefore it is assumed that during maximum velocities the log-layer extends at least to the region under the hull of the ferry (~ 17 m above the bed). Table 2.5 lists the correlation coefficients and parameters of the logarithmic and power-law profiles. The power-law profiles have better fits (95-99%) than the logarithmic profiles (91-98%). In particular, this is the case close to the bottom, where the logarithmic profiles have more curvature than the power-law profiles. Higher in the water column, the differences between the logarithmic and power-law profiles are generally small. During flood tides the velocity profiles are more linear than during ebb tides, and as a result, the least-squares fits with the data are not as good.

    The tidal-mean streamwise currents in Fig. 2.11 reflect a similar pattern of inflow to the south and outflow to the north as in Fig. 2.6. The vertical shear on the south side of the

Table 2.5. Coefficients of determination and parameter values for the logarithmic and power-law profiles at neap and spring and ebb and flood.

		neap		spring	
		ebb	flood	ebb	flood
logarithmic	r^2 [%]	98	92	98	91
	u_* [cm s^{-1}]	5.58	9.60	11.07	14.95
	z_0 [cm]	0.59	23.18	5.01	15.81
	C_D	0.0030	0.0121	0.0060	0.0099
power law	r^2 [%]	98	95	99	95
	a	0.74	0.45	0.91	0.84
	q	6.96	3.40	4.87	3.81

inlet is positive, similar to the streamwise currents during flood, whereas on the north side the vertical shear is negative, similar to the currents during ebb. The secondary tidal-mean current patterns reveal two counter rotating circulation cells with surface convergence and bottom divergence, similar to what is observed during ebb tide. The magnitude of the tidal-mean secondary currents is about 50-80% of the instantaneous secondary currents, indicating that the secondary currents are primarily due to other processes than the tides.

A similar harmonic analysis was performed for the u and v velocities. Following Prandle (1982) and Soulsby (1990), tidal ellipse parameters, i.e. semi-major axis U_a, semi-minor axis U_b, eccentricity $E_c = U_b/U_a$, phase ϕ, and inclination ψ as a function of depth, were calculated for the M_2, S_2, and M_4 constituents and plotted in Fig. 2.12. The spatial distribution of ellipse parameters of M_2 and S_2 is quite similar. The largest U_a occurs near the surface above the deepest part of the inlet. The eccentricity of the M_2 and S_2 tidal ellipses is small (< 0.05), an indication that the flow is rectilinear. E_c is largest on the south flank, and decreases towards the surface. This coincides with a relatively high r^2 for the transverse velocities, suggesting that tides are relatively important here. In general, the rotation is counterclockwise, but clockwise on the north and south sides of the inlet. The M_2 and S_2 currents in the deepest part of the inlet lag behind the currents on the south and north sides by a maximum of about 20° or about 40 min. The
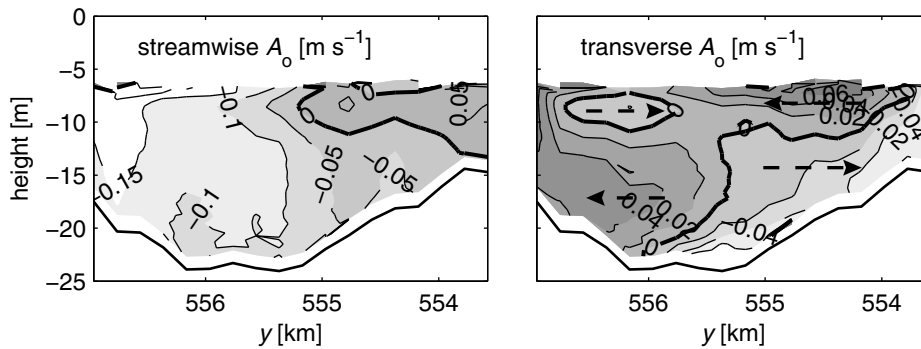
Figure 2.11. Streamwise and transverse tidal-mean velocities for the two-year period 2001-2002.
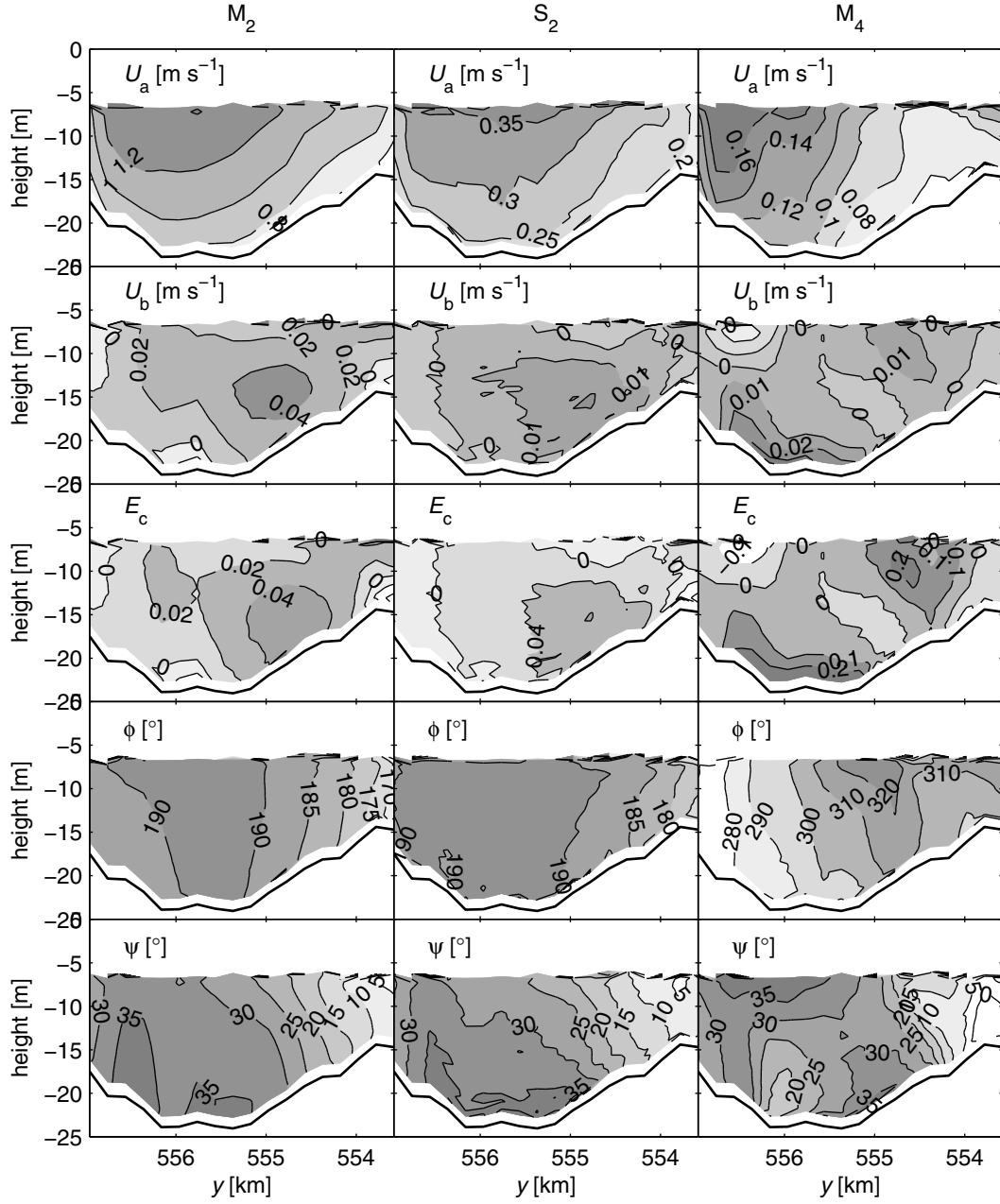
Figure 2.12. Tidal ellipse parameters for the M_2, S_2, and M_4 constituents for the two-year period 2001-2002. U_a and U_b are velocity amplitudes along the semi-major and semi-minor axes, $E_c = U_b/U_a$ is the eccentricity, ϕ the phase, and ψ the inclination. Positive (negative) values of U_b and E_c indicate counterclockwise (clockwise) rotation. Positive angles ϕ and ψ are counterclockwise relative to the x-axis.

vertical phase difference between the bottom and the underside of the ferry of 3° (about 6 min) is much smaller, with surface flow lagging behind bottom flow. The inclination ψ rotates clockwise with increasing height above the bed. At the inlet centre the directional difference over the vertical can be as much as 10°. The spatial distribution of the M_4 constituent is different from the M_2 and S_2 constituents. The reason is that M_4 is locally generated due to nonlinear terms in the momentum and continuity equations, while the origin of the M_2 and S_2 constituents is astronomic.

2.5   Discussion and conclusions

This chapter presents a unique five year long data set of current measurements from early 1998 to the end of 2002 obtained with a ferry-mounted ADCP in the Marsdiep tidal inlet, the Netherlands. Water velocities measured relative to the ADCP were corrected for ship speed and heading using DGPS and gyrocompass. To reduce the large amount of data, the data were gridded in 18 horizontal and 40 vertical bottom-following grid cells.

The ferry does not sail at night and consequently the data set is non-equidistant in time. Therefore, a least-squares harmonic analysis is the preferable method to study the contribution of the tides. The harmonic analysis was applied to the water transport through the inlet, the depth-averaged currents under the ferry, and the currents at all horizontal and vertical grid cells. With 144 constituents, up to 98% of the variance in the water transport and streamwise currents is explained due to the tides. However, a good fit of 96% is still obtained using the top 15 largest constituents. While the tides dominate in the streamwise direction, the variance explained for the transverse currents is maximally 50%.

Streamwise currents in the inlet are predominantly governed by the semi-diurnal astronomic M_2 tide, which in turn is modulated by the second-largest S_2 constituent ($\sim$27% of M_2) and the third largest N_2 constituent ($\sim$15% of M_2). The 40° phase advance of the semi-diurnal constituents of the water transport relative to the water level indicates that the tidal waves are between progressive and standing. In contrast, the phase advance of the diurnal constituents is about 60°, being more of a standing wave. Compared to the semi-diurnal tidal waves, the diurnal tidal waves are less affected by bottom friction (Zimmerman, 1992). As a consequence, the amplitude of the diurnal tidal wave that is reflected at the head of the basin is not entirely dampened at the mouth, contributing to the more standing character. While the annual Sa and semi-annual Ssa constituents are important for the water level-fluctuations (14.6% and 3.2% of M_2 amplitude) they are not important for the tidal currents (1.8% and 1.3% of M_2 amplitude).

Following Taylor (1919), it can be illustrated that for a progressive M_2 tidal wave the net energy flux into the Marsdiep basin through the Marsdiep inlet does not equal zero. The energy flux through a cross-section consists of the work done by the horizontal pressure and the potential and kinetic energy contained in the fluid passing through the cross-section. In this example, the small contribution of energy from the Vlie basin and the small contribution due to the tide generating force in the Marsdiep basin are neglected. Moreover, it is assumed that the imported energy is dissipated by bottom friction, which

is not further specified here. The energy flux averaged over a tidal cycle reads:

$$F = \frac{1}{T} \int\limits_0^T \int\limits_0^B \left(\frac{1}{2}\rho u(2g\eta^2 + H|\mathbf{u}|^2 + \eta|\mathbf{u}|^2) + \rho g H \eta u \right) \mathrm{d}y\mathrm{d}t, \qquad (2.9)$$

where T is the M_2 tidal period, B the width of the cross-section in the inlet, ρ the density, $|\mathbf{u}| = \sqrt{u^2 + v^2}$, u and v the velocities perpendicular to and along the cross-section, H the water depth below mean sea level, η the water level relative to mean sea level, and g the gravitational acceleration. Taylor (1919) showed that the quadratic terms are an order of magnitude smaller and can be ignored. If it is assumed that $Q \approx \int_0^B Hu\mathrm{d}y$ and η and ρ are constant over the cross-section, the mean energy flux is equal to:

$$F = \frac{\rho g}{T} \int\limits_0^T Q\eta\mathrm{d}t. \qquad (2.10)$$

After inserting $Q = Q_2 \cos(\omega t - \phi_Q)$ and $\eta = \eta_2 \cos(\omega t - \phi_\eta)$ and tidal averaging, the following is obtained:

$$F = \frac{1}{2}\rho g Q_2 \eta_2 (\cos\phi_Q \cos\phi_\eta + \sin\phi_Q \sin\phi_\eta), \qquad (2.11)$$

where $\omega = 2\pi/T$, Q_2 and η_2 are amplitudes, and ϕ_Q and ϕ_η phases. Using values from Table 2.2 for the amplitudes and phases of Q and η, $\rho = 1023$ kg m^{-3}, and $g = 9.81$ m s^{-2} the following are obtained: $F = 167 \times 10^6$ W or $F/B = 4.8 \times 10^4$ W m^{-1}, with $B = 3600$ m. For comparison, the mean tidal energy flux into the North Sea through the northern North Sea and the English Channel combined is about 4.8×10^{10} W (7.4×10^4 W m^{-1}) (Barthel et al., 2004). Thus, less than 1% of the energy dissipation occurs in the Marsdiep tidal basin. The mean energy flux into the Marsdiep basin is indicative of a partially progressive wave. If the tidal wave were standing, then there would be no net energy exchange through the Marsdiep inlet. This is also illustrated by Eqs. (2.10) and (2.11), which would be zero in the case of a standing wave ($\phi_\eta - \phi_Q = 90°$).

In addition to astronomic constituents, compound and overtides are important in the Marsdiep tidal inlet. The most significant are: $2MS_2$ (13.7% of M_2 amplitude), $2MN_2$ (10.9%), M_4 (10.3%), and M_6 (10.0%). Compound and overtides are due to the nonlinear terms in the continuity and momentum equations. The distortion of the M_2 tide by its quarter-diurnal overtide M_4 favours a flood-dominated tidal-current asymmetry in the southern two-thirds of the Marsdiep inlet. The presence of overtides is more pronounced during spring tides, resulting in distorted water level and velocity curves (Figs. 2.5 and 2.7). The stronger manifestation of compound and overtides during spring tides becomes apparent if the harmonic fit of the water level is separated into a contribution due to the astronomic constituents and due to the compound and overtides (Fig. 2.13; results for currents are identical). Similar to the astronomic tides, the compound and overtides show a distinct spring-neap cycle, with higher amplitudes during spring tides. This is to be expected since during spring tides the water-level gradients and related velocities are stronger, causing stronger nonlinearities. It is also during spring tides that the double high water, or agger, becomes apparent.
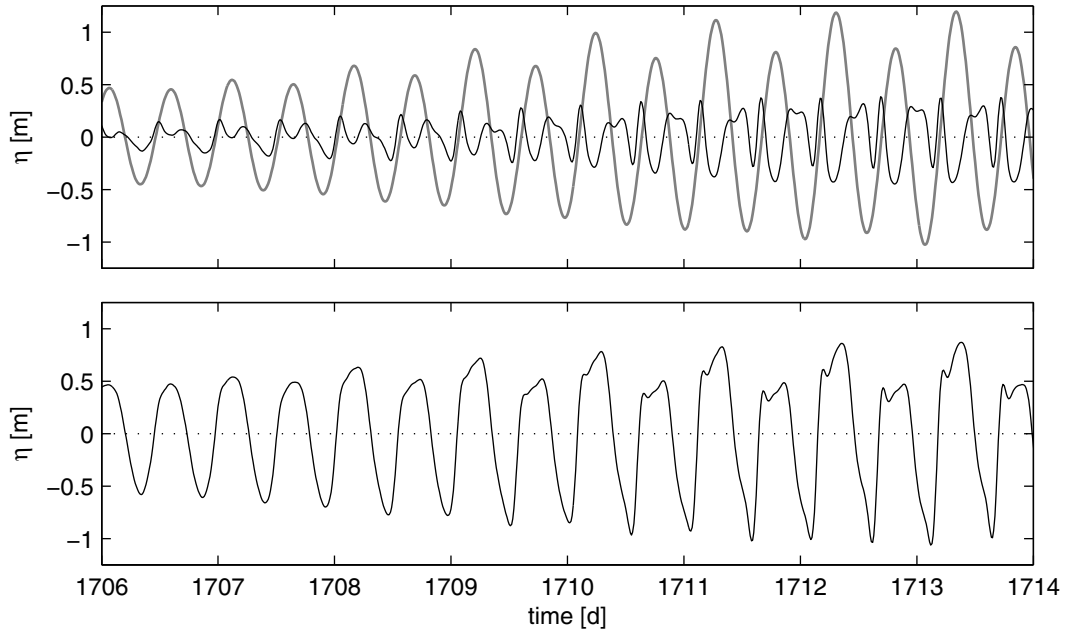
Figure 2.13. Harmonic representation comprising all astronomic constituents (grey line) and all compound and overtides (black line) in the top panel and the harmonic representation of all 144 constituents (black line) in the bottom panel for water level η from September 3 (neap) to September 11, 2002 (spring).

The currents in the inlet are sheared vertically and horizontally, with the highest currents at the surface above the deepest part of the inlet. During spring tides, surface currents can be as large as 1.8 m s^{-1}. The M$_2$ tidal currents at the inlet centre lag behind the currents at the shores by maximally 20° ($\sim$40 min). This lag can be attributed to the relative importance of inertia compared to bottom friction in the deeper inlet channel and the travel time of the tidal wave. The M$_2$ currents under the ferry lag 3° behind in phase (about 6 min) with the currents near the bottom. This indicates the importance of friction near the bottom and the importance of inertia higher in the water column. Vertical velocity profiles have a slightly better fit to the power-law profiles used by Van Veen (1938) than to the logarithmic profiles. The values for q in Eq. (2.7) and Table 2.5, however, are generally smaller than 7 proposed by Soulsby (1990) and $\sim$5 proposed by Van Veen (1938). The fits are best during ebb tides. During flood and in particular during spring tides the velocity profiles are nearly linear. The estimated values for C_D vary around 0.008 and are higher than the commonly accepted value for inlets of 0.0025 (Soulsby, 1990). These higher values may be attributed to the large bedforms that are observed in the depth measurements. These bedforms feature heights of several metres and wavelengths of hundreds of metres.

The currents in the Marsdiep inlet are strongly rectilinear. The instantaneous secondary currents have small amplitudes of maximally 20% of the streamwise currents. Both the clockwise rotation in the vertical plane during flood and the counterclockwise rotation of the southern cell during ebb (Fig. 2.9) suggest that these secondary currents are due to Coriolis forcing (Kalkwijk and Booij, 1986). At the inlet centre near $y = 555.5$

km, these counter-rotating cells during flood and ebb cause the M_2 main axis to veer counterclockwise from the seabed to the surface by about 10° (Fig. 2.12). During ebb there is one clockwise circulation cell on the north side of the inlet. The same sense of rotation during flood and ebb of this cell may be attributed to the rectification of the currents due to the bathymetry, for example due to channel curvature. The tidal-mean secondary circulation patterns in Fig. 2.11 are similar to the circulation patterns during ebb. The magnitude of the tidal-mean currents is about 50-80% of the instantaneous secondary currents, reflecting the small tidal influence. However, without knowledge of transverse density gradients and curvature of the streamlines, the driving mechanisms behind these secondary circulation cells remain unknown. The driving mechanisms are investigated in Chapter 3.

The outward Eulerian residual currents in the deeper channel to the north and the inward residual currents in the shallower channel to the south in Figs. 2.6 and 2.11 are part of a large residual eddy that extends northeastward for several kilometres. This large residual eddy and similar ones in other locations in the western Wadden Sea were first observed in the field by Zimmerman (1976b) and in model results of a two-dimensional hydrodynamical numerical model by Ridderinkhof (1988a). This model only featured tidal currents and no freshwater discharge. In a subsequent study, Ridderinkhof (1989) applied the vorticity conservation equation to the model output to explain these residual eddies and found that they are primarily due to the advection of the spatial gradient of tidal vorticity. The main source of this vorticity is the torque from bottom friction by depth gradients transverse to the tidal flow. The vorticity is generated near topographic features with a length scale comparable to the tidal excursion and advected towards areas with low vorticity production. Consequently, the residual vorticity may cause a residual circulation cell similar to the one observed in the Marsdiep inlet. The residual velocities due to this mechanism are $\mathcal{O}(0.1 \text{ m s}^{-1})$. The mechanisms that cause residual vorticity have also been extensively discussed in Robinson (1983).

An additional mechanism that may explain the outflow in the deep channel and the inflow over the shoals is discussed by Li and O'Donnel (1997). They applied the depth-averaged momentum equations with linearised quadratic friction terms to a rectangular tidal basin with a v-shaped channel. After applying a perturbation technique, they found the along-channel residual transport velocity to be dependent on a term that originates from both the linearised friction term and the 'Stokes' flux, an advection term, and a water slope term:

$$u_{\text{T}} = 2\frac{\langle \eta_{\text{p}} u_{\text{p}} \rangle}{H} - \frac{H}{\beta}\left(\langle u_{\text{p}}\frac{\partial u_{\text{p}}}{\partial x}\rangle + g\frac{\partial \langle \eta' \rangle}{\partial x}\right), \tag{2.12}$$

where β is the linearised bottom friction coefficient, $\langle \rangle$ indicates averaging over a tidal cycle, and $_{\text{p}}$ and $'$ refer to the zeroth-order and first-order solutions, respectively. The residual Eulerian velocity $\langle u' \rangle$ is equal to (2.12) with a 1 instead of a 2 in front of the first term on the right-hand side. Neglecting the small contribution of the advective term, Eq. (2.12) shows that with a progressive tidal wave the Stokes term drives an inward flux over the shoals, the influx sets up a water level gradient, and the water level gradient drives a return flow in the deeper channel. Inserting typical values for the Marsdiep basin yields a residual Eulerian velocity of $\mathcal{O}(0.01 \text{ m s}^{-1})$. Therefore, it can be concluded that, in addition to a contribution from throughflow from the Vlie tidal basin, the differential

advection of vorticity is the dominant mechanism for the observed residual circulation in the inlet.

While vorticity can be transferred from the tidal field to the tidal-mean field, it can also be transferred to higher harmonics, such as M_4, as was illustrated by Zimmerman (1980). The latter mechanism may play a role on the north side of the inlet channel. Both Table 2.4 and Fig. 2.12 show that the amplitude of the major axis of the M_4 constituent is particularly large on the north side and that the large amplitude coincides with strong streamwise residual currents (Fig. 2.11).

The strong rectifying mechanism due to the transfer of tidal vorticity may dominate over the longitudinal density gradient. Fig. 2.11 shows that the vertical shear in the tidal-mean streamwise velocity profile is positive to the south and negative to the north. It is speculated that the shear is due to a residual current modified by bottom friction, i.e. positive residual currents cause positive vertical shear and vice versa. Hansen and Rattray (1965) demonstrated that freshwater discharge at the head of the basin sets up a density gradient that drives a vertical circulation cell with surface outflow and bottom inflow. This estuarine circulation features a negative vertical shear in the streamwise residual velocity profile. With a mean freshwater discharge of about 450 m^3 s^{-1} at the head of the basin (Ridderinkhof, 1990) one would expect estuarine circulation. However, it is only to the north that the negative shear is similar to the shear related to estuarine circulation. If it is assumed that the longitudinal pressure gradient is constant over the cross-section, the estuarine circulation is expected to enhance the shear due to tidal rectification to the north and to counteract the shear due to tidal rectification to the south. The fact that the shear is still positive to the south suggests that the estuarine circulation does not dominate.

A large part of the net outflow of 2.91×10^3 m^3 s^{-1} comprises throughflow from the Vlie tidal basin (Ridderinkhof, 1988a) and is higher than numerical model results. Ridderinkhof (1988a) used a model driven by a semi-diurnal tide and two overtides and found a tidal-mean outflow of 0.82×10^3 m^3 s^{-1}. Recently, Elias et al. (2006) obtained a tidal-mean value of 2.13×10^3 m^3 s^{-1} with a model that was forced with water levels based on about 100 harmonic constituents (Edwin Elias, pers. comm., 2006). Although these model results feature smaller tidal-mean flow, they are still of the same order as the data and have the same sign.

Chapter 3

Variability of secondary currents in a weakly stratified tidal inlet with low curvature

Abstract

Ferry-ADCP data collected between early 2000 and the end of 2002 were analysed to determine the variability in instantaneous secondary (cross-channel) currents in well-mixed and stratified conditions in the 4 km wide and 25 m deep Marsdiep tidal inlet, the Netherlands. ADCP data and vertical profiles of density collected during several 13-h surveys were applied in the transverse momentum equation to determine the mechanisms that govern the variability in the secondary currents. Centrifugal and Coriolis accelerations and baroclinic pressure gradients are $\mathcal{O}(10^{-4}$ m s$^{-2})$ and govern the observed secondary circulations. In the weakly curved Marsdiep inlet ($|R_s| \approx 10$ km), local curvature dominates over Coriolis forcing in driving secondary currents in well-mixed conditions. However, in stratified conditions with vertical density gradients of maximally ~ 0.1 kg m^{-3} m^{-1}, observations suggest that transverse density gradients and Coriolis forcing, which act over larger spatial and time scales, can dominate over local curvature. During ebb, the spatial asymmetry in both turbulent mixing and freshwater discharge causes stable stratification in the southern half of the Marsdiep inlet. In these stratified conditions, near-surface secondary currents can reach values of about 0.4 m s^{-1} ($\sim 30\%$ of the streamwise currents).[1]

---

[1] This chapter is based on a manuscript submitted to Cont. Shelf Res.

3.1   Introduction

Instantaneous secondary (cross-channel or transverse) currents in estuaries are horizontal currents in the plane perpendicular to the depth-averaged (streamwise) currents. They are generally small, less than 10% of the streamwise currents, and arise from three basic mechanisms: 1) transverse density gradients, 2) channel curvature, and 3) Coriolis forcing. These mechanisms often act simultaneously and work with a similar magnitude, and it is therefore not straightforward to distinguish their individual contributions (e.g. Geyer, 1993; Dronkers, 1996; Lacy and Monismith, 2001).

Observations have primarily been reported of secondary currents in estuaries due to transverse density gradients and curvature. Nunes and Simpson (1985) observed two counter-rotating secondary circulation cells with surface convergence during flood in the well-mixed Conway estuary and attributed this to transverse density gradients that originated from the differential advection of density in the streamwise direction. Geyer (1993) observed curvature-driven secondary currents near Gay Head in Vineyard Sound that were larger than the currents according to the theory by Kalkwijk and Booij (1986; hereafter referred to as KB). Secondary currents measured in a bend in the well-mixed Volkerak estuary by Dronkers (1996) were also larger than predicted. Both Geyer (1993) and Dronkers (1996) argued that reduced internal friction due to stratification, enhanced streamwise shear, and/or transverse density gradients may have enhanced the secondary currents. Chant and Wilson (1997) observed a balance between the transverse baroclinic pressure gradient and the centrifugal acceleration downstream of a headland in the highly stratified Hudson estuary. The curvature-driven secondary currents tilted the isopycnals, and adverse baroclinic pressure gradients shut down and even reversed the secondary currents. Seim and Gregg (1997) observed in the Tacoma Narrows of Puget Sound that curvature-driven secondary currents can overturn the existing stratification if they pass a certain threshold.

To date, no observations of tidal secondary currents due to Coriolis forcing in tidal channels have been presented. They have only been studied analytically (e.g. KB; Mied et al., 2002; Lerczak and Geyer, 2004) and numerically (e.g. Geyer et al., 1998; Mied et al., 2000; Handler et al., 2001; Lerczak and Geyer, 2004; Alaee et al., 2004). In well-mixed conditions, the contribution of Coriolis forcing in the transverse momentum balance is often small in comparison to the centrifugal acceleration. Geyer (1993) illustrated this with the curvature-Rossby number: $Ro = 2\bar{u}_s/(fR_s)$, where $\bar{u}_s$ is the depth-mean streamwise current, f the Coriolis parameter, and R_s the streamwise radius of curvature. In a well-mixed estuary, with $\bar{u}_s = 1$ m s^{-1} and $f = 10^{-4}$, Coriolis acceleration becomes as important as curvature ($Ro = 1$) when $R_s = 20$ km. In other words, the Coriolis term is only important in driving secondary currents in a nearly straight tidal channel with uniform bathymetry and in absence of transverse density gradients.

In this chapter, ADCP data collected with the ferry 'Schulpengat' between early 2000 and the end of 2002 and ADCP data collected during several 13-h surveys reveal large variability in secondary currents in the 4 km wide and 25 m deep Marsdiep inlet, the Netherlands. The weak curvature of the inlet ($|R_s| \approx 10$ km) and the discharge of freshwater are indications that centrifugal and Coriolis accelerations and density gradients may affect secondary circulation in the Marsdiep inlet. The main research questions of this

chapter are: 1) What is the spatial and temporal variation in the instantaneous secondary circulation in the Marsdiep inlet? 2) What are the mechanisms that govern the secondary circulation?

The layout of this chapter is as follows. After a brief description of the study area, the transverse momentum equation is presented. In the Long-term ferry observations section, the variability in the secondary circulation observed with the ferry ADCP is analysed for well-mixed and stratified conditions. The collection of spatial ADCP and density data during several 13-h surveys is critical for the determination of the mechanisms behind the secondary circulation. These data are presented and applied in the transverse momentum equation in the 13-h surveys section. In the Discussion section, the results of the ferry and 13-h surveys are combined to form one coherent picture. The last section deals with the conclusions.

3.2   Study area

The study area encompasses the inlet of the Marsdiep tidal basin (52.985° N and 4.785° W) in the western Dutch Wadden Sea (Fig. 3.1). The inlet is bordered by the island of Texel to the north and the town of Den Helder to the south. The main channel entering the inlet from the North Sea makes a moderate righthand bend near Helsdeur ($R_s \approx 10$ km), a weak lefthand bend at the ferry transect ($R_s \approx -10$ km), and bifurcates in the Texelstroom and Malzwin channels to the east of the ferry transect. At the ferry transect, the inlet is about 4 km wide and maximally 25 m deep. The seafloor in the inlet consists of sand and is covered with large bedforms with heights of $\mathcal{O}(1$ m) and lengths of $\mathcal{O}(100$ m) (Chapter 5).

Tides constitute up to 81% of the total variance of the water levels and 98% of the currents (Chapter 2). The semi-diurnal tidal constituent M_2 is the most dominant in the vertical and horizontal tides, significantly modulated by the second largest S_2 constituent. Water levels feature amplitudes between 1 and 2 m and near-surface streamwise currents between 1 m s^{-1} and 2 m s^{-1} for neap and spring tides, respectively. Currents are flood dominated in the southern half and ebb dominated in the northern half of the inlet. The subtidal water transport through the inlet is primarily governed by tidal stresses and wind (Ridderinkhof, 1988a; Chapter 4).

Changes in salinity in the western Wadden Sea are mainly due to freshwater discharge from the Lake IJssel sluices at Den Oever (DO) and Kornwerderzand (KWZ) (Zimmerman, 1976a). The DO and KWZ sluices are located at the landward end of the Malzwin and Texelstroom channels (Fig. 3.1). The mean discharge at the DO and KWZ sluices for the period 1998-2004 is 333 m^3 s^{-1} and 239 m^3 s^{-1}, respectively. The discharge at each sluice portrays a seasonal fluctuation with high discharge in fall and winter (> 1000 m^3 s^{-1}) and low discharge in the summer months. Zimmerman (1976a) estimated that about two-thirds of the freshwater discharge from the KWZ sluices flows northward to the adjacent Vlie basin. The higher discharge of freshwater into and the shorter transit time (Ridderinkhof, 1990) of the Malzwin channel result in lower salinities in the Malzwin channel than in the Texelstroom channel. This spatial salinity difference greatly affects the secondary circulation in the Marsdiep inlet.
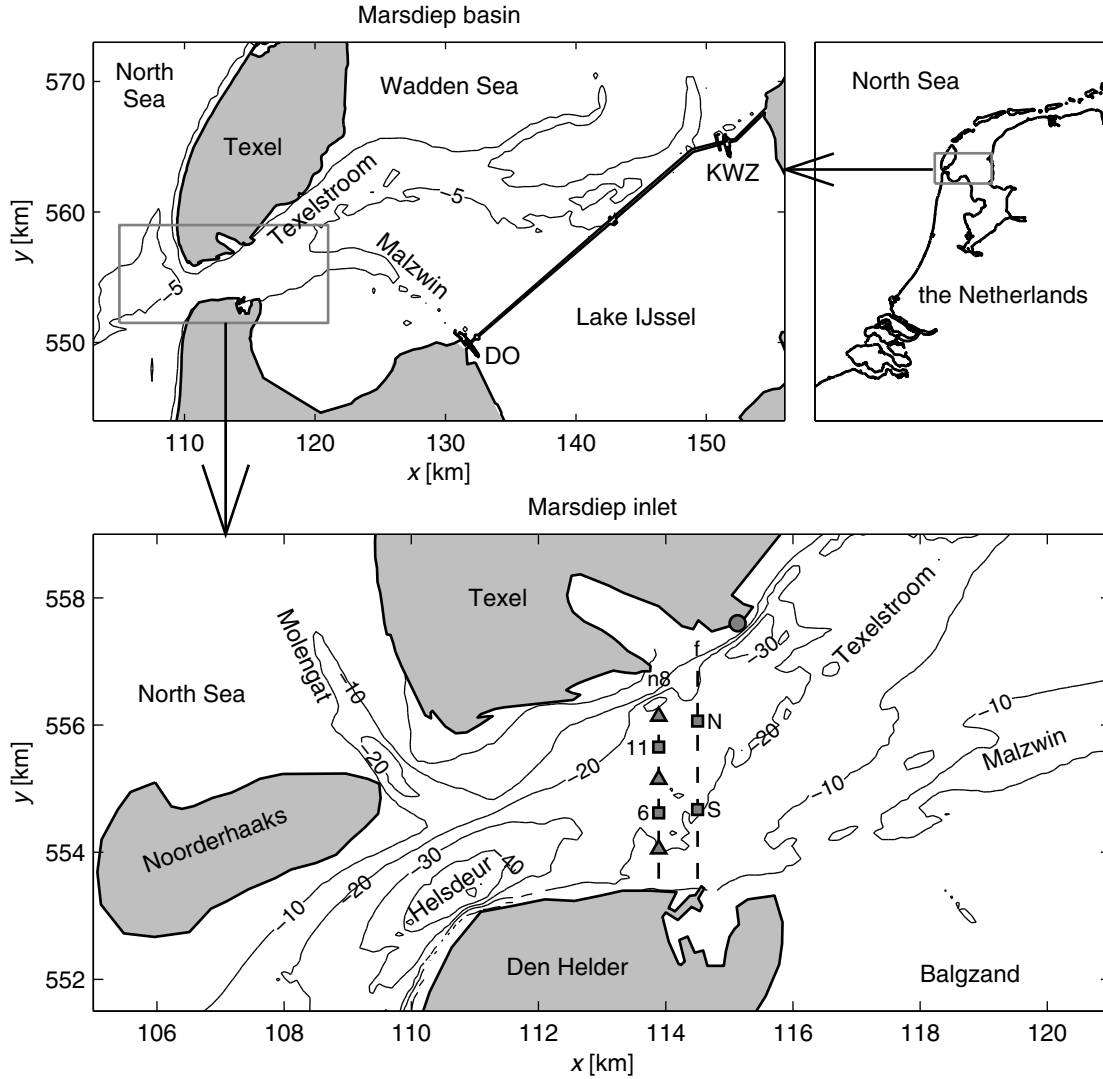
Figure 3.1. The Marsdiep basin (top left panel) and inlet (bottom panel) in the Netherlands (top right panel). DO and KWZ refer to discharge sluices of freshwater and are abbreviations for Den Oever and Kornwerderzand. The vertical dashed lines in the bottom panel mark the locations of the Navicula transect n8 and the ferry transect f. The grey triangles are locations of CTD stations and the grey squares mark stations 6 and 11 and bins South (S) and North (N). The grey circle indicates the NIOZ jetty on Texel. Bathymetry is contoured in [m] relative to mean sea level.

3.3 Equations

3.3.1 Transverse momentum balance

The orthogonal curvilinear transverse momentum balance is used to asses the importance of the centrifugal and Coriolis accelerations and transverse density gradients. Following

Kalkwijk and De Vriend (1980) and KB it is written as:

$$\underbrace{\frac{\partial u_n}{\partial t}}_{\text{A}} + \underbrace{u_s \frac{\partial u_n}{\partial s}}_{\text{B1}} + \underbrace{u_n \frac{\partial u_n}{\partial n}}_{\text{B2}} + \underbrace{u_z \frac{\partial u_n}{\partial z}}_{\text{B3}} - \underbrace{\frac{u_s^2}{R_s}}_{\text{C1}} + \underbrace{\frac{u_s u_n}{R_n}}_{\text{C2}} + \underbrace{f u_s}_{\text{D}} + \underbrace{\frac{1}{\rho}\frac{\partial p}{\partial n}}_{\text{E}} - \underbrace{\frac{\partial}{\partial z}\left(K_z \frac{\partial u_n}{\partial z}\right)}_{\text{F}} = 0, \qquad (3.1)$$

where s, n, and z indicate the streamwise, transverse, and vertical coordinate axes, u_s, u_n, and u_z are the streamwise, transverse, and vertical velocities, R_s and R_n are the radii of curvature along the streamwise and transverse coordinate axes, f is the Coriolis parameter, p the pressure, ρ the density, and K_z the eddy viscosity. The curvilinear momentum balance differs from its cartesian equivalent in the inclusion of the streamwise and transverse curvature terms C1 and C2. The remaining terms are: A is the local acceleration term, B1, B2, and B3 the streamwise, transverse, and vertical advection terms, D the Coriolis term, E the pressure term, and F the friction term. The positive s-axis is directed in the eastward flood direction, the positive n-axis is directed northward, the positive z-axis is directed upward with the origin at the water surface. The radius R_s (R_n) is positive when the positive n-lines (s-lines) diverge. The pressure term can be split up into barotropic (E1) and baroclinic (E2) components (Chant and Wilson, 1997):

$$\frac{1}{\rho}\frac{\partial p}{\partial n} = g\frac{\partial \eta}{\partial n} + \frac{g}{\rho}\frac{\partial}{\partial n}\int_z^0 \rho(z')\mathrm{d}z', \qquad (3.2)$$

where η is the water level.

3.3.2 Curvature and Coriolis forcing

KB obtained separate solutions for secondary currents as a function of depth due to curvature and Coriolis forcing in a well-mixed water column. They assumed a stationary and fully developed flow, in which the centrifugal or Coriolis accelerations balance with friction. KB omitted terms A, B, C2, and E2 in Eq. (3.1) and subtracted the depth-averaged form of Eq. (3.1) from Eq. (3.1) to eliminate the water slope term E1. The resulting equations read:

$$-\frac{u_s^2 - \overline{u_s^2}}{R_s} - \frac{\partial}{\partial z}\left(K_z\frac{\partial u_{n\mathrm{r}}}{\partial z}\right) - \frac{\tau_{n\mathrm{r}}}{\rho h} = 0 \qquad (3.3\mathrm{a})$$

$$-f(u_s - \bar{u}_s) - \frac{\partial}{\partial z}\left(K_z\frac{\partial u_{n\mathrm{f}}}{\partial z}\right) - \frac{\tau_{n\mathrm{f}}}{\rho h} = 0, \qquad (3.3\mathrm{b})$$

where the over bar indicates depth-averaging, h the water depth, $u_{n\mathrm{r}}$ and $u_{n\mathrm{f}}$ are secondary currents, and $\tau_{n\mathrm{r}}$ and $\tau_{n\mathrm{f}}$ are the bottom shear stresses due to the centrifugal and Coriolis accelerations, respectively. KB solved Eq. (3.3) assuming a logarithmic velocity profile and a parabolic eddy viscosity that depends on the depth-mean streamwise flow and a bottom friction coefficient. They used the following boundary conditions: no slip conditions at the bottom, the vertical integral of u_n is zero, and the shear stress at the surface vanishes. KB provided simple linearised solutions for $u_{n\mathrm{r}}$ and $u_{n\mathrm{f}}$ that agree well with the analytical solutions. Using these linearised solutions, expressions for surface secondary currents due

to curvature and Coriolis forcing for a bottom drag coefficient $C_D = 0.0025$ read (Geyer, 1993):

$$u_{nr,\max} \simeq 7 \frac{|\bar{u}_s| h}{R_s} \tag{3.4a}$$

$$u_{nf,\max} \simeq -\text{sign}(\bar{u}_s) 3.5 f h. \tag{3.4b}$$

Eqs. (3.3) and (3.4) reveal some interesting characteristics of secondary currents due to curvature and Coriolis forcing in well-mixed conditions. Secondary currents due to Coriolis forcing reverse when the main flow reverses, whereas secondary currents due to curvature maintain the same direction. It is remarkable that in Eq. (3.4), Coriolis-driven secondary currents do not depend on $\bar{u}_s$, while curvature-driven secondary currents scale with $\bar{u}_s$. As highlighted by Chant (2002), the driving force in Eq. (3.3a) is quadratically dependent on $\bar{u}_s$ and K_z is linearly dependent on $\bar{u}_s$. In order to balance the equation, an increase of $\bar{u}_s$ should also yield an increase in u_n. From Eq. (3.3a) follows that the larger the vertical shear in u_s, the larger the forcing term. In well-mixed conditions, an increase in $\bar{u}_s$ is proportional to an increase in the vertical shear in u_s, and an increase in u_n. The linear relation between u_n and $\bar{u}_s$ and the vertical shear in u_s was illustrated with observations by Chant (2002). In contrast, the Coriolis forcing in Eq. (3.3b) is only linearly dependent on $\bar{u}_s$. To balance the equation, u_n does not need to be dependent on $\bar{u}_s$.

When a flow enters a curve, it takes some time before the curvature-driven secondary circulation is fully developed. In this case the centrifugal acceleration balances with friction and the streamwise advection term B1. KB derived a relaxation length scale $L = h(1 - 2\alpha)/(2\alpha\kappa^2)$, where $\alpha = \sqrt{C_D}/\kappa$ and $\kappa = 0.4$ the Von Karman's constant. L indicates the length over which the secondary flow has increased to 63% of its final value. The same applies when a flow leaves a curve. L is similar for Coriolis-driven flow. In well-mixed conditions L is relatively short: with $C_D = 0.0025$ and $h = 20$ m, $L = 375$ m.

3.3.3   Dampening of turbulent mixing

The dampening of turbulent mixing due to vertical density stratification allows secondary currents to be larger than predicted and persist longer (e.g . Geyer, 1993; Dronkers, 1996; Lacy and Monismith, 2001; Lacy et al., 2003; Winterwerp et al., 2006). The relation between turbulent mixing and density stratification can be represented by several turbulence models (see Abraham (1988) for an extensive overview). For simplicity, the relation by Munk and Anderson (1948) is adopted:

$$K_z = K_{z0} \mathcal{F}(Ri) = K_{z0}(1 + \alpha Ri)^{-\beta}, \tag{3.5}$$

where Ri is the gradient Richardson number, K_{z0} is the eddy viscosity for unstratified conditions ($Ri = 0$), $0 < \mathcal{F}(Ri) < 1$ the dampening function, and α and β are constants. K_{z0} is represented by (Van de Kreeke and Zimmerman, 1990):

$$K_{z0} = C_D \bar{u}_s h. \tag{3.6}$$

While Munk and Anderson (1948) found coefficients $\alpha = 10$ and $\beta = 1/2$, other values have been reported. Recently, Simpson et al. (2005) found that observations of K_z in a weakly

stratified estuary agreed better with $\alpha = 5$ and $\beta = 2$ determined by Pacanowski and Philander (1981). Ri expresses the competition between shear-induced turbulent mixing of the main flow and vertical density stratification, which dampens turbulent mixing. It is formulated as:

$$Ri = \frac{g}{\rho} \frac{\partial \rho}{\partial z} \left(\frac{\partial u_s}{\partial z} \right)^{-2} . \tag{3.7}$$

Eq. (3.5) shows that the larger Ri the stronger the dampening of K_z. $\mathcal{F}(Ri)$ quickly decreases near $Ri = 0.25$. Miles (1961) found that when $Ri < 0.25$ turbulent mixing can overcome stratification and when $Ri > 0.25$ stratification dampens turbulent mixing.

3.4   Long-term ferry observations

3.4.1   Data handling

The multi-year ferry-ADCP data set is well suited to study the spatial and temporal variability in the instantaneous secondary currents in the Marsdiep inlet. Although the measurements with the ferry-mounted ADCP started in early 1998, ADCP data collected between March 4, 2000, and December 25, 2002, are used in this chapter. This period coincides with surface salinity and temperature collected at the NIOZ jetty, located on the northern side of the inlet (Fig. 3.1). The methodology to analyse the ADCP-current data was presented in Chapter 2 and is cursorily described here. The ferry Schulpengat crosses the Marsdiep inlet between the town of Den Helder and the island of Texel (Fig. 3.1) twice per hour at a speed of about 17 km h^{-1}, up to 32 times per day, 7 d per week, up to 320 d per year. At the beginning of each year, the ferry is out of service for maintenance for 1-2 months. To the end of 2002, data were collected with a Nortek 1.5-MHz ADCP that measured at a rate varying between 0.26 Hz and 0.35 Hz. The differential global positioning system (DGPS) aboard the ferry was used to correct for vessel speed and heading. The ADCP was mounted under the ferry at 4.3 m below the water surface and recorded eastward velocities u, northward velocities v, upward velocities w, and acoustic backscatter (ABS) in bins of 0.5 m. The blanking distance was equal to 0.5 m. Water depths from the ADCP were obtained by locating the peaks in each of the three ABS signals. The velocity data were gridded in 18 'stations' with a horizontal spacing of about 200 m along a straight line (Fig. 3.1) and 40 vertical bottom-following σ-coordinates.

The variability in the secondary velocities observed with the ferry-mounted ADCP was analysed at bins South and North along the ferry transect (Fig. 3.1). Each bin coincides with one of the two secondary circulation cells that are present at the location of the ferry transect (Fig. 3.2; results are discussed in the next section). To reduce the influence of noise, the secondary currents were averaged over stations 6-7 (bin South) and stations 13-14 (bin North). Each bin has a near-surface and bottom layer of equal thickness. The mean water depths of bin South and North are 19.9 m and 23.7 m and the mean layer thicknesses are 5.6 m and 7.5 m, respectively. The eastward $u(z)$ and northward $v(z)$ velocities at each station were mapped to the surface and bottom layer of each bin and mean velocities were calculated for all layers. The depth-mean main axis of each bin was determined and the velocities were transformed to the streamwise s and transverse n-axes, yielding u_s and

u_n, respectively. The instantaneous secondary circulation at each bin is represented by the transverse shear $\partial u_n/\partial z = (u_{n,\text{surface}} - u_{n,\text{bottom}})/(z_{\text{surface}} - z_{\text{bottom}})$, where z_{surface} and z_{bottom} are the mean elevations of the surface and bottom layers, respectively. Positive (negative) transverse shear implies a counterclockwise (clockwise) circulation when looking in the eastward flood direction.

Half-hourly measurements of surface salinity (accuracy 0.2 psu) and temperature (accuracy 0.1°C) were obtained with Aanderaa sensors attached to the NIOZ jetty between March 4, 2000, and December 25, 2002. Density was calculated from the equation of state (Millero and Poisson, 1981). For each tidal cycle, coinciding with the ferry ADCP data, the minimum and maximum density was computed, resulting in a maximum tidal density difference $\Delta\rho_t$. $\Delta\rho_t$ is a proxy for the longitudinal density gradients in the inlet, i.e. the larger $\Delta\rho_t$ the larger these gradients. It follows from observations that, on days with large $\Delta\rho_t$, the transverse density gradients and the vertical stratification are also large. It is assumed that the water column is well-mixed for $|\Delta\rho_t| < 0.25$ kg m^{-3}. This concerns about 4% of the total number of observations.

3.4.2 Observations

Well-mixed conditions

In the absence of vertical and horizontal density gradients (well-mixed conditions), the secondary circulation is only due to centrifugal and Coriolis accelerations. According to the theory by KB, the secondary currents due to these accelerations reach their maximum values at maximum streamwise flood and ebb velocities. These secondary currents are shown in the left panels of Fig. 3.2. They were computed by rotating u and v to the depth-averaged main axis at each station and by averaging all u_n that occur at maximum streamwise velocities and coincide with $|\Delta\rho_t| < 0.25$ kg m^{-3}. Note that the ferry ADCP only measures usable velocities for $z < -7$ m. At maximum flood, the secondary circulation is clockwise across nearly the entire channel and secondary velocities under the ferry are ~ 0.06 m s^{-1}. At maximum ebb, there are two secondary circulation cells with surface convergence, featuring secondary velocities < 0.03 m s^{-1}.

The vertical shear in the secondary currents $\partial u_n/\partial z$ in bins South and North was correlated with $\Delta\rho_t$, the depth-mean streamwise velocity $\bar{u}_s$, and the vertical shear in the streamwise currents $\partial u_s/\partial z$ for well-mixed conditions. $\partial u_s/\partial z$ was calculated in a similar way as $\partial u_n/\partial z$. The results are presented in Fig. 3.3. $\partial u_n/\partial z$ in bins South and North is negative at maximum flood, i.e. clockwise circulation. Over the entire range of $\bar{u}_s$, the mean secondary currents at the surface amount to -0.07 m s^{-1} and -0.08 m s^{-1} for bins South and North, respectively. Note that these velocities were calculated by multiplying the transverse shear with the entire water depth and dividing by 2. The correlation of $\partial u_n/\partial z$ with $\Delta\rho_t$ at maximum flood in bins South and North is poor ($r^2 \leq 2\%$), indicating that the influence of $\Delta\rho_t$ on $\partial u_n/\partial z$ is small under these well-mixed conditions. Although the scatter in the data is still relatively large, an increase in $\bar{u}_s$ coincides with a negative increase in $\partial u_n/\partial z$ in bins South and North (r^2 is maximally 28% in bin South). The response of $\partial u_n/\partial z$ to $\partial u_s/\partial z$ is similar, but the correlations are larger (r^2 is maximally 52% in bin North).
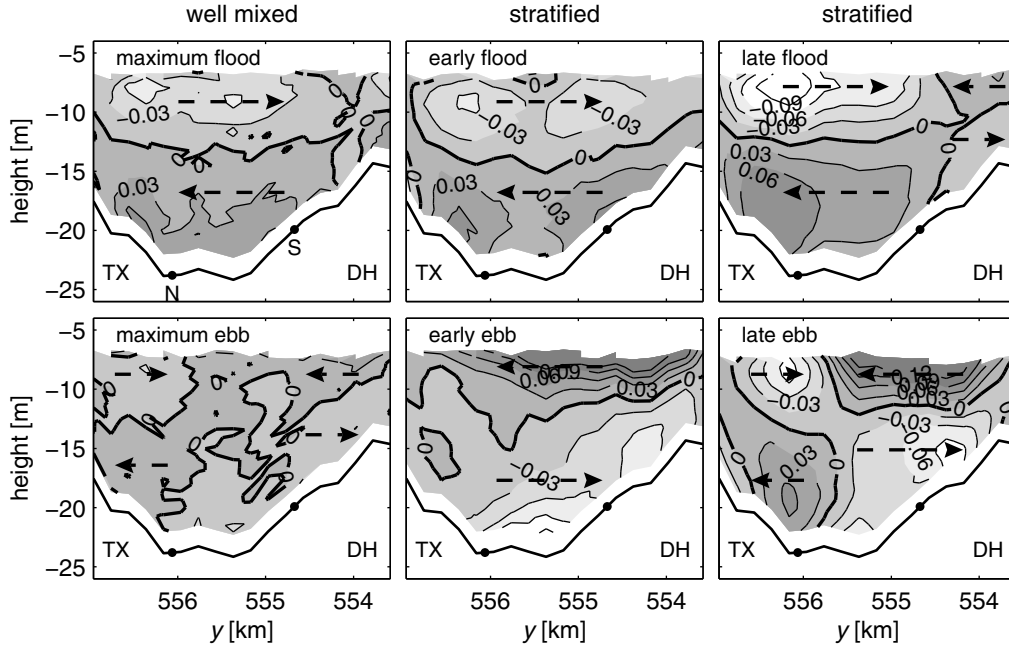
Figure 3.2. Mean secondary velocities u_n in [m s^{-1}] at maximum streamwise flood and ebb velocities during well-mixed conditions ($|\Delta\rho_t| < 0.25$ kg m^{-3}; left panels) and secondary velocities averaged over the first half of flood and ebb (early flood and ebb; middle panels) and the second half of flood and ebb (late flood and ebb; right panels) during stratified conditions ($\Delta\rho_t > 4$ kg m^{-3}). u_n is based on ferry-ADCP data collected in the period 2000-2002. Dashed arrows and dark (light) shades of grey indicate northward (southward) secondary flow. The view is eastward in the flood direction. TX and DH are abbreviations for Texel and Den Helder. The locations of bins South (S) and North (N) are indicated by the black dots on the bottom profile.

In contrast to maximum flood, the secondary circulation at maximum ebb is less well defined. $\partial u_n/\partial z$ in bin South is generally positive, whereas $\partial u_n/\partial z$ in bin North is positive for small negative $\bar{u}_s$ and negative for large negative $\bar{u}_s$. For all values, this amounts to mean secondary velocities at the surface of 0.02 m s^{-1} and -0.01 m s^{-1} in bins South and North, respectively. The correlation of $\partial u_n/\partial z$ with $\Delta\rho_t$ in bins South and North is small with $r^2 \leq 15\%$. In bin South, $\partial u_n/\partial z$ is poorly correlated with $\bar{u}_s$ ($r^2 \leq 6\%$), whereas in bin North the correlation is relatively large ($r^2 = 29\%$). There is a poor correlation between $\partial u_n/\partial z$ and $\partial u_s/\partial z$ ($r^2 \leq 2\%$) at maximum ebb.

Stratified conditions

The response of the secondary currents was studied as a function of $\Delta\rho_t$ for early and late flood and ebb. Mean secondary currents during early flood (ebb) were calculated by averaging all currents that occur between the slack water after ebb (flood) and the maximum flood (ebb) streamwise velocities. Mean secondary currents during late flood (ebb) were calculated by averaging all currents that occur between the maximum flood (ebb) streamwise velocities and the slack water after flood (ebb). Fig. 3.2 shows the
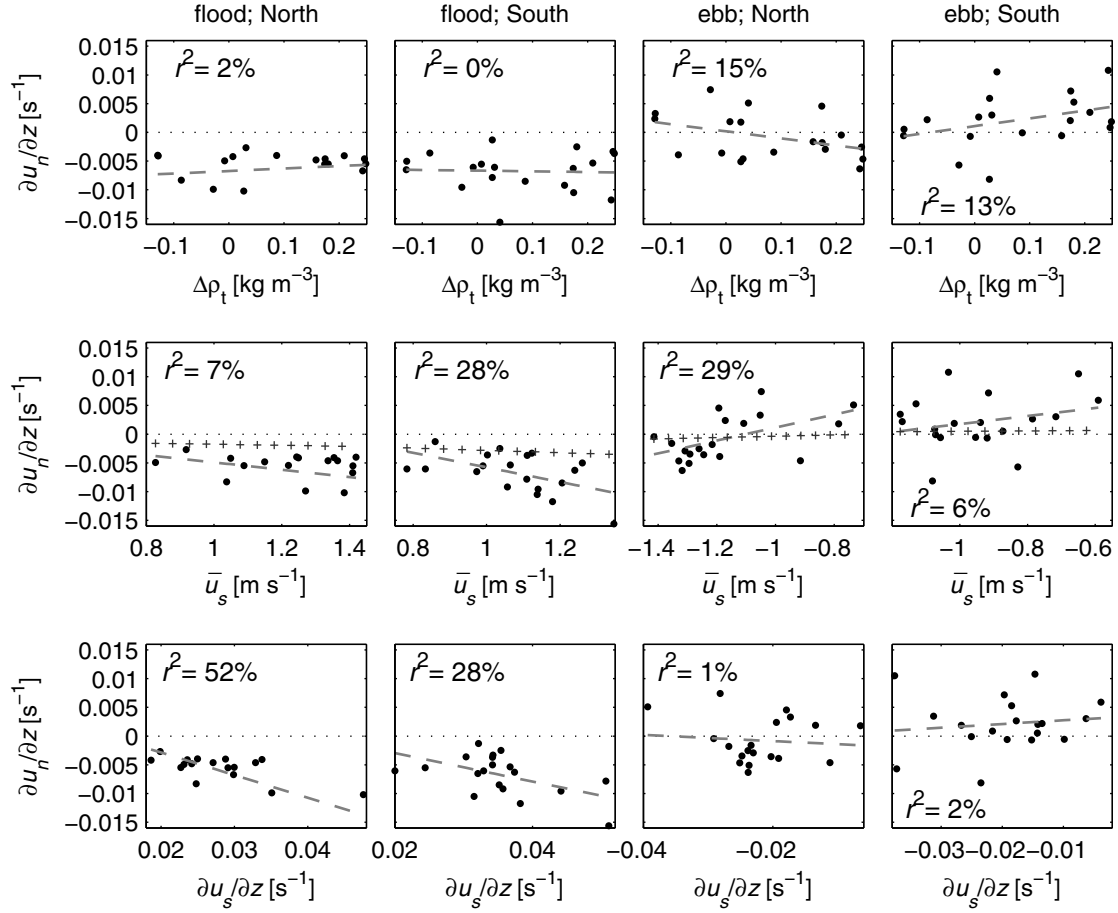
Figure 3.3. Correlations between transverse shear $\partial u_n/\partial z$ at maximum streamwise flood and ebb velocities during well-mixed conditions ($|\Delta\rho_t| < 0.25$ kg m^{-3}) on the one hand and $\Delta\rho_t$ (top panels), $\bar{u}_s$ (middle panels), and $\partial u_s/\partial z$ (bottom panels) on the other. Correlations were computed in bins South and North with the ferry-ADCP and jetty data collected in the period 2000-2002. The dots represent the data, the dashed lines the linear least-squares fits, and the crosses in the middle panels the predicted $\partial u_{n,\mathrm{KB}}/\partial z$ for curvature and Coriolis-driven secondary currents according to Eq. (3.4). The predictions are discussed in the Discussion section.

mean secondary currents for $\Delta\rho_t > 4$ kg m^{-3} (stratified conditions). In comparison to well-mixed conditions, the mean secondary currents are significantly larger. During early flood, the secondary circulation is clockwise across the entire channel. In the northern two-thirds of the channel during late flood, the circulation is clockwise with $\langle u_n \rangle > 0.09$ m s^{-1} ($\langle\rangle$ indicates time averaging). In the southern part of the channel, the circulation has reversed to counterclockwise. During early ebb, the circulation is counterclockwise across the entire channel with $\langle u_n \rangle > 0.12$ m s^{-1}. During late ebb, the circulation remains counterclockwise in the southern half of the inlet, whereas the circulation has reversed to clockwise in the northern half.

The response of $\langle \partial u_n/\partial z \rangle$ to $\Delta\rho_t$ during early and late flood and ebb is presented in Fig. 3.4. The correlations of $\langle \partial u_n/\partial z \rangle$ with $\bar{u}_s$ and $\partial u_s/\partial z$, averaged over early and late
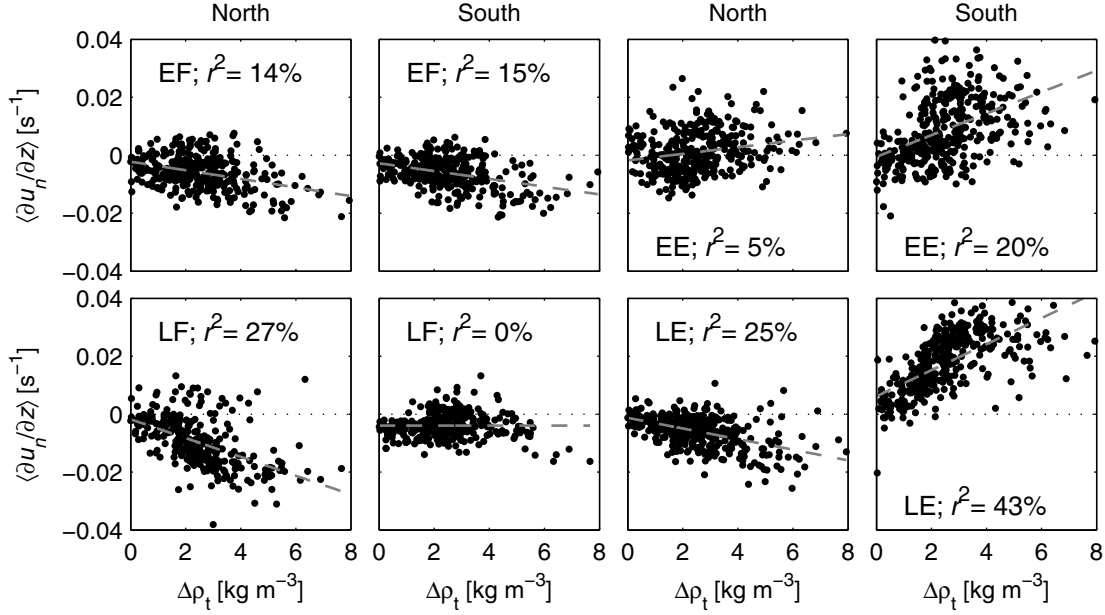
Figure 3.4. The correlation between transverse shear $\langle \partial u_n/\partial z \rangle$ and $\Delta \rho_t$ for early flood (EF), early ebb (EE), late flood (LF) and late ebb (LE) for all $\Delta \rho_t$. Correlations were computed in bins South and North with the ferry-ADCP and jetty data collected in the period 2000-2002.

flood and ebb are insignificant and are not shown here. During early flood, $\langle \partial u_n/\partial z \rangle$ becomes more negative with increasing $\Delta \rho_t$ ($r^2 \leq 15\%$). During late flood, the response at bin North is similar but stronger ($r^2 = 27\%$). The best fit of $\langle \partial u_n/\partial z \rangle$ at 4 psu for late flood and bin North amounts to a mean surface secondary velocity of about -0.17 m s^{-1}. During late flood, there is no correlation at bin South. However, in accordance with Fig. 3.2, stations to the south of bin South reveal a positive relation between $\langle \partial u_n/\partial z \rangle$ and $\Delta \rho_t$.

During early ebb at bin North, $\langle \partial u_n/\partial z \rangle$ increases slightly with increasing $\Delta \rho_t$ ($r^2 = 5\%$). The correlation is larger ($r^2 = 20\%$) at bin South, where the counterclockwise secondary circulation becomes larger with increasing $\Delta \rho_t$. During the second half of ebb, the circulation has reversed to clockwise at bin North and increases in magnitude with increasing $\Delta \rho_t$ ($r^2 = 25\%$). The response of $\langle \partial u_n/\partial z \rangle$ is strongest at bin South ($r^2 = 43\%$). The best fit of $\langle \partial u_n/\partial z \rangle$ at 4 psu for late ebb and bin South amounts to a mean surface secondary velocity of about 0.24 m s^{-1} .

In summary, the clockwise circulation cell during flood and the two counter-rotating circulation cells during ebb in well-mixed conditions are also present in stratified conditions, only with larger secondary velocities. Unfortunately, with only the ferry-ADCP data the sense of rotation and the differences between well-mixed and stratified conditions cannot be explained. For this purpose, a number of 13-h surveys was conducted, in which ADCP and horizontal and vertical density data were collected. These data are discussed in the next section.

3.5 13-h surveys

In this section, the ADCP and density data obtained during several 13-h surveys are applied to the transverse momentum balance Eq. (3.1) to determine the mechanisms behind the observed secondary circulations. Observations and the evolution of the terms in the transverse momentum equation during a day with large density differences (June 15, 2006) are discussed in detail.

3.5.1 Data handling

ADCP and density data were collected during several 13-h surveys with the NIOZ research vessel 'Navicula'. These surveys were conducted on September 16, 2003 (n1), November 18, 2003 (n2), June 2, 2004 (n3), July 7, 2004 (n4a and n4b), September 15, 2005 (n5), November 22, 2005 (n6), March 9, 2006 (n7), June 15, 2006 (n8), and September 5, 2006 (n9). The transect locations are indicated in Figs. 3.1 and 3.8. Surveys n5-n9 approximately coincide with survey n8 in Fig. 3.1. The Navicula sailed with a speed of about 10 km h^{-1} up and down the transects. The duration of the crossings varied between 15 and 30 min. A Nortek 1.0-MHz ADCP was used to measure current velocities and depths. The uncertainty of the velocity measurements is about 1% of their magnitude. The 1.0-MHz ADCP was mounted at about 1 m below the water surface, has a blanking distance and bin size of 1.0 m, and measures at a rate of 1 Hz. The 1.0-MHz ADCP uses bottom tracking to correct for vessel speed and heading. The 1.0-MHz ADCP was calibrated during dedicated cruises before performing the 13-h surveys. Velocity data in the first cell under the ADCP and the first cell above the bottom and outliers were removed. Similar to the ferry-ADCP data, velocities u and v were gridded in horizontal cells (stations) with a width of 150-200 m and 40 bottom following σ-coordinates between the bottom and water surface.

Every second or third crossing, at generally three locations along each transect, vertical profiles of conductivity, temperature, and depth (CTD) were obtained with Seabird sensors to determine vertical and horizontal density gradients. The accuracy of these sensors is 0.005 psu, 0.004°C, and ∼0.05 m, respectively. Moreover, surface conductivity and temperature were continuously measured with Seabird sensors at about 1 m below the water surface. Water density was calculated using the equation of state (Millero and Poisson, 1981).

3.5.2 Observations on June 15, 2006

Velocity and density data collected with the research vessel Navicula on June 15, 2006, are presented to illustrate the effects of large transverse and vertical density gradients on secondary currents. The daily maximum density difference $\Delta\rho_t$ on this day inferred from the surface salinity measured with the Navicula at the northern part of transect n8 is about 4 kg m^{-3}. It follows from the jetty measurements that about 86% of the observations has a $\Delta\rho_t < 4$ kg m^{-3}. This implies that June 15 is a day with relatively large density gradients. The maximum density difference for all CTD profiles across the entire inlet is about 7.9 kg m^{-3}. Streamwise and secondary currents and density ($\sigma = \rho - 1000$ kg m^{-3}) at five

points in the semi-diurnal tidal cycle are presented in Fig. 3.5 and the surface density and secondary currents along transect n8 for the entire tidal cycle in Fig. 3.6.
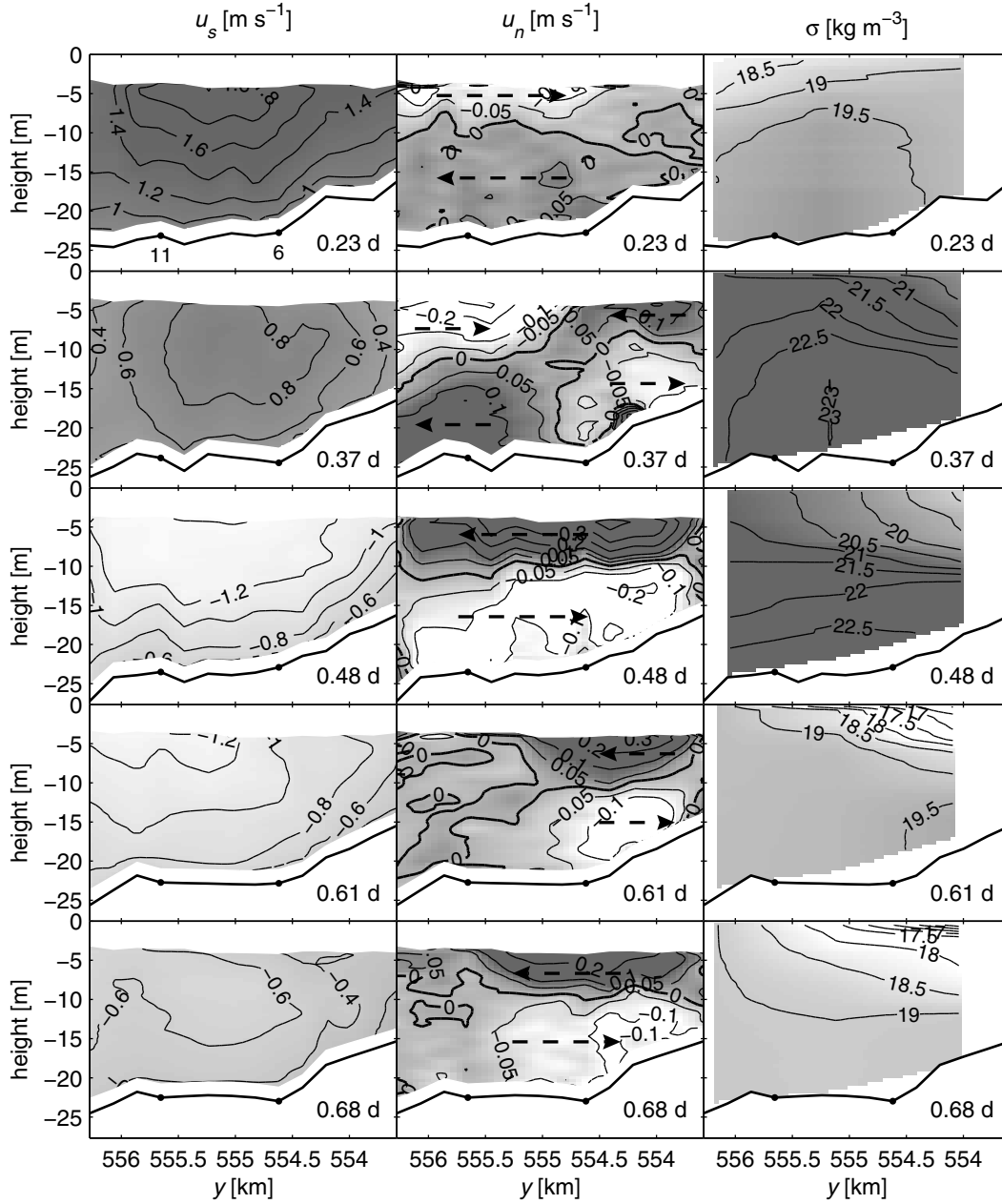
Figure 3.5. Streamwise and secondary velocities and density for five times on June 15, 2006. Times in the tidal cycle are also indicated in Fig. 3.9. In the left column, dark (light) shades of grey refer to floodward (ebbward) u_s. In the middle column, dashed arrows and dark (light) shades of grey indicate northward (southward) u_n. In the right column, dark (light) shades of grey indicate high (low) density. The location of stations 6 and 11 is indicated by the dots on the bottom profile. The view is eastward in the flood direction.
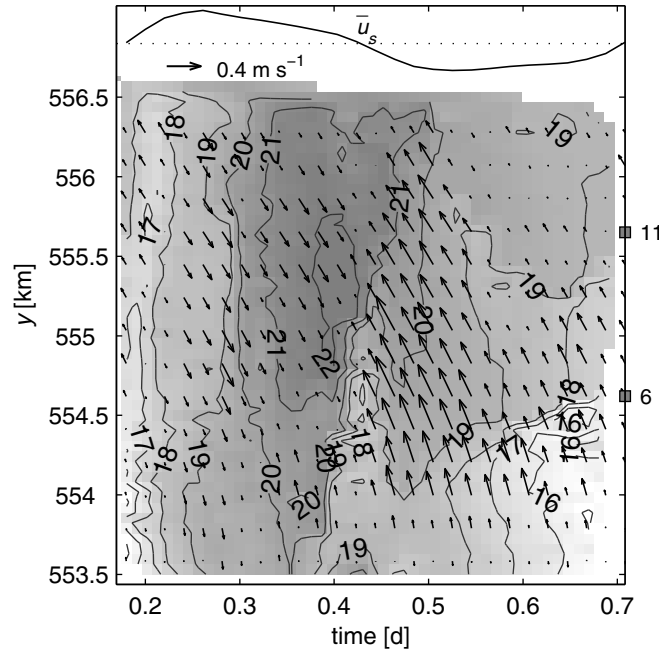
Figure 3.6. Surface density (σ) and surface secondary currents (arrows) as a function of time and y for survey n8 on June 15, 2006. Dark (light) shades of grey indicate high (low) σ. σ is contoured in 1 kg m^{-3}. The scaled depth-mean streamwise velocity curve at the top of the figure indicates flood (above dotted line) and ebb (below dotted line). Stations 6 and 11 are marked by the squares on the right axis.

Near maximum flood at 0.23 d, the inlet is weakly stratified. The secondary circulation is clockwise across the entire inlet featuring surface velocities of maximally 0.1 m s^{-1}. As the flood progresses at 0.37 d, denser water is advected to the inlet centre. The heavy dome of salt water spreads out to the channel sides, causing two secondary circulation cells with surface convergence and surface speeds larger than 0.2 m s^{-1}. The advection of water with small u_s from the sides to the channel centre, causes a decrease of u_s at the channel centre and a sinking of the core with the highest u_s. Before maximum ebb at 0.48 d, the water column portrays the strongest stratification of the entire tidal cycle ($\Delta\rho \approx 2.5$ kg m^{-3}). The secondary circulation is counterclockwise and features the largest velocities of maximally 0.4 m s^{-1} near the surface. This is about 30% of u_s at the surface. The influx of fresher water from the Malzwin channel is visible near the south shore and causes axial density fronts that are visible as foam lines on the water surface (Fig. 3.7). The fronts gradually progress northward (visible in Fig. 3.6 between $y = 554$ km and $y = 554.5$ km). After maximum ebb at 0.61 d, the water column has become well-mixed to the north of $y = 555$ km, whereas it remains stratified due to the lower mixing and the influx of fresher water in the southern part. In the well-mixed part of the inlet the clockwise secondary circulation is very small, while in the stratified southern part the counterclockwise secondary circulation features velocities of maximally 0.25 m s^{-1}. At the end of ebb at 0.68 d, the streamwise velocities in the northern half of the inlet have decreased significantly to allow the freshwater front to spread northward again (Fig. 3.6).

Figure 3.7. An axial foam line marks a density front in the southern half of the Marsdiep inlet. View is westward. Photo by Frans Eijgenraam.

Simultaneously, the secondary circulation is counterclockwise across the entire inlet. The northward advection of water with low streamwise velocities causes northward tilting of the high velocity core at the centre of the inlet. The effects of transverse advection of streamwise velocities on the vertical streamwise velocity profile during late flood and ebb have also been observed by Lacy and Monismith (2001) and Lacy et al. (2003) and modelled by Lerczak and Geyer (2004).

3.5.3 Evaluating the transverse momentum equation

Radius of curvature

The radius of curvature needed to estimate the centrifugal acceleration was determined using Navicula surveys n1-n4. Depth-mean velocities were calculated and main axes of depth-mean velocities were determined for flood and ebb at each station along transects n1-n4. These axes were linearly interpolated on a 150-m^2 grid. Each main axis is aligned with the streamwise axis. The change of orientation of the main axis over a small distance along a streamline yields R_s:

$$\frac{\mathbf{e}_n}{R_s} \equiv \frac{\partial \mathbf{e}_s}{\partial s},\tag{3.8}$$

where $\mathbf{e}_s$ and $\mathbf{e}_n$ are unit vectors tangent and perpendicular to the main (s) axes. R_s was calculated in each grid point using Eq. (3.8). In a final step, values for R_s used in the transverse momentum equation were interpolated from these grids over several 100 m upstream of each bin and station during flood and ebb and averaged.

The main axes of the depth-mean currents and R_s during flood and ebb are presented in Fig. 3.8. A righthand bend in the positive streamwise direction corresponds to positive curvature. Fig. 3.8 reveals subtle differences in curvature between flood and ebb. During
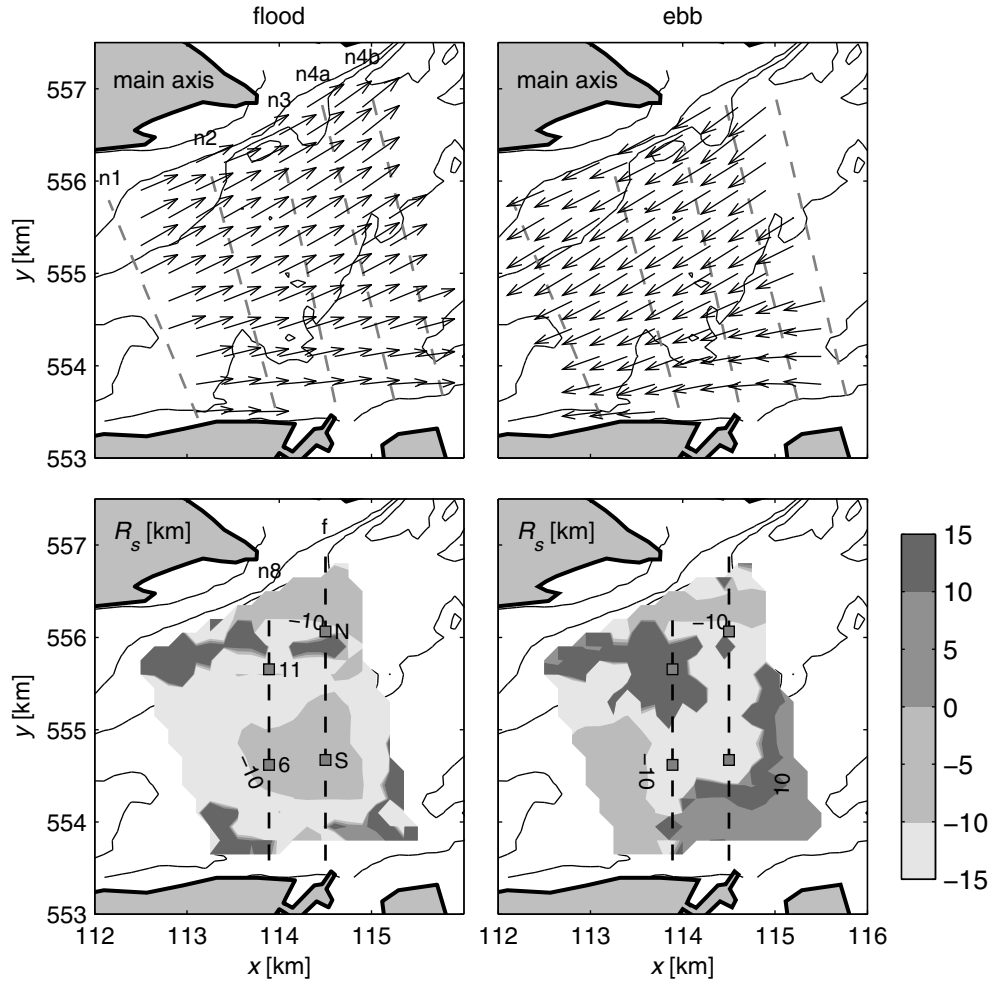
Figure 3.8. Depth-mean main axes of flow during flood and ebb (top panels) and radius of curvature during flood and ebb (bottom panels). Main axes and R_s were calculated using the Navicula surveys n1-n4, indicated by the grey dashed lines in the top panels. The grey squares in the bottom panels indicate stations 6 and 11 along the Navicula transect n8 and bins South (S) and North (N) along the ferry transect f.

flood, the flow is concentrated in the deep (< -30 m) and prismatic main channel that hugs the southern shoreline to the west of $x = 113$ km. Between $x = 113$ km and $x = 116$ km, the main channel bifurcates in the primary Texelstroom channel to the north and the secondary Malzwin channel to the south. The bulk of the flow is forced in a lefthand curve to stay in the northeast trending Texelstroom channel. This causes R_s to be generally negative in the entire study area. In the southern half of the inlet at the location of the n8 and f transects, $R_s > -10$ km. Moreover, some smaller bathymetric features on the north side of the Texelstroom channel near the n8 and f transects also cause $R_s > -10$ km.

In contrast to flood, areas with both negative and positive curvature are present during ebb. The differences between flood and ebb can be attributed to the inertia of the flow in response to changing bathymetry. During ebb the bulk of the flow is concentrated in

Table 3.1. Scaling in [m s^{-2}] for well-mixed conditions (MC) and stratified conditions (SC). B, S, and h refer to the width of the inlet, the length scale of streamwise advection, and the water depth, respectively.

	$T = 44676/4$ s; $B = 4$ km; $S = 5$ km; $h = 20$ m; $R_s = 10$ km; $R_n = 10$ km; $f = 10^{-4}$ s^{-1}; $g = 9.81$ m s^{-2}; $\rho = 1000$ kg m^{-3}; $\Delta\eta = 0.10$ m; $u_s = 1.25$ m s^{-1}; $u_z = 0.001$ m s^{-1}; $\Delta u_n = 0.1$ m s^{-1} MC: $u_n = 0.05$ m s^{-1}; $\Delta\rho = 0$ kg m^{-3}; SC: $u_n = 0.2$ m s^{-1}; $\Delta\rho = 2$ kg m^{-3}								
	A	B1	B2	B3	C1	C2	D	E1	E2
	$\frac{u_n}{T}$	$u_s\frac{\Delta u_n}{S}$	$u_n\frac{u_n}{B}$	$u_z\frac{2u_n}{h}$	$\frac{u_s^2}{R_s}$	$\frac{u_s u_n}{R_n}$	fu_s	$g\frac{\Delta\eta}{B}$	$\frac{g}{\rho}\frac{\Delta\rho h}{B}$
MC	10^{-6}	10^{-5}	10^{-6}	10^{-6}	10^{-4}	10^{-5}	10^{-4}	10^{-4}	-
SC	10^{-5}	10^{-5}	10^{-5}	10^{-5}	10^{-4}	10^{-5}	10^{-4}	10^{-4}	10^{-4}

the Texelstroom channel. The flow is forced in a moderate righthand bend ($R_s > -10$ km) in the southern half of the inlet to the west of n8. Similar to flood, local bathymetric features cause $R_s > -10$ km at the northern parts of transects n8 and f. During ebb, at the confluence of the Malzwin and Texelstroom channels ($x > 114$ km and $y < 555.4$ km), the flow is forced in a lefthand bend featuring $R_s < 10$ km.

Estimating the terms in the transverse momentum equation

Before applying the Navicula data in the transverse momentum balance Eq. (3.1), the relative importance of the terms was estimated for well-mixed and stratified conditions in the Marsdiep inlet. The friction term F in Eq. (3.1) was difficult to parameterise and its magnitude was not determined. The results of this analysis are presented in Table 3.1.

In well-mixed conditions the secondary currents are about 0.05 m s^{-1} at the surface during flood and very small during ebb. To estimate the local acceleration term A, the duration T was chosen equal to a quarter of the M$_2$ tidal cycle. During flood, when the tidal flow enters the Marsdiep inlet, it first goes through a weak righthand bend near Helsdeur with $R_s \approx 10$ km (Fig. 3.1) and about 5 km downstream at the ferry transect through a weak lefthand curve with $R_s \approx -10$ km (Fig. 3.8). Consequently, the secondary circulation changes from counterclockwise to clockwise. This yields $\Delta u_n \approx 0.1$ m s^{-1} at the surface for the B1 term. The inclination of the main axis of the depth-averaged currents varies about 20° across the ferry transect. This yields $R_n \approx 10$ km. Table 3.1 shows that the largest terms of $\mathcal{O}(10^{-4}$ m s$^{-2})$ are the streamwise curvature (C1), Coriolis (D), and water-level gradient (E1) terms. The remaining terms are at least an order of magnitude smaller. Consequently, this scaling indicates that in well-mixed conditions it suffices to only consider the local forcing terms C1, D, and E1. In stratified conditions, the horizontal density gradient is about 0.5 kg m^{-3} km^{-1}. Surface secondary currents during flood and ebb are about 0.20 m s^{-1} and can have opposing signs. The baroclinic pressure term E2 is $\mathcal{O}(10^{-4}$ m s$^{-2})$ and of similar importance as C1, D, and E1. Compared to the well-mixed conditions, the secondary currents are larger and result in larger local acceleration and transverse and vertical advection terms of $\mathcal{O}(10^{-5}$ m s$^{-2})$.

The scaling analysis illustrates that in the moderately curved and weakly stratified Marsdiep inlet the centrifugal and Coriolis accelerations and the barotropic and baroclinic

pressure terms are the most important. It is assumed that these forcing terms balance with friction and/or local acceleration. While this scaling deals with scales > 4000 m, it is possible that advection is more important on smaller scales (e.g. near density fronts or due to strong local curvature).

Methodology

The transverse momentum balance was analysed for surveys n3 and n5-n9 at stations located in the southern and northern half of the Marsdiep inlet. Each station is situated in the middle of two CTD locations. The distance between the CTD locations is about 1 km. The evolution of the terms of the transverse momentum balance at stations 6 and 11 along transect n8 (Fig. 3.1) is discussed in detail in the next section.

Terms A, C1, D, and E2 in Eq. (3.1) were estimated as follows. The horizontal velocities u and v were regridded on an equidistant time grid with a time step of about 30 min. Main or s-axes for the depth-mean currents were determined for the duration of each 13-h survey. At stations 6 and 11, the s-axes make counterclockwise angles of $25.5°$ and $32.8°$ with the positive x-axis, respectively. Currents u and v were transformed to u_s and u_n, along and perpendicular to the s-axes. Term A was computed according to $(\partial u_n/\partial t)_i \approx (u_{n,i+1} - u_{n,i-1})/(t_{i+1} - t_{i-1})$, where i is an index indicating the time step. Term E2 was calculated over a distance perpendicular to the s-axis. For every time step, the transverse momentum balance was integrated and averaged over the vertical height of the near-surface and near-bottom layers, which feature equal heights of 6-8 m. The contribution of the water-level gradient term E1 was eliminated by subtracting the averaged transverse momentum equation of the bottom layer from the equation of the surface layer, yielding $\Delta(\partial u_n/\partial t)$, $\Delta(-u_s^2/R_s)$, $\Delta(f u_s)$, and $\Delta(1/\rho\partial p_c/\partial n)$ for terms A, C1, D, and E2, respectively. Similarly, mean values of u_s and u_n of the bottom layer were subtracted from mean values of the surface layer, yielding Δu_s and Δu_n.

Unfortunately, the internal friction could not be calculated from the data. The influence of stratification on turbulent mixing was illustrated with estimates of K_z and Ri. K_z was obtained using Eqs. (3.5) and (3.6), $\alpha = 5$, and $\beta = 2$. The gradient Richardson number for two layers was calculated according to:

$$Ri_{\mathrm{L}} = \frac{g\Delta\rho\Delta h}{\rho(\Delta u_s)^2},$$

(3.9)

where Δh is the difference in height of the layer centres and $\Delta\rho$ the difference in density between the layers. The density as a function of depth at each station was interpolated from the adjacent CTD locations.

Transverse dynamics on June 15, 2006

The relation between the secondary currents and terms in the transverse momentum equation on June 15, 2006, at stations 6 and 11 is evaluated in Fig. 3.9. Fig. 3.9 shows $\bar{u}_s$ (top panels), Δu_s and Δu_n (second panels), $\Delta(\partial u_n/\partial t)$, $\Delta(-u_s^2/R_s)$, $\Delta(f u_s)$, $\Delta(1/\rho\partial p_c/\partial n)$, Δsum, and $K_z = \mathcal{F}(Ri)K_{z0}$ (third and fourth panels), and the two-layer gradient Richardson number Ri_{L} (bottom panels). Δsum is the sum of the Coriolis, curvature, and baroclinic pressure terms. R_s was estimated from Fig. 3.8 and equals about -10 km and -11
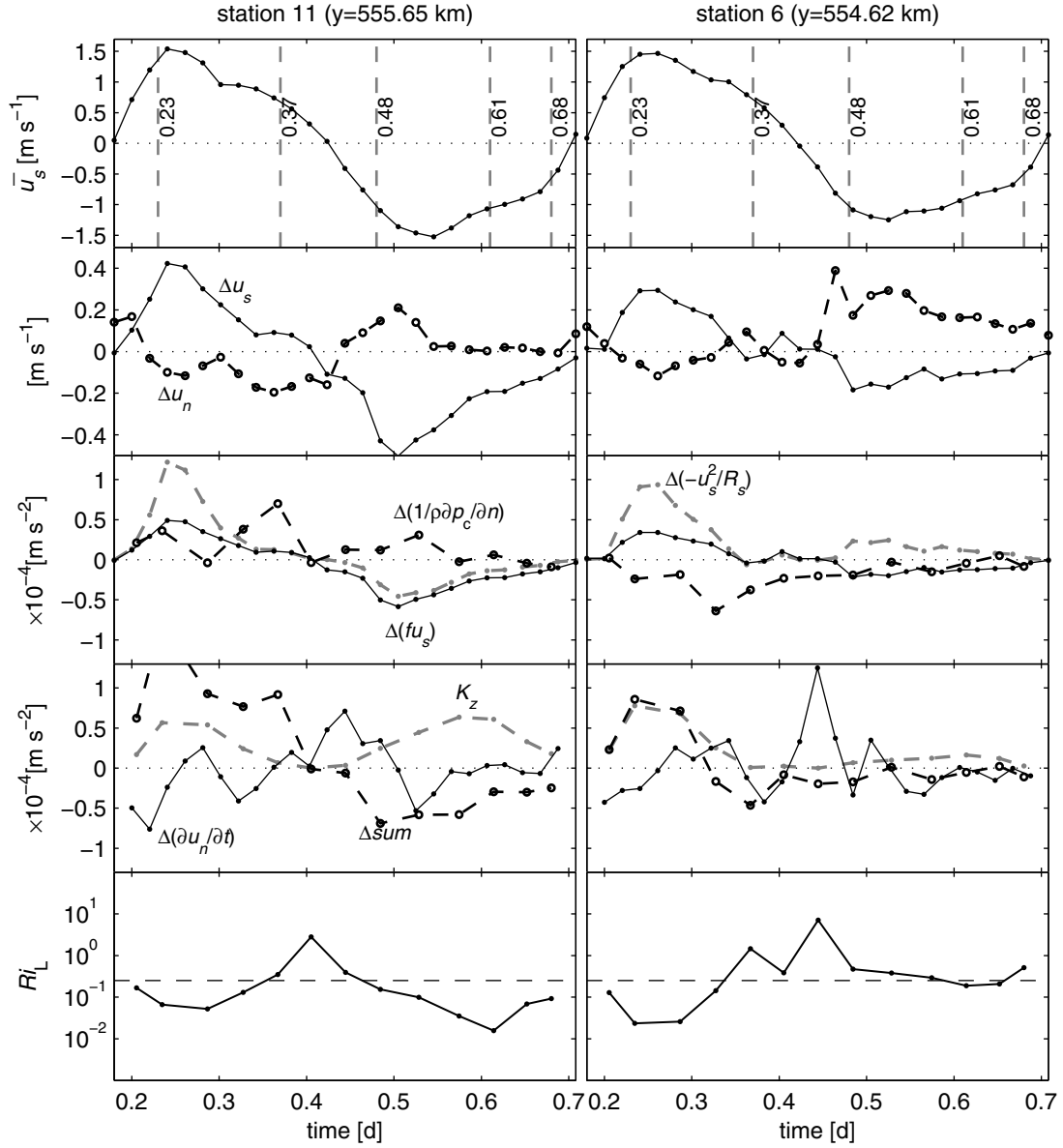
Figure 3.9. The depth-mean streamwise velocity (top panels), the top to bottom difference in velocity (second panels), the top to bottom difference in the terms of the transverse momentum equation (third and fourth panels), the dampened eddy viscosity ($\times 10^{-3}$; fourth panels), and the two-layer gradient Richardson number (bottom panels) at stations 6 and 11 along transect n8 on June 15, 2006. In the bottom panels, $Ri_L = 0.25$ is indicated by the horizontal dashed line. The vertical dashed grey lines in the top panels correspond to the times in Fig. 3.5.

km at stations 6 and 11 during flood and -18 km and 30 km at stations 6 and 11 during ebb, respectively. The Coriolis parameter was set to $f = 1.16 \times 10^{-4}$ s^{-1}.

At maximum flood near 0.23 d, Δu_s coincides with a small minimum in Δu_n (clockwise circulation) at stations 6 and 11. At this time, the curvature and Coriolis terms have the same sign, and their forcing agrees with the observed secondary circulation. Ri_L is below

the stability threshold of 0.25, indicating a well-mixed water column and a relatively large K_z. As a consequence, the secondary currents are small. As the flood progresses near 0.35 d, a core of dense water appears at the inlet centre due to differential advection (0.37 d in Fig. 3.5). The resulting baroclinic pressure gradients are negative at station 6 and positive at station 11 and are the largest of the tidal cycle. These gradients correspond to a $\partial\bar{\rho}/\partial n$ of about 1 kg m^{-3} km^{-1}. For comparison, $\partial\bar{\rho}/\partial s$ ($= -1/\bar{u}_s\partial\bar{\rho}/\partial t$) is about 0.2 kg m^{-3} km^{-1} at each station and constant over the tidal cycle. The baroclinic pressure gradients dominate over the Coriolis and centrifugal accelerations and cause the secondary circulation to reverse to counterclockwise at station 6 and to increase at station 11. The increase and reversal coincide with an increase in stratification and a dampening of turbulence. At station 6 near 0.40 d, the secondary circulation reverses again to clockwise, against the dominant baroclinic pressure gradient. This may be attributed to the fact that station 6 is situated on the northern edge of the counterclockwise circulation cell (Fig. 3.5).

At the onset of ebb near 0.42 d, the water column is strongly stratified across the entire inlet. At station 11, the secondary circulation reverses quickly to counterclockwise simultaneously with a strong increase in Δu_s. They both peak near 0.51 d. The increase of the secondary circulation may be attributed to a strong increase of the Coriolis acceleration, which is larger and opposite to the baroclinic pressure gradient, and a strongly dampened turbulent mixing. At station 6 during the entire ebb, the secondary circulation remains strongly counterclockwise. Note that Δu_n is larger than Δu_s. Although small, the baroclinic pressure gradient and the Coriolis acceleration have the same magnitude and sign. They are able to maintain a strong secondary circulation due to the dampening of turbulence due to the persistent stratification ($Ri > 0.25$ and $K_z \approx 0$). Although the centrifugal forcing opposes the Coriolis and baroclinic forcing, it is not strong enough to overcome them. In addition, the Coriolis and baroclinic forcing have been able to accelerate u_n over several km, while the centrifugal forcing acts locally and is not able to reverse the actual secondary circulation. The secondary circulation is further maintained due to $\partial u_n/\partial t$. At station 6 during ebb, the shear in u_s is small and the turbulent mixing is not strong enough to break down the stratification. Moreover, the stratification is maintained by the secondary circulation, which causes the northward spread of fresher surface water. In contrast, at station 11 after maximum ebb near 0.52 d, the secondary circulation is nearly shut down. The stratification has been destroyed due to vigourous turbulent mixing. Consequently, the Coriolis and curvature acceleration terms balance with turbulent mixing and in agreement with the theory by KB this results in small secondary currents.

Multiple 13-h surveys

The transverse dynamics and mixing are similar for Navicula surveys n3 and n5-n9. For every time step (represented by a black dot), for flood and ebb at the northerly and southerly stations, $\partial u_n/\partial z$ is plotted against $\partial sum/\partial z$, Ri_{L}, and K_z in Fig. 3.10. $\partial u_n/\partial z$ and $\partial sum/\partial z$ represent Δu_n and Δsum normalised by the vertical distance Δh between the layers.

The general trend is that during flood $\partial sum/\partial z$ is positive and $\partial u_n/\partial z$ negative, whereas during ebb $\partial sum/\partial z$ is negative and $\partial u_n/\partial z$ positive. This indicates that the sum of the accelerations governs the observed secondary circulations. Although $\partial sum/\partial z$
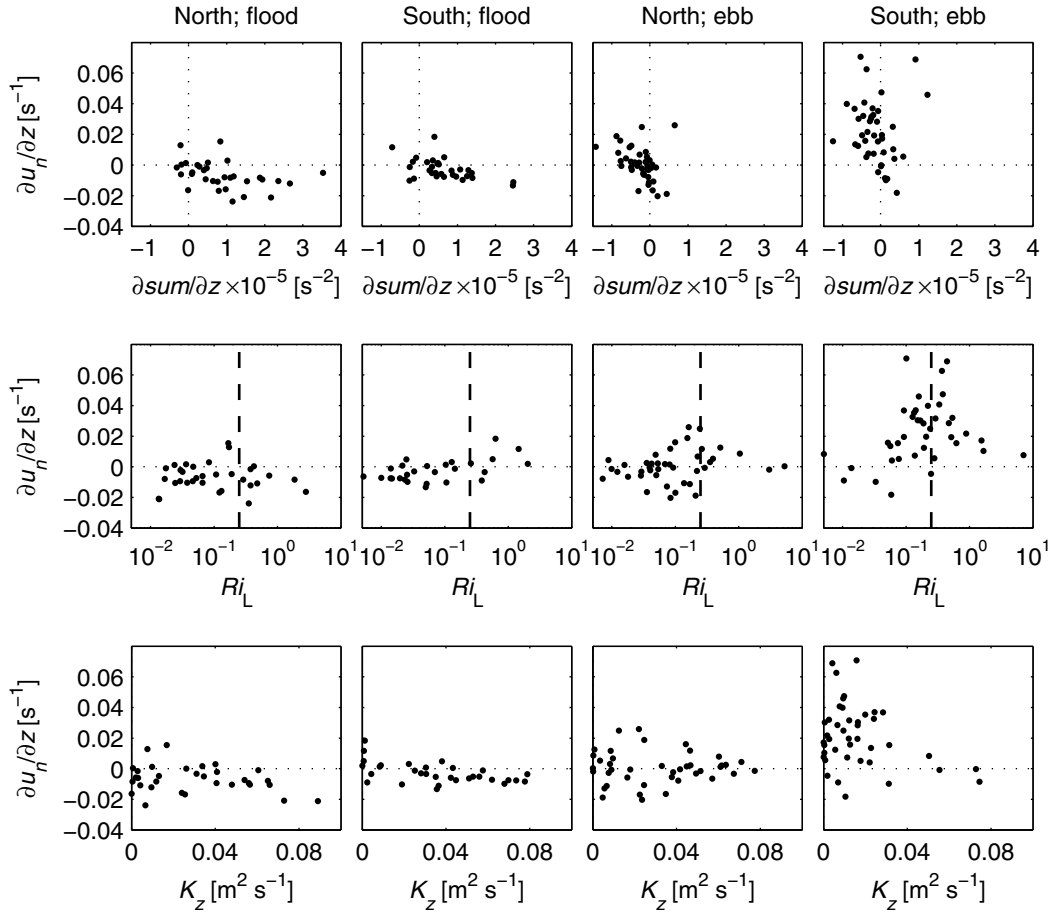
Figure 3.10. Instantaneous values of $\partial sum/\partial z$, Ri_L, and K_s for 13-h surveys n3 and n5-n9 are plotted against $\partial u_n/\partial z$ for flood and ebb at the northerly and southerly stations.

at both stations is largest during flood, $|\partial u_n/\partial z|$ is relatively small (< 0.02 s^{-1}). This can be attributed to strong streamwise currents that cause strong turbulent mixing, which inhibits stratification. At the southerly and northerly stations $Ri_L > 0.25$ for 23% and 28% of the observations, respectively. During ebb at the northerly stations the influence of freshwater discharge is small and mixing large. Hence, $Ri_L > 0.25$ for only 20% of the observations. The strong mixing keeps $|\partial u_n/\partial z| < 0.02$ s^{-1}. At the southerly stations during ebb $|\partial sum/\partial z|$ is smallest, whereas $|\partial u_n/\partial z|$ is largest. As a result of freshwater discharge from the Malzwin channel and weak mixing ($K_z < 0.04$ m^2 s^{-1}), $Ri_L > 0.25$ for 33% of the observations. In these stratified conditions, a small forcing can accelerate the secondary currents to large values.

3.6   Discussion

In this section the mechanisms that govern the secondary circulation at the ferry transect are discussed. It is assumed that the influence of density gradients, measured at the Navicula transects, is similar at the ferry transect. The dominant forcing terms and
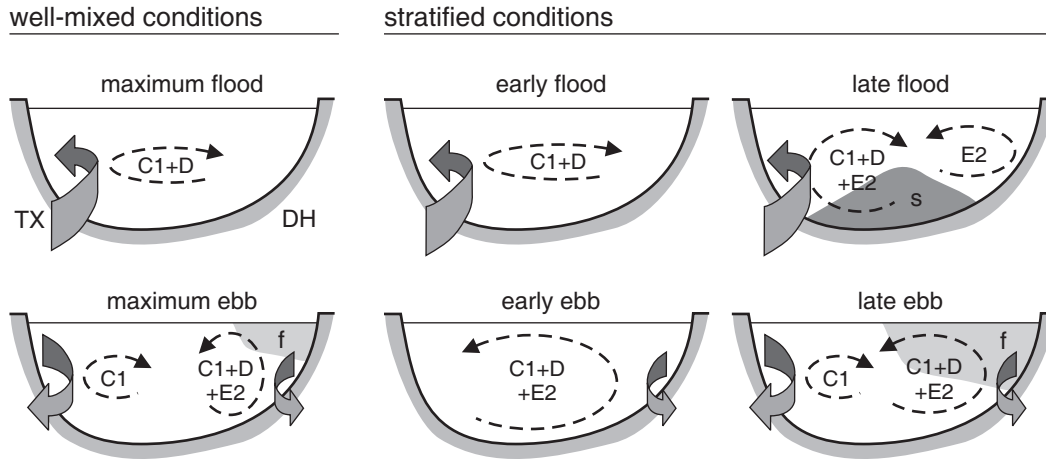
Figure 3.11.   Conceptual model of the secondary circulation and the governing terms of the transverse momentum equation at the location of the ferry transect. Figure shows secondary circulation at maximum flood and ebb during well-mixed conditions and at early and late flood and ebb during stratified conditions. The dashed (shaded) arrows indicate the secondary circulation (curvature of the channel). The governing terms C1, D, and E2 from Eq. (3.1) are the curvature, Coriolis, and the baroclinic pressure gradient terms. The influx of saline (fresh) water during flood (ebb) is indicated with s (f). The Den Helder (Texel) side of the inlet is indicated with DH (TX). The view is in the flood direction.

the sense of rotation during flood and ebb and well-mixed and stratified conditions is illustrated in the conceptual model in Fig. 3.11.

3.6.1   Well-mixed conditions

The secondary circulation during well-mixed conditions (low $\Delta\rho_{\mathrm{t}}$) is best illustrated with the ferry measurements in Fig. 3.2 and Fig. 3.3. It is assumed that the centrifugal and Coriolis accelerations balance with friction at maximum streamwise velocities. The measured secondary currents were compared with the predicted secondary currents according to Eq. (3.4). u_n was calculated for values of R_s equal to -7 km and -15 km at bins South and North during flood and -45 km and -7 km at bins South and North during ebb (Fig. 3.8). The shear in the secondary currents $\partial u_{n,\mathrm{KB}}/\partial z$ that follows from these predictions is plotted as a function of $\bar{u}_s$ in Fig. 3.3.

At maximum flood, the clockwise secondary circulation in the Marsdiep inlet agrees with the forcing due to negative centrifugal and Coriolis accelerations. The predicted secondary currents due to curvature are about twice as large as those due to Coriolis forcing, indicating that negative curvature is the dominant forcing mechanism. Fig. 3.8 shows that upstream from the ferry transect and over the width of the inlet the curvature is also negative, indicating that the secondary circulation is nearly fully developed at the ferry transect. However, the magnitude of the computed transverse shear is smaller than the measurements (Fig. 3.3). The sums of predicted surface secondary currents due to Coriolis and centrifugal accelerations for $\bar{u}_s = 1.2$ m s^{-1} are about 0.02 m s^{-1} and 0.03 m s^{-1} at bins South and North, whereas measured currents amount to 0.09 m s^{-1} and

0.08 m s^{-1} at bins South and North, respectively. Measured secondary currents that are larger than predicted secondary currents due to curvature were also observed by e.g. Geyer (1993), Dronkers (1996), and Lacy and Monismith (2001). They attributed the differences to enhanced streamwise shear and vertical and transverse density gradients. In the Marsdiep inlet, it may be that a small stratification or stronger streamwise shear enhances u_n. Similar to observations by Chant (2002), measured $\partial u_n/\partial z$ increases in magnitude with increasing $\bar{u}_s$ and $\partial u_s/\partial z$ (Fig. 3.3). This linear relation can be attributed to curvature, as is illustrated by the linear dependency of $u_{nr,\max}$ on $\bar{u}_s$ in Eq. (3.4a). In agreement with the ferry observations, centrifugal and Coriolis accelerations govern the clockwise secondary circulation during maximum flood at the Navicula transect (Fig. 3.9). It is shown in Fig. 3.9 that at maximum flood near 0.25 d the secondary currents peak simultaneously with the centrifugal and Coriolis accelerations. This immediate response to the forcing is typical of well-mixed conditions ($Ri_\mathrm{L} \ll 0.25$), where forcing is balanced by friction (Lacy and Monismith, 2001).

While it is clear that centrifugal and Coriolis accelerations govern the secondary circulation at maximum flood at the ferry transect, there is more room for speculation about the mechanisms that govern the circulation at maximum ebb. In well-mixed conditions, the theory by KB indicates that curvature dominates over Coriolis forcing when $|R_s| < 20$ km and that the relaxation length scales are $\sim$400 m. This suggests that in the Marsdiep inlet with its complicated bathymetry secondary currents are mainly governed by curvature and that in well-mixed conditions the secondary circulation becomes fully developed over short distances. At maximum ebb, two weak counter-rotating circulation cells with surface convergence are present in the Marsdiep inlet (Fig. 3.2). The clockwise rotation of the northern cell agrees with the negative curvature present at this location (Fig. 3.8). However, in bin North in Fig. 3.3 the sign of $\partial u_{n,\mathrm{KB}}/\partial z$ only agrees with the measured shear for large negative $\bar{u}_s$. It is shown in Fig. 3.2 that bin North is just on the southern edge of the clockwise circulation cell. It may be that during strong streamwise currents, the secondary currents are larger, as well as the transverse advection of secondary currents, extending the circulation cell farther southward. To the south of $y = 556$ km in Fig. 3.2, the secondary circulation is weak and predominantly counterclockwise. Between $y = 554.5$ km and $y = 556$ km (which includes bin South) forcing due to curvature is weak ($R_s > -20$ km) and smaller than Coriolis forcing. To the south of $y = 554.5$ km the counterclockwise secondary circulation is more defined and agrees with positive curvature (local $R_s < 10$ km in Fig. 3.8). The dominance of curvature in the transverse momentum equation near the south and north shore of tidal inlets was also observed in numerical model simulations by Hench et al. (2002). The Navicula surveys indicate that $\Delta\rho_\mathrm{t}$ is generally higher in the southern half of the inlet due the continuous discharge of fresher water from the Malzwin channel. This can result in stratification that dampens turbulence and transverse density gradients that contribute to the counterclockwise circulation.

3.6.2 Stratified conditions

The influence of density gradients on the secondary circulation is illustrated with the ferry observations (Figs. 3.2 and 3.4) and the momentum analysis for survey n8 (Fig. 3.9). In stratified conditions, transverse density gradients and the suppression of turbulence due

to stratification ($Ri_L \gtrsim 0.25$) allow secondary currents to become larger than in well-mixed conditions. In contrast to curvature, which acts locally, transverse density gradients act over several km and Coriolis forcing acts everywhere and continuously. In stratified conditions, the Coriolis and baroclinic forcings can accelerate secondary currents to larger equilibrium values and these secondary currents are not easily reversed by local curvature (e.g. during early ebb in the northern half of the inlet on June 15, 2006).

During early flood in stratified conditions, the secondary circulation resembles the circulation during maximum flood in well-mixed conditions and centrifugal and Coriolis accelerations dominate over transverse density gradients (Fig. 3.9). During late flood, two counter-rotating circulation cells appear with surface convergence (Figs. 3.2 and 3.5). These cells result from the differential advection of denser water at the inlet centre (Nunes and Simpson, 1985). In the Marsdiep inlet, the resulting transverse density gradients enhance (counteract) the centrifugal and Coriolis accelerations in the northern (southern) half of the inlet. The large forcing and the stratification cause surface secondary currents of about 0.3 m s^{-1} in the northern half of the inlet near 0.37 d on June 15, 2006 (Fig. 3.5).

During early and late ebb and stratified conditions, the counterclockwise circulation in the southern half of the inlet is strong and well-correlated with $\Delta\rho_t$ in Fig. 3.4. According to Fig. 3.9, this circulation can be attributed to the contribution of the baroclinic pressure gradient and the Coriolis acceleration. Although their forcing is small, the strong dampening of turbulence during ebb ($Ri_L \gtrsim 0.25$) permits large secondary currents > 0.4 m s^{-1} near the surface on June 15, 2006 (about 30% of the magnitude of the streamwise currents). Moreover, at the southern half of the ferry transect the counterclockwise secondary circulation may also be enhanced by positive curvature (Fig. 3.8).

The ferry measurements in Figs. 3.2 and 3.4 indicate that during early ebb in the northern half of the inlet the secondary circulation is weakly counterclockwise and poorly correlated with $\Delta\rho_t$. From the Navicula survey on June 15, 2006, follows that during early ebb near 0.48 d the water column is strongly stratified. In these stratified conditions local negative curvature at the ferry transect cannot reverse the counterclockwise circulation set up by Coriolis forcing and/or density gradients. Indeed, Fig. 3.9 shows that Coriolis forcing is the dominant forcing mechanism during early ebb. While during early ebb the secondary circulation is counterclockwise along the northern half of the ferry transect, during late ebb it is clockwise (Fig. 3.4). Navicula survey n8 as well as other surveys indicate that this reversal coincides with a well-mixed water column ($Ri_L < 0.25$) and that density gradients are negligible (Figs. 3.5 and 3.9). In these well-mixed conditions the secondary currents are small and local forcing is important. Hence it is concluded that negative curvature causes the clockwise circulation at the northern part of the ferry transect. Compared to maximum ebb and well-mixed conditions (bottom left subplot of Fig. 3.2), the secondary currents are larger during late ebb. The reason is that during stratified conditions $\partial u_s/\partial z$ is more negative than during well-mixed conditions. This is due to the larger longitudinal density gradient ($\partial u_s/\partial z < -0.04$ s^{-1} for $\Delta\rho_t > 4$ psu; observations are not shown). The enhanced $\partial u_s/\partial z$ leads to a larger vertical shear in the centrifugal acceleration term and a larger secondary circulation.

3.6.3   Spatial asymmetry in turbulent mixing

It is shown in Fig. 3.10 that the southern half of the Marsdiep inlet during ebb has the highest Ri_{L} values, close to the threshold of stable stratification, and the lowest eddy viscosities. Moreover, the stratification can persist during the entire ebb phase (Fig. 3.9). The stratification is due to the influx of more buoyant water from the Malzwin channel and also due to lower turbulent mixing. During ebb, the streamwise velocities are smallest in the southern half of the inlet, whereas they are largest in the northern half of the inlet. This tidal asymmetry in streamwise velocities is visible in Fig. 3.5. It causes a horizontal residual circulation cell with flood-dominant residual currents in the southern half and ebb-dominant residual currents in the northern half of the inlet (Chapter 2). In addition to a residual circulation cell, the asymmetry in streamwise currents also governs an asymmetry in turbulent mixing. The lower currents result in lower mixing in the southern half of the inlet and vice versa in the northern half of the inlet. The weaker mixing during ebb in the southern half of the inlet allows for stable stratification, further dampening turbulent mixing and enhancing secondary currents.

The spatial asymmetry in mixing also affects the northward progression of the density front. Figs. 3.5 and 3.9 (left column) indicate that well-mixed water from the Texelstroom channel limits the northward progression of fresher Malzwin water near 0.55 d. At 0.68 d in Fig. 3.5, the streamwise currents and mixing have decreased significantly to allow the northward progression of the front. These observations are similar to observations by Lacy et al. (2003) in northern San Francisco Bay that show that the position of an axial front is controlled by mixing during flood.

3.7   Conclusions

In this chapter, ferry-ADCP data collected between March 2000 and December 2002 and Navicula-ADCP data collected during nine 13-h surveys in the period 2003-2006 have been used to study instantaneous secondary currents in the Marsdiep inlet, the Netherlands. The ferry data were used to determine the spatial and temporal variability in the secondary currents during well-mixed and stratified conditions. ADCP and density data collected during 13-h surveys were applied in the transverse momentum equation to determine the mechanisms that govern the secondary circulation. The sense of secondary circulation and the governing mechanisms are illustrated in Fig. 3.11. The most important findings are summarised below.

- The centrifugal and Coriolis accelerations and the transverse baroclinic pressure gradient are of $\mathcal{O}(10^{-4} \mathrm{~m~s}^{-2})$ and govern the instantaneous secondary circulation in the Marsdiep inlet. The magnitude of the secondary currents is affected by vertical density stratification.

- In well-mixed conditions at maximum flood, the secondary circulation is clockwise along the ferry transect due to centrifugal ($R_s \approx -10$ km) and Coriolis accelerations. The observed secondary currents are a factor 2-3 larger than the predictions based on the theory by Kalkwijk and Booij (1986). At maximum ebb, there are two

weak circulation cells with surface convergence. The circulation is clockwise due to negative curvature in the northern half of the inlet and counterclockwise in the southern half due to positive curvature, transverse density gradients that are set up due to the influx of fresher water from the Malzwin channel, and Coriolis forcing.

- In stratified conditions, dampening of turbulence and density gradients affect the secondary circulation. During late flood, the differential advection of denser water in the inlet centre creates two counter-rotating circulation cells with surface convergence. During ebb, the inflow of fresher water from the Malzwin channel sets up density gradients that govern the counterclockwise secondary circulation in the southern half of the inlet. After maximum ebb in the northern half of the inlet, the water column becomes well-mixed and the secondary circulation becomes clockwise due to local negative curvature.

- The asymmetry in streamwise currents not only causes residual floodward currents in the southern and residual ebbward currents in the northern half of the inlet (Chapter 2), it also causes a spatial asymmetry in turbulent mixing, with weaker mixing in the southern and stronger mixing in the northern half of the inlet. The weaker mixing and the influx of fresher water during ebb in the southern half of the inlet result in a stratified water column. In these conditions surface secondary currents of about 0.4 m s^{-1} have been observed.

- Although the curvature is weak ($R_s = \mathcal{O}(10$ km$)$), it still dominates over Coriolis forcing in well-mixed conditions. In stratified conditions however, secondary currents can be accelerated to larger equilibrium values due to Coriolis accelerations and transverse baroclinic pressure gradients. They act over larger spatial and temporal scales than local curvature, and as a consequence, curvature may not be able to reverse the secondary circulation. Coriolis forcing was important during ebb in the southern half of the inlet and during early ebb in the northern half of the inlet on June 15, 2006.

Chapter 4

Water transport at subtidal frequencies in the Marsdiep inlet

Abstract

A long-term time series of subtidal water transport in the 4 km wide Marsdiep tidal inlet in the western Dutch Wadden Sea has been analysed. Velocity data were obtained between 1999 and the end of 2002 with an acoustic Doppler current profiler that was mounted under the hull of the ferry 'Schulpengat'. Velocities were integrated over the cross-section and low-pass filtered to yield subtidal water transport. A simple analytical model of the connected Marsdiep and Vlie tidal basins was extended to include wind stress, water-level gradients, and density gradients and applied to the time series of subtidal water transport. In accordance with the observations, the model calculates a mean throughflow from the Vlie to the Marsdiep basin. The mean water transport through the Marsdiep inlet consists of an export due to tidal stresses and freshwater discharge and an import due to southwesterly winds. In contrast, the variability in the subtidal water transport is mainly governed by wind stress. In particular, southwesterly winds that blow along the main axis of the Marsdiep basin force a throughflow from the Marsdiep to the Vlie basin, whereas northwesterly winds that blow along the main axis of the Vlie basin force a smaller mean water transport in the opposite direction. The contribution of remote sea-level change to the water transport, or coastal sea-level pumping, has been found to be much smaller than the contribution of local wind stress.[1]

---

[1] This chapter is based on Buijsman and Ridderinkhof (2007b) that is in press and available online.

4.1   Introduction

This chapter discusses the subtidal water transport between the North Sea and the Marsdiep tidal basin in the Netherlands. The Marsdiep basin is connected to the adjacent Vlie tidal basin. These two connected basins can be schematised as a simple tidal channel with two inlets. In tidal basins with only one ocean-basin connection, the subtidal water transport is governed by remote water-level fluctuations of the ocean, i.e. coastal sea-level pumping (e.g. Garvine, 1985; Wong, 2002), by local along-estuary winds that set up water-level differences inside the estuary (e.g. Garvine, 1985; Janzen and Wong, 1998, 2002), and by freshwater river discharge. However, in connected tidal basins, tidal stresses may also play an important role in driving mean water transport as was illustrated by e.g. Van de Kreeke and Dean (1975), Van de Kreeke (1978), and Ridderinkhof (1988b). The tidal stress terms result from averaging the nonlinear terms in the equations of motion and continuity over a tidal cycle. Due to differences in amplitude and phase of the semi-diurnal tidal wave at both inlets, mean water transport is generated. Moreover, subtidal water transport can be generated by water-level and density differences between the inlets (e.g. Van de Kreeke, 1978; Lee and Smith, 2002).

Ridderinkhof (1988b) applied an analytical model to the connected Marsdiep and Vlie tidal basins to study the influence of tidal stresses on the subtidal water transport. However, Ridderinkhof (1988b) ignored the contribution of non-tidal mechanisms to the subtidal water transport. In this study, Ridderinkhof's analytical model was adopted and extended to include the effects of wind stress and subtidal water-level and density gradients. The objective was to quantify the variability in the subtidal depth-integrated water transport in the Marsdiep inlet and to determine the tidal and non-tidal forcing. The model was applied to the water-transport measurements in the Marsdiep inlet that were obtained with a ferry-mounted ADCP between 1999 and the end of 2002. This data set was extensively discussed in Chapter 2.

In the remainder of this chapter, first an overview is given of the study area. Then, the equations of the analytical model are presented. In the Data and methodology section, the ADCP, wind, and water-level data and the methodology are discussed. In the Results section, the relation between observed subtidal wind stress, water levels, and water transport is analysed and the analytical model is tested against the data. Simple correlation and coherence analyses are applied to study the variability. The last section contains a discussion and conclusions.

4.2   Study area

The study area encompasses the connected Marsdiep and Vlie basins in the western Dutch Wadden Sea (Fig. 4.1). The tidal basins consist of deep tidal channels ($\sim$20 m) flanked by shallow sand and mud flats. The Marsdiep inlet (52.985° N and 4.785° W) bifurcates in the two main channels Texelstroom and Malzwin. The branches of the Texelstroom channel are connected with branches of the Vliestroom channel, which is one of the major channels in the Vlie basin. The Marsdiep and Vlie basins drain into the southern North Sea, which is a shallow coastal sea with depths of 25-35 m. Since the beginning of 1998,
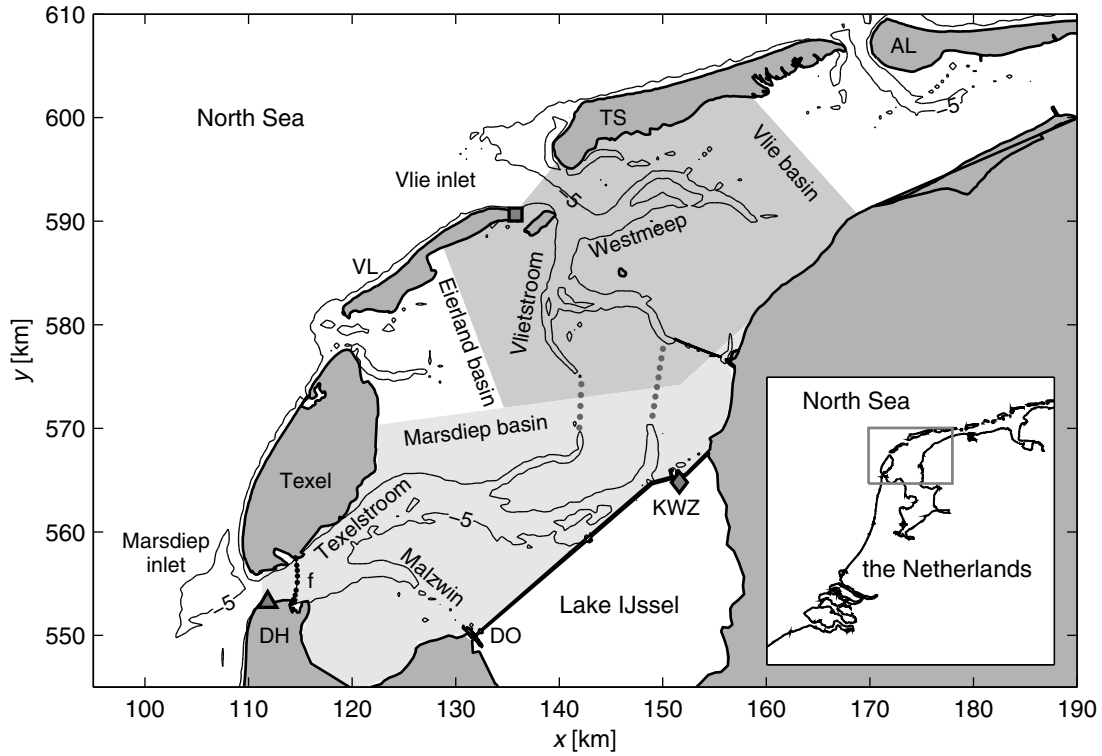
Figure 4.1. The western Wadden Sea in the Netherlands. The Marsdiep and Vlie basins are indicated by light and darker shades of grey, respectively. The town of Den Helder is indicated by DH, the Lake IJssel sluices at Den Oever and Kornwerderzand by DO and KWZ, and the barrier islands of Vlieland, Terschelling, and Ameland by VL, TS, and AL, respectively. The ferry transect in the Marsdiep inlet is indicated by the black dotted line and 'f'. The connections between the Marsdiep and Vlie tidal basins are marked by the grey dotted lines. The contourlines are in [m] relative to mean sea level. The locations of the water-level gauges at Den Helder, Kornwerderzand, and Vlieland are indicated by the grey triangle, diamond, and square, respectively.

ADCP data have been collected with the ferry 'Schulpengat', which crosses the Marsdiep inlet. The inlet is bordered by the island of Texel to the north and the town of Den Helder to the south and is about 4 km wide and maximally 28 m deep at the location where the ferry crosses.

In Chapter 2 it was shown with a harmonic analysis that tides in the Marsdiep inlet constitute up to 81% of the total variance of the water levels measured at Den Helder and 98% of the water transport and current velocities. The semi-diurnal tidal constituent M_2 is the most dominant in the vertical and horizontal tides, significantly modulated by the second largest S_2 constituent. Water levels feature tidal ranges between 1 and 2 m and near-surface streamwise currents range between 1 and 1.8 m s^{-1} (Chapter 2). In accordance with model results by Ridderinkhof (1988a), the measurements presented in Chapter 2 show a net outflow of $\mathcal{O}(10^3 \text{ m}^3 \text{ s}^{-1})$.

Zimmerman (1976a) extensively described the salinity distribution in the western Wadden Sea. He showed that the salinity in the western Wadden Sea is primarily governed

by freshwater discharge from the Lake IJssel sluices at Den Oever and Kornwerderzand (Fig. 4.1), which featured an average discharge of about 400 m^3 s^{-1}, and by freshwater from the river Rhine that is advected northward along the Dutch coast. Zimmerman (1976a) found that the salinity varied around 30 psu at the seaward side of the Marsdiep inlet and around 32.5 psu at the seaward side of the Vlie inlet and attributed this difference to dilution of the Rhine water as it progressed northward along the Dutch coast.

At the inlet, winds primarily blow from southwestern directions, with the strongest winds during fall and winter (Heijboer and Nellestijn, 2002). Zimmerman (1976a) observed by means of salinity distributions that strong winds enhance water transport from basin to basin. During southwesterly winds, water is blown from the Marsdiep basin into the Vlie basin and vice versa during northerly winds.

4.3   Equations

The total subtidal water transport in the Marsdiep inlet Q_0 comprises a throughflow Q_{0t} between the Marsdiep and Vlie inlets, a pumping effect due to remote water-level change in the adjacent North Sea Q_{0r}, and freshwater discharge in the tidal basin Q_{fr}:

$$Q_0 = Q_{0t} + Q_{0r} + Q_{fr}. \tag{4.1}$$

In the following, the contributions to Q_0 are discussed. It is assumed that Q_0 is constant on time scales of a semi-diurnal tidal cycle.

Residual throughflow in tidal channels with open ends was studied by e.g. Van de Kreeke and Dean (1975), Van de Kreeke (1978), and Ridderinkhof (1988b). Van de Kreeke and Dean (1975) set up an analytical model for a straight tidal channel with two inlets to study the influence of tidal stresses on subtidal throughflow. Van de Kreeke (1978) extended the model for subtidal water-level and density gradients. Ridderinkhof (1988b) applied the model of Van de Kreeke and Dean (1975) to the western Dutch Wadden Sea and extended it to include a tidal channel with varying width and depth and to implicitly include the Bernoulli effect. The latter effect represents a drop in subtidal water levels in inlets due to strong tidal currents. Ridderinkhof (1988b) found that the larger water-level amplitude at the Vlie inlet forced a throughflow from the Vlie to the Marsdiep tidal basin.

This paragraph briefly discusses the solution of the mean water transport Q_{0t} for a semi-diurnal tidal cycle. The dimensional solution of the tidal-stress component of Q_{0t} is presented in Appendix 4.A. The connected Marsdiep and Vlie tidal basins are schematised as a simple tidal channel with length L, width B, and depth below still water H. Ridderinkhof (1988b) showed that the effect of varying bathymetry is of minor importance, and therefore a channel with a constant width and depth was used. However, the tidal channel is not straight in plan view, but it has the shape of letter L that is rotated about 130° counterclockwise with the eastward x-coordinate. The southern branch of this channel is roughly parallel to the main axis of the Marsdiep basin, which is rotated 40° counterclockwise with the eastward x-coordinate. The northern branch is roughly parallel to the main axis of the Vlie basin and perpendicular to the main axis of the Marsdiep basin. The along-channel (streamwise) coordinate s is positive in northward direction. The Marsdiep and Vlie inlets are located at $s = -1/2L$ and $s = 1/2L$, respectively. The

z-axis is positive upwards from the still water level. The basic shallow water momentum equation for a tidal channel reads:

$$\frac{\partial Q}{\partial t} + \frac{\partial}{\partial s}\left(\frac{Q^2}{BD}\right) + gBD\frac{\partial \eta}{\partial s} + \frac{1}{2}\frac{gBD^2}{\rho}\frac{\partial \rho}{\partial s} + \frac{kQ|Q|}{BD^2} - \frac{B(\tau_a + \tau_b)}{\rho_r} = 0, \qquad (4.2)$$

where Q is the water transport, t time, $D = H + \eta$ the total depth, η the water elevation relative to the still water level, k the bottom-friction coefficient, g the gravitational acceleration, ρ the cross-sectionally averaged water density, and τ_a and τ_b are wind stresses. The wind stresses along the x and y-axes were rotated to match the main axes of the Marsdiep and Vlie basins, yielding τ_a and τ_b, respectively. Stress τ_a is positive in northeastern direction and τ_b is positive in northwestern direction. In this way, the model can deal with southwesterly winds that push water from the North Sea via the Marsdiep inlet to the Vlie basin and with northwesterly winds that push water from the North Sea via the Vlie inlet to the Marsdiep basin. After linearising the quadratic friction term, substituting series expansions for Q and η, assuming that ρ, τ_a, and τ_b are constant over a semi-diurnal tidal cycle and τ_a and τ_b are constant in space, and averaging over a semi-diurnal tidal cycle, the following is obtained:

$$\frac{\partial}{\partial s}\left(\frac{\langle Q_1^2 \rangle}{BH} + gB\frac{\langle \eta_1^2 \rangle}{2} + gBH\eta_0 + \frac{1}{2}gBH^2\frac{\rho}{\rho_r}\right) + \frac{F_1 Q_0}{H} - \frac{F\langle _1 Q_1 \eta_1 \rangle}{H^2} - \frac{B(\tau_a + \tau_b)}{\rho_r} = 0, \quad (4.3)$$

where $_1$ and $_0$ indicate the time-varying and the tidal-mean part of Q and η, F_1 is the linearised bottom friction coefficient and ρ_r a reference density, and $\langle \rangle$ indicates the mean over a semi-diurnal tidal period. The linearised bottom friction coefficient is defined as:

$$F_1 = \frac{8C_D}{3\pi}\frac{|Q|}{BH}, \qquad (4.4)$$

where C_D is the drag coefficient, $|Q|$ a characteristic tidal water transport amplitude, and $|Q| \gg |Q_0|$. After integrating over the channel length, the expression for the subtidal throughflow reads:

$$Q_{0t} = P_1(a_1^2 - b_1^2) + P_2 a_1 b_1 \sin\delta + \frac{gBH^2}{F_1}\frac{a_0 - b_0}{L} + \frac{gBH^3}{2\rho_r F_1}\frac{\rho_a - \rho_b}{L} + \frac{HB(\tau_a + \tau_b)}{F_1 \rho_r}, \quad (4.5)$$

where P_1 and P_2 are elaborate functions that are evaluated in Appendix 4.A, δ is the phase difference of the tidal water levels at the inlets, and a_1 and b_1, a_0 and b_0, and ρ_a and ρ_b are the tidal water-level amplitudes, the subtidal water levels, and the depth-averaged water densities at the Marsdiep and Vlie inlets, respectively. It is assumed that variables a_1, b_1, a_0, b_0, ρ_a, and ρ_b are constant on the time scale of a semi-diurnal tide and that they vary on longer time scales. The tidal stresses and the Bernoulli effect are incorporated in $P_1(a_1^2 - b_1^2)$ and $P_2 a_1 b_1 \sin\delta$ in Eq. (4.5). The first (second) term represents the water transport due to the difference in amplitude (phase) of the tidal water levels at the inlets. These terms do not include the effect of local wind on water levels in the tidal channel. The last three terms on the RHS of Eq. (4.5) represent the water transport due to subtidal water-level and density gradients over the full length of the channel and the wind stresses. The subtidal water-level gradient term in Eq. (4.5) is only due to wind

set-up on the North Sea and excludes water-level gradients due to the Bernoulli effect and water-level differences in the basin due to local wind. From Eq. (4.5) follows that a subtidal throughflow from the Marsdiep to the Vlie inlet is generated when $a_1 > b_1$, $a_0 > b_0$, $\rho_a > \rho_b$, $\tau_a > 0$, $\tau_b > 0$, and $0 < \delta < \pi$.

In addition to throughflow, subtidal water transport from the North Sea to the Marsdiep basin may also be due to wind set-up in the adjacent North Sea, i.e. pumping. Garvine (1985) showed with a simple analytical model that the subtidal wave lengths of the water levels due to wind set-up in the ocean are much larger than the length scales of most tidal basins. Consequently, the water level in the tidal basin follows the water level at the inlet with a very small phase lag. Therefore, the subtidal water-level changes at the inlet may be a good indicator of the pumping effect. Under these assumptions, the subtidal water transport due to pumping is described by:

$$Q_{0r} = \frac{\partial \eta_0}{\partial t} A_a, \qquad (4.6)$$

where A_a is the horizontal area of the Marsdiep inlet. Moreover, it is assumed that pumping at the Marsdiep and Vlie inlets does not force an exchange of water between the basins. In addition to pumping, local winds may cause water-level differences in the Marsdiep basin. The tilted water levels allow for extra storage of water. It is illustrated later in the text that, compared to pumping, this storage does not result in significant water transport through the Marsdiep inlet.

4.4   Data and methodology

4.4.1   Subtidal water transport

This section discusses terms occurring in Eq. (4.1), or more specifically, Eqs. (4.5) and (4.6). The subtidal water transport was calculated using velocity data obtained between early 1999 and the end of 2002 with a Nortek ADCP mounted under the ferry Schulpengat. An extensive description of the ferry data and data handling was provided in Chapter 2 and here only a brief description is given. During the study period, the ferry crossed the Marsdiep tidal inlet twice per hour, up to 16 h per day, about 320 d per year. The ADCP was mounted at 4.3 m below the water surface and measured at a rate of maximal 0.35 Hz. The eastward u and northward v velocities were gridded in 18 horizontal grid cells and 40 bottom-following grid cells. The eastward velocities were integrated over the cross-section, which is perpendicular to the eastward velocities, to obtain the instantaneous water transport Q. Near the surface and bottom no velocity data were available. The near-surface velocities were assumed to be equal to the mean of the velocities in the first five vertical grid cells with available data. The near-bottom velocities were determined as the mean of zero and the first velocity value above the bottom.

Time series of subtidal water transport Q_0 were obtained with low-pass filtering. However, apart from the occasional ferry crossing due to ambulance transport, there was no regular data collection during night time. Moreover, the ferry went into dock for maintenance at the beginning of each year, yielding data gaps of up to 50 d. A number of steps was taken to make the non-equidistant water transport time series suitable for low-pass
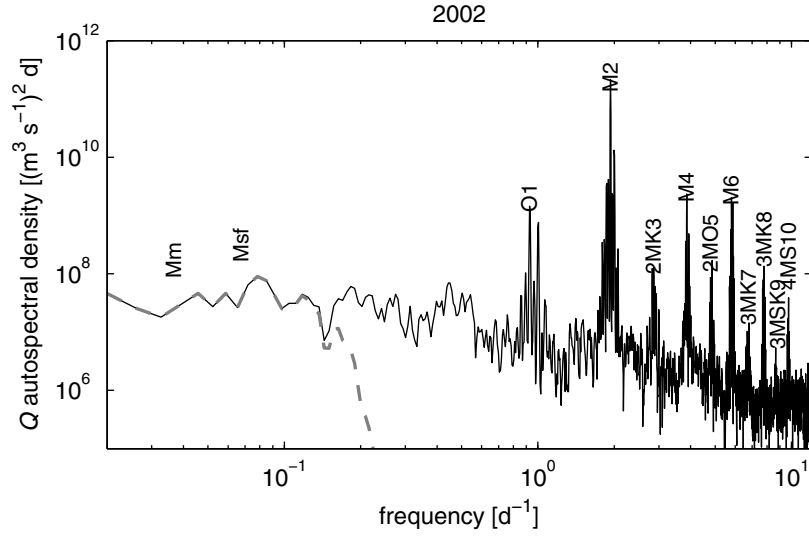
Figure 4.2. Autospectral density function of unfiltered water transport (Q_{gap}; black line) and low-pass filtered water transport (Q_0; thick grey dashed line) measured in 2002.

filtering. In 1998 and early 1999 there were not enough continuous ADCP data or the data contained too much noise. Therefore these data were rejected and the analysis starts on 465 d in 1999 (0 d starts at midnight of January 1, 1998). A least-squares harmonic analysis was applied to every subsequent 13 months of water transport data using 131 tidal frequencies and fits were obtained of $r^2 \approx 98\%$. In this way a continuous harmonic time series was created. The mean difference between the predicted and measured water transports was calculated over a period of minimally one M_2 tidal cycle at both sides of each data gap. If the gap was longer than an M_2 period, the periods at both sides were extended equivalently. Each data gap was filled with the predicted water transports and the average of both mean differences was also added. The new data series with filled-up gaps were interpolated on a time grid with time steps of 30 min, yielding Q_{gap}. In a final step, the subtidal water transport Q_0 was computed by low-pass filtering Q_{gap} with a butterworth filter with a cutoff frequency of 3 d. The autospectral density function of the unfiltered and filtered water transport in 2002 is presented in Fig. 4.2. Frequencies up to the tenth diurnal period can be distinguished. Most of the energy is in the semi-diurnal M_2 frequency and all its even compound and overtides. There is very little energy in frequencies lower than one day. The low-pass filtered water transport is plotted in Fig. 4.3.

As follows from Eq. (4.4), the friction coefficient F_l in Eq. (4.3) is dependent on the tidal water-transport amplitude $|Q|$. This amplitude is affected by spring-neap variability and lower frequencies. To calculate $|Q|$ and capture its variability, the M_2 constituent was least-squares fitted to Q_{gap} for a window with a duration of exactly 5 M_2 cycles (2.6 d). This window was advanced in one-day time steps. In addition to the M_2 amplitude, the phase and tidal-mean water transport were obtained, which were not used here. The use of a window with a duration of 2.6 d was optimal for reducing noise, while still capturing fluctuations on longer time scales. In a final step $|Q|$ was low-pass filtered. It is shown in the second panel of Fig. 4.3 that the amplitude varies between 50×10^3 and 80×10^3 m^3
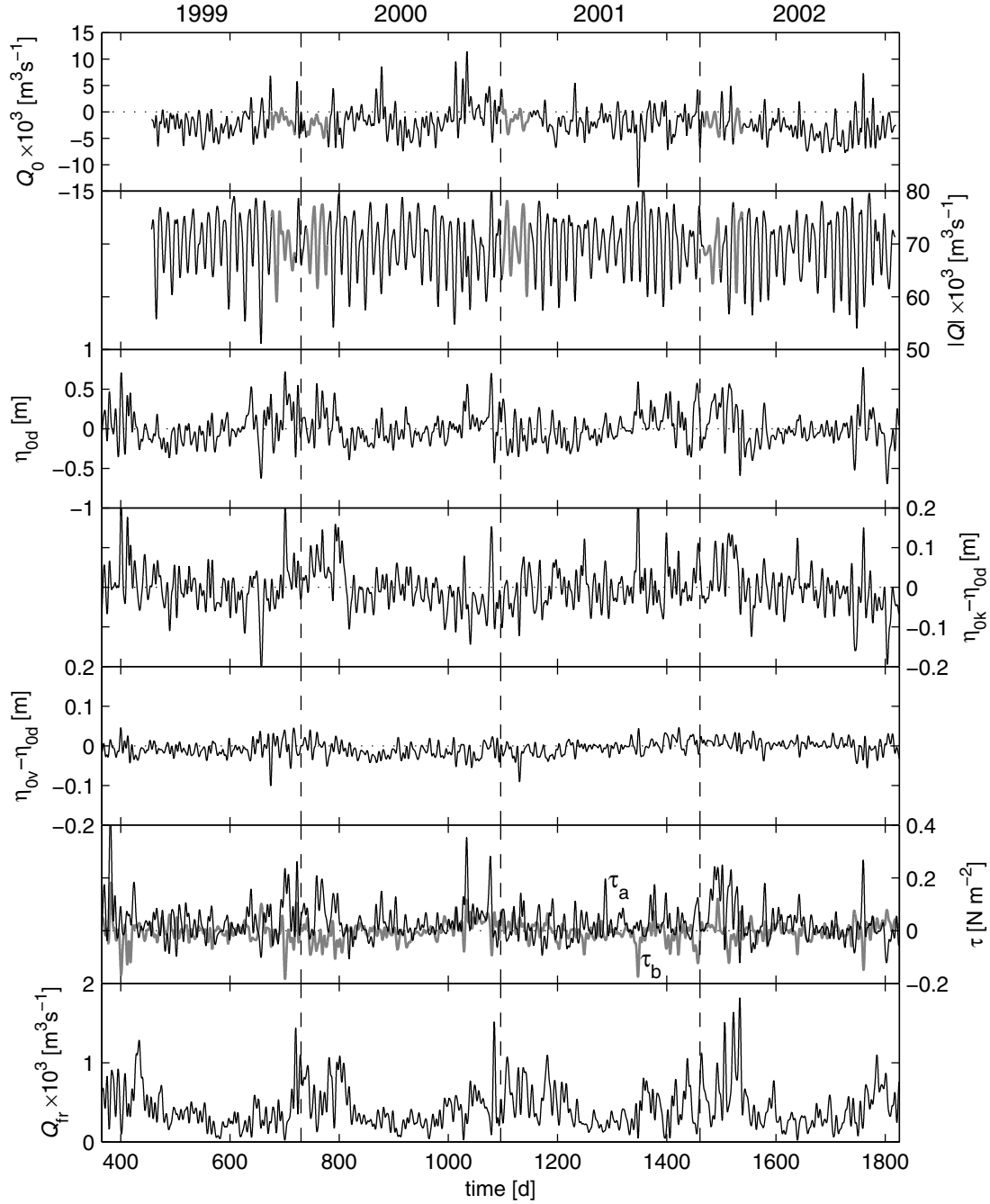
Figure 4.3. Time series of low-passed water transport Q_0 (top panel), low-passed water transport amplitude $|Q|$ (second panel), low-passed water level η_{0d} at Den Helder (third panel), low-passed water-level differences between Kornwerderzand and Den Helder ($\eta_{0k} - \eta_{0d}$; fourth panel) and Vlieland and Den Helder ($\eta_{0v} - \eta_{0d}$; fifth panel), low-passed wind stresses τ_a and τ_b (sixth panel), and low-passed freshwater discharge Q_{fr} from the Lake IJssel sluices (bottom panel). The mean was removed from all water levels. In the two top panels, the thick grey lines indicate data gaps of more than one week that only contain tidal predictions. The vertical dashed lines indicate midnight of each new year. The years are plotted above the top panel.

s^{-1} and that it is significantly modulated by the spring-neap cycle.

4.4.2 Water levels

Water-level data for the period 1998-2002, measured at the tide gauges of Den Helder (η_d), Kornwerderzand (η_k), and Vlieland (η_v) (Fig. 4.1), were obtained from the Dutch Ministry of Transport, Public Works and Water Management. The mean was removed from all water-level time series to exclude influences of surveying offsets and the Bernoulli effect. The M_2 amplitudes a_1 and b_1 and phases of the water levels at Den Helder and Vlieland were obtained by the same method used to calculate $|Q|$. The phase difference between Den Helder and Vlieland yielded δ. Variables a_1, b_1, and δ have mean values of 0.69 m, 0.84 m, and 48°, respectively. A phase difference of 48° implies that the tidal wave is traveling northward along the North Sea coast and that it arrives about 1.7 h later at the Vlie inlet. Values for $(a_1^2 - b_1^2)$ and $a_1 b_1 \sin \delta$ from Eq. (4.5) were calculated and low-pass filtered. Then they were multiplied by functions P_1 and P_2 to yield a value for the water transport. The subtidal water-level change $\partial \eta_{0d} / \partial t$ at Den Helder was calculated for instantaneous water levels, low-pass filtered, and multiplied by the horizontal area of the Marsdiep inlet A_a to obtain water transport due to tidal pumping. The subtidal water-level gradient between Vlieland and Den Helder $(a_0 - b_0)/L$ was calculated by subtracting the instantaneous water levels and low-pass filtering. The subtidal water level at Den Helder η_{0d} ($= a_0$), and the subtidal water-level differences between Kornwerderzand and Den Helder ($\eta_{0k} - \eta_{0d}$) and Vlieland and Den Helder ($\eta_{0v} - \eta_{0d}$) are plotted in Fig. 4.3. The standard deviations of η_{0d}, $\eta_{0k} - \eta_{0d}$, and $\eta_{0v} - \eta_{0d}$ are 0.20 m, 0.05 m, and 0.02 m, respectively. The standard deviations of $\eta_{0k} - \eta_{0d}$ and $\eta_{0v} - \eta_{0d}$ are small compared to the standard deviation of η_{0d}. This is an indication that the subtidal water levels at the inlets and in the basins move coherently, justifying the use of Eq. (4.6).

4.4.3 Wind stress

Hourly wind speeds and directions, measured at the Den Helder airport 'De Kooy', located about 5 km south of the Den Helder ferry harbour, were obtained from the Royal Netherlands Meteorological Institute. The accuracy in the measured wind speed and direction is ± 5 cm s^{-1} and $\pm 5°$, respectively. The probability distribution of the hourly winds in Fig. 4.4 shows that southwesterly winds are the strongest and most prevailing. Following Large and Pond (1981), hourly wind stresses were calculated along the x (eastward) and y (northward) coordinate axes. These stresses were rotated to align with the main axes of the Marsdiep and Vlie basins and low-pass filtered, yielding τ_a and τ_b. The stresses are plotted in Fig. 4.3. The figure shows that positive τ_a (southwesterly wind) is generally larger than negative τ_b (northwesterly wind) and that the peaks in the stresses clearly correlate with peaks in Q_0 and η_{0d}.

Wind speeds and directions measured at weather station s252 were also obtained from the Royal Netherlands Meteorological Institute (results not shown here). This station is located in the North Sea, about 100 km east of Den Helder. The low-passed wind stress vectors at De Kooy have a complex correlation coefficient of 0.94 and a veering of only 5° with low-passed wind stress vectors at station s252. This implies that wind measured
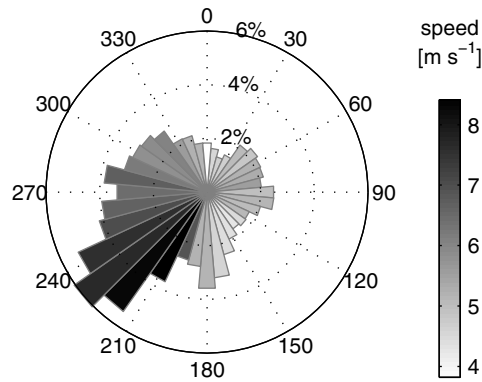
Figure 4.4. Probability of occurrence [%] per wind direction based on hourly wind data for 1998-2002. Bins are in 10° increments and point in the direction the wind is blowing from. Dark (light) shades of grey reflect high (low) mean wind speed per direction.

at the De Kooy is a good representation for both local wind in the Marsdiep basin and remote wind over the North Sea.

4.4.4   Freshwater discharge and density gradients

The largest contribution of freshwater discharge into the Marsdiep basin is from the Lake IJssel sluices at Den Oever and Kornwerderzand. Daily-mean freshwater discharge Q_{fr} data of these sluices were obtained from the Dutch Ministry of Transport, Public Works and Water Management. The mean discharge for the Den Oever and Kornwerderzand sluices for the period 1998-2002 amounts to 350 m^3 s^{-1} and 250 m^3 s^{-1}, respectively. The combined discharge is generally highest in the winter months, reaching maximum daily averages of about 3000 m^3 s^{-1}, while in the summer discharge is generally lower than 500 m^3 s^{-1}. Zimmerman (1976a) used a simple box model to estimate mixing time scales in the western Wadden Sea. The following assumption by Zimmerman was adopted: about one-third of the freshwater discharge from the Kornwerderzand sluices is transported to the North Sea via the Marsdiep inlet and about two-thirds is transported via the Vlie inlet. The total sum of freshwater discharge that leaves via the Marsdiep inlet for the period 1998-2002 was low-pass filtered and is presented in Fig. 4.3.

Unfortunately, no high resolution salinity and temperature data are available at the Vlie inlet and consequently a subtidal density gradient between the Marsdiep and Vlie inlets cannot be calculated. Zimmerman (1976a) showed that the salinity at the Vlie inlet is about 2.5 psu higher than at the Marsdiep inlet. This is equal to a density difference of about 2 kg m^{-3}. It is illustrated in the Results section that this gradient has a small contribution to Q_0.
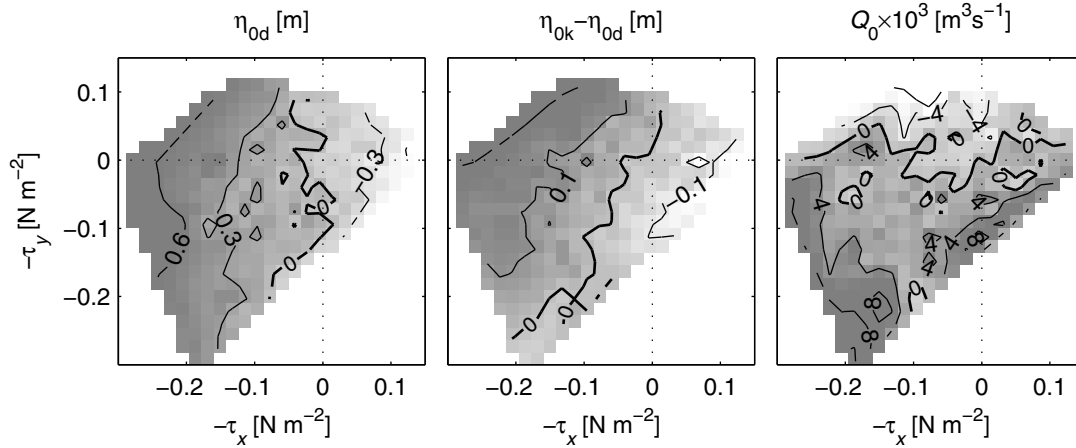
Figure 4.5. The relation between the subtidal wind stress and the subtidal water level at Den Helder (η_{0d}; left panel), the water-level difference between Kornwerderzand and Den Helder ($\eta_{0k} - \eta_{0d}$; middle panel), and the subtidal water transport (Q_0; right panel). The means of the water levels and water transport were removed. Dark (light) shades of grey indicate high (low) values. Note that the wind stress vectors are multiplied by -1 to indicate the direction the wind is blowing from.

4.5 Results

4.5.1 Observations of remote and local wind effects

The influence of wind on the subtidal water levels at Den Helder (η_{0d}), the subtidal water-level differences between Kornwerderzand and Den Helder ($\eta_{0k} - \eta_{0d}$), and the measured subtidal water transport in the Marsdiep inlet (Q_0) are presented in Fig. 4.5. The mean of the water transport was removed for this purpose. The variability of the subtidal water level at Den Helder is governed by water-level fluctuations in the North Sea (i.e. remote effects). The largest set-up (> 0.6 m) at Den Helder occurs when the wind blows from (north)westerly directions, perpendicular to the Dutch coast. Set-down occurs when the wind blows from easterly directions, away from the coast. The strongest winds from the south-southwest only cause a small set-up ($\sim$0.3 m). Southerly (northerly), shore-parallel winds do not cause a set-up (set-down) near the Dutch coast. This contrasts with observations along the coasts of relatively deep oceans, where shore-parallel winds force an Ekman transport to the right of the wind, creating significant set-up or set down (e.g. Wong and Garvine, 1984; Janzen and Wong, 2002; Wong, 2002). The shallow depth of 25-35 m and the relative importance of bottom friction limit Ekman transport to the right of the wind in the southern North Sea.

The water-level differences in the Marsdiep inlet are maximally 0.2 m due to northwesterly winds (middle panel of Fig. 4.5) that push water against the impermeable mainland dike to the southeast. A set-down of maximally 0.1 m occurs with southeasterly winds. The open connection between the Marsdiep and Vlie basins prevents a large set-up in the Marsdiep basin during strong southwesterly winds. Instead, these winds push water from the Marsdiep basin into the Vlie basin, causing an import through the Marsdiep inlet of

Table 4.1. Characteristics of the Marsdiep and Vlie tidal basins (Ridderinkhof, 1988b) and default values for model calculations.

characteristics	Marsdiep	Vlie	combined
L [km]	40	20	60
H [m]	4.5	3.0	3.83
B [m]	15	24	18
A [km^2]	600	480	1080
ρ [kg m^{-3}]	1023	1025	-

$$\sigma = 1.41 \times 10^{-4} \text{ s}^{-1}; \text{ g=9.81 m s}^{-2}; \rho_\text{r} = 1000 \text{ kg m}^{-3}$$

maximally 8×10^3 m^3 s^{-1} (right panel of Fig. 4.5). During north-northwesterly winds the opposite occurs and water leaves through the Marsdiep inlet. From a coherence analysis follows (results not shown here) that the remote and local water levels as well as the sub-tidal water transport are most coherent with wind stress at the same frequencies (periods > 3 d). Fig. 4.5 indicates that water transport occurs mainly when wind blows along the south-north axis, whereas remote and local set-up occurs mainly when wind blows along the east-west axis. This suggests that wind stress is more important for water transport than water-level set-up.

4.5.2 Model-data comparison

Analytical model results

Eqs. (4.5) and (4.6) were applied to determine the driving mechanisms behind the observed water transport from early 1999 to the end of 2002. The time series of Q_0 are continuous and include predictions in all small and large data gaps. Basin characteristics and default values determined by Ridderinkhof (1988b) were used and are listed in Table 4.1. The model was run for four scenarios s1-s4. In scenarios s1, s2, and s3, C_D is equal to 0.0015, 0.0025, and 0.0035, respectively, and the friction depends on $|Q|$ as a function of time. In scenario s4, $|Q|$ has a constant value of 69.7×10^3 m^3 s^{-1} and $C_\text{D} = 0.0025$. In all runs a constant $(\rho_\text{a} - \rho_\text{b}) = -2$ kg m^{-3} was used. The mean values and standard deviations of the modelled water transport that result from the individual driving terms are shown in Table 4.2 for scenario s2 and in Fig. 4.6 for all scenarios. The modelled and observed water transport as a function of time and the water transport due to the tidal and wind stresses for the default scenario s2 are plotted in Fig. 4.7.

Table 4.2. Time-mean values and standard deviations of contributions to Q_0 in [m^3 s^{-1}] for scenario s2. Note that the transports associated with the 'abbreviated' terms $a_1^2 - b_1^2$, $a_1 b_1 \sin \delta$, etc. are calculated using the complete terms in Eqs. (4.5) and (4.6).

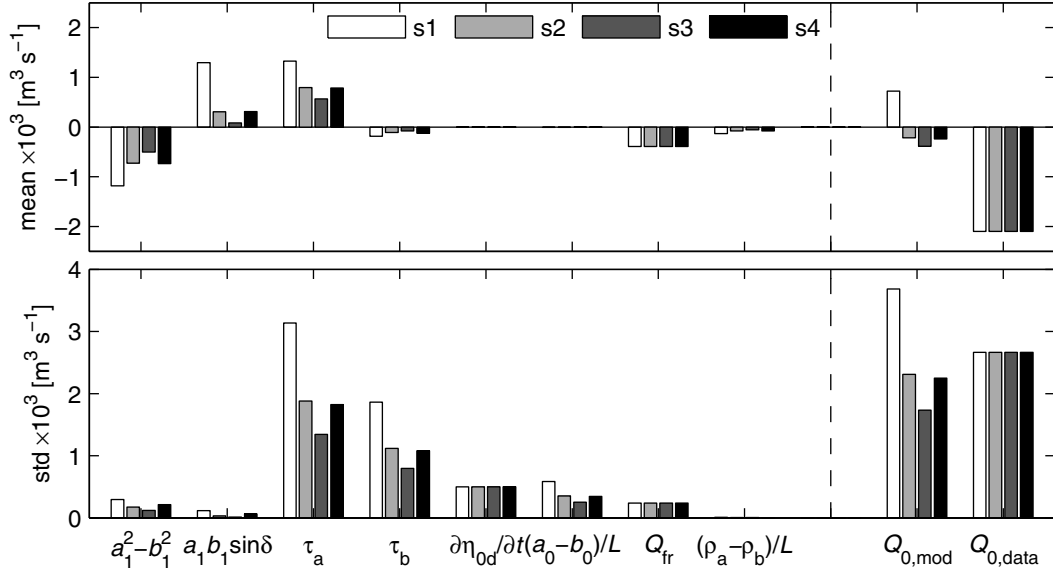|	$a_1^2 - b_1^2$	$a_1 b_1 \sin \delta$	τ_a	τ_b	$\frac{\partial \eta_\text{0d}}{\partial t}$	$\frac{a_0 - b_0}{L}$	Q_fr	$\frac{\rho_\text{a} - \rho_\text{b}}{L}$	$Q_\text{0,mod}$	$Q_\text{0,data}$
mean	-727	304	794	-110	-1	-5	-392	-78	-215	-2098
std	174	32	1881	1117	500	351	237	6	2308	2664

Figure 4.6. Time-mean values and standard deviations (std) of contributions to Q_0 for four scenarios: s1 ($C_D = 0.0015$), s2 ($C_D = 0.0025$), s3 ($C_D = 0.0035$), and s4 ($C_D = 0.0025$ and $|Q|$ is constant).

Fig. 4.6 shows that for all scenarios the predicted water transport $Q_{0,\text{mod}}$ is more positive than the measured water transport $Q_{0,\text{data}}$. The largest negative mean contribution is from the tidal stress term due to $(a_1^2 - b_1^2)$. The contribution due to $a_1 b_1 \sin \delta$ is positive and smaller. Although the tidal water-level amplitude is larger at the Vlie than at the Marsdiep inlet, the amplitude of the tidal water transport at the Marsdiep inlet is larger than at the Vlie inlet for all scenarios. This results in lower tidal-mean water levels in the Marsdiep inlet and a 'Bernoulli transport' from the Vlie to the Marsdiep inlet. The Bernoulli transport is generally small compared to the total transport due to the tidal stresses. For scenario s2, the Bernoulli transport amounts to -91 m^3 s^{-1} (results not shown), which is about 21% of the total transport due to the tidal stresses of -423 m^3 s^{-1}. The predominantly southwesterly winds push water from the North Sea via the Marsdiep inlet into the Vlie basin. This contribution is of the same order as $(a_1^2 - b_1^2)$. Due to the occurrence of northwesterly winds, τ_{b} drives a small mean water transport out of the Marsdiep basin. The third-largest contribution to $Q_{0,\text{mod}}$ is the freshwater discharge Q_{fr}. The negative contribution due to the density gradient is small in comparison to the tidal stresses and wind. The contribution of pumping and $(a_0 - b_0)/L$ to the mean water transport is almost zero. An increase of C_D generally reduces all terms affected by friction. An increase in friction results in a larger reduction of the water transport due to $a_1 b_1 \sin \delta$ than due to $(a_1^2 - b_1^2)$. The latter term is approximately linearly dependent on F_1, whereas the former term is approximately cubicly dependent on F_1 (see Eq. (4.A.3b) in Appendix 4.A). For low values of C_D (e.g. scenario s1), the contribution due to $a_1 b_1 \sin \delta$ leads to a positive $Q_{0,\text{mod}}$. The differences between a subtidal water transport based on a constant amplitude $|Q|$ (scenario s4) and a subtidal water transport based on a varying $|Q|$ (scenario s2) are small.

While the magnitude of time-mean $Q_{0,\text{mod}}$ is smaller than $Q_{0,\text{data}}$, the predicted vari-
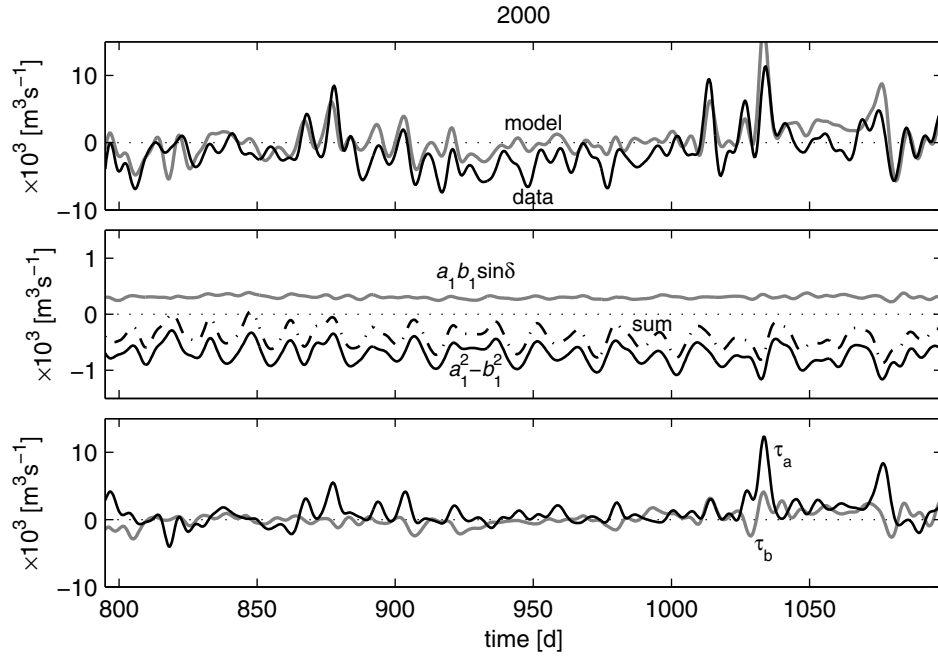
Figure 4.7. Top panel: predicted Q_0 according to scenario s2 and measured Q_0 in 2000. Middle panel: water transport due to tidal stresses $(a_1^2 - b_1^2)$, $a_1 b_1 \sin \delta$, and their sum. Bottom panel: water transport due to wind stresses τ_a and τ_b. Note the difference in the scale of the vertical axes.

ability is of the same order as the measured variability. The largest variability is due to τ_a and τ_b, followed by $\partial \eta_{0d}/\partial t$, $(a_0 - b_0)/L$, and Q_{fr}. Although the tidal stress terms, $(a_1^2 - b_1^2)$ in particular, are important for the mean transport, they have the smallest contribution to the variability in Q_0. The variability due to $(\rho_a - \rho_b)/L$ is only due to the variability in $|Q|$ in scenarios s1-s3. The variability in the Bernoulli transport is mainly due to the spring-neap and monthly tidal cycles and amounts to 23 m^3 s^{-1} in scenario s2 (results not shown). In contrast, the variability in transport due to $(a_0 - b_0)/L$ is mainly governed by remote water levels. This yields a variability of 351 m^3 s^{-1} (Table 4.2), which is significantly larger than the variability due to the Bernoulli term. Similar to the mean transport, an increase in C_D results in a reduction of the predicted variability.

Fig. 4.7 shows that the agreement between the modelled and observed water transport for scenario s2 in the year 2000 in the top panel is reasonably good ($r = 0.70$, $r^2 = 50\%$). In particular, the larger fluctuations are well represented and they coincide with peaks in the water transport due to wind stresses in the bottom panel. In agreement with Table 4.2, the predictions are generally more positive than the data in Fig. 4.7. Moreover, Fig. 4.7 indicates that the variability in transport due to the tidal stresses in the middle panel is mainly due to the spring-neap and monthly tidal cycles and that it is an order of magnitude smaller than the variability due to the wind stresses.

Table 4.3. Correlation coefficients r between terms of Eq. (4.1) and measured Q_0. 'Individual' refers to a correlation between Q_0 and the transport due to the current term and 'cumulative' refers to a correlation between Q_0 and the sum of transport due to the current term and all previous ones.

	τ_a	τ_b	$\frac{\partial \eta_{0d}}{\partial t}$	$\frac{a_0 - b_0}{L}$	Q_{fr}	$a_1^2 - b_1^2$	$a_1 b_1 \sin \delta$
r (individual)	0.50	0.34	0.34	0.34	0.05	0.01	0.24
r (cumulative)	0.50	0.65	0.68	0.69	0.69	0.70	0.70

Correlation and coherence

Individual transport terms τ_a, τ_b, $\partial \eta_{0d}/\partial t$, $(a_0 - b_0)/L$, $(a_1^2 - b_1^2)$, $a_1 b_1 \sin \delta$, and Q_{fr} (independent variables) and combinations thereof were correlated with the measured subtidal water transport (dependent variable) to investigate what determines the variability. This was done for simple cross-correlations for scenario s2 listed in Table 4.3 and for partial and multiple coherence shown in Fig. 4.8. Time series of independent and dependent variables from early 1999 to the end of 2002 were used for the coherence analysis.

Table 4.3 indicates that the correlation of τ_a with Q_0 is highest ($r = 0.50$), followed by τ_b ($r = 0.34$). The inclusion of τ_b significantly increases the correlation to $r = 0.65$, i.e. the wind stresses explain about 43% of the variance in Q_0. The correlation only slightly increases after inclusion of $\partial \eta_{0d}/\partial t$, $(a_0 - b_0)/L$, and $(a_1^2 - b_1^2)$, yielding a maximum cumulative correlation $r = 0.70$. Although the individual correlations of $\partial \eta_{0d}/\partial t$ and $(a_0 - b_0)/L$ are as large as τ_b, their contributions to the cumulative correlation are much smaller. Placing $\partial \eta_{0d}/\partial t$ and $(a_0 - b_0)/L$ ahead of τ_b in the cumulative correlation analysis still shows a small increase in cumulative correlation for $\partial \eta_{0d}/\partial t$ and $(a_0 - b_0)/L$ and a large increase for τ_b. This confirms that most of the variability in Q_0 is due to τ_a and τ_b.

Partial and multiple coherence (γ^2) techniques as discussed in Bendat and Piersol (1986) were applied to understand how well independent variables correlate with the dependent variable Q_0 per frequency band. These techniques yield a phase ϕ that indicates any lags between the independent and dependent variables per frequency band. The partial coherence technique can be used when the independent variables are coherent with each other because the technique removes any coherence between the independent variables. In the multiple coherence technique the coherence between a set of independent variables and the dependent variable is analysed. For partial and multiple coherence, $0 \leq \gamma^2 \leq 1$ applies.

Fig. 4.8 only presents results for independent variables τ_a, τ_b, and $(a_1^2 - b_1^2)$ because they explain most of the variance. The partial coherence of $a_1 b_1 \sin \delta$, $\partial \eta_{0d}/\partial t$, $(a_0 - b_0)/L$, and Q_{fr} is near or below the 95% confidence level for the entire range of frequencies. In the top panel of Fig. 4.8 it is shown that τ_a is most coherent with Q_0 (γ^2 is maximally 0.47) for cycles with periods smaller than about 10 d. The partial coherence of τ_b with Q_0 is second largest and it runs roughly parallel to τ_a. Stress τ_b has a maximum γ^2 of 0.45 at 0.1 d^{-1}. The partial coherence of $(a_1^2 - b_1^2)$ with Q_0 is only significant at 0.036 d^{-1} and 0.068 d^{-1}. These frequencies represent the monthly (28 d) and spring-neap cycles (15 d), respectively. The partial coherence is maximally 0.42 at 0.068 d^{-1}. Table 4.3 indicates that the individual correlation of $(a_1^2 - b_1^2)$ with Q_0 is rather low ($r = 0.01$). However, the
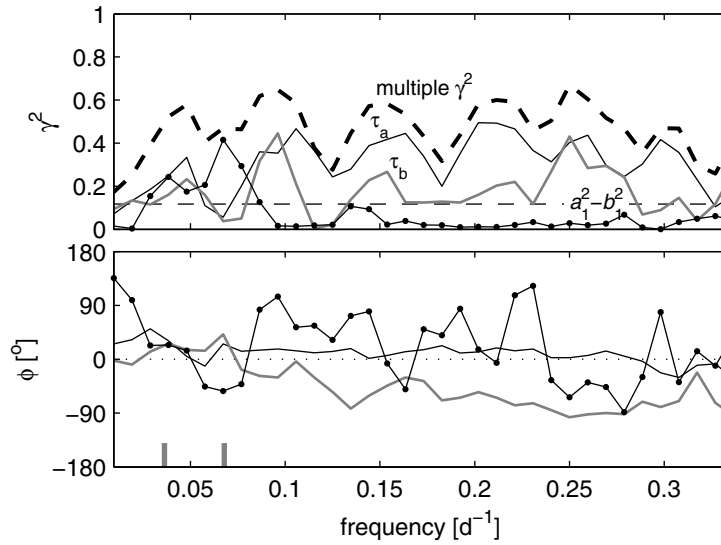
Figure 4.8. Partial and multiple coherence γ^2 (top panel) and phase ϕ (bottom panel) between τ_a, τ_b, and $a_1^2 - b_1^2$ on the one hand and measured Q_0 on the other. The horizontal black dashed line in the top panel indicates the 95% confidence level. The vertical grey sticks in the bottom panel at 0.036 d^{-1} and 0.068 d^{-1} refer to the monthly (28 d) and spring-neap cycles (15 d), respectively. A positive ϕ means that Q_0 leads.

relation between $(a_1^2 - b_1^2)$ and Q_0 is clearly visible in the frequency domain in Fig. 4.8. Low-frequency events with a relatively small amplitude, such as tidal stresses, are masked by high-frequency wind events with a higher amplitude in the correlation analysis. The contribution of these different frequencies is more effectively determined in the coherence analysis. The multiple coherence based on τ_a, τ_b, and $(a_1^2 - b_1^2)$ varies around $\gamma^2 = 0.5$ and reaches $\gamma^2 = 0.67$ near 0.25 d^{-1}.

The bottom panel of Fig. 4.8 shows that the phase difference between τ_a and Q_0 is close to zero for all frequencies. This is understandable because τ_a has an immediate effect on the water transport through the Marsdiep inlet. The phase lag between τ_b and Q_0 is negative (about 1 d), indicating that the subtidal water transport lags behind the wind stress. In this case τ_b is parallel to the axis of the Vlie tidal basin. The water that is pushed into the Marsdiep basin can only flow to the Marsdiep inlet due to a horizontal pressure gradient. This is confirmed in Fig. 4.5, which indicates that water levels near Kornwerderzand are higher than at Den Helder during northwesterly winds. The phase lag between $(a_1^2 - b_1^2)$ and Q_0 at 0.068 d^{-1} is $-53°$ ($\sim$2 d). The cause of this lag is not yet clear.

Storm events

Fig. 4.9 illustrates the response of the Marsdiep-Vlie basin system during a series of southwesterly storms from May 10 to June 9, 2000 (860-920 d) and a large northwesterly storm near September 10, 2001 (1348 d). The settings of scenario s2 were used for the model predictions. The southwesterly storm events are reasonably well predicted by the model. During these storms, the winds are predominantly aligned with the main axis of the Mars-
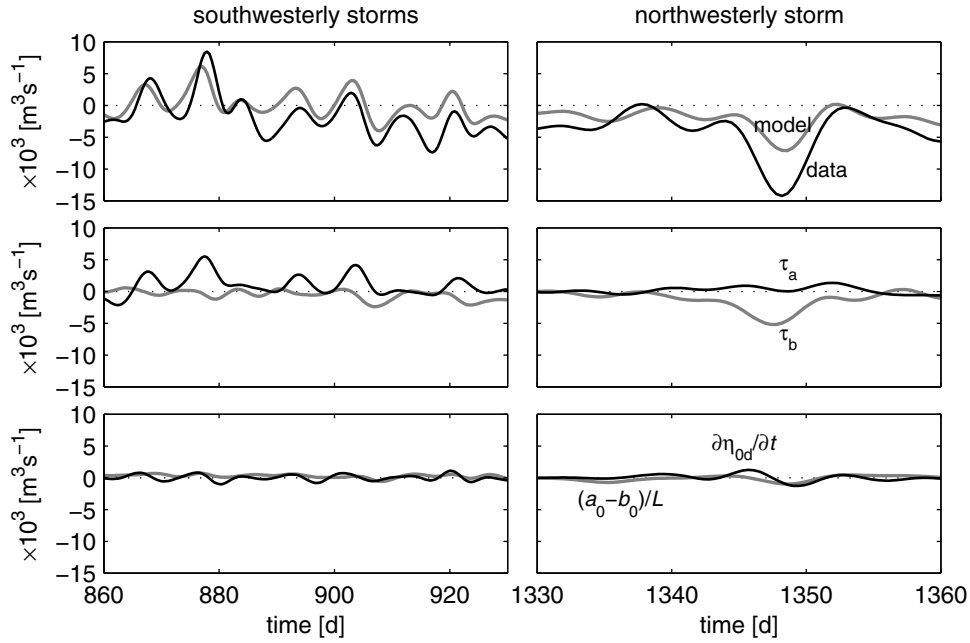
Figure 4.9. Series of southwesterly storms from May 10 to June 9, 2000 (860-920 d) in left panels and a large northwesterly storm near September 10, 2001 (1348 d) in right panels. Top panels show the model predictions for scenario s2 and data. Middle panels show water transport due to wind stresses τ_a and τ_b, and bottom panels show water transport due to pumping ($\partial\eta_{0d}/\partial t$; black line) and subtidal water-level gradients ($(a_0 - b_0)/L$; grey line).

diep basin and push water from the North Sea into the Marsdiep basin (middle panel of Fig. 4.9). Although there is water-level set-up during the storm and set-down after it, the resulting water transport due to pumping in the bottom panel has a negligible contribution to the total water transport. The contribution of subtidal water-level gradients is even smaller than pumping. Therefore, it can only be concluded that wind stress forces water from the North Sea via the Marsdiep basin into the adjacent Vlie basin during southwesterly storms.

During the northwesterly storm of September 10, 2001 winds blew predominantly along the main axis of the Vlie basin. There was a significant export of water from the Marsdiep tidal basin and after the storm this was not balanced by an import. Therefore, the increased export could only be due to a throughflow from the adjacent Vlie basin. Apparently, water is pushed from the North Sea into the Vlie tidal basin and this water leaves via the Marsdiep inlet. Similar to southwesterly storms, the transport due to pumping and subtidal water-level gradients is secondary to transport due to wind stress.

4.6   Discussion and conclusions

This chapter presents analyses of time series of low-pass filtered water transport Q_0 in the Marsdiep inlet in the western Dutch Wadden Sea. The data were obtained with a ferry-mounted ADCP between 1999 and the end of 2002. The analytical model of

Ridderinkhof (1988b) was extended to include wind stress, subtidal water-level gradients, and density gradients. The predicted subtidal water transport was compared with the observed subtidal water transport.

Although the predicted and observed time-mean water transport are directed out of the Marsdiep inlet, the magnitude of the observed time-mean water transport (-2098 m^3 s^{-1}) is larger than the magnitude of the predicted water transport (-215 m^3 s^{-1}). These differences may be attributed to the simplistic representation of physical processes and bathymetry in the analytical model. In scenario s2, the export due to tidal stresses (-423 m^3 s^{-1}), τ_b (-110 m^3 s^{-1}), Q_{fr} (-392 m^3 s^{-1}), and density gradients (-78 m^3 s^{-1}) amounts to -1003 m^3 s^{-1}. This volume is greatly reduced by an import due to τ_a of 794 m^3 s^{-1}. This indicates that the subtidal water transport is mainly governed by southwesterly winds, tidal stresses, and freshwater discharge. The predominant southwesterly winds push a large water volume from the Marsdiep to the Vlie basin, whereas northwesterly winds push a smaller volume in the opposite direction. The tidal stresses force a constant water transport from the Vlie to the Marsdiep basin because the tidal water-level amplitude at the Vlie inlet is larger than at the Marsdiep inlet. The magnitude and direction of tidal-mean transport due to the tidal stresses agrees with results by Ridderinkhof (1988b).

The variability in the subtidal water transport is predominantly governed by the wind stresses. Both τ_a and τ_b explain about 43% of the variance in the subtidal water transport. The contributions due to wind stresses, tidal stresses, pumping, and subtidal water-level gradients combined explain maximally 50% of the variability. The partial coherence analysis shows that both τ_a and τ_b are most coherent with Q_0 for cycles with periods smaller than 10 d. These periods are of the same duration as the time it takes for weather systems to move over the western Wadden Sea. The partial coherence of pumping, subtidal water-level gradients, and tidal stress $a_1 b_1 \sin \delta$ are below the 95% confidence level. Although the stress term $(a_1^2 - b_1^2)$ portrays a clear spring-neap variability (Fig. 4.7), the variability is not visible in the observed water transport and the correlation of $(a_1^2 - b_1^2)$ with Q_0 is small. Apparently, the contribution of $(a_1^2 - b_1^2)$ to the variability is masked by higher-frequency wind events with a larger amplitude. It is only illustrated with the partial coherence analysis that $(a_1^2 - b_1^2)$ and Q_0 are most coherent at the frequencies of the spring-neap and monthly cycles.

The contribution of pumping and water-level gradients to the variability in the subtidal water transport is minimal. This is illustrated in Figs. 4.6 and 4.9, which show that the variability due to wind stress is up to a factor four larger. Observations presented in Fig. 4.5 also indicate that remote and local water-level fluctuations are less important than wind stresses in driving subtidal water transport: the largest variability in remote and local water levels occurs when the wind blows along the west-east axis, whereas the largest variability in subtidal water transport occurs when the wind blows along the south-north axis. Wind set-up in the Marsdiep basin due to local wind is not represented in the analytical model. Fig. 4.5 indicates that it is justified to ignore water transport due to local water-level set-up: the local set-up is maximally one-third of the remote set-up for the same wind stress.

The observations contrast with observations by Wong and Garvine (1984) and Wong (2002) and analytical model results by Garvine (1985). In Garvine's model, remote along-shore winds drive an Ekman transport that produces sea-level fluctuations at the mouth

of the estuary and local along-estuary winds set up a surface slope inside the estuary. Garvine (1985) showed via a simple scaling analysis that these fluctuations of the remote sea level can drive a water transport that is larger than the water transport due to local wind. As was recognised by Janzen and Wong (2002), local wind may only be important in these estuary-shelf systems if the wind blows perpendicular to the coast and along the estuary axis. While pumping and water transport due to local wind set-up may be important in tidal basins with one connection to the open sea, two additional mechanisms, namely throughflow due to local wind stresses and throughflow due to tidal stresses, come into play in connected tidal basins, such as the Marsdiep-Vlie system. Moreover, Garvine's model may not be applicable to the North Sea because the shallowness of the North Sea limits Ekman transport due to alongshore winds. The importance of wind for throughflow was previously observed in the Marsdiep inlet by Zimmerman (1976a) and in model studies of connected basins in the German Wadden Sea by Stanev et al. (2003).

Appendix 4.A   Analytical model solutions

Following Van de Kreeke and Dean (1975) and Ridderinkhof (1988b), the dimensional solution for tidal-mean water transport in a tidal channel for M_2 water-level boundary conditions, excluding density gradients, subtidal water-level gradients, and wind stress, is:

$$Q_{0t} = -\frac{BH}{F_1 L}\left(\frac{\alpha}{HB^2}(|Q|^2_{L/2} - |Q|^2_{-L/2}) + \frac{g}{2}(|\eta|^2_{L/2} - |\eta|^2_{-L/2})\right),\qquad(4.A.1)$$

with:

$$|Q|^2_{L/2} - |Q|^2_{-L/2} = -(a_1^2 - b_1^2)\sigma^2(GG^* - PP^*) + a_1 b_1 \sin(\delta)2\sigma^2 i(GP^* - PG^*),\quad(4.A.2a)$$

$$|\eta|^2_{L/2} - |\eta|^2_{-L/2} = -(a_1^2 - b_1^2),\qquad(4.A.2b)$$

$$P = \frac{2B}{\tau(e^{i\tau L} - e^{-i\tau L})},\qquad(4.A.2c)$$

$$G = B\frac{e^{i\tau L} + e^{-i\tau L}}{\tau(e^{i\tau L} - e^{-i\tau L})},\qquad(4.A.2d)$$

$$\tau^2 = \frac{1}{gH}\left(\sigma^2 - \frac{F_1}{H}i\sigma\right),\qquad(4.A.2e)$$

where σ is the M_2 tidal frequency, $|Q|$ and $|\eta|$ are the tidal water-transport and water-level amplitudes at $s = -L/2$ and $s = L/2$, * indicates the complex conjugate, and $\alpha = 3/4$ when the Bernoulli effect is not accounted for and $\alpha = 1/2$ when it is accounted for. Functions P_1 and P_2 in Eq. (4.5) can be written as:

$$P_1 = \frac{BH}{F_1 L}\left(\frac{\alpha}{HB^2}\sigma^2(GG^* - PP^*) + \frac{g}{2}\right),\qquad(4.A.3a)$$

$$P_2 = \frac{BH}{F_1 L}\left(\frac{\alpha}{HB^2}2\sigma^2 i(PG^* - GP^*)\right).\qquad(4.A.3b)$$

Chapter 5

Long-term evolution of sand waves in the Marsdiep inlet
I: High-resolution observations

Abstract

A seven-year long data set, from 1998 to 2005, of sand waves in the Marsdiep tidal inlet in the Netherlands is presented. The sand waves are visible on digital terrain models (DTMs) that were compiled from water depths obtained with a ferry-mounted acoustic Doppler current profiler. This multi-year data set allows for the study of the spatial and temporal evolution of sand-wave migration, height, length, asymmetry, and orientation. Horizontal migration rates were successfully obtained with a simple cross-correlation technique similar to techniques used in particle tracking. The study area can be roughly divided in two sections. In the southern half, the sand waves are of the progressive type with area-mean wave heights of 3 m and lengths of 200 m. In the northern half of the inlet, the sand waves are asymmetric-trochoidal with area-mean wave heights between 1.5 and 3 m and lengths between 140 and 200 m. Across the inlet, the sand waves migrate in the flood direction with rates between 0 and 90 m y^{-1}. Only the progressive waves in the southern half migrate in directions perpendicular to their crests. A striking observation is the seasonal variability in sand-wave heights and migration of the sand waves in the northern half of the inlet. The sand-wave heights are about 0.5 m higher in fall than in spring and the migration rates are about 30 m y^{-1} higher in winter than in summer. In this chapter, the observations are presented and in Chapter 6 the ADCP-current data will be applied to explain the spatial and seasonal variability of the sand waves.[1]

---

[1] This chapter is based on a manuscript submitted to Cont. Shelf Res.

5.1   Introduction

In this chapter two techniques are presented that have not been applied often: 1) a technique to ensemble bathymetric maps using water depths recorded with a ferry-mounted ADCP, and 2) a spatial cross-correlation technique to track the migration of sand waves that are visible on the bathymetric maps.

These two techniques were applied to gain insight in the evolution of sand waves in the inlet. Sand waves are prominent bedforms on sandy seabeds of coastal shelf seas and estuaries with heights of $\mathcal{O}(1$ m$)$ and wave lengths of $\mathcal{O}(100$ m$)$. In contrast to similarly shaped desert and river dunes, sand waves on sandy seabeds are formed due to oscillatory (tidal) currents (e.g. Hulscher, 1996; Gerkema, 2000). In his seminal work, Van Veen (1935) classified sand waves as trochoidal (symmetrical) or progressive (asymmetrical). It has been observed by many researchers that sand waves migrate in the direction faced by the steeper (lee) slope and that their migration direction coincides with the direction of the strongest current (e.g. Van Veen, 1935; Terwindt, 1971; McCave, 1971; Allen, 1984; Bartholdy et al., 2002; Ernstsen et al., 2005). Their migration direction and shape are used to infer sediment transport pathways (e.g. Van den Berg, 1987; Lobo et al., 2000). Their presence affects navigation and pipeline construction (e.g. Bartholdy et al., 2002; Morelissen et al., 2003).

In observational studies, depth measurements of sand waves have generally been acquired with (multibeam) echo sounders. The recent application of multibeam echo sounders has resulted in high-resolution and high-quality bathymetric maps (e.g. Ernstsen et al., 2005; Van Dijk and Kleinhans, 2005; Duffy and Hughes-Clarke, 2005). Although the main purpose of an ADCP is to measure currents and acoustic backscatter, it can also be used to measure water depths. Subsequently, these can be assembled into accurate bathymetric maps. The application of an ADCP to obtain water depths was first demonstrated by Donato et al. (1997) and Trump and Marmorino (1998). They used horizontal and vertical positions of the intercepts between the bottom and each of the four ADCP beams to characterise the size, shape, and orientation of bedforms. They obtained this data along a single track line and did not assemble bathymetric maps. Dinehart and Burau (2005) compiled bathymetric maps of about 150×250 m^2 with a grid size of 1 m^2 using ADCP-depth data collected along multiple parallel track lines. Their maps revealed bedforms with heights < 1 m.

So far, the bathymetry that has been obtained with an ADCP has been small in horizontal area, measured infrequently, and/or measured only a few times. The use of an ADCP to make bathymetric maps may only be beneficial if the measurements are conducted over a larger area, continuously, and for longer periods of time. In this chapter, it is demonstrated how depth measurements obtained with a ferry-mounted ADCP between 1998 and 2005 were used to compile a series of bathymetric maps. The ADCP is mounted under the ferry 'Schulpengat', which traverses the 4 km wide Marsdiep inlet. In addition to water depths, the ADCP has recorded current velocities and acoustic backscatter since 1998. The bathymetric maps cover a horizontal area of about 1000×3500 m^2 and reveal sand waves with different orientations and shapes, heights of 1-7 m, lengths of 125-250 m, and migration speeds of 0-90 m y^{-1}.

A simple but very efficient spatial cross-correlation technique was used to quantify

the sand-wave migration. This technique was originally developed for particle tracking in fluids to determine velocities (e.g. Maas et al., 1993; Kieft et al., 2002) and it was first applied by Duffy and Hughes-Clarke (2005) to determine velocity vectors of migrating bedforms on a tidal sand bank. While Duffy and Hughes-Clarke (2005) applied it to six repeat multibeam surveys with a one-month interval, the seven-year duration of the ferry measurements allows for the successful application of the correlation technique to 27 time steps of about three months.

These relatively new techniques were used to quantify the spatial and temporal variability in height, length, asymmetry, orientation, and migration of the sand waves in the Marsdiep inlet. The observations presented in this chapter raise questions about the processes that govern the spatial and temporal variability. These questions will be addressed in Chapter 6 using the water-velocity data that were also measured with the ferry-mounted ADCP.

In the next section, the study area is briefly described. The Data handling and techniques section extensively discusses the horizontal and vertical corrections and uncertainty in the depth measurements. The creation of bathymetric maps, or digital terrain models, is demonstrated and the working of the spatial cross-correlation technique is explained. The spatial and temporal variability in sand-wave characteristics is presented in the Results section. Interesting findings are the significant seasonal variability in both height and migration speed of the sand waves in the northern half of the inlet. This chapter ends with a discussion and conclusions.

5.2   Study area

In cooperation with the ferry company 'Texels Eigen Stoomboot Onderneming' (TESO), the Royal Netherlands Institute for Sea Research (NIOZ) has conducted measurements with an ADCP mounted under the ferry Schulpengat in the Marsdiep tidal inlet since 1998. The ferry crosses the inlet between the ferry harbours of Den Helder and Texel. The Marsdiep inlet at 52.985° N and 4.785° W is the southwesternmost inlet of the Wadden Sea in the Netherlands (Fig. 5.1). To the north the inlet is bordered by the sand plains of barrier island Texel and to the south by the sea dike of mainland city Den Helder. The Marsdiep inlet drains the 600 km^2 large Marsdiep tidal basin. The inlet is about 4 km wide and maximally 27 m deep at the location where the ferry crosses. At the basin side of the study area the inlet channel bifurcates in the northern main channel Texelstroom and the southern secondary channel Malzwin. Sha (1990) performed grain size analyses of surface grab samples and box cores collected around the Marsdiep ebb tidal delta and inlet. He found well-sorted sediment with grain sizes larger than 0.3 mm in the inlet. As shown in Chapter 2, tidal currents are dominated by the semi-diurnal tidal components, with surface velocities up to 2 m s^{-1}. In the southern half of the inlet flood currents are stronger than ebb currents, while in the northern half ebb currents are stronger. The inlet is considered well-mixed through most of the tidal cycle.
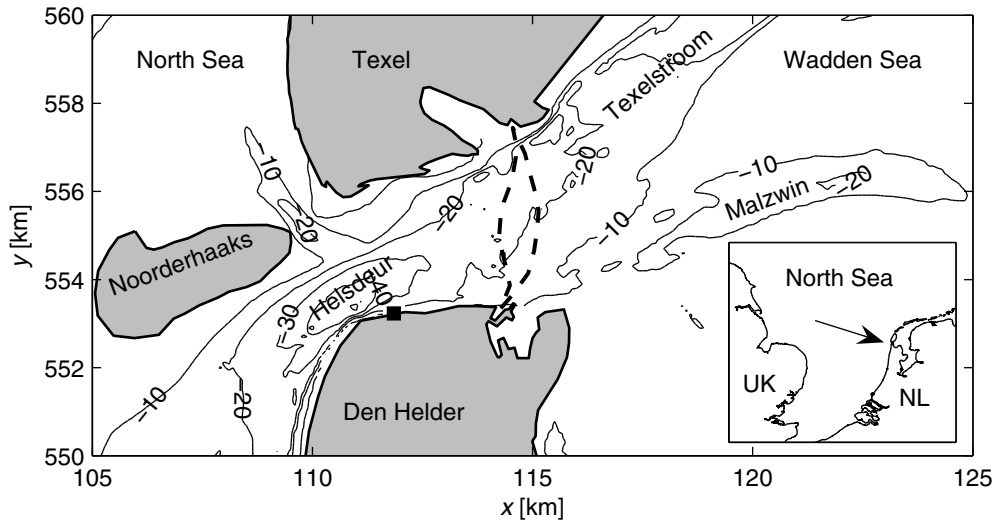
Figure 5.1. The Marsdiep tidal inlet in the Netherlands. In the inset, the arrow points to the location of the Marsdiep inlet. The Netherlands and the United Kingdom are indicated by NL and UK, respectively. In the main figure, east (north) is in the positive x (y) direction. The thick dashed lines indicate the envelope of ferry crossings. The Den Helder tide gauge is indicated by the black square. The bathymetry is contoured in 10-m intervals.

5.3   Data handling and techniques

5.3.1   Data collection

The water depths measured with the ADCP were used to generate detailed bathymetric maps or digital terrain models (DTMs) of the Marsdiep inlet. These DTMs form the basis of the sand-wave analysis. In Chapter 2 the ADCP configuration was extensively discussed. Only a brief description is given here. The ADCP is mounted under the hull at 4.3 m below the water surface near the horizontal centre of the ferry. The ferry crosses the Marsdiep inlet twice per hour at a speed of about 17 km h^{-1}, up to 32 times per day, 7 days per week, up to 320 days per year. At the beginning of each year, the ferry is out of service for one to two months due to maintenance. Till the end of 2002, depth data were collected with a Nortek 1.5-MHz vessel-mounted ADCP that measured at a rate varying between 0.26 Hz and 0.35 Hz. The 1.5-MHz ADCP has a blanking distance and cell size of 0.5 m. The water depths from the 1.5-MHz ADCP were obtained by locating the peaks in each of the three ABS signals. In early 2003, the 1.5-MHz ADCP was replaced by a 1-MHz Nortek ADCP, featuring a blanking distance and cell size of 1 m. This ADCP measures at a rate of 1 hz. In addition to the standard signal to determine the current speed, the 1-MHz ADCP emits an extra signal from its three transceivers to determine the bottom location and the bottom movement. The depth measurements determined with this signal were used to create DTMs. Till August 12, 2004, horizontal positions and heading were determined with two Leica MX412 differential global positioning system (DGPS) stations located at the front and rear end of the ferry and a Sperry SR220 gyrocompass. After this date, a Furuno SC60 GPS and gyrocompass, centrally located on the ferry, were used.

5.3.2 DTM creation

To create a DTM a number of steps were taken. First, all horizontal GPS positions were corrected for horizontal offsets and mapped to the actual ADCP positions using the heading data. Then, water depths were corrected for vertical and horizontal offsets. For each measurement, a median depth was calculated based on the three depth values. This median water depth was corrected for the vertical tide measured at a tide gauge near Den Helder (Fig. 5.1). These data were obtained from the Dutch Ministry of Transport, Public Works and Water Management. Data gaps in the measured water levels were filled in with predicted water levels. Smooth transitions between the measured and predicted water levels were obtained by adding the linear transition of the differences between the measured and predicted water levels at the beginning and end of each data gap.

In the next step, DTMs were generated by collecting all corrected data within a 30-day window, by rounding all data to the nearest grid points of a 15×15 m^2 grid, and by taking the median depth h of all data per grid point. The 30-day window was used because this period contains sufficient data to cover a large enough area. The 15-m grid size was used because with this size a sufficient resolution is obtained while keeping the number of empty grid points in the DTM to a minimum. In the last step, the vertical and horizontal outliers were removed and the empty grid points were filled in by linear interpolation. In addition to DTMs based on h, DTMs were also created that represent the variance around the mean water depth h'. At each grid point, h' was calculated by subtracting an area-mean depth $\{h\}$ from h, where $\{\}$ indicates area averaging. The area-mean depth is based on all water depths within a horizontal square of 255×255 m^2 centred around the grid point. New DTMs were generated by shifting the window 5 days and repeating all steps. In this way, 361 DTMs of h and h' were generated for the period from March 17, 1998 to April 14, 2005. DTMs from before 2003 are based on about 200,000 depth measurements, while DTMs from 2003 onwards are based on about 600,000 depth measurements. Fig. 5.2 shows the data density per grid point for a 30-day window centred around July 7, 2000, the standard deviation σ_h of all water depths per grid point, and the DTMs based on h and h'. As can be expected, the data density is highest along a straight line connecting both ferry harbours. The bedforms are better visualised with h' than with h. Large bedforms are found on the shallow south slope of the inlet channel, while smaller bedforms occur in the deeper main channel to the north. In the next section σ_h is discussed.

5.3.3 Accuracy of the data

The depth measurements are affected by a number of vertical and horizontal errors. The vertical errors are as follows: 1) The uncertainty in each depth measurement per transceiver is 0.25 m for the 1.5-MHz ADCP and a few centimetres for the 1-MHz ADCP. 2) The water-level measurements occur about 3 to 4 km westward of the ferry transect. As a result of spatial differences in travel time of the tidal wave, offsets between the local water level and the water level at the tide gauge can be as large as $\sim$0.10 m. 3) The ADCP beams make an angle of 25° with the vertical. The 'footprint' of the beams on the seafloor has a maximum length of about 20 m for a water depth of 25 m. As a result,
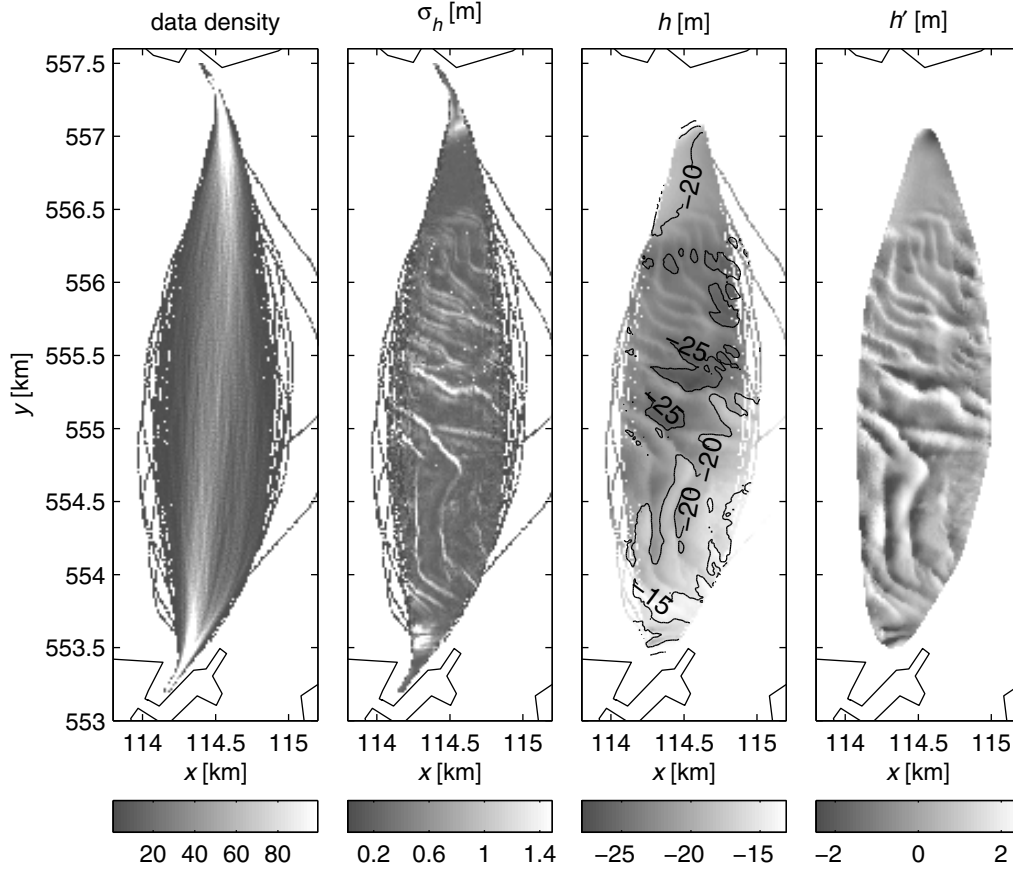
Figure 5.2. Four panels showing from left to right: data density per 15-m grid point, standard deviation σ_h of all depths per grid point, depth h, and variance around the mean depth h'. Dark (light) shades of grey indicate less (more) positive values. In the h plot, bathymetry is contoured in 5-m intervals. The coastlines of the ferry harbours of Texel and Den Helder are plotted to the north and south, respectively. The median date of the data is July 7, 2000.

the beam depths above the sand waves with the steepest slopes can differ by as much as the sand-wave height of $\mathcal{O}(1\text{ m})$. Annual standard deviations over the difference between the median depth and the individual beam depths vary between 0.4 m and 0.8 m. 4) The ADCP uses the speed of sound in water to determine the cell locations and water depth. The depth is determined with a speed of sound as a function of the water temperature and a constant salinity of 30 psu. Deviations from 30 psu introduce systematic errors that affect all depth measurements. In the Marsdiep inlet the salinity varies around 30 psu, but drops occasionally by maximally 15 psu following days with high fresh-water discharge. This introduces an error of maximally 0.30 m for a depth measurement of 25 m.

Uncertainties in horizontal positioning and heading are represented by standard deviations that were determined while the ferry was docked for (un)loading (see Chapter 2). The ferry always docks in the same location, and the movement of the ferry is minimal during the docking. The standard deviations of the Leica DGPS are about 0.84 m along the x-axis (positively eastward) and 1.31 m along the y-axis (positively northward). In the period from January 6 to April 1, 1999, the standard deviations are 2.36 m and 6.03

m along the x and y-axes. Unfortunately, these large values cannot be explained. The standard deviation of the Sperry gyrocompass is fairly small at about 0.16°. The standard deviations of the Furuno GPS and gyrocompass are slightly larger: 1.51 m and 2.28 m along the x and y-axes and 0.5°, respectively. The effect of the standard deviations of the gyrocompass on the horizontal positions is less than 0.4 m. The mean ADCP positions in the harbours of Texel and Den Helder are within a range of 2 m.

Finally, the construction of the DTMs also causes errors. They are as follows: 1) The rounding error of ± 7.5 m introduces a vertical error of $\mathcal{O}(1$ m) near the steep slopes of the sand waves. 2) The sand waves migrate a few metres in the 30-day window. This also creates errors near the steep slopes. Some of the errors mentioned above are represented by σ_h in Fig. 5.2. σ_h is smallest on gentle slopes ($\sigma_h < 0.5$ m) and largest near steep slopes ($\sigma_h > 1$ m).

To validate the ADCP depth measurements, additional depth measurements were conducted with a vessel-mounted echo sounder on March 30, 2005. The measurements were performed with a Furuno FE 700 echo sounder mounted under the hull of the NIOZ research vessel Navicula. The horizontal positions were accurately determined with a Furuno SC120 GPS. Conditions during the measurements were calm. Similar to the ferry ADCP data, the echo sounder measurements were corrected for the vertical tide. The echo sounder has a sampling rate of 1 Hz and an accuracy of about 0.1 m. These data were compared with data interpolated from the DTM of April 1, 2005 along three transects (see also Fig. 5.13 that is discussed in the Results section). The agreement between the echo sounder and the ADCP depths is good and all large features are captured. Due to the coarser resolution of the DTM, the sand-wave crests are more rounded and mega ripples are absent on the transects interpolated from the DTM. The root-mean-square difference between water depths derived from the echo sounder and the ADCP is about 0.3 m.

In conclusion, most of the errors in water depth are small compared to the large bedforms with heights of $\mathcal{O}(1$ m) and lengths of $\mathcal{O}(100$ m). The largest errors of $\mathcal{O}(1$ m) result from the beam angles of 25° and the rounding error. However, the large number of depth measurements per grid point (Fig. 5.2) reduces this error significantly.

5.3.4   Cross-correlation technique

A visual inspection of the seven-year data set reveals that there is significant spatial variation in sand-wave migration. It appears as if the sand waves migrate in directions that are not perpendicular to the crests. Simply tracking the crests of sand waves along transects perpendicular to the crests would provide a limited picture. Following Duffy and Hughes-Clarke (2005), a simple but efficient cross-correlation technique was used to determine the spatial migration of the sand waves. Duffy and Hughes-Clarke (2005) used the 'Weighted centroid' technique to calculate migration vectors, rather than the maximum correlation. Moreover, they used spatial gradient maps rather than bathymetric maps. For the purpose of this research, the use of the 'maximum correlation' technique and bathymetric maps appeared to give robust results.

In the cross-correlation technique, spatial patterns on subsequent time steps t_1 and t_2 on DTM_1 and DTM_2 are compared (Fig. 5.3). A square box, i.e. 'fit matrix', centred around a grid point on DTM_1 is defined. The fit matrix with the bottom-depth informa-
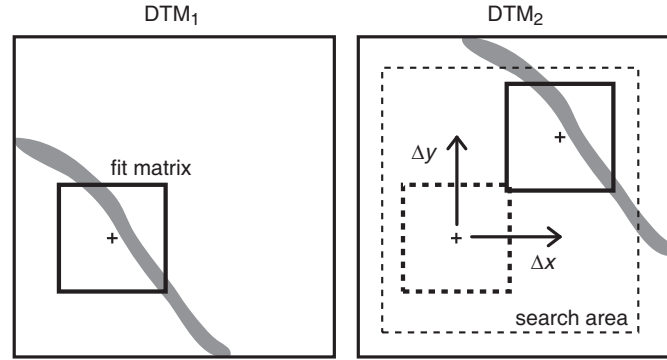
Figure 5.3. Illustration of the cross-correlation technique. To obtain the migration vector of the sand wave (shaded area) the following procedure is used. For every grid point, the fit matrix on DTM_1 on time t_1 is shifted in x and y directions within the search area on DTM_2 on time t_2. For every displacement a correlation between the height in the fit matrices on DTM_1 and DTM_2 is calculated. The highest correlation within the search area yields the displacements Δx and Δy of the fit matrix.

tion (h or h') of t_1 is moved around with prescribed displacement increments Δx and Δy within a 'search area' on DTM_2. When doing so, it is important to choose the maximum displacement larger than the expected pattern migration. The size of the displacement increments, equal to a multiple of the grid size, determines the accuracy of the migration vectors. To obtain a higher accuracy, the DTMs were regridded on 3-m grids by linear interpolation. Regridding is beneficial for a higher accuracy because the correlation technique tracks three-dimensional shapes. The rows of the fit matrices were placed in succession to yield vectors a and b at t_1 and t_2, respectively. Finally, for every displacement, a correlation r between vectors a and b was calculated. If the patterns are exactly the same, $r = 1$, whereas if they are in antiphase, $r = -1$. The correlation coefficient is defined as:

$$r = \frac{S_{ab}}{S_a S_b}, \tag{5.1}$$

S_a (and S_b) the variance and S_{ab} the covariance:

$$S_a{}^2 = \frac{1}{n-1} \sum_{j=1}^{n} (a_j - \{a\})^2, \ S_{ab} = \frac{1}{n-1} \sum_{j=1}^{n} (a_j - \{a\})(b_j - \{b\}),$$

where $\{a\}$ and $\{b\}$ are the mean elevations, and n the number of data points within each vector. After determining r for every displacement, its maximum value within the search area yielded the displacements Δx and Δy of the pattern within the fit matrix. To save computation time, migration vectors were only calculated for each 15-m grid point.

An example of the cross-correlation technique is presented in Fig. 5.4 for the period from December 18, 2001 to April 2, 2002 (105 days). In this example, DTMs based on h' were used. The fit matrix has a size of 210 m. The displacement vectors in the left panel of Fig. 5.4 have directions ranging from east to north. The vector field is smooth and changes gradually. Only near the boundaries occasional outliers occur. The large migration vectors north of $y = 556.5$ are due to the absence of bedforms. Here the technique does not find
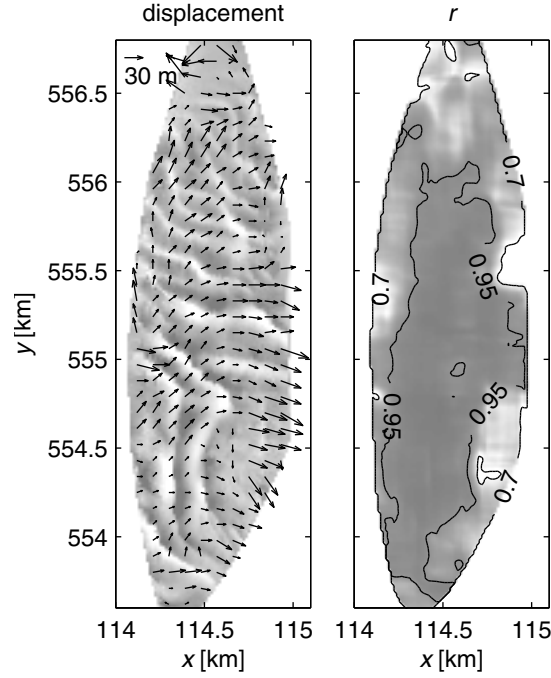
Figure 5.4. Sand-wave migration (left) and correlation coefficient r (right) calculated with the cross-correlation technique for the period from December 18, 2001 to April 2, 2002 (105 days). The size of the fit matrix equals 210 m. In the left panel, the background is a shaded contour map of h' with a median date of December 18, 2001 and the migration vectors are plotted every 90 m. In the right panel, dark (light) shades of grey indicate high (low) r values.

good matching patterns. These outliers correspond to lower correlation coefficients. In general however, the matches are good and correlation coefficients are higher than 0.9.

The sensitivity of the correlation technique was studied for fit matrix sizes of 60, 120, 180, 210, 240, and 270 m. The sensitivity is indicated by standard deviations σ_u and σ_v of migration rates u and v along the x and y directions, respectively. Migration rates were calculated for time steps of three months, from March 1998 to March 2005. They are presented in the Results section. For every time step, σ_u and σ_v were calculated for all u and v within areas I-IV (Fig. 5.8). Mean standard deviations were then simply calculated over all time steps and areas and plotted as a function of the fit matrix size in Fig. 5.5. Also plotted is the mean percentage of migration vectors with a correlation smaller than 0.9. Within the different areas there is some variation in migration speed (compare Fig. 5.4 and Fig. 5.8), and as a result, the standard deviations are never zero. Therefore, the results of the sensitivity analysis should be considered relative to each other. Fig. 5.5 shows a decrease in the standard deviations and the percentage of 'bad fits' with larger fit matrices. On a typical DTM, wave lengths range from 125 m to 250 m. Apparently, the fit matrix with the size of 60 m is not able to track the large bedform patterns correctly. There are too many incorrect pattern matches, resulting in a chaotic migration-velocity field and high standard deviations. The results pertaining to fit matrixes with sizes larger than 120 m are much better. On the other hand, it is more
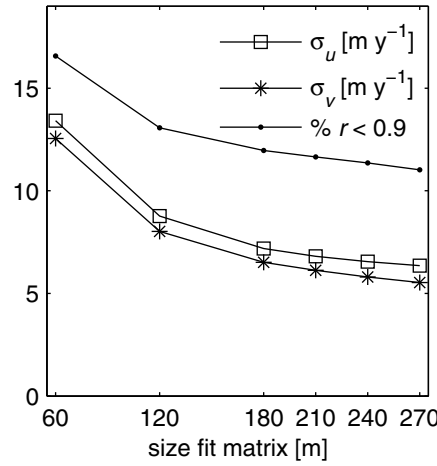
Figure 5.5. Standard deviations σ_u and σ_v and the percentage of $r < 0.9$ as a function of the size of the fit matrix.

difficult to track smaller bedforms with fit matrices that are too large. On the basis of this analysis and visual inspection of progressive vector diagrams, such as Fig. 5.7, a fit matrix size of 210 m was selected for the cross-correlation technique. The dots in Fig. 5.7 represent integrated migration vectors. With a size of 210 m, the clustering of the dots is minimal and the migration pathways of the dots are smoothest. The cross-correlation technique was applied to both h and h'. The differences between the results are small, but progressive vector diagrams show that the migration pathways are a little smoother for h'. Therefore h' was used for the cross-correlation calculations. Fig. 5.7 will be further discussed in the Results section.

5.4   Results

5.4.1   Sand-wave migration

The evolution of sand waves in time steps of about one year from March 1998 to March 2005 is presented in Fig. 5.6. Over the course of seven years the sand waves retain their shapes remarkably well, and therefore, bedform features can easily be tracked through time. This is done manually for eight bedform features. Note that in 2002 a new sand wave ($5'$) appears on the 1998 location of 5. This feature is also tracked through time. The sequence of DTMs shows remarkable deviations from a relatively simple and regular train of migrating sand waves. Sand waves parallel to sand wave 1-2 primarily migrate in eastern directions, while the sand waves to the north of 2 migrate in northeastern directions. The eastward migration of sand wave 2 is higher than that of sand wave 3, and as a result, sand wave 2-3 rotates about 30° counterclockwise. The northeastward migration speed of sand wave 5 is much higher than 3. Apparently, this triggers the formation of a new sand wave $5'$ in the space between sand waves 3 and 5. Sand wave $5'$ follows the same pathway as 5. The migration speed of sand wave 4 is much lower than of sand waves 5 and $5'$. These waves merge with and break apart from sand wave 4. It is also interesting to note the eastward migration of the fork near 6 in the first 3.5 years.
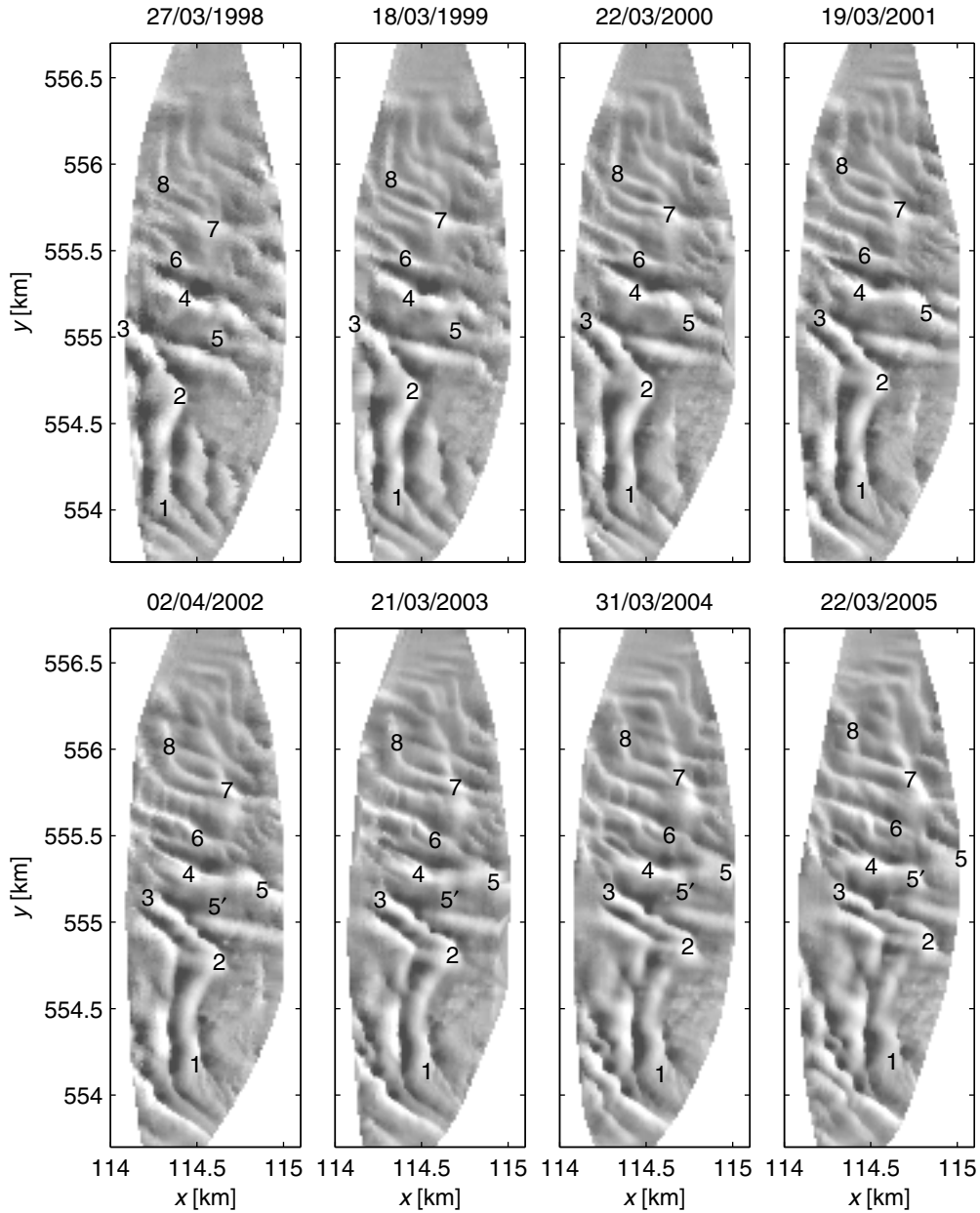
Figure 5.6. Eight DTMs (h') in time steps of about one year from March 1998 to March 2005. Numbers indicate bedform features that can be tracked through time. Note that in 2002 a new sand wave ($5'$) appears on the 1998 location of 5. The dates on top of each figure represent *day/month/year*.

While the fork migrates eastward and sand wave 7 northeastward, a new sand wave (wave G in Fig. 5.13) forms in the growing space between the fork and sand wave 7. In the last 3.5 years, the southern branch of the fork deteriorates. The sand waves to the north of sand waves 7 and 8 continuously change shape, break apart, merge, appear, or deteriorate and therefore it is more difficult to track individual bedforms in this area.

The complex spatial migration of sand waves illustrated in Fig. 5.6 was quantified with

Figure 5.7. Progressive vector diagrams showing the migration pathways of dots. The pathways are interpolated from migration rates obtained with the 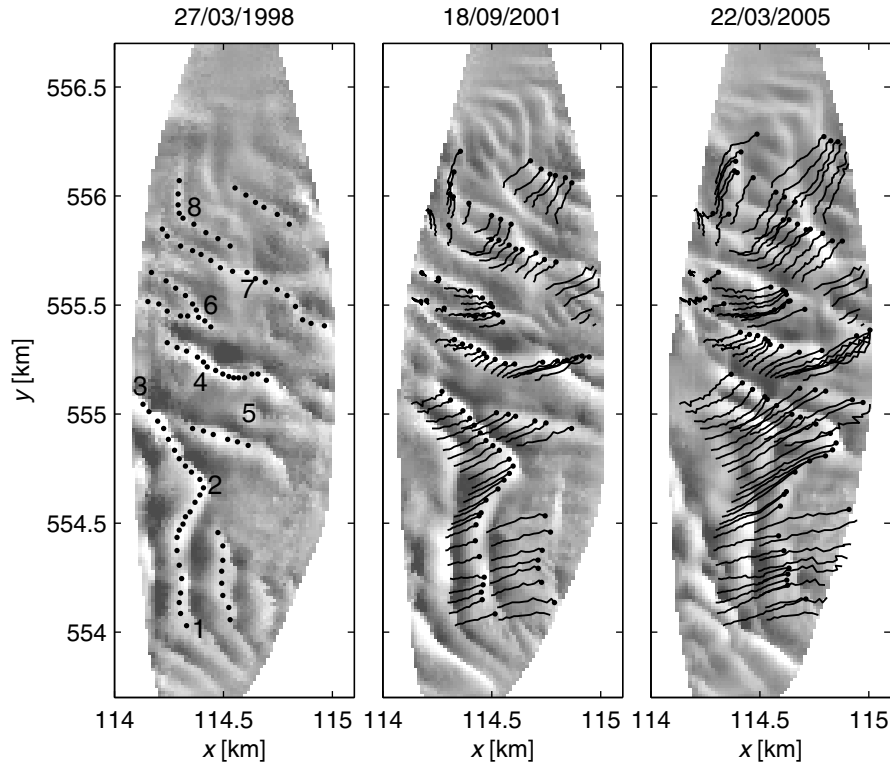correlation technique. The initial positions of the dots on March 27, 1998 are shown in the left panel; the halfway point is September 18, 2001 in the middle panel; the final positions on March 22, 2005 are shown in the right panel. The numbers indicate bedform features also shown in Fig. 5.6.

the cross-correlation technique. The technique was applied from March 1998 to March 2005 and the time steps match the four seasons: winter (December-March), spring (March-June), summer (June-September), and fall (September-December). The dates of selected DTMs generally fall in the second half of each month. Only in 2004, spring and summer are combined into one period due to lack of data. The results of the cross-correlation technique are presented in Figs. 5.7, 5.8, 5.9, and 5.10.

The functioning of the cross-correlation technique is confirmed with progressive vector diagrams in Fig. 5.7. The position of 100 dots, initially placed on crests, is tracked through time by the integration of eastward (u) and northward (v) migration velocities. Fig. 5.7 shows migration pathways of dots from March 27, 1998 to March 22, 2005. Overall, the cross-correlation technique is able to track the bedforms patterns. To the south of $y = 555.3$ km, the technique works well and the dots in the final position are still situated on the large bedforms. The tracking of bedform patterns is more difficult to the north because here the sand-wave patterns change more rapidly.

Fig. 5.8 presents mean migration vectors ($\langle u \rangle, \langle v \rangle$), where $\langle \rangle$ indicates time averaging, and absolute mean velocities $\langle U \rangle$ calculated for the entire time series. In the right panel, four areas are plotted that group sand waves with distinct migration velocities, height, length, and orientation. Areas I-IV are used to calculate area-mean sand-wave character-
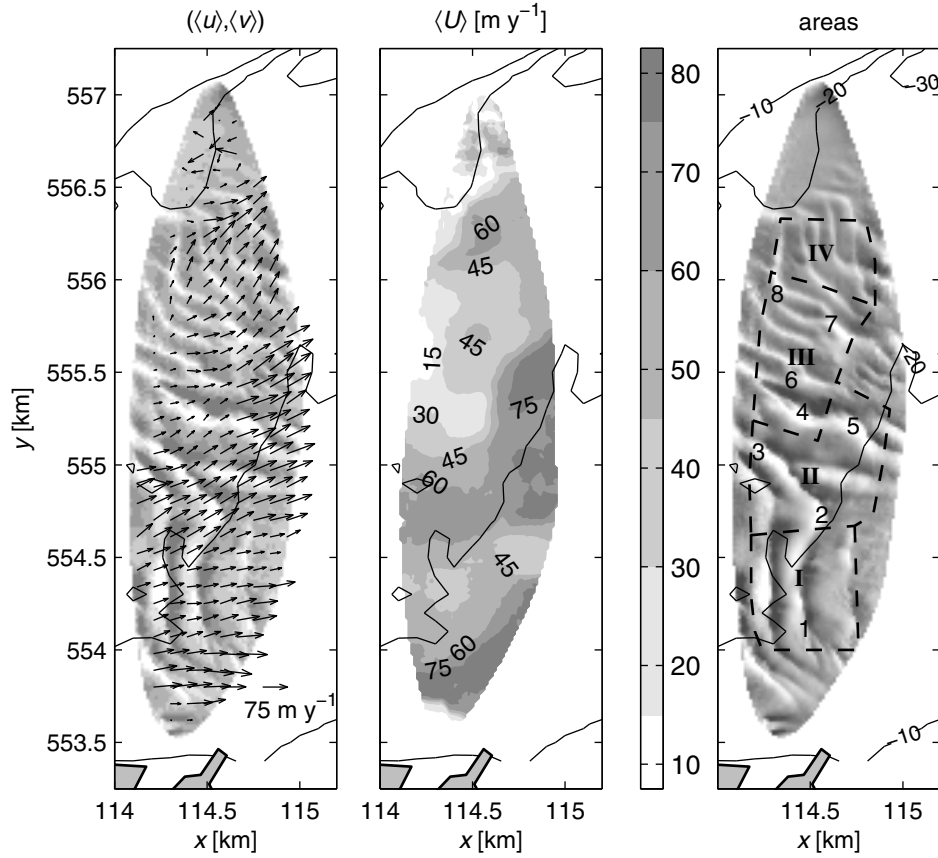
Figure 5.8. Mean migration vectors $(\langle u\rangle,\langle v\rangle)$ in the left panel, absolute mean migration rates $\langle U\rangle$ in m y^{-1} in the middle panel, and the location of areas I-IV in the right panel. Mean migration rates were calculated for the period from March 1998 to March 2005. Vectors in the left panel are plotted every 90 m. The numbers in the right panel indicate bedform features also shown in Fig. 5.6. Shaded background in left and right panels resemble h' of October 5, 2000. In all panels the bathymetry is contoured in 10-m intervals.

istics. Two additional areas to the south of area I and to the north of area IV can be identified, but these areas are too small to calculate area-mean characteristics. The area to the south of area I is marked by a narrow band with mean eastward migration rates higher than 75 m y^{-1}. The migration vectors make a clockwise angle of about 50° with the normal to the crests. Area I encompasses sand waves with a south-north orientation. These sand waves migrate up slope in eastern direction with mean migration speeds between 45 and 60 m y^{-1}. The migration direction is approximately perpendicular to the sand-wave crests. While migrating up slope they gradually disappear. Area II marks a transition of sand-wave crests with an orientation from north to south to an orientation from northwest to southeast. This area runs roughly parallel with the southern -20 m isobath in Fig. 5.8. This area features the highest migration rates between 60 and 90 m y^{-1} in directions to the northeast. The migration vectors make a clockwise angle of about 40° with the crest normals. The sand waves in area III have the smallest mean migration rates between 0 and 45 m y^{-1}. In this area, the angle between the migration vectors and
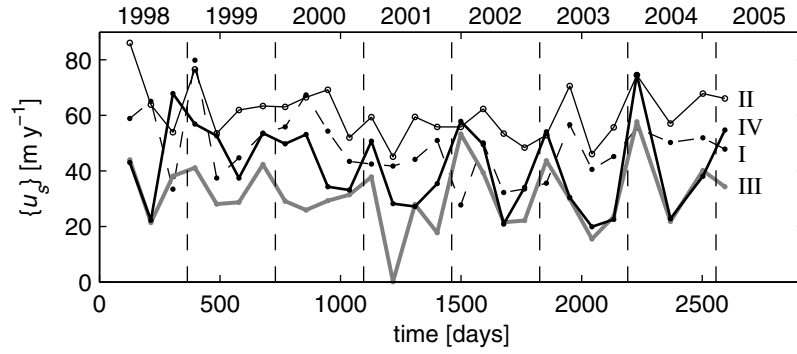
Figure 5.9. $\{u_s\}$ as a function of time for areas I-IV. The vertical dashed lines indicate midnight of each new year. The years are printed above the graph.

the crest normals varies around 65°. The abrupt transition from low migration rates in area III to high migration rates in Area II is remarkable. In Fig. 5.8 along sand wave 4-5′, the mean migration rate increases from below 30 m y^{-1} to above 75 m y^{-1} over a distance of about 130 m in eastward direction. In area IV the sand waves migrate with rates between 30 m y^{-1} and 60 m y^{-1} in northeastern directions. The migration vectors make a 40° clockwise angle with the crest normals. On the northern boundary of area IV, there is a zone of converging migration vectors and a steep gradient in migration rates. To the north of area IV, the sand waves disappear and the mean bedform migration is chaotic but towards the west.

The seasonal variability in migration rates is evident in Figs. 5.9 and 5.10. Fig. 5.9 shows the area-mean migration rate $\{u_s\}$. Velocity $\{u_s\}$ is defined along the main or s-axis, which is aligned with the direction of maximum variability in area-mean migration rates $(\{u\}, \{v\})$. In areas I and II, $\{u_s\}$ is highest around 60 m y^{-1} but portrays little seasonal variability. In contrast, the migration rates in areas III and IV are lower, but the seasonal variability is much larger. The variability is present in area IV in the entire record, with mean winter rates as high as 80 m y^{-1} and summer rates as low as 20 m y^{-1}. The seasonal variation in area III is less strong and most regular from the winter of 2001-2002 to the end of the record. The variability in $\{u_s\}$ is primarily due to the variability in the eastward velocities.

The seasonal variability is even better emphasised with $\{u_s\}'$ in the top panel of Fig. 5.10. Velocity $\{u_s\}'$ was calculated by subtracting the annual mean from $\{u_s\}$ for each year and by averaging over all residuals per season. This figure confirms that the seasonal variability is indeed largest for areas III and IV. The figure also reveals some variability in areas I and II. However, compared to areas III and IV, the maximum and minimum migration rates are delayed one season and occur in spring and fall, respectively.

5.4.2 Sand-wave characteristics

The long-term measurements allow tracking of the temporal evolution of sand-wave height H, length L, and asymmetry A. The wave length and height are defined in Fig. 5.11. Note
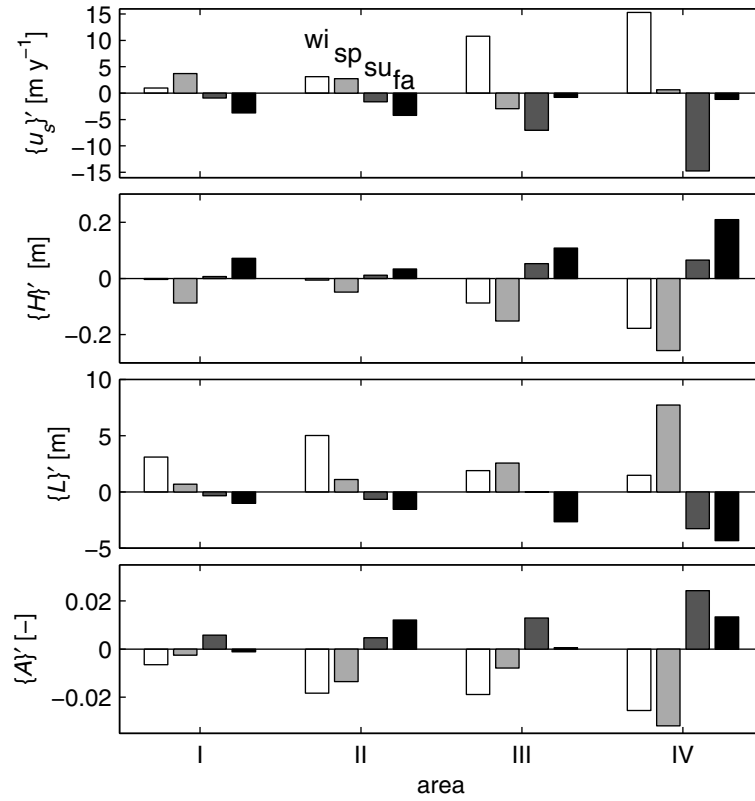
Figure 5.10. Variables $\{u_s\}'$, $\{H\}'$, $\{L\}'$, and $\{A\}'$ indicate the seasonal variability for areas I-IV for winter (wi), spring (sp), summer (su), and fall (fa) seasons.

that $L = L_1 + L_2$. The asymmetry is defined as (Knaapen, 2005):

$$A = \frac{L_1 - L_2}{L_1 + L_2}. \tag{5.2}$$

The asymmetry has values between -1 and 1. Sand waves are symmetrical when $A = 0$. A positive asymmetry indicates that the steepest slope of a sand wave faces the positive x or y direction. Values of H, L, and A were calculated for every sand wave along the x and y grid lines on each DTM. Irregularities and bedforms smaller than 60 m were filtered out. Area-mean values of H, L, A, and water depth h, i.e. $\{H\}$, $\{L\}$, $\{A\}$ and $\{h\}$, were determined for the four areas I-IV shown in Fig. 5.8. The evolution of these characteristics is plotted in Fig. 5.12. Also included in the bottom panel is the evolution of the mean depth over the inlet cross-section between Den Helder and Texel ($\{h_c\}$). In areas II and III the crest normals make a clockwise angle of 18° with North. In these areas, H, L, and A were calculated along the y-axis, and only L was transformed to the crest normal. In areas I and IV, H, L, and A were calculated along the crest normal which is approximately parallel with the x-axis. It should be noted that the sand-wave patterns in area IV are rather complex. This area features small sand waves with crests from northwest to southeast and larger sand waves with crests from north to south. The estimation of L may be affected by this. Moreover, the limited size of the areas may also affect the statistics. Three transects numbered 1-3 with sand-wave profiles in Fig. 5.13
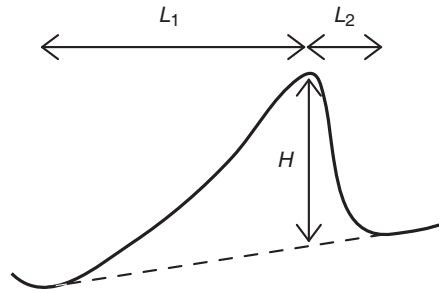
Figure 5.11. Schematic of a sand wave and the dimensions H and $L = L_1 + L_2$. The dashed line is drawn between the troughs.

aid the following discussion about the evolution of the sand-wave characteristics. Note that capitals are used instead of numbers to indicate the sand waves.

The sand waves in the southern half of the inlet are largest. In area I and along transect 1, the mean heights vary between 3 and 3.5 m and lengths between 170 m and 200 m. The sand-wave height comprises about 17% of the mean water depth of 18.5 m. These bedforms are most asymmetric with $A \sim 0.5$ and can be classified as progressive. The steepest slopes have maximum angles of about 30°. This is about equal to the angle of final repose of sand under water (Dyer, 1986). Area II includes sand waves C and D along transects 2 and 3 and features similar size sand waves as in area I. The only differences are that these waves are more symmetric $(0 < \{A\} < 0.2)$ and that they are in larger water depths ($\sim$22 m). These waves are of the asymmetrical-trochoidal type. The steepest slopes are about 20°. Farther northward in areas III and IV, the sand waves become smaller. An exception is sand wave E in area III (sand wave 4 in Fig. 5.6), which is one of the largest bedforms in the study area with a height of 7 m and a length of 250 m. Area III also includes sand waves F-H and features mean wave heights between 2.5 and 3 m and lengths between 160 and 180 m. These sand waves are asymmetrical-trochoidal with asymmetries of $\sim$0.2. The steepest slopes range between 10° and 20°. Area IV, situated in the deepest part of the inlet $(\{h\} \approx -25$ m), has the smallest sand waves with heights between 1 m and 2.5 m and lengths between 140 m and 200 m. Sand waves I, J, K, and L are located in area IV. The waves are asymmetrical-trochoidal with $0 < \{A\} < 0.2$ and the steepest slopes are around 5°.

The evolution of $\{H\}$, $\{L\}$, and $\{A\}$ from March 1998 to April 2005 in Fig. 5.12 reveals significant seasonal and inter-annual variability. The seasonal variability is also illustrated in Fig. 5.10, in which $\{H\}'$, $\{L\}'$, and $\{A\}'$ represent the mean seasonal variability around the annual mean of $\{H\}$, $\{L\}$, and $\{A\}$, respectively. The area-mean wave heights portray the strongest seasonal variability of all variables. In this seasonal cycle, the sand-wave heights are lowest in early spring in March or April and highest in early fall in September or October. Fig. 5.10 shows that the same variability is present in all areas, but it is strongest in areas III and IV. In area IV, the seasonal height difference is about 0.5 m, which is about 25% of the sand-wave height. The amplitude of the seasonal height variation decreases as the sand waves get larger in volume. The seasonal variation in height in areas I and II is up to 0.3 m (10% of height). Sand-wave profiles show that in fall the sand-wave crests are higher and the troughs are deeper, whereas in spring the crests are lower and the troughs
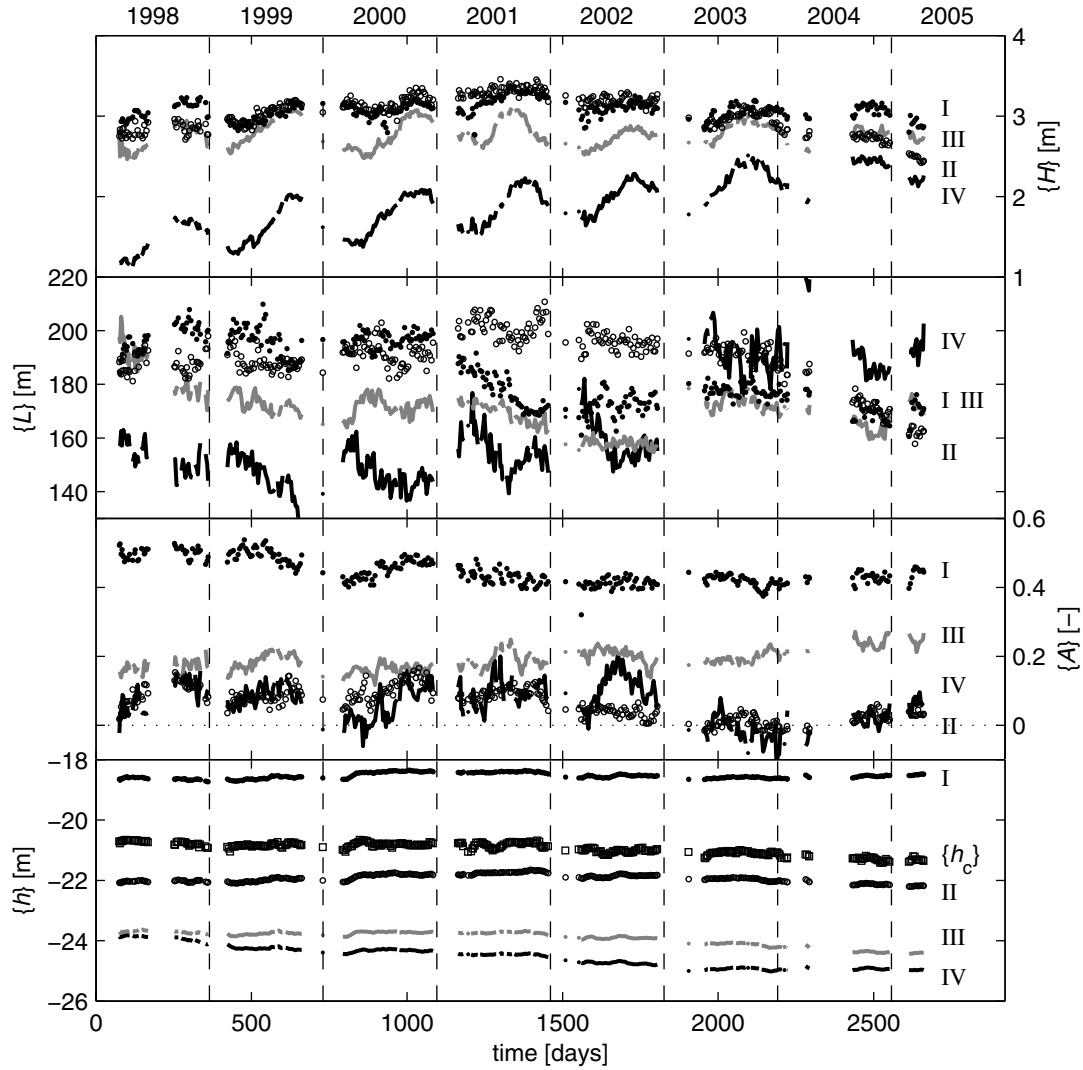
Figure 5.12. Evolution from 1998 to 2005 of area-mean wave height $\{H\}$, wave length $\{L\}$, asymmetry $\{A\}$, and water depth $\{h\}$. The solid dots, the open circles, the grey line, and the black line refer to areas I, II, III, and IV, respectively. In the bottom panel, the squares refer to the cross-section averaged water depth $\{h_c\}$.

are shallower. This and the absence of any seasonal variability in $\{h\}$ suggests that the volume of sediment in the areas is conserved. In contrast to the small inter-annual trends in areas I-III, the mean wave height in area IV shows a gradual increase from 1.5 m to 2.25 m.

The seasonal variability in sand-wave lengths is as much as 15% of the total length. In winter or spring the lengths are larger than in summer or fall. The variability in area IV is remarkably large and it is in antiphase with the wave height. In winter and spring in area IV, sand waves deteriorate and gaps appear in the crests. As a result, along some grid lines sand waves are no longer visible and neighbouring sand waves appear to have larger wave lengths, increasing the area-mean wave length. The seasonal and inter-annual variability of the wave length is also affected by the migration of large or small waves into
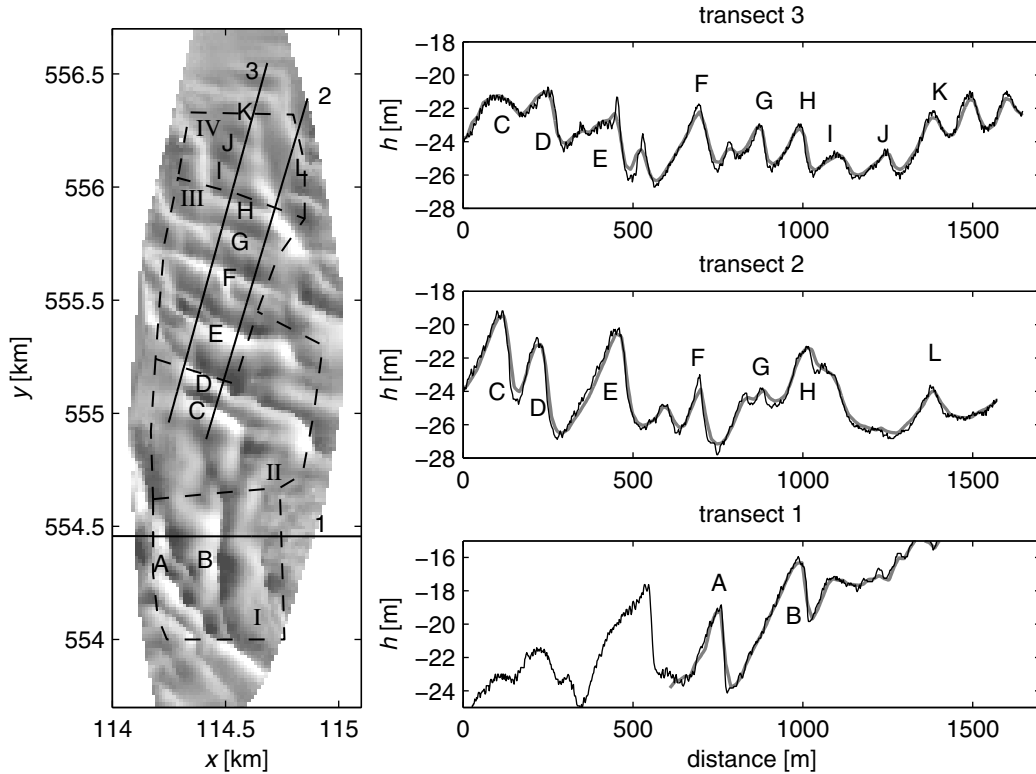
Figure 5.13. Sand waves along three transects across the Marsdiep sea floor. Black lines represent the echo-sounder measurements performed on March 30, 2005. Thick grey lines represent transects interpolated from the DTM with the median date April 1, 2005. Capitals refer to sand waves on the overview map. The overview map shows h' with the median date of April 1, 2005 and the boundaries of areas I-IV (dashed lines).

or out off the areas. For example, the reduction in mean wave length by 30 m in area I in 2001 in Fig. 5.12 is due to the deterioration of the sand wave to the east of sand wave 1-2 and its migration out of the area. Consequently, the large wave length of this sand wave no longer contributes to the mean. A systematic inter-annual trend is the increase in wave length from 140 m to 170 m in area IV. This increase occurs simultaneously with an increase in wave height and also with a decrease in the mean depth.

The sand-wave asymmetry also shows consistent seasonal trends for all areas with a higher asymmetry in summer or fall and a lower asymmetry in winter or spring. Fig. 5.10 illustrates that the seasonal change is nearly in phase with the wave height. The amplitude is again largest for area IV. The inter-annual changes are small. It is interesting to note that in 2003 the sand waves in area II are symmetric and the sand waves in area IV have a negative asymmetry.

While any seasonal variability in area-mean water depth is absent, inter-annual trends are certainly present. The largest systematic change occurs in area IV, which deepens by 1.2 m. The mean depth of the inlet $\{h_c\}$ also increases by 0.7 m. This is a relative change of 3%.

5.5   Discussion and conclusions

This chapter demonstrates that it is possible to generate accurate digital terrain models (DTMs) of the sea floor of the Marsdiep tidal inlet with an ADCP mounted under the ferry Schulpengat. The 7-year long data set from March 1998 to April 2005 consists of 361 DTMs and allows for a detailed spatial and temporal bedform analysis. DTMs with grid sizes of 15×15 m^2 reveal the existence of sand waves with wave lengths of $\mathcal{O}(100$ m) and heights of $\mathcal{O}(1$ m). The accuracy of the DTMs is mainly influenced by beam angles of the ADCP and rounding errors. These vertical errors are of $\mathcal{O}(1$ m) near the steepest slopes of the sand waves. However, the large number of depth samples per grid point greatly reduces these errors. This is illustrated in Fig. 5.13, which shows the good agreement between depths interpolated from a DTM and depths obtained with an echo sounder.

To the author's knowledge, it is the first time that a spatial cross-correlation technique has been applied to a multi-year data set of sand-wave observations and that it has been successful in determining seasonal variability in sand-wave migration speed. The large data set is well suited for this technique because the bedform patterns deviate from straight crested sinusoids and retain their shapes within three-month time steps. A fit matrix size of 210 m, about the size of a wave length, yields the best results. The choice of this size is in part subjective and is based on visual inspection of progressive vector diagrams. However, area-mean migration rates are barely affected by deviations from this value.

The DTMs reveal remarkable deviations from simple and regular bedform patterns. The bedform fields contain many defects and the crests of the sand waves are rarely longer than 500 m. Bedform fields that contain many defects reorient on shorter time scales than fields with low defect density, such as linear bedforms (Werner and Kocurek, 1997). The bedform pattern to the north of the inlet shows several branches (e.g. near 6, 7, and 8 in Fig. 5.6). These irregular bedforms have also been observed in laboratory experiments with an oscillating flow over vortex ripples (Hansen et al., 2001) and in numerical modelling (Pannell et al., 2002). The sequence of DTMs also shows the formation, deterioration, merging and breaking apart of the bedforms.

The variability in migration rates, height, length, and asymmetry has been studied for four areas (I-IV). Based on these results, the Marsdiep tidal inlet can be divided in roughly two halves. The southern half of the inlet encompasses areas I and II and the northern half areas III and IV. In the southern half, areas I and II feature the largest sand waves. Area I has progressive sand waves with area-mean heights of 3 m and wave lengths of 200 m. The crest orientation is north-south. The migration direction is eastward in the flood direction, perpendicular to the sand-wave crests, and averages about 48 m y^{-1}. Area II is a transitional area from area I to area III. The sand waves have similar dimensions as in area I but they are less progressive and the crests have a different orientation. Area II features the highest migration rates of 60-90 m y^{-1} in a 500 m wide band parallel to the southern 20-m isobath (Fig. 5.8). Due to the northward decrease in migration speed, sand waves in this zone not only undergo a northeastward translation but also a counterclockwise rotation. On the northeastern boundary of this zone high spatial gradients of 35 m y^{-1} per 100 m are observed. This zone marks the transition from the progressive sand waves in the southern half to asymmetrical-trochoidal sand waves in the northern half in areas

III and IV. In these areas the sand waves are also smaller, featuring area-mean heights between 1.5 and 3 m and wave lengths between 140 and 200 m. The orientation of the crests is from the northwest to the southeast in area III and more from north to south in area IV. The sand waves migrate in eastern to northeastern directions, but the mean migration directions are not perpendicular to the crests and deviations can be as large as $50°$. Area III features the lowest migration rates of about 31 m y^{-1} and area IV features the second lowest migration rates of about 42 m y^{-1}.

The shape and dimensions of the sand waves in the Marsdiep inlet compare well with sand waves observed in, for example, the Danish Wadden Sea (e.g. Bartholdy et al., 2002; Ernstsen et al., 2005) or the North Sea (e.g. Terwindt, 1971; McCave, 1971). Flemming (1988) found a best fit equilibrium relation $H = 0.0677 L^{0.8098}$ for 1491 bedforms of different dimensions in unidirectional and reversing flows. The sand waves in the Marsdiep inlet cluster just below this best fit line. The migration speeds of the sand waves are also comparable to observations in other tidal inlets. For example, Ludwick (1972) observed migration speeds ranging between 35 and 150 m y^{-1} in Chesapeake Bay, Aliotta and Perillo (1987) measured average migration rates of 33 m y^{-1} in Bahia Blanca, Bartholdy et al. (2002) found eight year average migration speeds of sand waves of 32 m y^{-1} in the ebb-dominated Gradyb inlet, and Ernstsen et al. (2005) reported migration speeds ranging between 9 and 31 m y^{-1} in the Gradyb inlet. Compared to tidal inlets with their stronger tidal currents, migration speeds in coastal shelf seas are generally lower: Besio et al. (2004) published migration rates in the North Sea ranging from 3.5 to 8.8 m y^{-1} and Van Dijk and Kleinhans (2005) observed rates in the North Sea between 3.4 and 20 m y^{-1}.

Fig. 5.10 shows that the division of the inlet in roughly a southern and a northern half also applies to the seasonal variability in primarily $\{u_s\}$ and $\{H\}$ and in $\{L\}$ and $\{A\}$ to a lesser degree. The seasonal variability is strongest in area IV, followed by area III, and smallest in areas I and II. In area IV, the migration rate is about 30 m y^{-1} higher in winter than in summer and the sand-wave height is about 0.5 m higher in fall than in spring. As the sand waves migrate faster, the height decreases, the wave length increases, the asymmetry decreases, and vice versa. The cause of this variability is yet unknown. The occurrence of the strong seasonal variability in $\{u_s\}$, $\{H\}$, $\{L\}$, and $\{A\}$ in area IV suggests that it may be due to the same process. The sand waves in area IV have the smallest sand volume. As a consequence, the response time of these sand waves is smaller and therefore the amplitude of the response larger. To date there have been few studies that report on seasonal changes in shape and migration of sand waves in tidal environments. Seasonal changes in sand-wave height were observed by Terwindt (1971), Ludwick (1972), and Langhorne (1982). They attributed this variability to stronger currents and orbital velocities that occur during storms. Currents and orbital velocities stir up and transport sediment and this may cause the erosion of the crests.

The spatial and temporal variability in sand-wave characteristics across the inlet is significant and suggests large gradients in the governing hydrodynamics. For the sake of brevity, the hydrodynamics were not considered in this chapter. In Chapter 6 the ferry-ADCP current measurements are applied to gain insight into the spatial and seasonal sand-wave variability.

Chapter 6

Long-term evolution of sand waves in the Marsdiep inlet
II: Relation to hydrodynamics

Abstract

A discussion is presented about the mechanisms that govern the spatial and seasonal variability in sand-wave height and migration speed in the 4 km wide Marsdiep tidal inlet, the Netherlands. Since 1998, current velocities and water depths have been recorded with an ADCP that is mounted underneath the ferry 'Schulpengat'. In this chapter, the current measurements are used to explain the sand-wave observations presented in Chapter 5. Across nearly the entire inlet, the sand waves migrate in the flood direction. In the flood-dominated southern part of the inlet, the measured (i.e. based on sand-wave shape and migration speed) and predicted bedload transport agree in direction, magnitude, and trends, whereas in the ebb-dominated northern part the predicted bedload transport is opposite to the sand-wave migration. It is hypothesised that in the northern part of the inlet suspension transport dominates over bedload transport in driving the sand-wave migration. The relative importance of suspension transport also explains why the sand waves are smaller, more rounded, and more three-dimensional to the north. The sand waves in the ebb-dominated part of the inlet feature the largest seasonal variability in height and migration speed. This seasonal variability may be attributed to the tides or a seasonal fluctuation in fall velocity. In both cases sediment transport is enhanced in winter, increasing sand-wave migration and decreasing sand-wave height. The influence of storms and estuarine circulation on the sand-wave variability is not important.[1]

---

[1] This chapter is based on a manuscript submitted to Cont. Shelf Res.

6.1   Introduction

This chapter builds upon the work presented in Chapter 5. In Chapter 5, long-term records of water depths measured with a ferry-mounted ADCP were used to quantify the characteristics of migrating sand waves. In this chapter, currents measured with the same ferry-mounted ADCP are applied to better understand the spatial and temporal variability in sand-wave height and migration. The ADCP-current measurements have been extensively discussed in Chapter 2.

Sand waves are rhythmic features that occur on sandy seabeds in estuaries and coastal shelf seas and have wave lengths up to several hundreds of metres and wave heights of several metres. Theoretical linear stability analyses (e.g. Hulscher, 1996; Gerkema, 2000) have shown that in tidal environments, sand waves form due to the rectification of oscillatory tidal currents over a flat bed with small perturbations. At both sides of the crests of these small perturbations, residual circulation cells cause flow convergence over the crests. This results in sand transport towards the crests, forming and maintaining the sand-wave shapes. Moreover, theoretical studies show that sand-wave migration is governed by residual currents superimposed on the M_2 constituent (Nemeth et al., 2002) or by tidal asymmetry between the M_2 and M_4 constituents (Besio et al., 2004).

It is generally assumed that the formation and migration of sand waves is largely governed by bedload transport, in particular in medium to coarse sand (Van den Berg, 1987). Consequently, the shape and migration direction of these bedforms may provide insight in bedload-transport pathways (e.g. McCave, 1971; Lobo et al., 2000; Elias et al., 2006). Suspended load becomes more important when finer sands are present. Currents may erode sand from the stoss sides and deposit it in the troughs, contributing to the migration of the sand waves. Near the tip of the sand wave where there is an area of turbulent flow separation, sand may also be suspended instead of avalanching down the lee slope (i.e. the steeper slope). Strong suspension transport may lead to the disintegration of sand waves because the suspended load can settle out at random locations. McCave (1971) observed that in northward direction the sand-wave height along the Dutch coast in the North Sea decreased and that megaripples disappeared. He attributed this to a decrease in sediment size and, as a consequence, an increase in suspension transport. Studies by Rubin and McCulloch (1980), Flemming (2000), Bartholdy et al. (2002) and Ernstsen et al. (2005) also indicate that there is a grain-size control on sand-wave height.

To date there have been few studies that report on seasonal changes in shape and migration of sand waves in tidal environments. In general, the majority of the surveys is only performed once or annually, missing any seasonal change. Seasonal changes in sand-wave height were observed by Terwindt (1971), Ludwick (1972), and Langhorne (1982). They attributed the reduction and increase in height to the occurrence of storms featuring high orbital velocities and calm weather, respectively. Moreover, Langhorne (1982) observed sand-wave height reduction and an increase in migration speed during spring tides and vice versa during neap tides. In the past it has been difficult to observe any sand-wave migration or seasonal variability in migration due to the relatively large error in horizontal positioning of the observation platform (ship) compared to the migration velocity (e.g. Terwindt, 1971). Ludwick (1972) observed mean migration speeds ranging from 35 to 150 m y^{-1} in Chesapeake Bay. Although this data set clearly shows significant variability

within the 17 month surveying period, Ludwick (1972) did not relate this variability to the hydrodynamics. Duffy and Hughes-Clarke (2005) obtained six repeat multibeam surveys with a 30-day interval of a sand-wave field near a headland and determined monthly sand-wave migration vectors using a spatial cross-correlation technique. They did not report on temporal variability in sand-wave migration.

It is only recently that ferry-ADCP observations obtained between 1998 and 2005 as presented in Chapter 5 have allowed for the detection of seasonal sand-wave variability in shape and migration in the Marsdiep inlet. In Chapter 5 it was shown that digital terrain models (DTMs) can be constructed using water depths measured with the ADCP mounted under the ferry 'Schulpengat'. The DTMs show that the Marsdiep inlet is covered with sand waves with heights of 1-7 m and wave lengths of 100-250 m. The sand waves are asymmetric with their steepest (lee) slopes facing in the flood direction. In agreement with their asymmetry, the sand waves also migrate in the flood direction with speeds of 0-90 m y^{-1}. The height and migration speed of the sand waves to the north show a distinct seasonal cycle, featuring the highest (lowest) migration speeds in winter (summer) and the highest (lowest) heights in fall (spring).

The present chapter has two objectives. The first objective is to determine the mechanisms that govern the sand-wave migration. Therefore, 'measured' bedload transport was calculated based on sand-wave dimensions and migration rates and compared with 'predicted' bedload transport based on the current data obtained with the ferry-mounted ADCP. The second objective is to get insight in the seasonal variability in sand-wave height and migration. The seasonal variability was correlated with the occurrence of storms, estuarine circulation, tides, and fall velocity.

Following the section about the study area, equations are presented for the measured and predicted bedload transport. In the Data and methodology section, the DTM technique is briefly explained, the ADCP, temperature, salinity, wind, and sediment data are presented, and the application of this data in the bedload equations is discussed. In the Results and discussion section, measured and predicted bedload transport are compared and the mechanisms that govern the seasonal variability are investigated. The main findings are summarised in the Conclusions section.

6.2   Study area

The study area encompasses the inlet of the Marsdiep tidal basin (52.985° N and 4.785° W), located in the western Dutch Wadden Sea (Fig. 6.1). The tidal basin consists of deep tidal channels flanked by shallow sand and mud flats. The Marsdiep inlet bifurcates in the main Texelstroom channel and the secondary Malzwin channel. The branches of the Texelstroom channel are connected to branches of the Vliestroom channel, which is one of the major channels in the adjacent Vlie tidal basin. The inlet is bordered by the island Texel to the north and the town of Den Helder to the south and is about 4 km wide at the location where the ferry crosses. At the ferry transect, the northern half of the inlet is deeper than 20 m, while the southern half is shallower.

In Chapter 2 a discussion was presented about the tides in the Marsdiep inlet. The inlet is considered well-mixed and tides constitute up to 81% of the total variance of
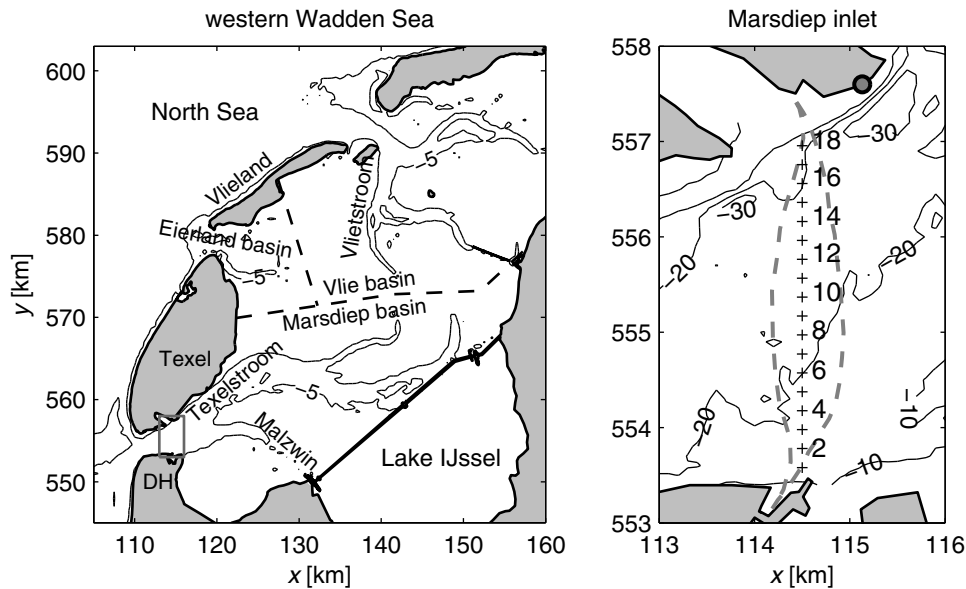
Figure 6.1. The western Wadden Sea and the Marsdiep tidal inlet in the Netherlands. In the left panel, the town of Den Helder is indicated by DH. The thick dashed lines indicate the approximate locations of the watersheds. The tidal channels are marked by the isobath of -5 m (relative to mean sea level). The box with the grey lines in the left panel marks the axes of the right panel. In the right panel, the locations of the 18 grid points or 'stations' are indicated by the crosses and the envelope of ferry crossings by the thick grey dashed line. The bathymetry is contoured in intervals of 10 m. The location of the NIOZ jetty on Texel is indicated by the grey circle.

the water levels and 98% of the currents. The semi-diurnal tidal constituent M_2 is the most dominant in the vertical and horizontal tides, significantly modulated by the second largest S_2 constituent. Water levels feature amplitudes between 1 and 2 m and near-surface streamwise currents between 1 and 2 m s^{-1} for neap and spring tides, respectively. Currents are flood dominated in the southern half and ebb dominated in the northern half of the inlet. The subtidal water transport through the inlet is primarily governed by tidal stresses and wind (Ridderinkhof, 1988a; Chapter 4). Tidal stresses maintain a steady flow from the Vlie to the Marsdiep basin, whereas southwesterly winds reduce or reverse and northwesterly winds enhance this subtidal flow.

Sha (1990) performed grain-size analyses of surface grab samples and box cores and found that near the ferry transect the seafloor is covered with medium sands larger than 300 μm. Moreover, Sha (1989a) determined the thickness of the holocene layer of the Marsdiep inlet and ebb-tidal delta based on boreholes and seismic records. Although his contour plots of the thickness do not extend eastward beyond the ferry transect, it is inferred that at this location the holocene layer is at least 2 m thick near Den Helder and 20 m thick near Texel. Consequently, it is concluded that there is an abundance of sand available for transport and the formation of bedforms.

6.3 Equations

In this chapter, 'measured' bedload transport is compared with 'predicted' bedload transport. Measured bedload is inferred from sand-wave shape and migration speed. Predicted bedload transport is determined by applying the ADCP-current data to some well-known bedload transport predictors. In this section, relations for measured and predicted bedload transport and fall velocity are presented.

6.3.1 Measured bedload transport

It is generally assumed that, in environments where little sand is transported in suspension, the volumetric sediment transport rate or bedload transport can be estimated from the migration of the bedforms. The bedload transport (q_{w} [m^3 s^{-1} m^{-1}]) excluding pore-water reads (Van den Berg, 1987; Hoekstra et al., 2004):

$$\frac{q_{\mathrm{w}}}{(1-\eta)} = \frac{U_{\mathrm{w}}}{L}V_{\mathrm{w}} = \frac{U_{\mathrm{w}}}{L}\beta H L = \beta U_{\mathrm{w}} H, \tag{6.1}$$

where U_{w} is the absolute bedform migration rate, L the wave length, H the wave height, V_{w} the volume of sand in the sand wave per unit width, $\beta = V_{\mathrm{w}}/(HL)$ the shape factor, and η the porosity amounting to 0.4. For bedforms with a triangular shape $\beta = 0.5$. In reality values deviate from $\beta = 0.5$, and values that are smaller or larger have been reported. For example, in his bedload calculations, Van den Berg (1987) used $\beta = 0.6$. However, in environments where sands are finer, suspension transport may also contribute to the bedform migration, making Eq. (6.1) a poorer estimator (Hoekstra et al., 2004). In this chapter, as a first estimate, β is calculated based on sand-wave dimensions, ignoring the fact that suspension transport may also contribute to the migration.

6.3.2 Predicted bedload transport

Predictors by Meyer-Peter and Müller (1948) and Van Rijn (1984a) were applied to depth-averaged currents to estimate the magnitude and direction of the bedload transport. In these predictors, bedload transport q_{b} in [m^3 s^{-1} m^{-1}] is proportional to U^3, where U is the (depth-averaged) velocity. Besides, simple $q_{\mathrm{b}} = \alpha U^3$ and $q_{\mathrm{b}} = \alpha U^5$ relations were applied to both depth-averaged and near-bottom currents, where α is a constant that depends on e.g. grain size, grain and water density, kinematic viscosity, and bottom roughness. The αU^3 and αU^5 relations were only used to compare the directions of mean predicted transport. Therefore, α was set to 1 s^2 m^{-1} or 1 s^4 m^{-3}. In the αU^5 relation the peak velocities have more weight than in the αU^3 relation. For the Van Rijn and Meyer-Peter and Müller (MP&M) relations the approach followed by Ernstsen et al. (2005) was adopted. The non-dimensional bedload transport relations Φ_{b} are for MP&M:

$$\Phi_{\mathrm{b}} = 8(\theta' - \theta_{\mathrm{cr}})^{1.5}, \tag{6.2}$$

and Van Rijn:

$$\Phi_{\mathrm{b}} = 0.053 \frac{T^{2.1}}{D_*^{0.3}}, \qquad T < 3$$
$$\Phi_{\mathrm{b}} = 0.1 \frac{T^{1.5}}{D_*^{0.3}}, \qquad T \geq 3 \tag{6.3}$$

where θ' is the grain-related Shield's parameter, and θ_{cr} the value of θ' at the threshold of motion, $T = (\theta' - \theta_{\mathrm{cr}})/\theta_{\mathrm{cr}}$, and D_* the dimensionless grain size. The latter is represented by:

$$D_* = \left[\frac{(s-1)g}{\nu^2} \right]^{\frac{1}{3}} d_{50}, \tag{6.4}$$

where g is the gravitational acceleration, $s = \rho_{\mathrm{s}}/\rho$, ρ_{s} and ρ the densities of the sediment and water, ν the kinematic viscosity of water, and d_{50} the median grain diameter. A constant grain density of 2650 kg m^{-3} was used. The Shields parameter is defined as:

$$\theta' = \frac{u_*'^2}{g(s-1)d_{50}}, \tag{6.5}$$

where u_*' is the skin friction velocity for turbulent flow:

$$u_*' = \sqrt{g}\frac{U}{C'}, \tag{6.6}$$

where C' is the grain-related Chézy roughness coefficient, which is defined as:

$$C' = 18 \log \left(\frac{12h}{k_{\mathrm{s}}'} \right), \tag{6.7}$$

where h is the water depth and k_{s}' the grain roughness. Meyer-Peter and Müller (1948) used $k_{\mathrm{s}}' = d_{90}$, while Van Rijn (1984a) used $k_{\mathrm{s}}' = 3d_{90}$, where d_{90} is the grain size for which 90% is finer by mass. A larger k_{s}' increases u_*', which increases bedload transport. According to Soulsby (1997) the Shield's parameter for the threshold of motion is:

$$\theta_{\mathrm{cr}} = \frac{0.30}{1 + 1.2D_*} + 0.055[1 - e^{(-0.020D_*)}]. \tag{6.8}$$

The dimensionless bedload transport can be related to the volumetric bedload transport excluding pore-water q_{b}:
$$q_{\mathrm{b}} = \Phi_{\mathrm{b}}[g(s-1)d_{50}^3]^{0.5}. \tag{6.9}$$

Instantaneous transport vectors $q_{\mathrm{b}x}$ and $q_{\mathrm{b}y}$ were calculated according to:

$$(q_{\mathrm{b}x}, q_{\mathrm{b}y}) = (q_{\mathrm{b}}\frac{u}{U}, q_{\mathrm{b}}\frac{v}{U}), \tag{6.10}$$

where $U = \sqrt{u^2 + v^2}$, u and v are velocities along the x and y-axes, and x and y are positive in eastward and northward directions, respectively.

6.3.3 Fall velocity

The fall velocity (w_s) was used to indicate the level of suspension in the stability diagram (Fig. 6.4) and to investigate the mechanisms behind the seasonal variability in sand-wave height and migration velocity (Fig. 6.9 and Fig. 6.10). The fall velocity for natural sand reads (Soulsby, 1997):

$$w_\mathrm{s} = \frac{\nu}{d_{50}} \left(\sqrt{10.36^2 + 1.049 D_*^3} - 10.36 \right). \tag{6.11}$$

6.4 Data and methodology

6.4.1 Ferry ADCP data

Current data

For this analysis, ADCP velocity data from April 2, 1999 to December 25, 2002 were used. The methodology to analyse the current data was presented in Chapter 2 and is only cursorily described here. The ADCP was mounted under the ferry Schulpengat at 4.3 m below the water surface and it recorded eastward velocities u, northward velocities v, and upward velocities w in bins of 0.5 m. In addition to velocities, the ADCP measured water depths along each beam. The velocity data were corrected for ferry speed and heading using the differential global positioning system (DGPS) and gyro aboard the ferry. The velocity data were gridded in 18 'stations' with a spacing of about 200 m (Fig. 6.1) and 40 vertical bottom-following σ-coordinates. Although the ferry measurements commenced in early 1998, the data collected in 1998 and early 1999 were not used because the time series contains many gaps and outliers. The velocity data after 2002 were collected with an ADCP with bottom-track correction. These data are still subject to analysis.

The current data set features 8-h gaps at night and gaps of several days to weeks due to poor quality data or ferry maintenance. To create a continuous data series, the gaps were filled with a harmonic fit similar to Chapter 4. This was done for both depth-averaged and near-bottom currents. The near-bottom currents were determined by averaging over the first three σ-cells with data closest to the bottom, on average between 2 and 2.4 m above the bottom. Following Chapter 2, a harmonic least-squares analysis was used to obtain a harmonic fit. First, 47 tidal constituents were selected that yielded the largest amplitude. A loop was run over the data from 1999 to 2002 for time steps of 14 months. The 14-month time step was chosen to obtain the best possible fit of the data. All data within this 14-month period were selected and the linear trend was removed. A harmonic analysis was performed for the de-trended u and v currents. The amplitudes, phases, the tidal-mean current A_0, and the linear trend were used to construct the harmonic fit on a 30-min grid. The average of the mean currents at both sides of each gap was added to the harmonic fit in the gap. Depending on the length of the gap, mean currents were calculated over at least a tidal period at both sides of the gap. Finally, the filled-in time series were gridded on a 30-min time grid. In the remainder of this chapter this data set is referred to as 'data set I'.

At each station, mean predicted bedload transport was calculated for the period from early 1999 to the end of 2002 and for periods of a week to several months. The mean

bedload transport for each period was calculated with the trapezium rule and by averaging over the duration of the period. For the bedload transport predictors, a mean water depth per station was used instead of a combination of measured data and a harmonic fit. A sensitivity analysis showed that the water depth had a minor influence on the mean predicted bedload transport.

Digital terrain models

In this study DTMs were used based on data collected within a 30-day window and a seven-day window. The process to create the first type of DTM was extensively described in Chapter 5. The general process is briefly listed here. First, the median value was taken of the water depths measured along the three beams of the ADCP. All depths were corrected for offsets and tides. Horizontal GPS positions were corrected for offsets and were rounded to the nearest grid points on a 15×15 m^2 grid. Then, median depths were calculated for each grid point for all depths collected in a 30-day window. The 30-day window was advanced by 5 days and a new DTM was created. In a next step, for each DTM, wave height H, wave length L, asymmetry A, and shape factor β were calculated for each sand wave with a length larger than 60 m along the lines $y = $ constant and $x = $ constant. H, L, and A are defined in Chapter 5. A varies between -1 and 1. Values of H, L, A, and β were mapped to the location of the crest of each sand wave along x and y. In Chapter 5, DTMs were created for the period from early 1998 to early 2005. In this chapter, the DTM technique was applied to include all depth data from 1998 to the end of 2005.

Sand-wave migration vectors (u_{w},v_{w}) were calculated in Chapter 5 with a cross-correlation technique for 90-day intervals from 1998 to early 2005. In this chapter, the cross-correlation technique was applied to 15-m DTMs and time intervals of about 73 days (± 25 days) to better study the seasonal variability. Moreover, the cross-correlation technique was applied to the end of 2005.

Around each station, rectangular polygons were designed with lengths of about 400 m along the x-axis and about 200 m along the y-axis. For each 73-day interval and each polygon, area-mean $\{H\}$, $\{L\}$, $\{A\}$, and $\{\beta\}$ were calculated, where $\{\}$ denotes area averaging or both area and time averaging. Variables that are only averaged over time are capsulated by $\langle\rangle$. Eq. (6.1) was then used to calculate measured bedload transport per interval. For comparison with predicted bedload transport, measured bedload transport per station was also integrated over the period 1999-2002 and averaged.

The second type of DTM was used to study in detail the effects of short-term events, such as storms, on the sand waves. These DTMs were created for a time window of seven days and the window was advanced by seven days to prevent overlap. In contrast to the 30-day window, the amount of depth data in the seven-day window is too small to get a bottom coverage without too many data gaps. Instead of rounding the available data to the nearest grid points, all depth data within the seven-day time window were linearly interpolated on a 10×10 m^2 grid.

6.4.2 Temperature, salinity, and wind data

The MP&M and Van Rijn predictors and fall velocity require water density and kinematic viscosity. The kinematic viscosity is mainly a function of temperature and to a lesser extent of salinity. The curve of the kinematic viscosity for 35 psu presented in Soulsby (1997) was tabulated and viscosity as function of temperature was calculated by interpolation. The daily temperature and salinity measurements were obtained for the period 1998-2004 from the NIOZ jetty located on the north side of the inlet (Fig. 6.1). It is assumed that they are representative of the entire cross-section. Water density was calculated by inserting salinity and temperature into the equation of state (Millero and Poisson, 1981). All parameters were linearly interpolated on the time grid of the current data. The daily maximum density difference $\Delta\rho$ at the NIOZ jetty was calculated to investigate the influence of estuarine circulation on the sand-wave variability. $\Delta\rho$ is a measure for the longitudinal density gradient and correlates well with estuarine circulation. In the Marsdiep inlet, the water temperature fluctuates between 3°C in winter and 20°C in summer. This yields a kinematic viscosity of 1.6×10^{-6} m^2 s^{-1} and 1.1×10^{-6} m^2 s^{-1} and a fall velocity of 0.04 m s^{-1} and 0.05 m s^{-1}, respectively. The salinity ranges between 16 psu and 33 psu and the water density between 1013 kg m^{-3} and 1025 kg m^{-3}. The seasonal variability in water density and viscosity has a negligible influence on the predicted bedload transport.

Hourly measurements of wind speeds and directions at the Den Helder airport 'De Kooy', located 5 km to the south of the Den Helder ferry harbour, were obtained from the Royal Netherlands Meteorological Institute and they were used to study the influence of storms on the sand waves. Following Large and Pond (1981), hourly wind stresses were calculated along the x and y-axes. These stresses were rotated to the s-axis, which is aligned with the main axis of the Texelstroom channel (40° counterclockwise from the x-axis), yielding the along-channel wind stress τ_s.

6.4.3 Sediment data

A total of 38 sediment samples were obtained across the inlet with a Van Veen grabber on crests and in troughs of sand waves on October 28, 2004. Samples were taken in nine groups numbered A to I (Table 6.1), resulting in up to three samples on crests and three samples in troughs of the same sand wave per group. The approximate locations of the groups can be inferred from Fig. 6.1 in combination with Table 6.1. The samples were split into two fractions. One fraction was treated with hydrochloric acid to remove all shell material. For both fractions, grain-size distributions were determined for grains smaller than 2 mm with laser diffraction, using a Coulter LS230. The differences in grain-size distributions between the treated and untreated fractions are small. The group-mean grain sizes d_{10}, d_{50}, and d_{90}, the sorting d_{90}/d_{10}, and the percentage of shells for both crests and troughs of the treated fractions are listed in Table 6.1. Sediments are well-sorted (single peak in size distribution) if $d_{90}/d_{10} < 2$ and well-mixed (multiple peaks in size distribution) if $d_{90}/d_{10} > 35$ (Soulsby, 1997). The d_{10}, d_{50}, and d_{90} grain sizes were linearly interpolated on the station locations. No samples were collected to the south of station 2 and to the north of station 16. Therefore, the mean was used over groups A-C

Table 6.1. Group-mean sediment characteristics.

group		A	B	C	D	E	F	G	H	I
y location [km] near station		553.8 2	554.4 5	554.8 7	555.1 9	555.3 10	555.6 11	555.9 13	556.2 14	556.6 16
number of samples	crest	1	5	2	2	2	3	2	2	1
	trough	2	3	2	2	2	3	2	2	0
d_{10} [μm]	crest	120	370	271	293	285	261	265	249	247
	trough	256	206	270	224	236	257	229	228	-
d_{50} [μm]	crest	365	652	545	598	648	410	390	413	361
	trough	510	405	470	352	356	391	346	340	-
d_{90} [μm]	crest	995	1211	1246	1247	1494	739	580	903	512
	trough	1109	745	1133	690	715	598	495	487	-
d_{90}/d_{10}	crest	8.3	3.3	4.6	4.2	5.2	2.8	2.2	3.6	2.1
	trough	4.3	3.6	4.2	3.1	3.0	2.3	2.2	2.1	-
shells [% weight]	crest	8	17	13	15	22	11	2	9	1
	trough	8	4	14	7	7	2	2	2	-

for station 1 and over groups G-I for stations 17 and 18.

6.5   Results and discussion

6.5.1   Currents, sand-wave characteristics, and sediment

Fig. 6.2 shows maximum flood and ebb currents during the spring tide of May 6, 2000, the depth-averaged tidal mean currents (A_0) for the year 2000 determined with a least-squares harmonic analysis, the DTM of March 19, 2001 with the mean water depth removed, and the M_2 tidal ellipses for depth-averaged currents. During flood the inflow is more uniform across the inlet, whereas during ebb the outflow is more concentrated in the deeper channel to the north. This inequality causes tidal-mean currents in the flood direction in the southern half and in the ebb direction in the northern half. The main axes of the M_2 ellipses of the depth-averaged currents gradually rotate counterclockwise from south to north and become more parallel in the main channel.

Parameters $\{H\}$, $\{L\}$, $\{A\}$, and $\{\beta\}$ along x, y, and the crest normal were computed for each station for the period 1999-2002 and are presented in Fig. 6.3. Fig. 6.3 also shows the DTM of March 19, 2001 with the mean water depth removed. The largest sand waves with area-mean heights of about 4 m and wave lengths of about 250 m occur to the north of station 3 and to the south of station 10. These sand waves are also most asymmetric with lee slopes facing in the flood direction. The steepest lee slopes are about 30°, which is the angle of repose of sand under water. The crests are oriented from south to north. To the north of station 7 the sand-wave crests have a general orientation from southeast to northwest. To the north of station 10 the sand waves become gradually smaller and
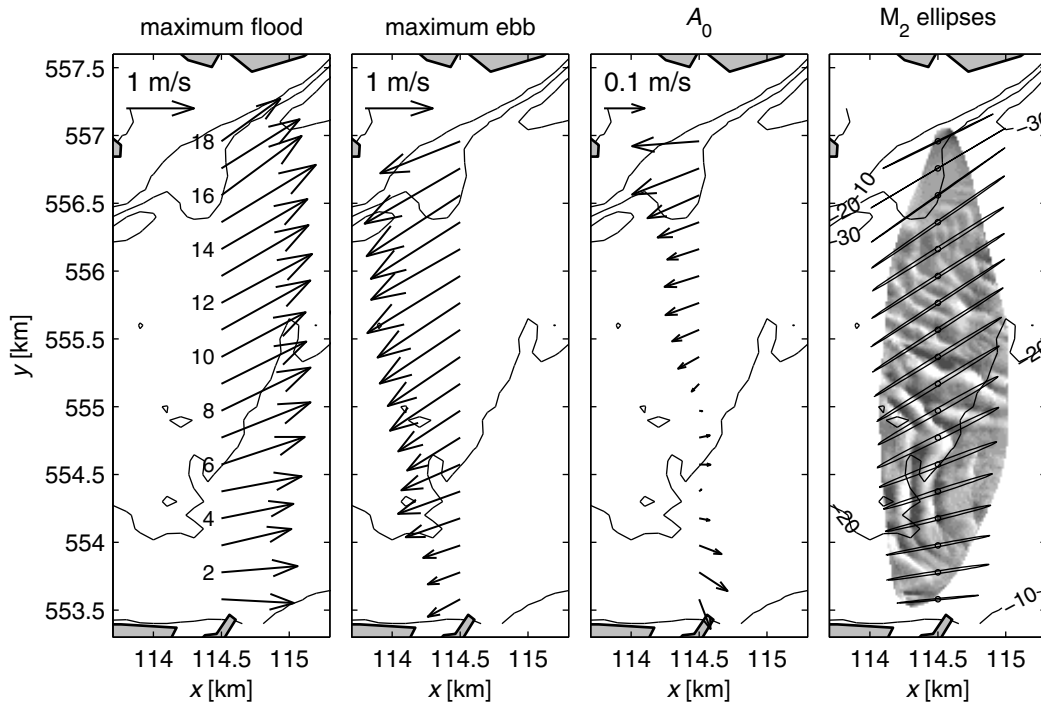
Figure 6.2. Left and second panel: measured depth-averaged maximum spring flood and ebb currents on May 6, 2000. Numbers refer to the stations. Third panel: tidal-mean currents determined with a harmonic analysis for the year 2000. Right panel: M_2 tidal ellipses for depth-mean currents. One m s^{-1} is equal to 500 m on the map. The background is a DTM of the sand waves showing the variance around the mean depth (median date is March 19, 2001). Dark (light) shades of grey indicate troughs (crests).

beyond station 16 they are difficult to detect with the ferry-mounted ADCP. The steepest lee slopes of these sand waves range between 5° and 20°. The progressive sand waves to the south are more linear in plan view, whereas the sand waves to the north are more symmetrical, more three-dimensional, and have branches and endpoints.

Table 6.1 indicates that the seafloor in the inlet is covered with sand of medium grain size (Soulsby, 1997) that decreases in size in northward direction. With the exception of group A, the sediment on the crests is coarser than in the troughs. For groups B to H, the d_{50} in the troughs varies between 470 μm in the south to 340 μm in the north, whereas the d_{50} on the crest varies between 652 μm in the south to 390 μm in the north. From group F northwards, where the sand waves are smaller, differences in d_{50} between crests and troughs are small, averaging 45 μm, while southwards, where the sand waves are larger, the mean difference is 215 μm. Generally, the sediment samples in the troughs are well-sorted, whereas they are more mixed on the crests. To the south of group F, the samples have a higher shell content, with the largest content on the crests (up to 22% in group E). The observations that the crests feature coarser sand than the troughs are identical to observations in the North Sea by Terwindt (1971) and Van Dijk and Kleinhans (2005). ADCP observations (not presented here) show that the peak current velocities are highest on the crests, and apparently they wash out all finer sediment. Therefore, the
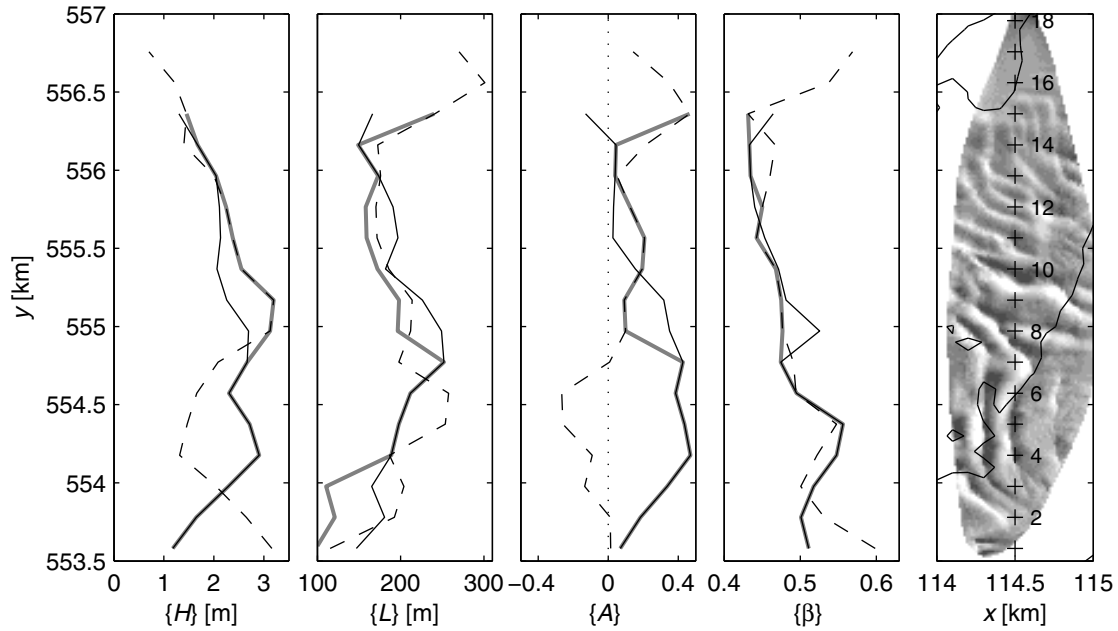
Figure 6.3. Mean sand-wave characteristics $\{H\}$, $\{L\}$, $\{A\}$, and $\{\beta\}$ for period 1999-2002 at stations 1-18 and a DTM showing the variance around the mean depth. Values along the x (y) axis are indicated by a thin black solid (dashed) line and along the crest normal by a thick grey line. Crosses and numbers in right panel refer to stations.

sand samples in the troughs may be more representative for sediment transport and they were used in the transport calculations.

6.5.2   Stability diagram

In order to better compare the sand waves in the Marsdiep inlet with observations in literature, the stability diagram of Van den Berg and Van Gelder (1993) was adopted and Eqs. (6.5)-(6.7) and $k'_s = 3D_{90}$ were used to calculate θ'. Combinations of D_* and θ' were calculated for peak flood velocities (dark grey dots) and peak ebb velocities (light grey dots) at each station and they are plotted in Fig. 6.4. Mean values at each station are indicated by the circles with numbers. Due to the dependency of D_* on ν, D_* is smaller in winter than in summer and the horizontal spread of D_* at each station is about 2.

The relative importance of sand in suspension is indicated in the diagram with lines of constant $w_s = 0.75u'_*$, $1.0u'_*$, $1.25u'_*$, and $2.5u'_*$. According to Dyer (1986), suspension occurs when the upward turbulent component of velocity, which is related to u'_*, exceeds the fall velocity for grains, i.e. when $w_s = 1.25u'_*$. However, on the basis of laboratory experiments, Van Rijn (1984b) found that the onset of suspension is $w_s = 2.5u'_*$. Van Rijn (1984b) argued that Rouse concentration profiles begin to develop when $w_s \approx u'_*$. The approach by Van Rijn (1984b) was adopted.

All sand waves in the Marsdiep inlet fall in the dunes regime, similar to the sand waves observed by Bartholdy et al. (2002) in the Danish Wadden Sea. The sand-waves are clustered in two groups encompassing stations 1-8 and stations 9-18 in Fig. 6.4. The location
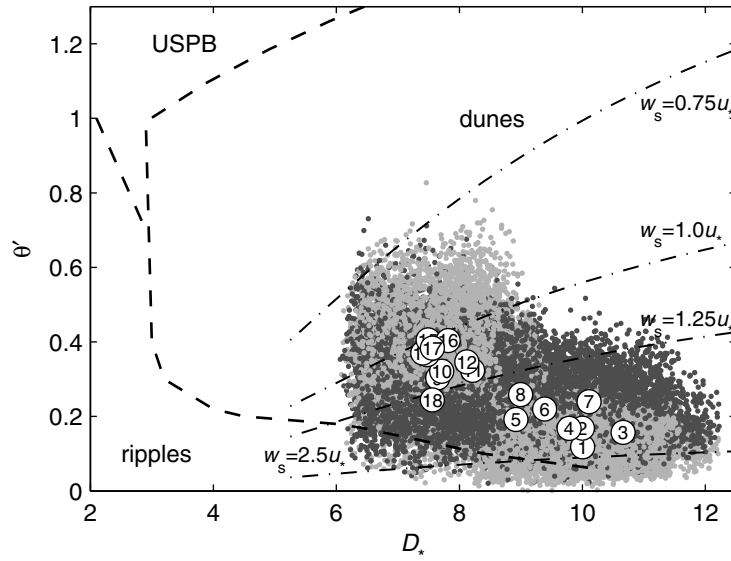
Figure 6.4. Stability diagram after Van den Berg and Van Gelder (1993). Mean θ' per station over all measured depth-averaged maximum flood and ebb velocities are indicated by encircled numbers. Dark (light) grey dots reflect θ' values during maximum flood (ebb). Number 4 overlaps 2, 10 overlaps 9, 12 overlaps 11, and 17 overlaps 13, 14, 15, and 16. Upper stage plane bed is abbreviated with USPB.

of stations 9-18 in Fig. 6.4 is higher than and to the left of stations 1-8 due to the finer sand and higher current velocities. This indicates that suspension transport is relatively more important at stations 9-18. The occurrence of larger and more asymmetrical sand waves with avalanche slopes at stations 1-8 suggests that bedload transport is relatively important here. At stations 9-18, the sand waves are smaller, have rounded crests, have lee slopes $< 20°$, and are more three-dimensional. These characteristics can be attributed to strong suspension transport. Flemming (2000) argued that sand waves cease to grow once $w_s = u'_*$ and that this criterion is reached earlier in finer sand. Bartholdy et al. (2002) observed that when $w_s < u'_*$ large progressive sand waves started to disintegrate. Bartholdy et al. (2002) attributed this to a transition from bedload transport to suspended load transport. Furthermore, Bartholdy et al. (2002) speculated that fallout from suspension transport reduces the lee-slope angles of the sand waves. The observations presented in this chapter also agree with observations by e.g. McCave (1971) and Ernstsen et al. (2005).

6.5.3   Comparing measured and predicted bedload transport

Direction and magnitude

The directions and magnitudes of the mean measured and predicted bedload transport (see the Equations section for definitions) for 1999-2002 are compared in Fig. 6.5. In this figure, predicted bedload transport was calculated for the depth-averaged currents of data set I for the αU^3, αU^5, MP&M, and Van Rijn relations. The measured bedload transport is directed floodward into the inlet at stations 1-16. At station 18, measured
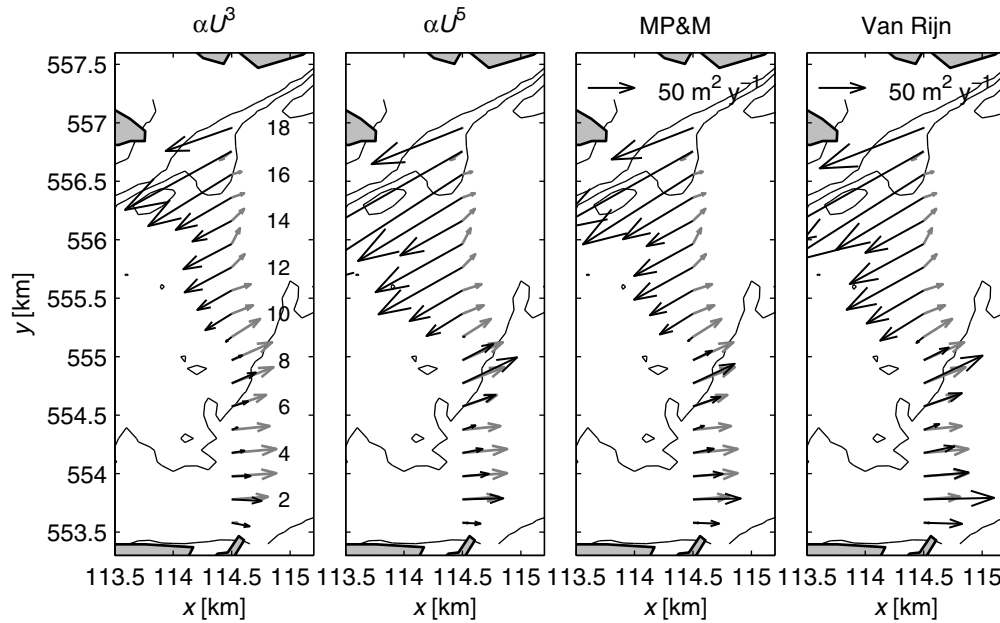
Figure 6.5. Comparison between mean measured (grey vectors) and mean predicted bedload transport based on depth-averaged currents (black vectors) for the period 1999-2002. The vectors representing measured bedload transport are identical in all panels.

bedload transport cannot be estimated because β and H cannot be determined well. At stations 1-8 the predicted bedload transport for αU^3, MP&M, and Van Rijn has the same direction as the measured transport, whereas at stations 9-16 the predicted bedload transport is ebbward, opposite to the measured transport. Only at station 17 do the small bedforms migrate ebbward, in agreement with the direction of the mean predicted bedload transport. The αU^5 relation yields larger transports than the αU^3 relation, but in general the directions remain the same. The transport direction calculated with the αU^5 relation only reverses to floodward at station 9. In the αU^5 relation, the peak flood velocities at station 9 have relatively more weight than the peak ebb velocities. Similar to Ernstsen et al. (2005), the Van Rijn predictor results in larger mean transports than MP&M. The application of near-bottom currents to the αU^3 and αU^5 relations does not reverse the direction of the predicted bedload transport at stations 9-16. These results are not presented here.

Fig. 6.6 shows the magnitudes of the mean measured and predicted transport for 1999-2002 along the streamwise s-axis at each station. The s-axis, also called the major or main axis, is defined as the axis along which the depth averaged velocities feature the largest variance. The left panel shows the mean flood, ebb, and total predicted bedload transport calculated with MP&M and the depth-averaged currents of data set I. The more uniform inflow during flood and the more asymmetric outflow during ebb in Fig. 6.2 are reflected in the mean flood and ebb transports. The stronger flood than ebb currents to the south result in floodward predicted bedload transport and vice versa to the north.

In the right panel of Fig. 6.6 the mean predicted transport calculated with MP&M and Van Rijn is compared with the mean measured bedload transport for 1999-2002.
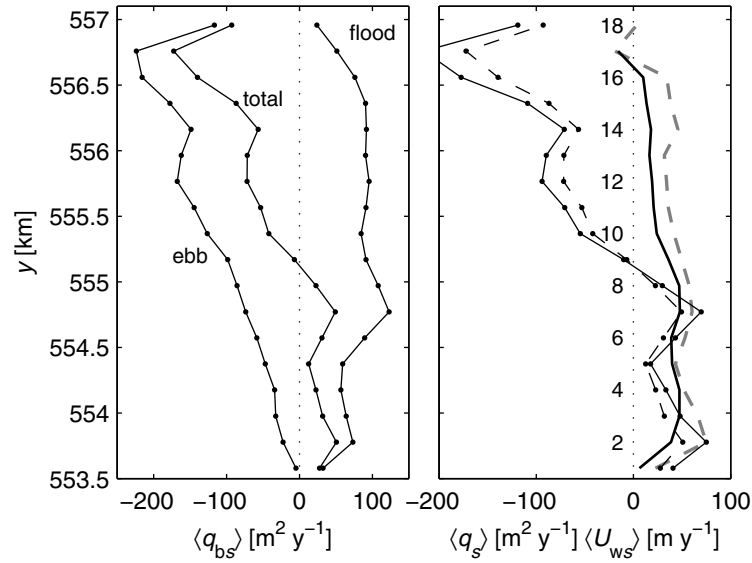
Figure 6.6. The left panel shows mean flood, ebb, and total predicted bedload transport for MP&M. The right panel shows mean predicted bedload for MP&M (thin black dash-dotted line) and Van Rijn (thin black dotted line), mean measured bedload transport (thick black line), and mean sand-wave migration velocity U_{ws} (thick grey dashed line). Numbers refer to stations. In both panels, mean bedload transport is calculated along the s-axis for the period 1999-2002 using depth-averaged currents.

The mean measured bedload transport is maximally 40-50 m^2 y^{-1} at stations 2-8 and decreases northward. To the south of station 9, the predicted bedload transport is of a similar direction and magnitude as the measured bedload transport. The measured bedload transport features two small peaks near station 4 and station 8. Interestingly, the same trend is also present in the predicted bedload transport, although the peaks are in different locations at stations 2 and 7. Remarkably, the trend in the mean predicted bedload transport has a better agreement with the mean sand-wave migration velocity $\langle U_{ws} \rangle$.

Measured and predicted bedload transport were integrated in the x direction along the y-axis using the depth-averaged currents of data set I for 1999-2002. The measured bedload transport for stations 1-8 is fairly constant and has a mean value of 63×10^3 m^3 y^{-1}. This compares reasonably well with the mean predicted transport of 46×10^3 m^3 y^{-1} (MP&M) and 67×10^3 m^3 y^{-1} (Van Rijn). To the north, the integrated measured transport at stations 9-17 is smaller, 26×10^3 m^3 y^{-1}, and greatly differs in magnitude and direction from the predicted transport of -118×10^3 m^3 y^{-1} (MP&M) and -150×10^3 m^3 y^{-1} (Van Rijn). The measured bedload transport at stations 1-17 amounts to 89×10^3 m^3 y^{-1}, whereas the predicted transport adds up to -72×10^3 m^3 y^{-1} (MP&M) and -83×10^3 m^3 y^{-1} (Van Rijn). This mismatch is due to the ebbward predicted transport at stations 9-16. The mean predicted transport integrated over all stations is about -89×10^3 m^3 y^{-1} (MP&M) and -105×10^3 m^3 y^{-1} (Van Rijn).
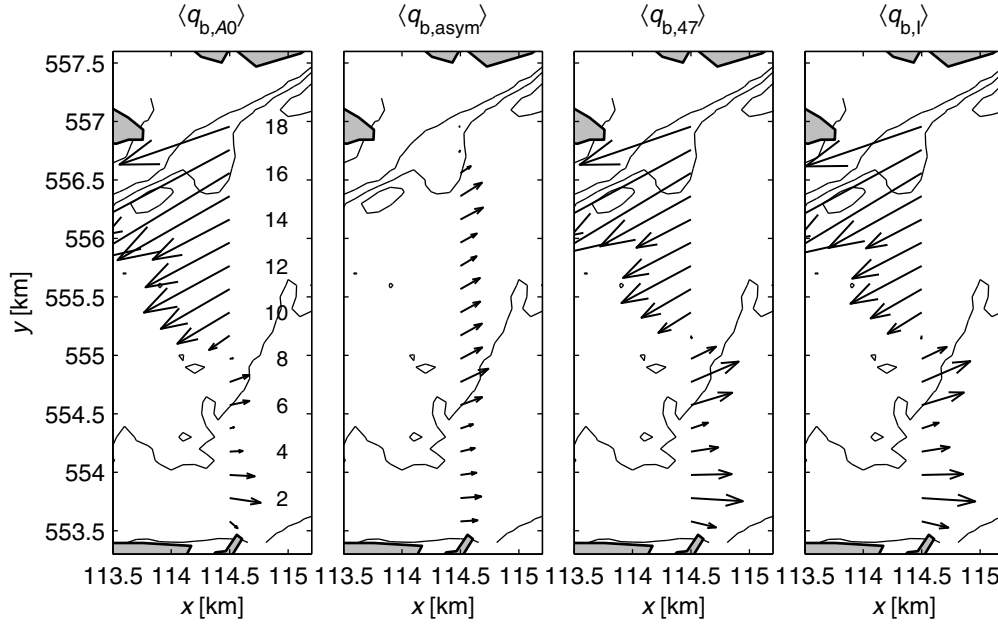
Figure 6.7. Mean predicted bedload transport $\langle q_{b,A_0} \rangle$, $\langle q_{b,\text{asym}} \rangle$, $\langle q_{b,47} \rangle$, and $\langle q_{b,\text{I}} \rangle$ based on depth-averaged currents for the period from April 1999 to April 2001. Numbers in left panel indicate stations.

Transport mechanisms

In this section, the tidal and non-tidal mechanisms that govern the mean predicted bedload transport are evaluated. It is assumed that tidal mechanisms, e.g. tidal-current asymmetries and mean currents, are represented by a harmonic fit of the current data, whereas non-tidal mechanisms, e.g. the effects of storms and density differences, are represented by the difference between the fit and the original data.

A least-squares harmonic analysis was applied to two years (April 1999-April 2001) of the depth-averaged currents of data set I to extract amplitudes and phases of the 47 most important tidal constituents and the tidal mean current A_0. The duration of exactly two years is to account for the annual fluctuation in the predicted bedload transport. Two current time series were created: data set II based on A_0 and the amplitudes and phases of the 47 constituents and data set III based on only the amplitudes and phases of the oscillating components. Data sets II and III were inserted into the generalised bedload predictor $q_b = \alpha U^3$, and mean predicted bedload transport $\langle q_{b,47} \rangle$ and $\langle q_{b,\text{asym}} \rangle$ were obtained after integrating and averaging over the two-year period. The mean predicted transport due to the interaction of A_0 with the tidal constituents, $\langle q_{b,A_0} \rangle$, was calculated by subtracting $\langle q_{b,\text{asym}} \rangle$ from $\langle q_{b,47} \rangle$. The mean transport based on data set I $\langle q_{b,\text{I}} \rangle$, which includes both tidal and non-tidal mechanisms, was also calculated. Transports $\langle q_{b,A_0} \rangle$, $\langle q_{b,\text{asym}} \rangle$, $\langle q_{b,47} \rangle$, and $\langle q_{b,\text{I}} \rangle$ are compared in Fig. 6.7. Table 6.2 presents the relative contributions of the mean predicted bedload transport for various transport components in the x direction for stations 1-8 and stations 9-18.

Several tidal asymmetries contribute to $\langle q_{b,\text{asym}} \rangle$. A characteristic of 'asymmetric' currents is that their contribution to the mean current is zero, while their contribution to the

Table 6.2. Relative transports in x direction at stations 1-8 and 9-18.

			transport at stations [%]	
			1-8	9-18
$\langle q_{b,47} \rangle$		relative to $\langle q_{b,I} \rangle$	97.8	96.8
$\langle q_{b,A_0} \rangle$		relative to $\langle q_{b,47} \rangle$	44.9	118.4
$\langle q_{b,\text{asym}} \rangle$			55.1	-18.4
$\langle q_b \rangle$ due to	$A_0 M_2$	relative to $\langle q_{b,A_0} \rangle$	83.8	83.5
$\langle q_b \rangle$ due to	$M_2 M_4$	relative to $\langle q_{b,\text{asym}} \rangle$	43.8	-30.1
	$M_2 M_4 M_6$		17.1	62.0
	$M_2 S_2 MS_4$		4.8	-25.1
	$M_2 MS_4 2MS_6$		8.8	31.4
	$M_4 S_2 2MS_6$		3.8	14.9
	$M_4 2MS_2 S_2$		-5.3	-6.7
	$M_6 2MS_2 MS_4$		-1.3	-4.5
	$M_2 O_1 K_1$		4.4	8.9

mean bedload transport is not zero. The most important tidal asymmetry results from the interaction of M_2 with its overtides M_4 and M_6 (Van de Kreeke and Robaczewska, 1993). Moreover, Hoitink et al. (2003) illustrated that the interaction between the astronomic constituents M_2, O_1, and K_1 also causes a mean sediment transport. In the Marsdiep inlet, S_2 is the second largest astronomic constituent (Chapter 2). The interaction of M_2 and its overtides with S_2 and its compound tides also results in asymmetries that enhance long-term mean bedload transport. The relative contribution to $\langle q_{b,\text{asym}} \rangle$ of the most important asymmetries, in particular at stations 1-8, is presented in Table 6.2. In Appendix 6.A, formulations of the long-term mean bedload transport of these asymmetries are presented and it is shown that these asymmetries are identical in behaviour to the $M_2 O_1 K_1$ asymmetry discussed by Hoitink et al. (2003).

From Fig. 6.7 and Table 6.2 the following is inferred. The mean predicted bedload transport $\langle q_{b,47} \rangle$ is about 97% of $\langle q_{b,I} \rangle$. This indicates that bedload transport is primarily governed by the tides and that non-tidal currents have a secondary influence. At stations 1-8 $\langle q_{b,\text{asym}} \rangle$ dominates over $\langle q_{b,A_0} \rangle$ (55% versus 45%), whereas to the north at stations 9-18, the ebbward $\langle q_{b,47} \rangle$ is largely governed by $\langle q_{b,A_0} \rangle$. The transport due the interaction of A_0 with M_2 governs about 84% of $\langle q_{b,A_0} \rangle$ across the inlet. Fig. 6.7 shows that the transport due to $\langle q_{b,\text{asym}} \rangle$ at stations 1-16 is floodward and that it has the same magnitude. At stations 1-8, the asymmetries listed in Table 6.2 explain about 76% of $\langle q_{b,\text{asym}} \rangle$, whereas at stations 9-18 they explain about 51%. Apparently, many asymmetries not listed contribute to $\langle q_{b,\text{asym}} \rangle$ in the northern half of the inlet. Transport $\langle q_{b,\text{asym}} \rangle$ is primarily the result of the interaction of astronomic tides with compound and overtides. The only important asymmetry based on astronomic tides, $M_2 O_1 K_1$, explains 4% to 9% of $\langle q_{b,\text{asym}} \rangle$. The sum of contributions of the $M_2 M_4$ and $M_2 M_4 M_6$ asymmetries is 61% at stations 1-8 and 32% at stations 9-18. In the southern half of the inlet $M_2 M_4$ is more important than $M_2 M_4 M_6$ and vice versa in the northern half. The asymmetries related to S_2, of which $M_2 S_2 MS_4$

and $M_2MS_42MS_6$ are most important, contribute about 10% to $\langle q_{b,asym} \rangle$. In addition to a mean transport, asymmetries due to S_2 cause $q_b(t)$, where t is time, to fluctuate with the spring-neap cycle of 14.76 d. In a modelling approach, Van de Kreeke and Robaczewska (1993) found that the triple interaction $M_2S_2MS_4$ did not cause a long-term mean bedload transport. However, the calculations in this chapter show that these triple interactions can cause a long-term mean transport. Most presumably, the difference between the analytical model of Van de Kreeke and Robaczewska (1993) and calculations presented in this chapter lies in the various approximations that are needed to obtain an analytical solution in their model. While not listed in Table 6.2, similar asymmetries that result from the interaction of M_2 with N_2 still contribute about 5% to $\langle q_{b,asym} \rangle$.

Analysis

The predicted bedload transport only agrees in direction, magnitude, and trends with the measured bedload transport at stations 1-8. At stations 9-16, the predicted bedload transport is opposite to the sand-wave migration. In general, it is accepted that for subcritical flow, sand waves migrate in the direction of the mean transport. Since the flow is subcritical in the Marsdiep inlet ($Fr < 0.1$) one may expect this to occur, i.e. the sand waves are not anti-dunes. Two possible explanations for this apparent discrepancy are discussed below.

One explanation is that in the northern half of the inlet suspension transport dominates over bedload transport in governing sand-wave migration. The location of stations 9-18 in Fig. 6.4, the finer sand, the stronger currents, and the sand-wave shapes are indications that suspension transport is important here. While instantaneous Eulerian current velocities govern bedload transport, this is not the case for suspension transport. For suspension transport, mechanisms such as advection, scour lag, and settling lag are important (Dyer, 1986). These mechanisms can explain the floodward migration of the sand waves. Indeed, in Chapter 4 of Elias (2006) it is shown with a numerical model that the mean suspension transport for fine and medium sized sand is floodward in the Marsdiep inlet near stations 9-13 due to these mechanisms. Moreover, in the model of Elias (2006), suspension transports are an order of magnitude larger than the bedload transports. If suspension transport is the dominant mechanism, than it apparently governs the sand-wave migration, but it is not strong enough to completely disintegrate the sand waves.

A second possible explanation is estuarine circulation. The currents near the seabed are important for bedload transport. Unfortunately, they are not well resolved with the ADCP due to sidelobe interference. In the northern half of the inlet these near-bed currents may only govern the sand-wave migration when they are more floodward than the depth-averaged currents or the currents measured at ~ 2 m above the bed. Such a current profile can be due to estuarine circulation, which features floodward bottom and ebbward surface currents. To determine the magnitude of the estuarine circulation in the Marsdiep inlet, the de-tided vertical current shear ($\partial u / \partial z$) was correlated with the daily maximum density difference $\Delta \rho$, a proxy for the longitudinal density gradient (results not shown here). In particular in the deep channel to the north, $\partial u / \partial z$ correlates best with $\Delta \rho$ (coefficient of determination $r^2 = 43\%$): the larger $\Delta \rho$ the more negative
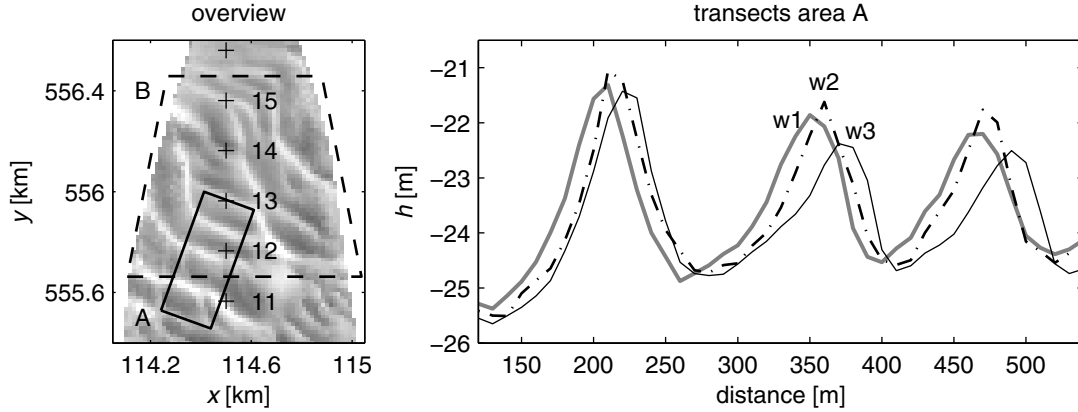
Figure 6.8. Left panel shows location of areas A (solid line) and B (dashed line). The background represents the DTM of September 29, 2002, with the mean water depth removed. Crosses mark the station locations. Right panel shows three sand-wave profiles with dates May 10, 2002 (w1), September 27, 2002 (w2), and March 29, 2003 (w3). The profiles represent the height along the long side of area A, averaged over the short side. The distance increases northward.

$\partial u/\partial z$. This suggests that estuarine circulation is important here. In order to get mean predicted bedload transport in the flood direction in the northern half, the near-bottom currents have to be at least 0.10 m s^{-1} more floodward than the depth-averaged or near-bed currents at $\sim$2 m above the bottom. However, a floodward increase of 0.10 m s^{-1} over 2 m does not seem realistic. Therefore, the dominance of suspension transport over bedload transport is a better explanation for the sand-wave migration in the northern half of the inlet.

6.5.4 Temporal variability

In Chapter 5 it was shown that the height and migration speed of the sand waves in the northern part of the Marsdiep inlet portray the largest seasonal variability. In this section, the influence of the tides - represented by the predicted bedload transport, surface wind stress τ_s, daily-mean density difference $\Delta\rho$, and fall velocity w_s on the variability is evaluated. The variability in wave height was analysed in area A and the variability in both height and migration speed was analysed in area B shown in Fig. 6.8.

In order to study the effects of short-term events, such as storms, on the sand-wave height in detail, DTMs were used that were created for time steps of seven days. A 200 m wide and 600 m long rectangular polygon (area A) was designed around three sand waves (Fig. 6.8) and sand-wave heights were calculated similarly to Chapter 5 for each seven-day time step along transects parallel to the long side of the polygon. The variability in the mean sand-wave height $\{H\}$ over all sand waves within area A per time step is shown in Fig. 6.9 for a three-year period. The mean surface wind stress $\langle\tau_s\rangle$, density difference $\langle\Delta\rho\rangle$, streamwise predicted bedload transport $\{q_{bs}\}$, and fall velocity $\langle w_s\rangle$ were calculated for the same time windows and time steps (Fig. 6.9). The mean bedload transport was calculated with MP&M and the depth-averaged currents of data
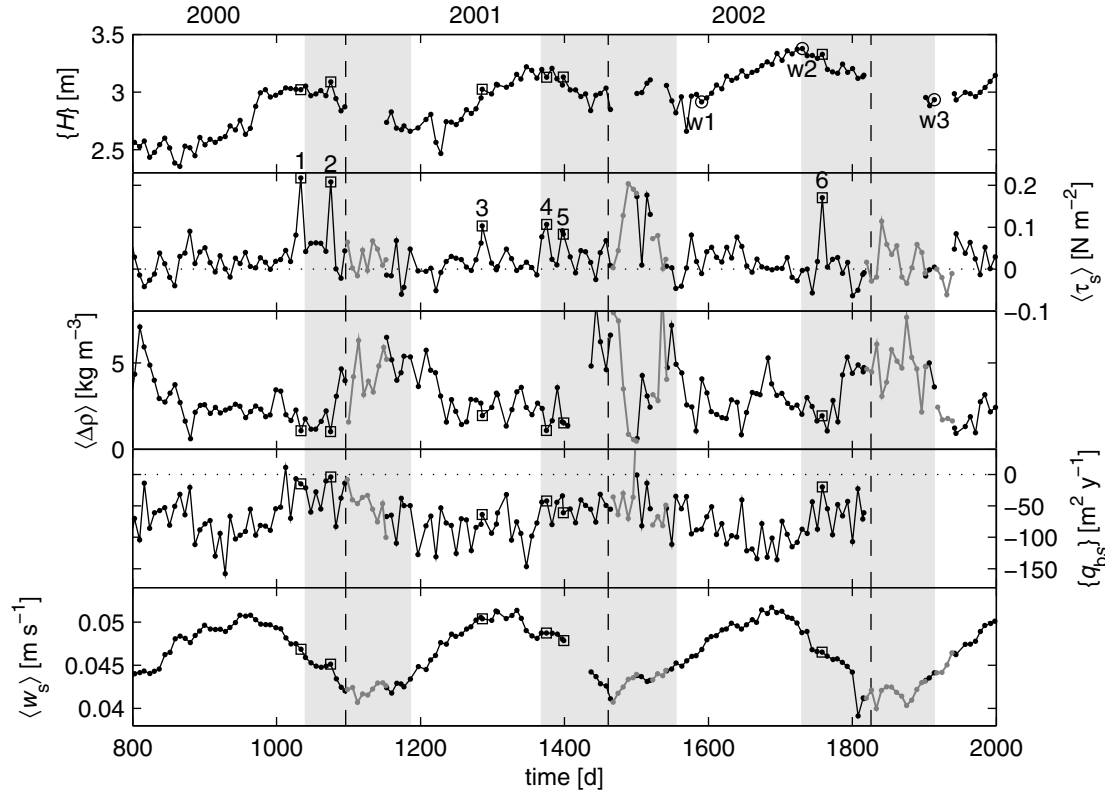
Figure 6.9. Time series of $\{H\}$ calculated for area A, $\langle\tau_s\rangle$, $\langle\Delta\rho\rangle$, $\{q_{bs}\}$ predicted with MP&M, and $\langle w_s\rangle$. Each dot represents the mean over seven days. The grey dotted lines coincide with periods for which no DTMs could be created. Open squares in all panels mark storms s1-s6 and open circles in top panel indicate dates of transects w1-w3 in Fig. 6.8. The light-grey boxes mark the decrease in $\{H\}$. The vertical black dashed lines indicate the beginning and end of the years printed above the top panel.

set I, and then by integrating and averaging over stations 11-13. The bedload transport was aligned with the main axis of the depth-averaged currents of stations 11-13.

Unfortunately, area A and the seven-day time steps are too small to calculate reliable migration velocities. Therefore, migration vectors were calculated with the cross-correlation technique for the larger area B for time steps of two to three months and DTMs were used based on the 30-day windows. Mean sand-wave height $\{H\}$, migration speed $\{U_{ws}\}$, measured bedload transport $\{q_{ws}\}$, wind stress $\langle\tau_s\rangle$, predicted bedload transport $\{q_{bs}\}$, and fall velocity $\langle w_s\rangle$ were calculated. They are plotted in Fig. 6.10. Sand-wave heights were determined along the crest normals. Migration speeds and measured and predicted bedload transports were calculated along the area-mean main axis of the depth-averaged currents.

Observations of sand-wave variability

The seasonal variability in $\{H\}$ is similar in areas A and B. The change is quite gradual and $\{H\}$ is about 0.5 m higher in fall than in spring. Transects w1-w3 in Fig. 6.8 reveal that in

the summer of 2002 (transect w2) the sand waves are higher than in spring (transects w1 and w3). In contrast to $\{H\}$, the area-mean water depth does not portray this seasonal variability (Chapter 5), suggesting that the amount of sand is conserved. Although not shown here, in the southern half of the inlet there is a similar, but smaller, seasonal variability in sand-wave height of about 0.10-0.30 m.

The seasonal variability in $\{U_{ws}\}$ and $\{q_{ws}\}$ is identical and most regular from the end of 2000. On average, the bedforms migrate about 40 m y^{-1} faster in winter than in summer in the northern half of the inlet. Generally, maximum values of $\{U_{ws}\}$ occur while $\{H\}$ is decreasing. It is assumed that this regular variability in $\{U_{ws}\}$ is also present before 2001. In this period, GPS and heading may be affected by inaccuracies and offsets that are difficult to correct for. While there is still a little variability in sand-wave height in the southern half of the inlet, no clear seasonal variability in migration speed can be detected.

Correlations

In this section, contributions to the variability in sand-wave height and migration speed are investigated. The wind stress is considered first. According to Terwindt (1971), Ludwick (1972), and Langhorne (1982) storm-driven currents and high orbital velocities may stir up sand from the sand-wave crests, leading to a reduction in height. Langhorne (1982) observed that after storms the sand wave was restored to its pre-storm condition within several days to weeks. Moreover, the storm-driven currents could enhance sediment transport, affecting sand-wave migration. Southwesterly along-channel winds are most prevailing in the Marsdiep inlet and they enhance floodward currents through the inlet (Chapter 4). In addition, it has been observed in the field that surface gravity waves up to 1-1.5 m with periods of several seconds are present in the 25 m deep channel in the northern half of the inlet during strong southwesterly storms. $\langle \tau_s \rangle$ was used as an indicator for the occurrence of strong currents and surface waves. Generally, most of the storms occur in periods when $\{H\}$ is decreasing. However, one would expect the impact of storms to be abrupt instead of gradual. In Fig. 6.9 the impact of a series of large storms s1-s6 is evaluated. $\{H\}$ is not affected due to the impact of storm s1. There is a lowering in height after storm s2, but it is not large. Although $\langle \tau_s \rangle$ is relatively low between 1080 and 1200 days the decrease in $\{H\}$ continues. Interestingly, while $\langle \tau_s \rangle$ is of a similar magnitude between 1550 and 1650 days, $\{H\}$ increases. The impact of smaller storms s3-s5 in 2001 on $\{H\}$ remains undetectable. Finally, the decrease in $\{H\}$ in the fall of 2002 started before and continues after the occurrence of storm s6. The influence of storms on $\{q_{bs}\}$ in Fig. 6.9 is also hardly noticeable. On the basis of this information it is inferred that storms do not cause the gradual change in sand-wave height. Similarly, it is argued that storms do not affect the variability in migration speed. $\langle \tau_s \rangle$ in Fig. 6.10 has peaks that roughly coincide with peaks in $\{U_{ws}\}$ in winters 1999-2000, 2000-2001, 2001-2002, and 2003-2004. This agreement with $\{U_{ws}\}$ yields the relatively high coefficient of determination of $r^2 = 37\%$. Although there is significant sand-wave variability in the winter of 2002-2003, there are very few storms. This suggests that the correlation is coincidental and that storms have little effect on the sand-wave migration.

As discussed previously, the daily maximum density difference $\Delta \rho$ is a proxy for es-
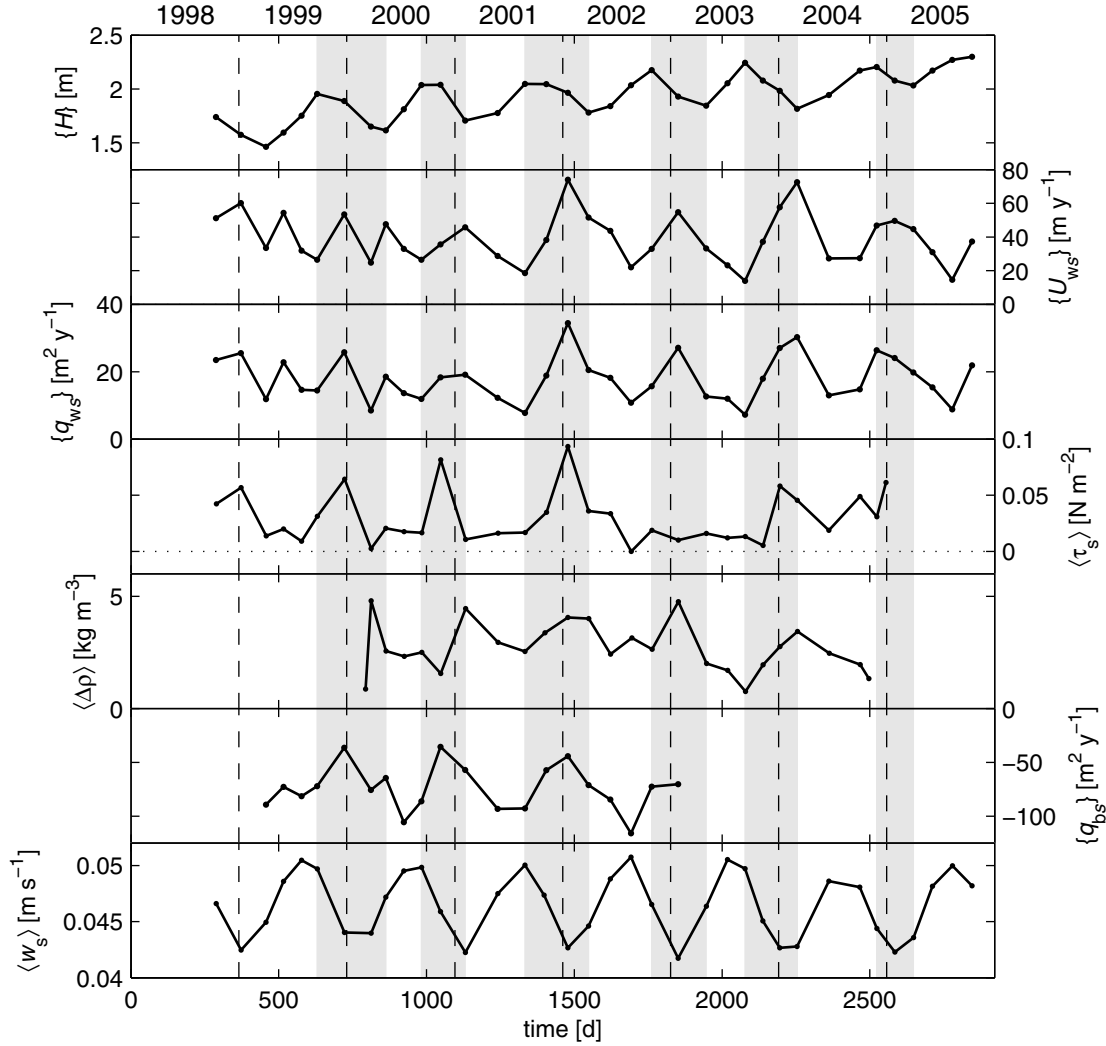
Figure 6.10. Time series of $\{H\}$, $\{U_{ws}\}$, $\{q_{ws}\}$, $\langle \tau_s \rangle$, $\langle \Delta \rho \rangle$, $\{q_{bs}\}$ predicted with MP&M, and $\langle w_s \rangle$. Values in all panels were averaged over two to three-month intervals, values in top three panels were averaged over area B, and $\{q_{bs}\}$ was averaged over stations 12-15.

tuarine circulation. The larger $\Delta \rho$, the more floodward the near-bottom currents. The stronger floodward bottom currents may enhance sediment transport, erode the sand waves and affect their migration. Similar to $\langle \tau_s \rangle$, $\langle \Delta \rho \rangle$ is also strongest in the periods that $\{H\}$ decreases in Fig. 6.9. However, the abrupt changes in $\langle \Delta \rho \rangle$ are not reflected in $\{H\}$, i.e. they are not linearly correlated. Moreover, in 2000, 2001, and in particular in 2002 the decrease in $\{H\}$ commenced earlier than the increase in $\langle \Delta \rho \rangle$. Furthermore, the increase in $\{H\}$ is not interrupted due to the increase in $\langle \Delta \rho \rangle$ in 2002 near 1670 days. In Fig. 6.10, the peaks in $\langle \Delta \rho \rangle$ also roughly coincide with $\{U_{ws}\}$, but its variability is more chaotic than the variability of $\{U_{ws}\}$. As a consequence, the coefficient of determination is low ($r^2 = 12\%$). Hence, it is concluded that estuarine circulation is not a likely cause of the sand-wave variability.

One candidate that may affect the gradual sand-wave variability is the tides. The

variability in $\{q_{bs}\}$ in Fig. 6.9 and Fig. 6.10 is largely due to the tides. As suggested in the previous section, bedload transport may not govern the sand-wave migration in the northern half, but it shows that the transport of sediment may be affected by a seasonal fluctuation due to the tides. Fig. 6.9 and Fig. 6.10 show that $\{q_{bs}\}$ is most positive or floodward in the period that $\{H\}$ is decreasing. If suspended sediment transport were to dominate the floodward sand-wave migration, then more floodward bedload transport would increase the total floodward transport, which could reduce the sand-wave height and increase the migration speed. Indeed, Fig. 6.10 shows that $\{q_{bs}\}$ correlates reasonably well with $\{U_{ws}\}$ ($r^2 = 38\%$): peaks in $\{q_{bs}\}$ coincide with peaks in $\{U_{ws}\}$ in winter. It should be noted that bedload transport due to near-bottom currents shows an identical pattern.

It has been shown in laboratory experiments (Kennedy, 1961; Julien and Raslan, 1998) and in the field (Shen et al., 1972) that a drop in temperature leads to an increase in suspension transport and a possible change of bed state from dunes to flat bed. Lower water temperatures increase the kinematic viscosity. More viscous water decreases fall velocity (Eq. 6.11), leading to more suspended sediment. These experiments and observations were for Froude numbers $0.1 < Fr < 1$ and $\theta' \gtrsim 1$. Under these conditions the dominant transport mode is suspension transport and changes in temperature have a large effect on the amount of transport. Although $\theta' < 1$ in the Marsdiep inlet, it still may be that seasonal temperature changes affect suspension. The seasonal variability in $\langle w_s \rangle$ is portrayed in Fig. 6.9 and Fig. 6.10. Every winter after 2000, the lowest values of $\langle w_s \rangle$ have coincided with the highest values of $\{U_{ws}\}$. This good agreement results in the highest coefficient of determination of $r^2 = 56\%$. A lower fall velocity implies that more sand is transported in suspension, which may lead to a deterioration of the sand wave and a higher migration rate.

Analysis

The gradual variability in $\{H\}$ in areas A and B does not appear to be affected by the more abrupt occurrence of storms and estuarine circulation. Similarly, the correlation of $\{U_{ws}\}$ with storms and estuarine circulation is also relatively poor. Therefore, it is concluded that storms and estuarine circulation have a limited effect on the sand-wave variability.

The gradual seasonal sand-wave variability may either be due to the tidal variability in sediment transport or the seasonal variability in fall velocity. In both cases they may increase the floodward sediment transport in winter, which decreases sand-wave height and increases migration speed. The 'fall velocity hypothesis' agrees well with the possibility that suspension transport governs the sand-wave migration in the northern half of the inlet.

It is not clear if the variability in height and migration speed is due to the same processes. One possibility is that the sand volume in the bedforms controls the migration speed. Under the same forcing conditions, smaller sand waves migrate faster than larger sand waves, as was observed by Ernstsen et al. (2005) in the Danish Wadden Sea. Fig. 6.10 shows that if the sand waves become smaller in winter in the Marsdiep inlet they migrate faster. This may also explain why the larger sand waves in the southern half portray

minimal seasonal variability. The second possibility is that the migration speed of the sand waves governs the sand-wave height. Apparently, if sand waves migrate faster less sand is used for build-up and they decrease in height. This is supported by the relatively good correlation of the migration speed with fall velocity and predicted bedload transport.

6.6   Conclusions

In this chapter, currents measured with a ferry-mounted ADCP in the period 1999-2002 have been applied to better understand the spatial and seasonal variability in sand-wave height and migration in the Marsdiep inlet, the Netherlands. The most important findings are summarised below.

- In the northern half of the inlet sand is finer and the current velocities are higher than in the southern half. As illustrated with the stability diagram (Fig. 6.4), suspended load transport is more important to the north than to the south. The occurrence of suspended load transport in the northern half explains why the sand waves are smaller, more rounded, and more three-dimensional than the larger and more progressive sand waves to the south, where bedload transport is relatively more important.

- Mean predicted bedload transport agrees in magnitude, trends, and direction with the floodward measured bedload transport in the southernmost 1600 m of the Marsdiep inlet. In this area, about 55% of the mean predicted bedload transport is due to tidal asymmetries and about 45% due to the interaction of the tidal-mean current with tidal constituents. In addition to the well-known M_2M_4 and $M_2M_4M_6$ asymmetries, the asymmetries that arise from the interaction of M_2 and its overtides with S_2 and its compound tides are also important in the Marsdiep inlet. In the northernmost 2000 m the ebbward predicted bedload transport is opposite to the measured bedload transport.

- It is hypothesised that suspension transport governs the floodward sand-wave migration in the northern half of the inlet. While bedload transport depends on local instantaneous current velocities, suspension transport depends on advection, scour lag, and settling lag. These observations are unique, if this hypothesis is correct. Generally, bedforms migrate in the direction of the strongest current. The floodward migration of the sand waves to the north cannot be due to estuarine circulation only.

- The seasonal variability in sand-wave height and migration is most pronounced in the northern half of the inlet featuring 0.5-m higher sand waves in fall than in spring and sand waves that migrate about 40 m y^{-1} faster in winter than in summer. This gradual variability cannot be explained with the abrupt occurrence of storms or estuarine circulation. It may be caused by the tides or by a fall velocity that depends on the kinematic viscosity. In winter, lower water temperatures increase kinematic viscosity, which decreases the fall velocity. It is hypothesised that either the tides or a lower fall velocity increase floodward (suspension) transport. As a consequence, the sand-wave height decreases and the sand-waves migrate faster.

Appendix 6.A   Tidal asymmetries

In addition to the well-known M_2M_4 and $M_2M_4M_6$ tidal asymmetries (Van de Kreeke and Robaczewska, 1993) and the $M_2O_1K_1$ asymmetry (Hoitink et al., 2003), tidal asymmetries may also result from the interaction of M_2 and its overtides with other astronomic constituents, such as S_2, N_2, K_2, etc., and their compound tides. Some important asymmetries are listed in Table 6.A.1. To obtain asymmetries that result from the interaction of M_2 with N_2 or K_2, replace S_2 with N_2 or K_2 in Table 6.A.1. Except for the M_2M_4 asymmetry, the asymmetries in Table 6.A.1 are due to the interaction of three constituents. Their behaviour is similar to the $M_2O_1K_1$ asymmetry already described by Hoitink et al. (2003). Hoitink et al. (2003) showed that the variation of the degree and orientation of the tidal asymmetry of $M_2O_1K_1$ is identical for consecutive oscillation periods with period $T = 13.66$ d, despite the fact that $U(t) \neq U(t + T)$, where U is the depth-mean velocity based on the M_2, O_1, and K_1 amplitudes and phases. A formulation for mean bedload transport for the $M_2O_1K_1$ asymmetry based on $q_b = \alpha U^3$ is calculated according to:

$$\langle \frac{q_b}{\alpha} \rangle_\infty = \lim_{\tau \to \infty} \frac{1}{\tau} \int_0^\tau U(t')^3 dt' = \frac{3}{2} U_{M_2} U_{O_1} U_{K_1} \cos(\phi_{O_1} + \phi_{K_1} - \phi_{M_2}), \qquad (6.A.1)$$

where U_{M_2} and ϕ_{M_2} are the amplitude and the phase of the M_2 constituent, respectively. If one plotted the cumulative transport $Q_b(t)/\alpha = \int_0^t U(t')^3 dt'$ against time, one would see a cumulative transport that fluctuates around an imaginary straight line. This imaginary line has a slope that is equal to the formulation for the mean bedload transport.

All formulations for the asymmetries based on three constituents in Table 6.A.1 are identical. In the formulations, the phase of the highest frequency is subtracted from the phases of the two other constituents with lower frequencies. Moreover, for each triple asymmetry, the sum of the lowest two frequencies minus the highest frequency is always zero. This is also true for the M_2M_4 asymmetry, if the M_4 frequency is subtracted from twice the M_2 frequency. The 'sum' of three different frequencies equal to zero is a prerequisite to obtain a formulation for the long-term mean bedload transport. This condition can be used to easily determine tidal asymmetries not listed in Table 6.A.1.

Table 6.A.1. Formulations for mean transport of several tidal asymmetries and the oscillation period T of each tidal asymmetry. The amplitudes and phases of the constituents are indicated by U and ϕ.

asymmetry	formulation for mean transport $\langle q_b/\alpha \rangle_\infty$	T [d]
M_2M_4	$3/4 U_{M_2}^2 U_{M_4} \cos(2\phi_{M_2} - \phi_{M_4})$	0.52
$M_2M_4M_6$	$3/2 U_{M_2} U_{M_4} U_{M_6} \cos(\phi_{M_2} + \phi_{M_4} - \phi_{M_6})$	0.52
$M_2S_2MS_4$	$3/2 U_{M_2} U_{S_2} U_{MS_4} \cos(\phi_{M_2} + \phi_{S_2} - \phi_{MS_4})$	14.77
$M_2MS_42MS_6$	$3/2 U_{M_2} U_{MS_4} U_{2MS_6} \cos(\phi_{M_2} + \phi_{MS_4} - \phi_{2MS_6})$	14.77
$M_4S_22MS_6$	$3/2 U_{M_4} U_{S_2} U_{2MS_6} \cos(\phi_{S_2} + \phi_{M_4} - \phi_{2MS_6})$	7.38
$M_42MS_2S_2$	$3/2 U_{M_4} U_{2MS_2} U_{S_2} \cos(\phi_{2MS_2} + \phi_{S_2} - \phi_{M_4})$	7.38
$M_62MS_2MS_4$	$3/2 U_{M_6} U_{2MS_2} U_{MS_4} \cos(\phi_{2MS_2} + \phi_{MS_4} - \phi_{M_6})$	4.92
$M_2O_1K_1$	$3/2 U_{M_2} U_{O_1} U_{K_1} \cos(\phi_{O_1} + \phi_{K_1} - \phi_{M_2})$	13.66

Chapter 7

Conclusions and recommendations

In this thesis, analyses of ADCP and CTD data collected with a ferry and during 13-h surveys have been presented. In Chapter 1 the following research questions were posed: what is the spatial and/or temporal variability in and what are the mechanisms that govern $Q1$) instantaneous streamwise and secondary currents and water transport, $Q2$) time-mean streamwise and secondary currents and water transport, and $Q3$) bedforms in the Marsdiep inlet? In this concluding chapter, these questions are addressed. First, the instantaneous streamwise currents and water transport are discussed, then the instantaneous secondary currents, followed by the subtidal water transport, and, finally, the bedforms. In the last section of this chapter some recommendations are made for future research.

7.1   Instantaneous streamwise currents and water transport

In Chapter 2, a five-year time series of streamwise currents and a five-year time series of water transport, both from early 1998 to the end of 2002, were applied to a least-squares harmonic analysis to study the tidal contribution. The current data obtained with the ferry ADCP were gridded in 18 horizontal and 40 vertical bottom-following grid cells. The water transport was computed by integrating the eastward velocities over the water depth and cross-section of the Marsdiep inlet.

With maximally 144 constituents, 98% of the variance in the water transport and streamwise currents is due to the tides, but a good fit of 96% is still obtained using the 15 largest constituents. In comparison, the variance explained by the tides is only 81% for the water levels measured at a tide gauge near the town of Den Helder. Water levels are more affected by wind set-up on the North Sea than the currents and water transport. Streamwise currents and water transport in the inlet are predominantly governed by the semi-diurnal astronomic M_2 tide, which in turn is modulated by the second-largest S_2 constituent ($\sim$27% of the M_2 amplitude) and the third largest N_2 constituent ($\sim$15% of M_2). The amplitude of the M_2 constituent of the water transport is about 66×10^3 m^3 s^{-1}. The 40° phase advance of the semi-diurnal constituents of the water transport relative to the water level variations indicates that the tidal wave is between progressive

and standing. In addition to astronomic constituents, compound and overtides are also important in the Marsdiep tidal inlet. The most significant are: $2MS_2$ (13.7% of M_2), $2MN_2$ (10.9%), M_4 (10.3%), and M_6 (10.0%). Compound and overtides are due to the nonlinearity of several terms in the continuity and momentum balance.

The currents in the inlet are sheared vertically and horizontally, with the highest currents at the surface above the deepest part of the inlet. During spring tides, currents under the ferry can be as large as 1.8 m s^{-1}. The M_2 tidal currents at the inlet centre lag behind the currents at the shores by maximally 20° ($\sim$40 min). This lag can be attributed to the relative importance of inertia compared to bottom friction in the deeper inlet channel and the travel time of the tidal wave. The M_2 currents under the ferry lag 3° behind in phase (about 6 min) with the currents near the bottom. This indicates the importance of friction near the bottom and the importance of inertia higher in the water column.

In addition to amplitudes and phases, the harmonic analysis also produces mean values of the time series. In the Marsdiep inlet the tidal-mean currents are of $\mathcal{O}(0.1$ m s$^{-1})$ and floodward in the southern half of the inlet and ebbward in the northern half. These currents are part of a horizontal residual eddy. The tidal-mean currents result from the interaction of the streamwise currents with the bathymetry: during flood the inflow is symmetrically distributed across the inlet, whereas during ebb the outflow is more concentrated on the north side of the inlet.

7.2   Instantaneous secondary currents

The mechanisms that govern the variability in the secondary currents observed with the ferry ADCP are investigated in Chapter 3. For this purpose, ADCP, vertical profiles of density, and surface density data were collected during several 13-h surveys along transects parallel to the ferry transect in the period 2003-2006. The 13-h survey data were applied in the transverse momentum balance to determine the governing mechanisms.

In well-mixed conditions at maximum flood, the secondary circulation is clockwise (northward bottom and southward surface transverse velocities) with velocities of about 0.05 m s^{-1} along the ferry transect due to primarily centrifugal accelerations and to a lesser extent to Coriolis accelerations. At maximum ebb, there are two weak circulation cells with surface convergence featuring velocities of about 0.01 m s^{-1}. The circulation is weakly clockwise due to negative curvature in the northern half of the inlet and counterclockwise due to positive curvature in the southern half. In the southern half, transverse density gradients that are set up due to the influx of fresher water from the Malzwin channel and Coriolis accelerations may also contribute to the counterclockwise circulation.

In stratified conditions, dampening of turbulence due to stratification and transverse density gradients affect the secondary circulation. In general during late flood, the differential advection of denser water in the inlet centre creates two counter-rotating circulation cells with surface convergence. This density-driven circulation is a common phenomena in well-mixed estuaries (Nunes and Simpson, 1985). The Marsdiep inlet is at the confluence of the Malzwin and Texelstroom channels. During ebb, the Malzwin channel is generally fresher than the Texelstroom channel. As a consequence, the inflow of fresher water from

the Malzwin channel into the Marsdiep channel during ebb sets up transverse density gradients that govern the counterclockwise secondary circulation in the southern half of the inlet. These transverse density gradients are several times larger than the longitudinal density gradients. After maximum ebb in the northern half of the inlet, the water column becomes well-mixed and the secondary circulation clockwise due to local negative curvature.

The spatial differences in inflow and outflow in the inlet not only set up a horizontal residual eddy (Chapter 2), but they also cause a spatial asymmetry in turbulent mixing. During ebb, mixing is stronger in the northern half and weaker in the southern half of the inlet. The weaker mixing and the influx of fresher water from the Malzwin channel during ebb in the southern half of the inlet result in a stratified water column. In these conditions surface secondary currents of about 0.4 m s^{-1} have been observed. The Marsdiep inlet has been generally regarded as vertically well-mixed. This analysis has shown that the water column can be stratified during days with large longitudinal density gradients, in particular before and after maximum flood and ebb velocities when the tide-generated turbulence is relatively low.

7.3   Subtidal water transport

While on small time scales the tides determine the variance in the water transport, on longer time scales this is not the case. To illustrate this, in Chapter 4 the water transport for the period from early 1999 to the end of 2002 was low-pass filtered with a cut off frequency of three days. The mechanisms that govern this subtidal water transport were determined with a simple analytical model. This model includes freshwater discharge from the sluices, coastal pumping due to (remote) wind set-up on the North Sea, and throughflow. The Marsdiep basin has an open connection with the adjacent Vlie basin and this open connection allows for basin to basin transport of water. The throughflow comprises water transport due to tidal stresses, subtidal water-level gradients, density gradients, and surface wind stresses.

Although both the predicted and observed time-mean water transport are directed out of the Marsdiep inlet, the magnitude of the observed time-mean water transport (-2098 m^3 s^{-1}) is larger than the magnitude of the predicted water transport (-215 m^3 s^{-1}). These differences may be attributed to the simplistic representation of physical processes and bathymetry in the analytical model. The time-mean subtidal water transport mainly consists of an export due to tidal stresses and freshwater discharge and an import due to southwesterly winds. The tidal stresses govern an export due to a larger tidal water-level amplitude at the Vlie inlet than at the Marsdiep inlet. The predominant southwesterly winds push water from the Marsdiep to the Vlie basin, whereas northwesterly winds govern water transport in the opposite direction.

The variability in the subtidal water transport is predominantly governed by the variability in the wind stresses. The wind stresses explain about 43% of the variance in the subtidal water transport, whereas all contributions combined explain maximally 50%. The contribution of the variability in tidal stresses, pumping, subtidal water-level gradients, density gradients, and freshwater discharge to the variability in the subtidal water trans-

port is minimal. The variability due to wind stress is minimally a factor four larger. The Marsdiep-Vlie system contrasts with tidal basins with one connection to the open sea. In the latter, remote and local wind set-up primarily govern the subtidal water transport.

7.4   Bedforms

As shown in Chapter 5, the ferry-mounted ADCP can also measure water depths in addition to currents. These depths, measured in periods of about 30 days, were combined in bathymetric maps or digital terrain models (DTMs) with a horizontal resolution of 15 m. The DTMs reveal the existence of sand waves with wave lengths of $\mathcal{O}(100$ m$)$ and heights of $\mathcal{O}(1$ m$)$. A spatial cross-correlation technique was applied to determine the horizontal migration velocities of these bedforms.

In the southern half, the sand waves are of the progressive type with area-mean wave heights of 3 m and lengths of 200 m. In the northern half of the inlet, the sand waves are asymmetric-trochoidal with area-mean wave heights between 1.5 and 3 m and lengths between 140 and 200 m. Across the inlet, the sand waves migrate in the flood direction with rates between 0 and 90 m y^{-1}. Only the progressive waves in the southern half migrate in directions perpendicular to their crests. A striking observation is the seasonal variability in sand-wave heights and migration of the sand waves in the northern half of the inlet. The sand-wave heights are about 0.5 m higher in fall than in spring and the migration velocities are about 30 m y^{-1} higher in winter than in summer.

In Chapter 6, the ferry-ADCP current measurements were applied to explain the mechanisms that govern the spatial and seasonal variability in sand-wave height and migration speed. For that purpose, grain-size distributions of sediment samples taken at the sand-wave crests and troughs were determined. 'Predicted' bedload transport was calculated using depth-averaged currents and compared with 'measured' bedload transport inferred from sand-wave shape and migration speed.

In the northern half of the inlet, sand is finer and the current velocities are higher than in the southern half. Consequently, suspended load transport is more important in the northern than in the southern half. The occurrence of suspended load transport in the northern half explains why the sand waves are smaller, more rounded, and more three-dimensional than the larger and more progressive sand waves to the south, where bedload transport is relatively more important.

Mean predicted bedload transport agrees in magnitude, trends, and direction with the floodward measured bedload transport in the southernmost 1600 m of the Marsdiep inlet. In this area, about 55% of the mean predicted bedload transport is due to tidal asymmetries and about 45% due to the interaction of the tidal-mean current with tidal constituents. In addition to the well-known M_2M_4 and $M_2M_4M_6$ asymmetries, the asymmetries that arise from the interaction of M_2 and its overtides with S_2 and its compound tides are also important. In the northernmost 2000 m the ebbward predicted bedload transport is opposite to the measured bedload transport.

It is hypothesised that suspension transport governs the floodward sand-wave migration in the northern part. While bedload transport depends on local instantaneous current velocities, suspension transport depends on advection, settling lag, and scour lag. These

observations are unique, since bedforms generally migrate in the direction of the strongest current.

The seasonal variability in sand-wave height and migration is most pronounced in the northern half of the inlet featuring 0.5-m higher sand waves in fall than in spring and sand waves that migrate about 30 m y^{-1} faster in winter than in summer. This gradual variability cannot be explained with the abrupt occurrence of storms or estuarine circulation. It may be caused by the tides or by a fall velocity that depends on the kinematic viscosity. In winter, lower water temperatures increase kinematic viscosity, which decreases the fall velocity. It is hypothesised that either the tides or a lower fall velocity increase floodward (suspension) transport. As a consequence, the sand-wave height decreases and the sand-waves migrate faster.

7.5   In final conclusion...

From this thesis it has become apparent that tides govern most of the physical processes in the Marsdiep inlet. They primarily drive the instantaneous streamwise currents and water transport. The instantaneous secondary currents do not appear to be driven by the tides directly: they are mainly governed by curvature (i.e. bathymetry) and transverse density gradients. However, the curvature-driven secondary currents depend on tidal streamwise currents. As a consequence, curvature-driven secondary currents can also be classified as tidal. The discharge of freshwater causes transverse density gradients that drive strong secondary currents. While these secondary currents are clearly non-tidal, the occurrence of the transverse density gradients and related secondary currents are strongly modulated by the semi-diurnal tidal cycle. The same applies to vertical mixing and density stratification, which depend on the tidal phase. The interaction of the tidal streamwise currents with the bathymetry also causes horizontal residual eddies. Hence, tides are important for the time-mean currents as well. On time scales longer than the diurnal cycle, the influence of tides becomes significantly smaller. Although tides, by means of tidal stresses, contribute to the subtidal water transport, the variability in the subtidal water transport is primarily governed by wind.

The sand-wave migration is also governed by the tides, in particular in the southern half, where the sand-wave migration is correlated well with the tidal bedload transport. The contribution of storm events or estuarine circulation to the bedload transport appears to be small. Most presumably, tides also govern the variability in height and migration speed of the sand waves in the northern half of the inlet via suspended load transport.

7.6   Recommendations

Although this thesis provides insight in some interesting physical processes in the Marsdiep inlet, the reader may argue that some classical concepts have not been addressed. One such concept that has not been studied quantitatively in the Marsdiep inlet is estuarine circulation (Hansen and Rattray, 1965). The ferry measurements as well as the 13-h surveys are well suited to study the variability in the estuarine circulation. However, as shown in Chapter 2, the residual currents are mainly due to tidal rectification and the

classical surface outflow and near-bottom inflow is not directly visible. Data analyses that are only cursorily discussed in Chapter 6 clearly reveal the influence of the longitudinal pressure gradient on the vertical shear in the streamwise currents. Thus, it is worthwhile to study the relation between the longitudinal density gradients and the vertical structure of the streamwise currents.

As discussed in Chapter 3, it proved to be difficult to correctly estimate the contribution of the advective terms to the secondary circulation. It may be a useful exercise to apply a three-dimensional numerical model and estimate the relative importance of these terms in well-mixed and stratified conditions. Moreover, the influence of the Coriolis acceleration could be studied better in a model.

A question that is partially addressed is the relation between the seasonal variability in sand-wave height and migration in the northern half of the inlet on the one hand and the sediment transport on the other. The resolution of the near-bottom velocities with the ferry-ADCP is poor: velocities within 2 m above the bottom cannot be accurately determined. It may be interesting to deploy a frame equipped with ADCP, CTD, and optical backscatter (OBS) devices in the northern part of the inlet for at least a spring-neap cycle in June/July, when the net bedload transport is less floodward, and in December/January, when the net bedload transport is more floodward. Simultaneously, (suspended) sediment samples should be collected to determine concentrations and grain-size distributions. Moreover, a broadband ADCP mounted on the frame could be used to get insight in vertical mixing, which may be relevant for studies on secondary currents. It may also be worthwhile to study the influence of kinematic viscosity on the sand-wave variability with a numerical model.

Finally, it is recommended that the data set and data analyses presented in this thesis be used for the calibration and validation of numerical models. In particular, the long-term temporal variability of the ferry data may be of great significance for modellers.

Bibliography

Abraham, G., 1988. Turbulence and mixing in stratified tidal flows. In: Dronkers, J., Van Leussen, W. (Eds.), Physical Processes in Estuaries. Springer-Verlag, Berlin, pp. 149–180.

Alaee, M. J., Ivey, G., Pattiaratchi, C., 2004. Secondary circulation induced by flow curvature and Coriolis effects around headlands and islands. Ocean Dyn. 54, 27–38.

Aliotta, S., Perillo, G. M. E., 1987. A sand wave field in the entrance to Bahia Blanca Estuary, Argentina. Mar. Geol. 76, 1–14.

Allen, J. R. L., 1984. Sedimentary Structures, their Character and Physical Basis (Developments in Sedimentology 30). Elsevier Amsterdam.

Barthel, K., Gade, H. G., Sandal, C. K., 2004. A mechanical energy budget for the North Sea. Cont. Shelf Res. 24, 167–181.

Bartholdy, J., Bartholomae, A., Flemming, B. W., 2002. Grain-size control of large compound flow-transverse bedforms in a tidal inlet of the Danish Wadden Sea. Mar. Geol. 188, 391–413.

Bendat, J. S., Piersol, A. G., 1986. Random Data. Analysis and Measurement Procedures, 2nd Edition. Wiley-Interscience, New York, USA.

Besio, G., Blondeaux, P., Brocchini, M., Vittori, G., 2004. On the modeling of sand wave migration. J. Geophys. Res. 109, C04018, doi:10.1029/2002JC001622.

Besio, G., Blondeaux, P., Vittori, G., 2006. On the formation of sand waves and sand banks. J. Fluid Mech. 557, 1–27.

Bonekamp, H., Ridderinkhof, H., Roelvink, D., Luijendijk, A., 2002. Sediment transport in the Texel tidal inlet due to tidal asymmetries. In: Smith, J. M. (Ed.), Proc. 28th Int. Conf. Coast. Eng. Reston, VA, pp. 2813–2823.

Bruun, P., 1978. Stability of Tidal Inlets: Theory and Engineering. Elsevier Scientific Pub. Co., Amsterdam.

Bruun, P., Gerritsen, F., 1959. Natural bypassing of sand at coastal inlets. J. Waterw. Harb. Div.-ASCE 85, 75–107.

Buijsman, M. C., Ridderinkhof, H., 2007a. Long-term ferry-ADCP observations of tidal currents in the Marsdiep inlet. J. Sea Res. 57, 237–256.

Buijsman, M. C., Ridderinkhof, H., 2007b. Water transport at subtidal frequencies in the Marsdiep inlet. J. Sea Res., doi: 10.1016/j.seares.2007.04.002.

Cáceres, M., Valle-Levinson, A., Atkinson, L., 2003. Observations of cross-channel structure of flow in an energetic tidal channel. J. Geophys. Res. 108 (C4), 3114, doi:10.1029/2001JC000968.

Carter, H. H., Pritchard, D. W., 1988. Oceanography of Chesapeake Bay. In: Kjerfe, B. (Ed.), Hydrodynamics of Estuaries: Dynamics of Partially Mixed Estuaries, vol. 1. CRC Press, Boca Raton FL, pp. 1–16.

Chant, R. J., 2002. Secondary circulation in a region of flow curvature: Relationship with tidal forcing and river discharge. J. Geophys. Res. 107 (C9), 3131, doi:10.1029/2001JC001082.

Chant, R. J., Wilson, R. E., 1997. Secondary circulation in a highly stratified estuary. J. Geophys. Res. 102, 23,207–23,215.

Cleveringa, J., Oost, A. P., 1999. The fractal geometry of tidal-channel systems in the Dutch Wadden Sea. Geol. Mijnbouw 78, 21–30.

Codiga, D. L., Aurin, D. A., 2007. Residual circulation in eastern Long Island Sound: Observed transverse-vertical structure and exchange transport. Cont. Shelf Res. 27, 103–116.

Day, J. W., 1989. Estuarine Ecology. John Wiley and Sons, New York.

Dinehart, R. L., Burau, J. R., 2005. Repeated surveys by acoustic Doppler current profiler for flow and sediment dynamics in a tidal river. J. Hydrol. 314, 1–21.

Donato, T. F., Askari, F., Marmorino, G. O., Trump, C. L., Lyzenga, D. R., 1997. Radar imaging of sand waves on the continental shelf east of Cape Hatteras, NC, U.S.A. Cont. Shelf Res. 17, 989–1004.

Dronkers, J., 1996. The influence of buoyancy on transverse circulation and on estuarine dynamics. In: Aubrey, D. G., Friedrichs, C. T. (Eds.), Buoyancy Effects on Coastal and Estuarine Dynamics. AGU, Washington D.C., pp. 341–356.

Dronkers, J., 2005. Advances Series on Ocean Engineering–Volume 25: Dynamics of Coastal Systems. World Scientific Publishing Co., Singapore.

Dronkers, J. J., 1964. Tidal Computations in Rivers and Coastal Waters. North-Holland Publishing Company, Amsterdam.

Duffy, G. P., Hughes-Clarke, J. E., 2005. Application of spatial cross correlation to detection of migration of submarine sand dunes. J. Geophys. Res. 110, F04S12, doi:10.1029/2004JF000192.

Dyer, K. R., 1986. Coastal and Estuarine Sediment Dynamics. John Wiley and Sons, Great Britain.

Elias, E. P. L., 2006. Morphodynamics of Texel inlet. Ph.D. thesis, Delft University of Technology.

Elias, E. P. L., Cleveringa, J., Buijsman, M. C., Roelvink, J. A., Stive, M. J. F., 2006. Field and model data analysis of sand transport patterns in Texel tidal inlet (the Netherlands). Coast. Eng. 53, 505–529.

Elias, E. P. L., Stive, M. J. F., Bonekamp, H., Cleveringa, J., 2003. Tidal inlet dynamics in response to human intervention. Coast. Eng. J. 45, 629–658.

Elias, E. P. L., Van der Spek, A. J. F., 2006. Long-term morphodynamic evolution of Texel Inlet and its ebb-tidal delta (The Netherlands). Mar. Geol. 225, 5–21.

Emery, W. J., Thomson, R. E., 2001. Data Analysis Methods in Physical Oceanography, second and revised Edition. Elsevier, Amsterdam.

Engelund, F., Fredsoe, J., 1982. Sediment ripples and dunes. Annu. Rev. Fluid Mech. 14, 13–37.

Ernstsen, V. B., Noormets, R., Winter, C., Hebbeln, D., Bartholomä, A., Flemming, B. W., Bartholdy, J., 2005. Development of subaqueous barchanoid-shaped dunes due to lateral grain size variability in a tidal inlet channel of the Danish Wadden Sea. J. Geophys. Res. 110, F04S08, doi:10.1029/2004JF000180.

Fischer, H. B., List, E. J., Koh, R. C. Y., Imberger, J., Brooks, N. H., 1979. Mixing in Inland and Coastal Waters. Academic Press, New York.

Flemming, B. W., 1988. Zur Klassifikation subaquatischer, stromungstransversaler Transportkorper. Boch. Geol. Geotech. Arb. 29, 44–47.

Flemming, B. W., 2000. The role of grain size, water depth and flow velocity as scaling factors controlling the size of subaqueous dunes. In: Trenteseaux, A., Garlan, T. E. (Eds.), Proc. Int. Workshop on Marine Sandwave Dynamics. University of Lille, Lille, France, pp. 55–60.

Garvine, R. W., 1985. A simple model of estuarine subtidal fluctuations forced by local and remote wind stress. J. Geophys. Res. 90, 11945–11948.

Gerkema, T., 2000. A linear stability analysis of tidally generated sand waves. J. Fluid Mech. 417, 303–322.

Geyer, W. R., 1993. Three-dimensional tidal flow around headlands. J. Geophys. Res. 98, 955–

966.

Geyer, W. R., Signell, R., 1990. Measurements of tidal flow around a headland with a shipboard acoustic Doppler current profiler. J. Geophys. Res. 95, 3189–3197.

Geyer, W. R., Signell, R. P., Kineke, G. C., 1998. Lateral trapping of sediment in a partially mixed estuary. In: Dronkers, J., Scheffers, M. (Eds.), Physics of Estuaries and Coastal Seas. Balkema, Rotterdam, pp. 115–126.

Godin, G., 1972. The Analysis of Tides. Liverpool University Press, Liverpool.

Groen, P., 1967. On the residual transport of suspended matter by an alternating tidal current. Neth. J. Sea Res. 3, 564–574.

Hanawa, K., Yoshikawa, Y., Taneda, T., 1996. TOLEX-ADCP monitoring. Geophys. Res. Lett. 23, 2429–2432.

Handler, R. A., Mied, R. P., Evans, T. E., Donato, T. F., 2001. Convergence fronts in tidally forced rotating estuaries. J. Geophys. Res. 106, 27,145–27,162.

Hansen, D. V., Rattray, M., 1965. Gravitational circulation in straits and estuaries. J. Mar. Res. 23, 104–122.

Hansen, J. L., Van Hecke, M., Haaning, A., Ellegaard, C., Andersen, K. H., Bohr, T., Sams, T., 2001. Instabilities in sand ripples. Nature 410, 324.

Hansen, W., 1952. Gezeiten und Gezeitenströme der halbtägigen Hauptmondtide M_2 in der Nordsee. Deutsch. Hydrogr. Z., Erg. Heft 1, 1–46.

Hayes, M. O., 1979. Barrier island morphology as a function of tidal and wave regime. In: Leatherman, S. P. (Ed.), Barrier Islands: From the Gulf of St. Lawrence to the Gulf of Mexico. Academic Press, New York, pp. 1–27.

Hayes, M. O., 1980. General morphology and sediment patterns in tidal inlets. Sediment. Geol. 26, 139–156.

Heijboer, D., Nellestijn, J. W., 2002. Klimaatatlas van Nederland: de Normaalperiode 1971–2000. Elmar, Rijswijk, the Netherlands.

Hench, J. L., Blanton, B. O., Luettich Jr., R. A., 2002. Lateral dynamic analysis and classification of barotropic tidal inlets. Cont. Shelf Res. 22, 2615–2631.

Hench, J. L., Luettich Jr., R. A., 2003. Transient tidal circulation and momentum balances at a shallow inlet. J. Phys. Oceanogr. 33, 913–932.

Hoekstra, P., Bell, P., Van Santen, P., Roode, N., Levoy, F., Whitehouse, R., 2004. Bedform migration and bedload transport on an intertidal shoal. Cont. Shelf Res. 24, 1249–1269.

Hoitink, A. J. F., Hoekstra, P., Van Maren, D. S., 2003. Flow asymmetry associated with astronomical tides: Implications for the residual transport of sediment. J. Geophys. Res. 108 (C10), 3315, doi:10.1029/2002JC001539.

Hulscher, S. J. M. H., 1996. Tidal-induced large-scale regular bed form patterns in a three-dimensional shallow water model. J. Geophys. Res. 101, 20,727–20,744.

Hulscher, S. J. M. H., De Swart, H. E., De Vriend, H. J., 1993. The generation of offshore tidal sand banks and sand waves. Cont. Shelf Res. 13, 1183–1204.

Janzen, C. D., Wong, K.-C., 1998. On the low-frequency transport processes in a shallow coastal lagoon. Estuaries 21, 754–766.

Janzen, C. D., Wong, K.-C., 2002. Wind-forced dynamics at the estuary-shelf interface of a large coastal plain estuary. J. Geophys. Res. 107 (C10), 3138, doi:10.1029/2001JC000959.

Jay, D. A., Smith, J. D., 1990. Circulation, density distribution and neap-spring transitions in the Columbia River Estuary. Prog. Oceanogr. 25, 81–112.

Joyce, T. M., 1989. On in situ 'calibration' of shipboard ADCPs. J. Atmos. Ocean. Tech. 6, 169–172.

Julien, P. Y., Raslan, Y., 1998. Upper-regime plane bed. J. Hydraul. Eng.-ASCE 124, 1086–1096.

Kalkwijk, J. P. T., Booij, R. B., 1986. Adaptation of secondary flow in nearly-horizontal flow. J. Hydraul. Res. 24, 19–37.

Kalkwijk, J. P. T., De Vriend, H. J., 1980. Computation of the flow in shallow river bends. J. Hydraul. Res. 18, 327–342.

Kennedy, J. F., 1961. Further laboratory studies of the roughness and suspended load of alluvial streams. Tech. Rep. KH-R-3, W.M. Keck Laboratory of Hydraulics and Water Resources, California Institute of Technology, Pasadena, California.

Kieft, R. N., Schreel, K. R. A. M., Van der Plas, G. A. J., Rindt, C. C. M., 2002. The application of a 3D-PTV algorithm to a mixed convection flow. Exp. Fluids 33, 603–611.

Knaapen, M. A. F., 2005. Sandwave migration predictor based on shape information. J. Geophys. Res.-Earth 110, F04S11, doi:10.1029/2004JF000195.

Komar, P. D., 1996. Tidal-inlet processes and morphology related to the transport of sediments. J. Coastal Res. SI 23, 23–45.

Lacy, J. R., Monismith, S. G., 2001. Secondary currents in a curved, stratified estuarine channel. J. Geophys. Res. 106, 31,283–31,302.

Lacy, J. R., Stacey, M. T., Burau, J. R., Monismith, S. G., 2003. The interaction of lateral baroclinic forcing and turbulence in an estuary. J. Geophys. Res. 108 (C3), 3089, doi:10.1029/2002JC001392.

Langhorne, D. N., 1982. A study of the dynamics of a marine sandwave. Sedimentology 29, 571–594.

Large, W. G., Pond, S., 1981. Open ocean momentum flux measurements in moderate to strong winds. J. Phys. Oceanogr. 11, 324–336.

Le Hir, P., Ficht, A., Jacinto, R. S., Lesueur, P., Dupont, J. P., Lafite, R., Brenon, I., Thouvenin, B., Cugier, P., 2001. Fine sediment transport and accumulations at the mouth of the Seine estuary (France). Estuaries 24, 950–963.

Lee, T. N., Smith, N., 2002. Volume transport variability through the Florida Keys tidal channels. Cont. Shelf Res. 22, 1361–1377.

Lerczak, J. A., Geyer, W. R., 2004. Modeling the lateral circulation in straight, stratified estuaries. J. Phys. Oceanogr. 34, 1410–1428.

Li, C., 2002. Axial convergence fronts in a barotropic tidal inlet-sand shoal inlet, VA. Cont. Shelf Res. 22, 2633–2653.

Li, C., O'Donnel, J., 1997. Tidally driven residual circulation in shallow estuaries with lateral depth variation. J. Geophys. Res. 102, 27,915–27,929.

Li, C., Valle-Levinson, A., Atkinson, L. P., Royer, T. C., 2000. Inference of tidal elevation in shallow water using a vessel-towed acoustic Doppler current profiler. J. Geophys. Res. 105, 26,225–26,236.

Lobo, F. J., Hernandez-Molina, F. J., Somoza, L., Rodero, J., Maldonado, A., Barnolas, A., 2000. Patterns of bottom current flow deduced from dune asymmetries over the Gulf of Cadiz shelf (southwest Spain). Mar. Geol. 164, 91–117.

Lorentz, H. A., 1926. Verslag Staatscommissie Zuiderzee 1918-1926. Algemene Landsdrukkerij, Den Haag.

Louters, T., Gerritsen, F., 1994. The riddle of the sands, a tidal system's answer to a rising sea level. Tech. Rep. RIKZ-94.040, Ministry of Transport, Public Works and Water Management, National Institute for Coastal and Marine Management (RIKZ), The Hague.

Ludwick, J. C., 1972. Migration of tidal sand waves in Chesapeake Bay entrance. In: Swift, D. J. P., Duane, D. B., Pilkey, O. H. (Eds.), Shelf sediment transport. Dowden, Hutchinson and Ross, Stroudsburg, Penn., pp. 377–410.

Lueck, R. G., Lu, Y., 1997. The logarithmic layer in a tidal channel. Cont. Shelf Res. 17, 1785–

1801.

Lwiza, K. M. M., Bowers, D. G., Simpson, J. H., 1991. Residual and tidal flow at a tidal mixing front in the North Sea. Cont. Shelf Res. 11, 1379–1395.

Maas, H. G., Grun, A., Papantoniou, D., 1993. Particle tracking in three-dimensional turbulent flows - Part I: Photogrammetric determination of particle coordinates. Exp. Fluids 15, 133–146.

McCave, I. N., 1971. Sandwaves in the North Sea off the coast of Holland. Mar. Geol. 10, 199–225.

Meyer-Peter, E., Müller, R., 1948. Formulas for bed-load transport. In: Report on the 2nd Meeting of the International Association for Hydraulic Structures Research. Stockholm, pp. 39–64.

Mied, R. P., Handler, R. A., Donato, T. F., 2002. Regions of estuarine convergence at high rossby number: A solution in estuaries with elliptical cross sections. J. Geophys. Res. 107 (C11), 3206, doi:10.1029/2001JC001050.

Mied, R. P., Handler, R. A., Evans, T. E., 2000. Longitudinal convergence fronts in homogeneous rotating channels. J. Geophys. Res. 105, 8,647–8,658.

Miles, J. W., 1961. On the stability of heterogeneous shear flow. J. Fluid Mech. 10, 496–508.

Millero, F. J., Poisson, A., 1981. International one-atmosphere equation of state of seawater. Deep-Sea Res. 28A, 625–629.

Morelissen, R., Hulscher, S. J. M. H., Knaapen, M. A. F., Nemeth, A. A., Bijker, R., 2003. Mathematical modelling of sand wave migration and the interaction with pipelines. Coast. Eng. 48, 197–209.

Munchow, A., Coughran, C. S., Hendershott, M. C., Winant, C. D., 1995. Performance and calibration of an acoustic Doppler current profiler towed below the surface. J. Atmos. Ocean. Tech. 12, 435–444.

Munk, W. H., Anderson, E. R., 1948. Notes on the theory of the thermocline. J. Marine Res. 7, 276–295.

Nemeth, A. A., Hulscher, S. J. M. H., De Vriend, H. J., 2002. Modelling sand wave migration in shallow shelf seas. Cont. Shelf Res. 22, 2795–2806.

Nunes, R. A., Simpson, J. H., 1985. Axial convergence in a well-mixed estuary. Estuar. Coast. Shelf S. 20, 637–649.

Oertel, G. F., 1988. Processes of sediment exchange between tidal inlets, ebb deltas and barrier islands. In: Aubrey, D. G., Weishar, L. (Eds.), Hydrodynamics and sediment dynamics of tidal inlets. Lecture notes on coastal and estuarine studies. Vol 29. Springer, New York, pp. 297–318.

Oost, A. P., 1995. Dynamics and sedimentary developments of the Dutch Wadden Sea with a special emphasis on the frisian inlet : a study of the barrier islands, ebb-tidal deltas, inlets and drainage basins. Ph.D. thesis, Faculteit Aardwetenschappen, Universiteit Utrecht.

Pacanowski, R. C., Philander, S. G. H., 1981. Parameterisation of vertical mixing in numerical models of tropical oceans. J. Phys. Oceanogr. 11, 1443–1451.

Pannell, M. A., O'Hare, T. J., Huntley, D. A., 2002. Modelling of sand ripple development by self-organization in unsteady flow conditions. In: Smith, J. M. (Ed.), Proc. 28th Int. Conf. Coast. Eng. World Scientific, Singapore, pp. 2837–2849.

Pape III, E. H., Garvine, R. W., 1982. The subtidal circulation in Delaware Bay and adjacent shelf waters. J. Geophys. Res. 87, 7955–7970.

Parker, B. B., 1991. The relative importance of the various nonlinear mechanisms in a wide range of tidal interactions. In: Parker, B. B. (Ed.), Tidal Hydrodynamics. John Wiley and Sons, New York, pp. 237–268.

Petersen, W., Petschatnikov, M., Schroeder, F., Wehde, H., 2004. Application of a FerryBox:

automatic measurements in the North Sea. In: OCEANS '04. MTS/IEEE TECHNO-OCEAN '04. Daishin Planning Co., Kobe, Japan, pp. 1399–1401.

Pingree, R. D., Griffiths, D. K., 1979. Sand transport paths around the British Isles resulting from M2 and M4 tidal interactions. J. Mar. Biol. Assoc. UK 59, 497–513.

Postma, H., 1954. Hydrography of the Dutch Wadden Sea. Arch. Néerl. Zool. 10, 405–511.

Postma, H., 1957. Size frequency distribution of sands in the Dutch Wadden Sea. Arch. Néerl. Zool. 12, 319–349.

Postma, H., 1961. Transport and accumulation of suspended matter in the Dutch Wadden Sea. Neth. J. Sea Res. 1, 148–190.

Postma, H., 1982. Hydrography of the Wadden Sea: movements and properties of water and particulate matter: final report on hydrography of the Wadden Sea Working Group. Tech. rep., Stichting Veth tot Steun aan Waddenonderzoek, Leiden.

Prandle, D., 1982. The vertical structure of tidal currents. Geophys. Astro. Fluid 22, 29–49.

Preddy, W. S., 1954. The mixing and movement of water in the estuary of the Thames. J. Mar. biol. Assoc. U.K. 33, 645–662.

Ridderinkhof, H., 1988a. Tidal and residual flows in the Western Dutch Wadden Sea, I: Numerical model results. Neth. J. Sea Res. 22, 1–22.

Ridderinkhof, H., 1988b. Tidal and residual flows in the Western Dutch Wadden Sea, II: An analytic model to study the constant flow between connected tidal basins. Neth. J. Sea Res. 22, 185–198.

Ridderinkhof, H., 1989. Tidal and residual flows in the Western Dutch Wadden Sea, III: Vorticity balances. Neth. J. Sea Res. 24, 9–26.

Ridderinkhof, H., 1990. Residual currents and mixing in the Wadden Sea. Ph.D. thesis, Rijksuniversiteit Utrecht, Utrecht.

Ridderinkhof, H., 1997. The effect of tidal asymmetries on the net transport of sediments in the Ems Dollard estuary. J. Coast. Res. SI, 41–48.

Ridderinkhof, H., Van Haren, H., Eijgenraam, F., Hillebrand, T., 2002. Ferry observations on temperature, salinity and currents in the Marsdiep tidal inlet between the North Sea and the Wadden Sea. In: Flemming, N. C., Vallerga, S., Pinardi, N., Behrens, H. W. A., Manzella, G., Prandle, D., Stel, J. H. (Eds.), Proc. 2nd Int. Conf. EUROGOOS. Operational Oceanography: Implementation at the European and Regional Scales. Elsevier Oceanography Series, 66, pp. 139–148.

Robinson, I. S., 1983. Tidally induced residual flows. In: Johns, B. (Ed.), Physical Oceanography of Coastal and Shelf Seas. Elsevier, New York, pp. 321–356.

Rubin, D. M., McCulloch, D. S., 1980. Single and superimposed bedforms: a synthesis of San Francisco Bay and flume observations. Sediment. Geol. 26, 207–231.

Seim, H. E., Gregg, M. C., 1997. The importance of aspiration and channel curvature in producing strong vertical mixing over a sill. J. Geophys. Res. 102, 3451–3472.

Sha, L. P., 1986. Sand transport patterns in the ebb-tidal delta of Texel inlet, Wadden Sea, the Netherlands. Mar. Geol. 86, 137–154.

Sha, L. P., 1989a. Holocene-Pleistocene interface and three-dimensional geometry of the ebb-delta complex, Texel inlet, the Netherlands. Mar. Geol. 89, 207–228.

Sha, L. P., 1989b. Variation in ebb-delta morphologies along the West and East Frisian Islands, the Netherlands and Germany. Mar. Geol. 89, 11–28.

Sha, L. P., 1990. Sedimentological studies of the ebb-tidal deltas along the West Frisian Islands, the Netherlands. Ph.D. thesis, Mededelingen van het Instituut voor Aardwetenschappen der Rijksuniversiteit te Utrecht, No. 64.

Shen, H. W., Mellema, W. J., Harrison, A. S., 1972. Temperature effects in high-transport,

flat-bed flows. J. Hydr. Eng. Div.-ASCE 104, 1–20.

Sherwood, C. R., Jay, D. A., Harvey, R. B., Hamilton, P., Simenstad, C. A., 1990. Historical changes in the Columbia River Estuary. Prog. Oceanogr. 25, 299–352.

Simpson, J. H., Mitchelson-Jacob, E. G., Hill, A. E., 1990. Flow structure in a channel from an acoustic Doppler current profiler. Cont. Shelf Res. 10, 589–603.

Simpson, J. H., Williams, E., Brasseur, L. H., Brubaker, J. M., 2005. The impact of tidal straining on the cycle of turbulence in a partially stratified estuary. Cont. Shelf Res. 25, 51–64.

Soulsby, R. L., 1990. Tidal-current boundary layers. In: Le Mehaute, B., Hanes, D. M. (Eds.), The Sea, Ocean Engineering Science 9 (Part A). John Wiley and Sons, New York, pp. 523–566.

Soulsby, R. L., 1997. Dynamics of Marine Sands. Thomas Telford, London.

Stanev, E. V., Wolff, J.-O., Burchard, H., Bolding, K., Flöser, G., 2003. On the circulation in the East Frisian Wadden Sea: numerical modeling and data analysis. Ocean Dyn. 53, 27–51.

Stive, J. F., Capobianco, M., Wang, Z. B., Ruol, P., Buijsman, M. C., 1998. Morphodynamics of a tidal lagoon and the adjacent coasts. In: Dronkers, J., Scheffers, M. (Eds.), Physics of Estuaries and Coastal Seas: Proceedings of the 8th International Biennial Conference on Physics of Estuaries and Coastal Seas. Balkema, Rotterdam, pp. 397–407.

Takikawa, T., Yoon, J., Cho, K., 2003. Tidal currents in the Tsushima Straits estimated from ADCP data by ferryboat. J. Oceanogr. 59, 37–47.

Takikawa, T., Yoon, J., Cho, K., 2005. The Tsushima Warm Current through Tsushima Straits estimated from ferry boat ADCP data. J. Phys. Oceanogr. 35, 1154–1168.

Taylor, G. I., 1919. Tidal friction in the Irish Sea. Philos. Tr. R. Soc. S.-A 220, 1–93.

Terwindt, J. H. J., 1971. Sand waves in the southern bight of the North Sea. Mar. Geol. 10, 51–67.

Trowbridge, J. H., Geyer, W. R., Bowen, M. M., Williams III, A. J., 1999. Near-bottom turbulence measurements in a partially mixed estuary: turbulent energy balance, velocity structure, and along-channel momentum balance. J. Phys. Oceanogr. 29, 3056–3072.

Trump, C. L., Marmorino, G. O., 1997. Calibrating a gyrocompass using ADCP and DGPS data. J. Atmos. Ocean. Tech. 14, 211–214.

Trump, C. L., Marmorino, G. O., 1998. Use of single-ping bottom-track ADCP data to characterize small-scale bathymetry. J. Atmos. Ocean. Tech. 15, 299–303.

Valle-Levinson, A., Li, C., Lwiza, K. M. M., 1995. The effects of channels and shoals on exchange between the Chesapeake Bay and the adjacent ocean. J. Geophys. Res. 100, 18,551–18,563.

Valle-Levinson, A., Li, C., Royer, T. C., Atkinson, L. P., 1998. Flow patterns at the Chesapeake Bay entrance. Cont. Shelf Res. 18, 1157–1177.

Van de Kreeke, J., 1978. Mass transport in a coastal channel, Marco River, Florida. Estuar. Coast. Mar. S. 7, 203–214.

Van de Kreeke, J., Dean, R. G., 1975. Tide-induced mass transport in lagoons. J. Waterway Div.-ASCE 101, 393–403.

Van de Kreeke, J., Robaczewska, K., 1993. Tide-induced residual transport of coarse sediment; application to the Ems estuary. Neth. J. Sea Res. 31, 209–220.

Van de Kreeke, J., Zimmerman, J. T. F., 1990. Gravitational circulation in well- and partially-mixed estuaries. In: Le Mehaute, B., Hanes, D. M. (Eds.), The Sea, Ocean Engineering Science 9 (Part A). John Wiley and Sons, New York, pp. 495–521.

Van den Berg, J. H., 1987. Bedform migration and bed-load transport in some rivers and tidal environments. Sedimentology 34, 681–698.

Van den Berg, J. H., Van Gelder, A., 1993. A new bedform stability diagram, with emphasis on the transition of ripples to plane bed in flows over fine sand and silt. Special publication of the International Association of Sedimentologists 17, 11–21.

Van der Vegt, M., Schuttelaars, H. M., De Swart, H. E., 2006. Modeling the equilibrium of tide-dominated ebb-tidal deltas. J. Geophys. Res. 111, F02013,doi:10.1029/2005JF000312.

Van Dijk, T. A. G. P., Kleinhans, M. G., 2005. Processes controlling the dynamics of compound sand waves in the North Sea, Netherlands. J. Geophys. Res. 110, F04S10,doi:10.1029/2004JF000173.

Van Dongeren, A. R., De Vriend, H. J., 1994. A model of morphological behaviour of tidal basins. Coast. Eng. 22, 287–310.

Van Ledden, M., 2003. Sand-mud segregation in estuaries and tidal basins. Ph.D. thesis, Delft University of Technology.

Van Leeuwen, S. M., Van der Vegt, M., De Swart, H., 2003. Morphodynamics of ebb-tidal deltas: a model approach. Estuar. Coast. Shelf S. 57, 1–9.

Van Rijn, L. C., 1984a. Sediment transport, part I: Bedload transport. J. Hydraul. Eng.-ASCE 110, 1431–1456.

Van Rijn, L. C., 1984b. Sediment transport, part II: Suspended load transport. J. Hydraul. Eng.-ASCE 110, 1613–1641.

Van Veen, J., 1935. Sand waves in the North Sea. Hydrographic Review 12, 21–29.

Van Veen, J., 1938. Water movements in the Straits of Dover. J. Cons. Perm. Int. Explor. Mer 13, 7–36.

Van Veen, J., 1950. Eb- en vloedschaar systemen in de Nederlandse getijwateren. Tijdschr. Kon. Ned. Aardrk. Gen. 67, 303–325.

Wang, Z. B., Louters, T., De Vriend, H. J., 1995. Morphodynamic modelling for a tidal inlet in the Wadden Sea. Mar. Geol. 126, 289–300.

Werner, B. T., Kocurek, G., 1997. Bedform dynamics: Does the tail wag the dog? Geology 25, 771–774.

Winkelmolen, A. M., Veenstra, H. J., 1974. Size and shape sorting in a Dutch tidal inlet. Sedimentology 21, 107–126.

Winterwerp, J. C., Wang, Z. B., Van der Kaaij, T., Verelst, K., Bijlsma, A., Meersschaut, Y., Sas, M., 2006. Flow velocity profiles in the Lower Scheldt estuary. Ocean Dyn. 56, 284–294.

Wong, K.-C., 2002. On the wind-induced exchange between Indian River Bay, Delaware and the adjacent continental shelf. Cont. Shelf Res. 22, 1651–1668.

Wong, K.-C., Garvine, R. W., 1984. Observations of wind-induced subtidal variability in the Delaware estuary. J. Geophys. Res. 89, 10,589–10,597.

Zimmerman, J. T. F., 1976a. Mixing and flushing of tidal embayments in the western Dutch Wadden Sea. Part I: Distribution of salinity and calculation of mixing time scales. Neth. J. Sea Res. 10, 149–191.

Zimmerman, J. T. F., 1976b. Mixing and flushing of tidal embayments in the western Dutch Wadden Sea. Part II: Analysis of mixing processes. Neth. J. Sea Res. 10, 397–439.

Zimmerman, J. T. F., 1980. Vorticity transfer by tidal currents. J. Mar. Res. 38, 601–630.

Zimmerman, J. T. F., 1992. On the Lorentz linearization of a nonlinearly dampened tidal Helmholtz oscillator. Proc. K. Ned. Akad. Wetensc. 95, 127–145.

Samenvatting

Begin 1998 werd een 'acoustic Doppler current profiler' (ACDP) onder het 'Schulpengat' gemonteerd. Het Schulpengat is een veerboot van de 'Texels Eigen Stoomboot Onderneming' (TESO). De TESO onderhoudt een permanente veerdienst in het Marsdiep, het zeegat tussen Den Helder en Texel in de westelijke Waddenzee. Dit proefschrift beschrijft analyses van stroomsnelheden en dieptes die met deze ADCP werden gemeten van begin 1998 tot eind 2005. Er worden drie onderzoeksvragen beantwoord: wat is de ruimtelijke en temporale variabiliteit in en wat zijn de mechanismen van $Q1$) instantane langs- en dwarsstromingen en watertransport, $Q2$) tijdsgemiddelde langs- en dwarsstromingen en watertransport en $Q3$) bodemvormen.

Hoofdstuk 2 gaat in op vragen $Q1$ en $Q2$. De bijdrage van het getij tot de langsstroming en watertransport wordt onderzocht met een harmonische analyse. Het watertransport wordt berekend door de oostwaartse snelheden te integreren langs het veerboottraject en over de waterdiepte. Met maximaal 144 getijfrequenties wordt 98% van de variabiliteit in het watertransport verklaard door het getij. De astronomische M_2 component is de belangrijkste frequentie en heeft een amplitude van 66×10^3 m^3 s^{-1} voor het watertransport. De op één na grootste is de S_2 component (27% van M_2). De getijgolf vervormt in de ondiepe Waddenzee en ondiepwatergetijden zoals $2MS_2$ (13.7% van M_2), $2MN_2$ (10.9%), M_4 (10.3%), M_6 (10%) worden ook gegenereerd. Gedurende vloed is de instroom symmetrisch in de geul met de hoogste snelheden in het midden en aan het oppervlak (maximaal 2 m s^{-1}). De uitstoom tijdens eb is asymmetrisch met de hoogste snelheden in de noordelijke helft van het zeegat. Deze verschillen resulteren in een getijgemiddelde stroming van ~0.1 m s^{-1} in de vloedriching in de zuidelijke helft van het Marsdiep en in de ebrichting in de noordelijke helft.

Hoofdstuk 3 beantwoordt vraag Q1. De metingen met het Schulpengat laten een grote variabiliteit zien in de instantane dwarsstroming (parallel aan de noord-zuid as) in het Marsdiep tijdens gemengde en gelaagde condities. De IJsselmeersluizen spuien zoetwater in de westelijke Waddenzee. In periodes dat er weinig gespuid wordt is de waterkolom goed gemengd. In periodes dat er veel gespuid wordt kan de waterkolom gelaagd zijn in dichtheid. Gedetailleerde metingen van dwarsstroomsnelheden en waterdichtheid met het onderzoeksschip de 'Navicula' geven inzicht in de mechanismen achter de dwarsstroming. Tijdens gemengde condities worden de grootse dwarstroomsnelheden van ~0.05 m s^{-1} gemeten tijdens maximale vloed. Gedurende vloed wordt het water in een bocht naar links (naar het noorden) gedwongen. De resulterende centrifugale versnelling veroorzaakt een zuidwaartse stroming aan het oppervlak en een noordwaartse stroming bij de bodem. De dwarssnelheden in gemengde condities tijdens eb zijn doorgaans klein (~0.01 m s^{-1}). Tijdens dagen met gelaagde condities zijn de dwarssnelheden veel groter (maximaal 0.4 m

s^{-1}). Deze snelheden ontstaan met name door horizontale dichtheidsgradiënten in combinatie met een sterke demping van de turbulentie door de gelaagdheid. Tijdens vloed heeft het water bij de bodem in het midden van de geul een grotere dichtheid dan het water aan de geulrand. Dit veroorzaakt twee circulatiecellen met convergentie aan het wateroppervlak. Het water dat tijdens eb uit de zuidelijke Malzwin geul stroomt is doorgaans zoeter dan het water uit de noordelijke Texelstroom geul. Het resulterende horizontale dichtheidsverschil veroorzaakt een noordwaartse stroming aan het oppervlak en een zuidwaartse stroming bij de bodem. Deze studie heeft aangetoond dat dichtheidsverschillen wel degelijk van belang zijn voor de waterbeweging in het Marsdiep.

Vraag Q2 wordt beantwoord in Hoofdstuk 4. Een eenvoudig wiskundig model van het Marsdiep en het naastgelegen Vlie bekken wordt toegepast om de mechanismen achter het laagfrequente watertransport in het Marsdiep te achterhalen. Dit transport gebeurd op tijdschalen groter dan drie dagen. Het Marsdiep heeft een open verbinding met het Vlie en in het model worden deze bekkens geschematiseerd als een rechte geul met aan weerskanten een opening naar de Noordzee. Het gemeten tijdsgemiddelde watertransport is 2098 m^3 s^{-1} en gaat van het Vlie, via het Marsdiep, naar de Noordzee. Het voorspelde laagfrequente watertransport heeft dezelfde richting maar is veel kleiner. In het model wordt dit transport hoofdzakelijk bepaald door het getij, zoetwaterafvoer en zuidwestenwinden. De variabiliteit in het laagfrequente watertransport wordt echter gedomineerd door zuidwesten- en noordwestenwinden. Zuidwestenwinden 'duwen' water van de Noordzee via het Marsdiep naar het Vlie en omgekeerd. In bekkens met één zeegat wordt het laagfrequente watertransport bepaald door windgerelateerde waterstandsveranderingen op de oceaan. Deze studie laat zien dat dit mechanisme voor het Marsdiep-Vlie systeem minder belangrijk is.

Hoofdstukken 5 en 6 gaan in op vraag Q3. Hoofdstuk 5 beschrijft hoe gedetailleerde bodemkaarten van het Marsdiep worden gemaakt met de waterdieptes die gemeten worden met de ADCP van de veerboot. Deze bodemkaarten tonen bodemvormen (zandgolven) met gemiddelde hoogtes van 3 m en lengtes van 200 m in de zuidelijke helft van het Marsdiep en zandgolven met kleinere afmetingen in de noordelijke helft van het Marsdiep. De bodemkaarten geven ook de veranderingen weer in de tijd. Alle zandgolven bewegen in de vloedrichting met snelheden van maximaal 90 m j^{-1} (meter per jaar). Opmerkelijk is dat de zandgolven in het noorden sneller bewegen in de wintermaanden en dat zij de grootste hoogte bereiken in de herfst. In Hoofdstuk 6 worden de watersnelheden gemeten met de ADCP gebruikt om inzicht te verkrijgen in de migratierichting en snelheid van de zandgolven en de seizoensvariabiliteit. De watersnelheden worden toegepast in transportformules die het zandtransport direct boven de bodem berekenen. Het 'voorspelde' zandtransport wordt gemiddeld over de tijd en vergeleken met het bodemtransport gebaseerd op de migratiesnelheid en dimensies van de zandgolven ('gemeten' transport). In het zuiden van het Marsdiep komen de grootte en richting van het voorspelde en gemeten transport overeen. Echter, in het noorden zijn de richtingen tegenovergesteld. Een verklaring is dat in het noorden, waar het zand fijner is dan in het zuiden, suspensietransport relatief belangrijk is. Een verklaring voor de seizoensvariabiliteit is een toename van het suspensietransport in de winter door het getij en/of door een hogere kinematische viscositeit van het water vanwege een lagere watertemperatuur. Stormen en estuariene circulatie blijken niet van belang voor de variabiliteit.

Dankwoord

Dit proefschrift is mede tot stand gekomen met de hulp van een aantal mensen die ik hierbij wil bedanken. Herman Ridderinkhof, ik dank je voor je advies, je beschikbaarheid, en je geduld. Sjef Zimmerman, dank je voor het doorlezen van de manuscripten en je suggesties. Leo Maas, jouw handige tips waren zeer waardevol. Theo Gerkema en Leo, bedankt voor het beantwoorden van al mijn fysica vragen. Frans Eijgenraam, zonder jou zou er geen veerbootdata in een hanteerbare vorm zijn. Hendrik van Aken bedankt voor het beschikbaar maken van de NIOZ jetty data. Sven Ober, Margriet Hiehle en Theo Hillebrand, ik dank jullie voor het faciliteren van de CTD en slipmetingen. De bemanning van de Navicula wordt gewaardeerd voor hun koersvastheid, de assistentie aan boord en de lekkere maaltijden. De medewerkers van de afdeling Marine Technologie worden bedankt voor de assistentie aan de wal. Dank je Katja Philippart, voor het beschikbaar stellen van de Navicula data. Wim Boer en Rineke Gieles en anderen van de afdeling Marine Chemie & Geologie worden bedankt voor de assistentie met het bepalen van de korrelgrootteverdelingen. Bert Aggenbach, ik waardeer je hulp met diverse foto's. Ik dank mijn voormalige kamergenoten Lucas Merckelbach voor het geduldig aanhoren van al mijn vragen en Janine Nauw voor de openhartige gesprekken. Voorts, waardeer ik de interactie met en de ondersteuning van collega's van het NIOZ en andere instituten die ik niet met naam genoemd heb. Stagiaires Maarten Bangma, Jaap de Vos, Frans Buschman en Renske Gelderloos ik dank jullie voor jullie pionierswerk aan het zandgolfonderzoek. Maarten Kleinhans, je tips m.b.t. zandtransport en zandgolven waren zeer welkom. Edwin Elias en Marcel Stive, bedankt voor de samenwerking en jullie flexibiliteit. Maarten van der Vegt bedankt voor je hulp met LATEX. Ook wil ik de TESO bedanken voor het onderseunen van de veerbootmetingen, Rijkswaterstaat voor het beschikbaarstellen van de bodemdata, waterstanden en spuidata en het Koninklijk Nederlands Meteorologisch Instituut voor de winddata. Vrienden, ik dank jullie voor de gezelligheid, de mentale afleiding en ondersteuning: Oscar en Jeroen, Wouter en Maaike, Erik en Leontine, Eric en Sabina, William en Ans, Martijn en Esther, Andre en Merel, Bas en anderen. Ik waardeer de interesse voor mijn onderzoek van mijn ouders, Frits en Renet, mijn zus Liza en haar vriend Kees en Ann haar ouders, Lonny en Mary. Ik dank viervoeters Lucy en Frank voor 'intelligently designing' deze wereld (wat zouden ze anders doen met hun tijd?). En uiteraard oneindig veel zoenen voor jou, Ann. Tenslotte waardeer ik Bill Watterson voor het bedenken van het geweldige levensmotto "there's treasure everywhere".

Maarten Buijsman, Los Angeles, 26 augustus 2007

About the author

Maarten Buijsman was born on November 28, 1973, in Den Helder, the Netherlands. While growing up, he spent his summer vacations on the island of Vlieland in the Wadden Sea. During these vacations, he began appreciating the natural beauty of the beaches, dunes, salt marshes, and the sea. After graduating from high school in the town of Den Helder in the summer of 1992, Maarten pursued an MSc degree in Civil Engineering at Delft University of Technology, the Netherlands. He specialised in hydraulic engineering and graduated *cum laude* in August 1997. After working at WL|Delft Hydraulics in Delft as a Coastal Engineer from September 1997 to February 1998, he moved to Olympia, Washington State, USA, to work as a coastal engineer at the Department of Ecology with the Southwest Washington Coastal Erosion Study. After enjoying hard work, many mountain adventures, and other life-enriching experiences, he moved back to the Netherlands to start his PhD research in February 2002 at the Physical Oceanography department of the Royal Netherlands Institute for Sea Research, located on the island of Texel. Maarten lived in Den Helder and traveled to work by ferry. Remarkably, the ferry also collected current and depth data that Maarten had to analyse as part of his research. It is worth mentioning that his grandfather Maarten Cornelis de Gorter was the director of the ferry company 'Texels Eigen Stoomboot Onderneming' (TESO) from 1963 to 1974. On August 1, 2007, Maarten started working as a postdoctoral researcher at the Department of Atmospheric and Oceanic Sciences of the University of California, Los Angeles, USA. On October 10, 2007, Maarten will receive his PhD degree at Utrecht University. For questions or remarks, Maarten can be reached by email at `maartenbuijsman@hotmail.com` or `mbui@atmos.ucla.edu`.

List of author's publications

Publications related to this thesis

Buijsman, M. C., Ridderinkhof, H., 2007. Long-term ferry-ADCP observations of tidal currents in the Marsdiep inlet. J. Sea Res. 57, 237–256.

Buijsman, M. C., Ridderinkhof, H., 2007. Water transport at subtidal frequencies in the Marsdiep inlet. J. Sea Res., doi: 10.1016/j.seares.2007.04.002.

Buijsman, M. C., Ridderinkhof, H., submitted. Long-term evolution of sand waves in the Marsdiep inlet. I: High-resolution observations. Cont. Shelf Res.

Buijsman, M. C., Ridderinkhof, H., submitted. Long-term evolution of sand waves in the Marsdiep inlet. II: Relation to hydrodynamics. Cont. Shelf Res.

Buijsman, M. C., Ridderinkhof, H., submitted. Variability of secondary currents in a weakly stratified tidal inlet with low curvature. Cont. Shelf Res.

Other publications

Stive, J. F., Capobianco, M., Wang, Z. B., Ruol, P., Buijsman, M. C., 1998. Morphodynamics of a tidal lagoon and the adjacent coasts. In: Dronkers, J., Scheffers, M. (Eds.), Physics of Estuaries and Coastal Seas: Proceedings of the 8th International Biennial Conference on Physics of Estuaries and Coastal Seas. Balkema, Rotterdam, pp. 397–407.

Cowell, P. J., Stive, M. J. F., Niedoroda, A. W., Swift, D. J. P., De Vriend, H. J., Buijsman, M. C., Nicholls, R. J., Roy, P. S., Kaminsky, G. M., Cleveringa, J., Reed, C. W., De Boer, P. L., 2003. The coastal-tract (part 2): Applications of aggregated modeling of lower-order coastal change, J. Coast. Res. 19, 828–848.

Buijsman, M. C., Kaminsky, G. M., Gelfenbaum, G., 2003. Shoreline change associated with jetty construction, deterioration, and rehabilitation at Grays Harbor, Washington. Shore and Beach, 71, 15–22.

Elias, E. P. L., Cleveringa, J., Buijsman, M. C., Roelvink, J. A., Stive, M. J. F., 2006. Field and model data analysis of sand transport patterns in Texel tidal inlet (the Netherlands). Coast. Eng. 53, 505–529.

Ruggiero, P., Buijsman, M. C., Kaminsky, G. M., Gelfenbaum, G., in press. Modeling the effects of wave climate and sediment supply variability on large-scale shoreline change. Mar. Geol.